NASA Contractor Report 156849

Analysis and Geological Interpretation of Gravity Data from GEOS-3 Altimeter

(NASA-CR-156849) ANALYSIS AND GEOLOGICAL INTERPRETATION OF GRAVITY DATA FROM GEOS-3 ALTIMETER Final Report, May 1978 (Lamont-Doherty Geological Inst.) 171 p HC A08/MF A01 CSCL 08G G3/46
N79-14656
Unclas
42056

M. Talwani, A.B. Watts, and M.E. Chapman

December 1978

National Aeronautics and
Space Administration

Wallops Flight Center
Wallops Island, Virginia 23337
AC 804 824-3411

NASA Contractor Report 156849

Analysis and Geological Interpretation of Gravity Data from GEOS-3 Altimeter

M. Talwani, A.B. Watts, and M.E. Chapman
Lamont-Doherty Geological Institute
Columbia University
Palisades, New York 10964

Prepared under Contract No. NAS6-2519

National Aeronautics and
Space Administration

Wallops Flight Center
Wallops Island, Virginia 23337
AC 804 824-3411

TABLE OF CONTENTS

INTRODUCTION

Existing gravity data in the Lamont-Doherty data library was used to construct or update gravimetric geoids in the northwest Pacific Ocean, Indian Ocean, and north Atlantic. These activities are described in detail in Chapters 2, 3, and 4. Our approach to constructing geoid maps differed somewhat from the approach of other investigators. We did not simply take the available data and use that to obtain 1° by 1° averages. On the other hand, a considerable amount of effort was spent in examining the shipboard data for accuracy, cross-checks, etc., and the knowledge of bathymetry was used to interpolate and extropolate data and therefore the deduction of 1° by 1° averages were not routine tasks. (In part, work was supported by other contracts and grants.) The averaged data was then used to obtain gravimetric geoids by employing Stokes' Formula.

Chapter 5 deals with techniques for interpretation of geoid data. Hithertofore the geoid has been an end product of geodetic investigations but the data from the GEOS-3 altimeter has changed that. The geoid undulations now will be used to interpret geological features within the earth. Therefore it was necessary to develop a set of procedure and computer programs which are principally aimed at obtaining the geoid undulations caused by bodies of known geometry. It is felt that these programs are going to be basic to the geophysical interpretation of geoid anomalies.

Chapter 6 discusses observed geoidal anomalies over oceanic structures. The importance of this chapter is simply to demonstrate that not only can the altimeter measure the geoid, but that large enough geoid undulations are actually present which can then be used for the interpretation of geological features.

The presence of these large geoidal undulations over distinct geological structures points to future directions in satellite altimetry in the support of geophysics. Chapter 7 discusses this aspect of the application of GEOS-3 data. Significantly large geoidal undulations are present over continental margins, over mid-ocean ridges, over trenches, over seamounts, and over large bodies of sediment deposited as in river deltas. Geological interpretation of these geoidal anomalies would be a very important task for the future.

An important amount of effort was expended in the rather routine job of examining the altimeter data received on tape, editing it, and reformatting it for use on the Lamont-Doherty computer system. In addition, programs were written for display of data in profile form and in map form at various projections. These activities were basic to the examination of the GEOS-3 data, but because of the routine nature, they will not be covered at any length in this report.

GRAVIMETRIC GEOID IN THE NORTHWEST PACIFIC OCEAN

INTRODUCTION

The figure of the Earth or geoid can be determined from terrestrial gravity and data obtained from the analysis of satellite orbits. The determination of the geoid from satellite observations has developed rapidly during the past 12 years and it is now possible to estimate the long-wavelength components of the geoid with considerable accuracy. Satellite derived models currently used in geophysical studies are the Smithsonian Astrophysical Observatory Standard Earth models SE 2 (Gaposchkin and Lambeck, 1971) and SE 3 (Gaposchkin, 1974) and the NASA Goddard Space Flight Center Earth Models GEM 6 (Lerch et al., 1974) and GEM 8 (Wagner et al., 1976). These models are combination solutions and include terrestrial gravity data wherever available. The SE 2 and GEM 6 models were developed through to degree and order $n = 16$, SE 3 to $n = 18$ and GEM 8 to $n = 25$. These models resolve information in the geoid with wavelengths of about 1600 km and greater.

The satellite derived models are in close agreement over the continents but large discrepancies occur over oceanic regions, particularly in the southern hemisphere (for example, Marsh and Vincent, 1974). Two problems contribute to these discrepancies. First, satellite tracking stations are restricted to land areas so that individual satellites can be "unseen" for large portions of their track over the oceans. Second, surface gravity data which contribute most to the high order harmonics ($n > 11$) of these solutions are sparse over the oceans. Although surface gravity data is relatively good in the northern hemisphere, coverage is poor in the southern hemisphere; particularly in the South Atlantic, Southeast Indian and Central Pacific oceans.

The most accurate geoids in oceans areas have been constructed using 1° x 1° averages of gravity data from well surveyed areas. 1°x 1° gravimetric geoids have been constructed of the western North Atlantic (Talwani et al., 1972) and Indian oceans (Kahle and Talwani, 1973). Marsh and Vincent (1974) constructed a global 1° x 1° geoid based on the GEM 6 Earth model and about 26,000 gravity anomaly averages. However, the surface data used in this study covers only 29% of the Earth's surface. The data set is most incomplete for the South Atlantic, Southeast Indian and Northwest Pacific oceans. These geoids contain information with wavelengths of 220 km and greater and differ from the satellite derived solutions by as much as 20 meters.

Recent developments in satellite altimetry (McGoogan et al., 1975; Leitao and McGoogan, 1975) currently provide the best opportunity to precisely define the geoid in oceanic regions. Satellite radar altimeters measure the distance between the ocean surface and the altimeter which, when subtracted from the calculated height of the altimeter above the reference ellipsoid, gives the geoid undulation. The accuracy of data obtained on the SKYLAB-4 mission (McGoogan et al., 1975) is estimated at a few meters and forthcoming missions (such as SEASAT-A) may have an accuracy of a few tens of cm. However, altimeter data coverage on a global basis is not yet available.

The purpose of this paper is to present a new 1° x 1° gravimetric geoid of the Northwest Pacific ocean. The geoid has been computed using 3708 1° x 1° free-air anomaly averages, based on about 147,000 surface ship and pendulum gravity measurements. We discuss the geoid in relation to tectonic features of the Northwest Pacific. Comparisons are made between the gravimetric geoid and recent satellite derived Earth models as well as available satellite radar altimeter data. Based on these comparisons the new geoid is estimated to be accurate to about ±6 meters.

GRAVITY MEASUREMENTS

Submarine pendulum measurements

The earliest gravity measurements in the Northwest Pacific were obtained with the Vening Meinesz pendulum apparatus on board a submarine. This apparatus was used extensively until about 1954 (Worzel, 1965). Additional measurements were obtained with a Russian built pendulum apparatus, mainly in the Sea of Okhotsk (Gainanov, 1955). The location of the 649 pendulum measurements used in this study are shown in Figure 1. These measurements are estimated to be reliable to about ±3 mgal (Worzel, 1965).

Surface-ship measurements

Since about 1959 gravity measurements in the Northwest Pacific have been obtained mainly with beam-type gravimeters on board U.S. Japanese, Russian and Canadian research vessels. The locations of the 147,000 surface ship measurements used in this study are shown in Figure 1. The accuracy of the individual measurements differ according to the type of instrumentation and navigation used. From studies of discrepancies at intersecting ship's tracks (Watts et al., 1976) it is estimated that for cruises which used satellite navigation and cross-coupling corrections individual measurements are accurate to about ±5 mgal. However, somewhat larger uncertainties would be expected for cruises which used celestial navigation and did not correct for cross-coupling.

The principal sources of the surface-ship measurements are:

a) Lamont-Doherty Geological Observatory of Columbia University during VEMA cruises 19, 20, 21, 24, 28; ROBERT D. CONRAD cruises 10, 11, 12, 13, 14 and ELTANIN cruise 30.

b) Institute of Geophysics and Planetary Physics of University of California at Los Angeles and Scripps Institute of Oceanography, San Diego during ARGO cruises "MONSOON" 1, 2 and "LUSIAD" 1, 2 (Helfer et al., 1963; Caputo et al., 1964) and WASHINGTON cruise "TASADAY' 7 (Sclater, personal communication).

c) Bedford Institute of Oceanography during HUDSON cruise, 1970 (Von Arx et al., 1970).

d) Environmental Science Services Administration (ESSA now NOAA) during PIONEER cruises, B, C, G through I (U.S. Department of Commerce, 1964) and PIONEER and SURVEYOR "SEAMAP" cruises (Chiburis et al, 1972a, 1972b, 1972c; Dowling et al., 1972a, 1972b, 1972c).

e) Institute of Oceanology, Moscow during VITYAZ cruises 49, 53 (Kogan, personal communication).

f) Ocean Research Institute, University of Tokyo during HAKUHO-MARU cruises 1965, 1968, 1971, 1972 and UMITAKA-MARU cruises 1963, 1967 (Segawa and Bowin, personal communication; Tomoda et al., 1968, 1970, 1973).

g) Hawaii Institute of Geophysics during DAMPIER cruise (Rose and Tracy, 1971), MAHI cruise (Khan et al., 1971) and CHARLES H. GILBERT cruise (Rose and Belshe, 1965; Malahoff and Woollard, 1968).

h) United States Coast and Geodetic Service during SHOUP cruises 1963-1964 (data obtained from National Geophysical and Solar Terrestrial Data Center, Washington, D.C.).

i) Pacific Oceanographic Laboratory (POL now NOAA) during OCEANOGRAPHER circum-Pacific cruises (data obtained from National Geophysical and Solar Terrestrial Data Center, Washington, D.C.).

A large number of these measurements have been incorporated in new free-air anomaly maps of the Northwest Pacific (Fig. 1; Watts and Talwani, 1975; Watts, 1975; Watts, 1976a; Watts et al., 1976).

Terrestrial measurements

Gravity measurements in land regions of the Northwest Pacific were obtained mainly from the Defense Mapping Agency, St. Louis, Missouri, We have used publishing listings of land gravity data wherever available. The free-air anomaly maps of Tomoda (1973) were used in the region of Japan. New maps were constructed for Korea, Philippine Islands and Taiwan. Maps could not be constructed for Vietnam, the mainland areas of China or the USSR due to a lack of available measurements.

The gravity measurements were reduced to free-air gravity anomalies using the International Gravity Formula of 1930 (flattening 1/297.0):

$$g = 9.78049\ (1 + 0.0052884 \sin^2 \theta - 0.0000059 \sin^2 \theta) \qquad (1)$$

where g is theoretical gravity and θ is the latitude.

DETERMINATION OF THE GRAVIMETRIC GEOID

The geoid undulations N were computed from surface gravity data using the simplified form of Stokes' equation (Heiskanen and Vening Meinesz, 1958, p. 65):

$$N = \frac{1}{4\pi\ Rg} \iint_a \Delta g \quad S(\psi) \quad da \qquad (2)$$

where $S(\psi)$ is Stokes' function, ψ is the central angle from the computation point to da, da is the differential area in which the gravity anomaly Δg based on some reference ellipsoid is given, g is mean value of gravity and R is the mean radius of the Earth. Equation (2) is valid provided the reference ellipsoid has the same potential as the geoid and the same mass of the Earth.

The practical computation of the geoid follows procedures described earlier by Strange et al. (1972), Talwani et al. (1972) and Kahle and Talwani (1973). The details of these procedures are:

1. Construct 1° x 1° free-air anomaly averages from maps where they are available and elsewhere from averages along individual ship's tracks.

2. Compute the satellite derived gravity field using the GEM 6 Earth model (Lerch et al., 1974).

3. Subtract the GEM 6 model from the 1° x 1° gravity anomaly averages to obtain 1° x 1° difference gravity anomalies.

4. Compute 1° x 1° geoid differences from these difference gravity anomalies using the simplified form of Stokes' equation in (2).

5. Add the 1° x 1° geoid differences to the GEM 6 geoid to obtain the total geoid.

Equation (2) requires that gravity anomalies are specified over the entire Earth's surface. However, since Stokes' function $S(\psi)$ changes rapidly near the computation point, it is sufficient to use 1° x 1° gravity anomaly averages within the map area and the GEM 6 field elsewhere. The GEM 6 field was also used within the map area where 1° x 1° averages were unavailable or could not be reliably estimated. These included parts of the Pacific basin and the USSR, China and Vietnam. Since difference gravity will be zero outside, Stokes' integration was only carried out within the map area.

The GEM 6 Earth model has been used as the reference field in the computation rather than other available satellite derived models. Comparisons in the next section show that the GEM 6 field is a good representation of the long-wavelength gravity field in the map area. The choice of a different satellite derived model can result in changes of up to 5 meters in the total geoid with wavelengths of about 4000 km (Marsh and Vincent, 1974). Since this study utilizes 1° x 1° gravity anomaly averages wherever available while Marsh and Vincent (1974) only used surface data within a 10° circle of the computation point, our solution may be less sensitive to the choice of satellite models.

The parameters assumed in equation (1) were:

$g = 9.789\ m/sec^2$

$R = 6371\ km$

Thus even though equation (2) gives geoid undulations with respect to a reference ellipsoid of some equatorial radius a_e, it is unnecessary to specify the value of a_e. It is that value which gives an ellipsoid of the same volume as the actual geoid.

REGIONAL GRAVITY ANOMALIES

1° x 1° free-air anomaly averages

1° x 1° free-air anomaly averages have been constructed from all available surface-ship, pendulum and land measurements in the Northwest Pacific. Averages were obtained directly from free-air anomaly contour maps where available (Fig. 1) and elsewhere as averages along individual ship's tracks. The averages along ship's tracks were constructed only if more than 10 measurements were present in an individual 1° x 1° 'square.' Pendulum measurements were arbitrarily weighted equivalent to 5 surface ship measurements because of their higher overall accuracy. A total of 3708 averages were obtained (Table 1), indicating an average of about 39 measurements in each 'square.'

The overall accuracy of the 1° x 1° free-air anomaly averages constructed from the maps is considered greater than those obtained along individual ship's tracks for two reasons. First, the free-air anomaly maps are based on bathymetry allowing a more accurate estimate of the gravity field to be made between ship's tracks. Second, systematic errors (which frequently occur in marine gravity surveys) are corrected for the most part in the contouring process. The accuracy of the averages obtained along ship's tracks can be estimated by examining the difference between 1° x 1° averages determined from different ships tracks within the same 1° x 1° 'square.' The RMS difference obtained in the Central Pacific is ±13 mgal indicating a probable error in each 1° x 1° average of about ±9 mgal.

The most prominent features of the 1° x 1° free-air anomaly map (Fig. 2) are the belts of large amplitude positive and negative anomalies associated with active island arc-trench systems in the Northwest Pacific. The average anomalies reach maximum values over the Japan, Kuril and Izu-Bonin arcs (+158 to +193 mgal) and minimum values over adjacent deep-sea trenches (-227 to -247 mgal). The Mariana, central Aleutian and Philippine arc-trench systems are associated with smaller maximum (+103 to +144 mgal) and minimum (-103 to -181 mgal) values. 1° x 1° free-air anomaly averages less than about ±58 mgal are associated with the western Aleutian and Ryukyu arc-trench systems.

A broad belt of positive gravity anomalies occurs seaward of deep-sea trenches (Fig. 2). These positive anomalies, termed the Outer Gravity High (Watts and Talwani, 1974), exceed +50 mgal seaward of the central Aleutian and Kuril trenches. The width of the positive anomalies changes seaward of different trenches. These anomalies are about 700 km wide seaward of the eastern Aleutian trench but decrease to about 250 km off the western Aleutians. Off the Kuril trench they are about 400 km wide decreasing to 300 km off the Izu-Bonin, Japan and Mariana trenches.

A variable pattern of 1° x 1° average anomalies is associated with the marginal basins behind island arcs. The Aleutian and Bowers basins, behind the central and eastern Aleutian arc, are associated with nearly zero anomalies. Positive anomalies in the range +15 to +30 mgal occur over the Kamchatka, Okhotsk Sea, Japan Sea, Parece Vela and Shikohu basins. In contrast, the West Philippine and South China sea basins are associated with negative anomalies in the range 0 to -15 mgal.

The 1° x 1° free-air anomaly field are remarkably uniform over the Pacific basin and generally in the range from -5 to -20 mgal. Large amplitude positive and negative anomalies with wavelengths of about 300 km disturb this field over the Hawaiian ridge (+331 mgal to -80 mgal), Emperor seamounts (+129 to -65 mgal) and Marcus-Necker ridge (+138 mgal). Smaller amplitude positive anomalies of up to +50 mgal with wavelengths of about 4000 km occur over the southeastern end of the Hawaiian ridge and the northern end of the Line islands ridge.

Comparison of the 10 x 10° free-air anomaly averages with the GEM 6 field

The 1 x 1° free-air anomaly averages (Table 1) were used to construct 10 x 10° averages in order to compare the surface gravity field to the satellite derived GEM 6 field (Lerch et al., 1974). The 10 x 10° averages were computed from at least 51 1 x 1° averages in each 10 x 10° 'square.' Each 10 x 10° average was an independent estimate so that an individual 1 x 1° average was not used more than once. The 10 x 10° average field and GEM 6 field resolve information in the Earth's gravity field with wavelengths longer than about 2200 km. Whereas the 10 x 10° field is based only on surface data the GEM 6 field incorporates both satellite derived and surface data.

The most prominent features of the 10 x 10° free-air anomaly map (Fig. 3) are positive anomalies with wavelengths of about 4400 km over the borders of the Northwest Pacific and negative anomalies with similar wavelengths over its interior. Positive anomalies, which reach maximum values of up to +30 mgal, occur over the eastern Aleutian, Japan, Kuril and Philippine island arc-trench systems. The eastern Aleutian high reaches its maximum value (+23 mgal) over the Gulf of Alaska, seaward of the eastern Aleutian trench. In contrast, the Japan-Kuril high reaches its maximum value over the Japan and Okhotsk marginal basins, landward of the arc. Positive anomalies do not occur over the Ryukyu, Izu-Bonin, Mariana and western Aleutian arc-trench systems (Fig. 3). The central part of the Pacific is associated with negative anomalies which reach minimum values of -18 mgal over deep, smooth sea-floor between the Shatsky rise and Hess rise. These negative anomalies are interrupted by a small amplitude positive anomaly of +8 mgal with wavelengths of about 3800 km over the southeastern end of the Hawaiian ridge.

There is a close agreement between the surface 10 x 10° free-air anomaly and the satellite derived GEM 6 fields, particularly over the borders of the Northwest Pacific and the southeastern end of the Hawaiian ridge (Fig. 3). The largest differences occur over the Pacific basin. In general, the GEM 6 field is more negative over the Pacific basin than the observed surface field. The GEM 6 field also shows a broad positive anomaly over the Line islands ridge which does not appear in the observed field.

DESCRIPTION OF THE 1 x 1° DIFFERENCE GEOID

The GEM 6 gravity field (Fig. 3) was subtracted from the 1 x 1° free-air anomaly averages (Table 1; Fig. 2) to obtain 1 x 1° difference gravity anomalies. The 1 x 1° difference geoid (Fig. 4) was then computed from the 1 x 1° difference gravity anomalies using equation (2). As indicated in previous studies (for example, Strange et al., 1972; Talwani et al., 1972) two precautions should be taken in the computations. First the GEM 6 field and the 1 x 1° free-air anomaly averages should be referred to the same reference ellipsoid. In this study the International Reference Ellipsoid (flattening 1/297.0) was used. Second, the difference between the 1 x 1° free-air anomaly averages based on the 1930 International Gravity Formula and the GEM 6 field based on geopotential coefficients with $n \geq 2$ should average close to zero over the map area. The areal average of the 1 x 1° difference anomalies over the map area was determined to be -0.2 mgal, indicating a close agreement between the GEM 6 field and the 1 x 1° free-air anomaly averages.

The difference geoid (Fig. 4) resolves geoid information with wavelengths of 220 to 2200 km, which cannot be seen in satellite derived solutions. The RMS difference geoid undulation is ±5.2 meters and values range from a maximum of +19 meters over Hawaii to a minimum of -31 meters at the junctions of the Aleutian and Kuril trench. The "observed" RMS difference is similar to the estimate of ±5.6 meters obtained by Rapp (1973) from predictive models for the behavior of the geoid.

The most prominent difference geoid undulations occur over the island arc trench systems of the Northwest Pacific (Fig. 4). Geoid heights of up to +10 meters are associated with active regions of the Japan, Izu-Bonin and Mariana arcs and geoid lows of up to -14 meters with adjacent deep-sea trenches. The eastern Aleutian, Philippine and Ryukyu arc-trench systems correlate with smaller amplitude geoid undulations of ± 6 meters. An intensive geoid low of -16 meters is associated with the Kuril trench. The absence of a complimentary geoid high over the Kuril arc is due in part to the lack of reliable gravity data in the Kuril islands and Kamchatka.

The seafloor seaward of deep-sea trenches in the Northwest Pacific is characterized by geoid highs of +3 to +6 meters. These highs are most prominent seaward of the Aleutian and Kuril trenches but can also be distinguished seaward of the Izu-Bonin trench. Similar amplitude geoid highs have been determined seaward of the Java and Sumatra trenches in the northeast Indian ocean (Kahle and Talwani, 1973).

A variable pattern of difference geoid undulations is associated with the marginal basins of the north and western Pacific. Geoid lows of up to -18 meters occur over the Japan Sea, Okhotsk Sea, South China Sea and West Philippine basins. In contrast, the Shikoku, Parece Vela and Mariana basins correlate with geoid highs of up to +9 meters. The West Philippine and Parece Vela basins are separated by a prominent N-S trending gradient (Fig. 5).

The difference geoid over the Pacific basin is relatively smooth. Geoid highs locally reach +19 meters over the Hawaiian ridge (Fig. 6). The difference geoid is regionally positive southeast of a line between the Mariana islands and Alaska since the GEM 6 gravity field is generally more negative in this region that the observed field (for example, Fig. 3).

SIGNIFICANCE OF THE TOTAL GEOID

The GEM 6 geoid referred to the best fitting reference ellipsoid (flattening 1/298.2) is shown in Figure 7. The total gravimetric geoid (Fig. 8) was obtained by adding the 1 x 1° difference geoid (Fig. 4) to the GEM 6 geoid (Fig. 7). These geoids are of tectonic significance since they contain information on density inhomogeneities in the Earth. The total geoid (Fig. 8) reveals geoidal information with wavelengths of about 220 km and greater.

The main features of the total geoid (Fig. 8) are long-wavelength (greater than about 2200 km) geoid highs southeast of the Philippine Islands and Alaska and geoid lows over the Pacific basin. These long-wavelength components of the geoid show no obvious relationship to surface geological features. The steep northeast boundary of the Philippine 'high' occurs over relatively deep smooth seafloor between the Hawaiian ridge and north of New Guinea. Thus the Pacific basin 'low' apparently occurs within the

Pacific plate but does not define the extent of it. Although the causes of these individual long-wavelength undulations is unclear, they are most probably caused by processes occurring deep in the Earth.

Prominent geoid undulations with wavelengths of about 2200 km occur over the Hawaiian ridge and the eastern part of the Philippine sea. Geoid undulations over the Hawaiian ridge correlate closely with the extent of the Hawaiian swell (Fig. 6). Watts (1976b) suggested the swell and its associated regional gravity anomalies are maintained by some pattern of flow occurring beneath the Pacific plate. Geoidal highs occur over the Shikoku, Parece Vela and Mariana marginal basins. These highs may be related to a dense downgoing slab which descends beneath these arcs. However, there are two problems with this interpretation. First, the dip of the downgoing slab, estimated from earthquake hypocenters, changes rapidly along these arcs while the geoid high is nearly constant in width. Second, there is an absence of a prominent geoid high behind the central Aleutian and Kuril island arcs even though a dense downgoing slab underlies both these arcs. This suggests the geoid high may be more closely related to the processes which generate oceanic crust in marginal basins than a dense downgoing slab.

Of particular tectonic significance are the short wavelength (about 220 to 900 km) geoid highs which occur seaward of deep-sea trenches in the Northwest Pacific. A nearly continuous belt of geoid highs extends from seaward of the Aleutian trench to about 28°N along the Izu-Bonin trench. These geoidal highs correlate closely with a regional rise in seafloor topography seaward of these trenches. Watts and Talwani (1974) have interpreted the regional rise and its associated gravity anomaly as caused partly by flexure of a strong Pacific plate as it approaches a deep-sea trench.

EVALUATION OF THE GRAVIMETRIC GEOID

Earth gravity models

The total geoid (Fig. 8) is compared to recent satellite derived Earth gravity models in Figure 9. The models used are SE 3 ($n = 18$), GEM 6 ($n = 16$) and GEM 8 ($n = 25$). These solutions differ mainly in the amount of satellite tracking and surface gravity data used. For example, the SE 3 field is based on 1 x 1° free-air anomaly averages covering 30% of the Earth's surface while the GEM 6 field is based on a coverage of 39%. The RMS differences between the total geoid (Fig. 8) and geoids computed from geopotential coefficients represented by these fields are tabulated (Table 2). The total geoid generally compares well with the Earth gravity models. The RMS differences for the two representative profiles in Figure 9 is ±4.6 meters for the GEM 6 field. The GEM 8 field does not fit as well as GEM 6 but both fields are an improved fit over the SE 3 field. This is illustrated off the eastern Aleutian trench where the high predicted by the SE 3 field is displaced nearly 5° from the high on the total geoid. The main differences between the total geoid and the Earth gravity models occur between the Line islands and the Aleutian trench and between the Bonin trench and Hawaii, where the total geoid is sytematically more positive than the gravity models. This difference exceeds 10 meters with wavelengths of about 4000 km and greater over the Hawaiian ridge at Midway.

We also compared the total geoid (Fig. 8) to the Marsh and Vincent (1974) detailed GEM 6 geoid in Figure 10. This geoid is based on the GEM 6 geoid (Fig. 7) and incorporates about 26,000 1 x 1° surface gravity anomaly averages. Comparison of the Marsh and Vincent (1974) geoid with the total geoid shows good general agreement over Hawaii and the eastern Aleutian trench. However, the two geoids differ markedly over the western Aleutian, Kuril, Izu-Bonin, Mariana and Philippine arc-trench systems. This is illustrated in Figure 10 which shows the two geoids differ by as much as 10 meters with wavelengths of 800 km north of New Guinea and over the Mariana island arc.

SKYLAB-4

During the SKYLAB-4 mission sea surface topography was continuously measured with a satellite radar altimeter along a 9000 km long profile of the Northwest Pacific (Fig. 8; McGoogan et al., 1975). The geoid undulations computed from the altimeter data by McGoogan et al. (1975) are compared to the total geoid in Figure 10.

Although the shape of the SKYLAB-4 and total geoids generally compare well, the two geoids appear to systematically differ by about 5 meters. This could be a result of orbital errors in SKYLAB-4 or errors in the gravimetric geoid. An exception to the close fit occurs in the region of the Yap islands (Fig. 10) where the SKYLAB-4 profile is about 10 meters higher than the total geoid. This probably arises because of errors in the total geoid due to a poor coverage of surface gravity data (Fig. 1). The RMS difference between SKYLAB-4 and the total geoid is ±6.2 meters compared to ±8.4 for the RMS difference obtained between SKYLAB-4 and the detailed GEM 6 geoid.

GEOS-3

As part of the continuing GEOS-3 mission (Stanley, personal communication) sea surface topography was measured with a radar altimeter along a profile of the Aleutian island arc-trench system at about 167°W. The resulting geoid undulations are compared to the total geoid in Figure 11.

The GEOS-3 and the total geoid generally compare well over the Aleutian arc-trench system (Fig. 11). The main differences occur seaward of the trench and over the trench and arc. Seaward of the trench the difference is up to 5 meters with wavelengths of about 1400 km. Part of this long-wavelength discrepancy can be attributed to errors in the total geoid near the edge of the map area. Over the trench and arc the two geoids differ by up to 7 meters with wavelengths of about 250 km. This discrepancy is most likely caused by the limited resolution of the 1 x 1° total geoid. Talwani et al. (1972) have shown that by specifying the difference gravity anomaly over a 10 x 10° 'square' rather than a 1 x 1° 'square' differences of up to 4 meters can occur in island arc-trench regions.

The SKYLAB-4 and GEOS-3 altimetric geoids agree well at the point of their intersection south of the eastern Aleutian trench (Figs. 8 and 10). At this point the two geoids are higher than the detailed GEM 6 geoid by about 4 meters and lower than the total geoid by a similar amount.

CONCLUSIONS

The 1 x 1° gravimetric or total geoid reveals new information in the geoid of the Northwest Pacific ocean. The RMS difference between the new geoid and currently used satellite derived geoids is about ±6 meters. Difference geoid undulations range from a maximum of +19 meters over the Hawaiian ridge to a minimum of -31 meters over the junction of the Kuril and Aleutian trench.

There is close correlation between geoid undulations and features of geological interest in the Northwest Pacific. The Hawaiian swell (Watts, 1976b) correlates with a geoid high of +15 meters with wavelengths of about 1600 km. The topographic rises seaward of deep-sea trenches (Watts and Talwani, 1974) correlate with geoid high of +3 to +6 meters with wavelengths of up to about 800 km. Geoid highs of +10 meters with wavelengths of about 1000 km occur behind island arcs in the western Pacific but they do not appear to be related to the effects of a dense downgoing slab.

The total geoid compares well to currently used satellite derived geoids except over the Pacific basin where discrepancies of up to 10 meters with wavelengths of about 4000 km occur. The agreement with the total geoid is best for the GEM 6 field and poorest for the SE 3 field.

There is generally a close agreement between the total geoid and available geoids derived from satellite radar altimeter data over the Northwest Pacific. The RMS difference between these geoids is about ±6 meters. Although the agreement between these geoids is generally good for wavelengths of about 300 km and greater, it is poor at shorter wavelengths. Discrepancies of up to 7 meters with wavelengths of 250 km occur over the Aleutian arc and trench.

The new geoid based on these comparisons is estimated to be accurate to about ±6 meters.

Caputo, M., Masada, R., Helfer, M.D., Hager, C.L., 1964, Gravity measurements in the Atlantic, Pacific and Indian Oceans, May 1962 - August 1963 (R/V ARGO), Interim Report, Univ. of Calif., Inst. of Geophys. and Planetary Physics, (unpub. manuscript).

Chase, T.E., 1975, Topography of the oceans, Scripps' Inst. of Oceanography, I.M.R. Tech. Rept., Series TR57.

Chiburis, E.F., Dowling, J.J., Dehlinger, P., and Yellin, M.J., 1972a, Pacific SEAMAP 1961-70 Data for Areas 16524-10 and 17624-10, NOAA Tech. Rep. NOS 50, U.S. Gov't. Printing Office, Washington, D.C.

Chiburis, E.F., Dowling, J.J., Dehlinger, P., and Yellin, M.J., 1972b, Pacific SEAMAP 1961-70 Data for Areas 16530-10 and 17530-10, NOAA Tech. Rep. NOS 49, U.S. Gov't Printing Office, Washington, D.C.

Chiburis, E.F., Dowling J.J., Dehlinger, P., and Yellin, M.J., 1972c, Pacific SEAMAP 1961-70 Data for Areas 15636-12, 15642-12, 16836-12, and 16842-12: NOAA Tech. Rep. NOS 51, U.S. Gov't Printing Office, Washington, D.C.

Dowling, J.J., Chiburis, E.F., Dehlinger, P., and Yellin, M.J., 1972a, Pacific SEAMAP 1961-70 Data for Area 15524-10, NOAA Tech. Rep. NOS 45, U.S. Gov't Printing Office, Washington, D.C.

Dowling, J.J., Chiburis, E.F., Dehlinger, P., and Yellin, M.J., 1972b, Pacific SEAMAP 1961-70 Data for Area 15530-10, NOAA Tech. Rep. NOS 46, U.S. Gov't Printing Office, Washington, D.C.

Dowling, J.J., Chiburis, E.F., Dehlinger, P., and Yellin, M.J., 1972c, Pacific SEAMAP 1961-70 Data for Area 15248-14, NOAA Tech. Rep. NOS 47, U.S. Gov't Printing Office, Washington, D.C.

Gainanov, A.G., 1955, Pendulum observations of gravity in the northwest Pacific Ocean, Tr. Intern. Okeanol., AN SSR, 12, 145 (in Russian).

Gaposchkin, E.M., 1974, Earth's gravity field to the eighteenth degree and geocentric coordinates for 104 stations from satellite and terrestrial data, J. Geophys. Res., 76, 5377-5411.

Gaposchkin, E.M., and Lambeck, K., 1971, Earth's gravity field to the sixteenth degree and station coordinates from satellite and terrestrial data, J. Geophys. Res., 76, 4855-4883.

Heiskanen, W.A., and Moriz, H., 1967, Physical Geodesy, W.H. Freeman and Co., San Francisco, 364 p.

Heiskanen, W.A., and Vening Meinesz, F.A., 1958, The Earth and its gravity field, McGraw-Hill, New York, 470 p.

Helfer, M.D., Caputo, M., and Harrison, J.C., 1062, Gravity measurements in the Pacific and Indian Oceans, Monsoon Expedition 1960-61, Interim Rep., Univ. of Calif., Inst. of Geophys. and Planetary Physics, (unpublished manuscript).

Kahle, H.G. and Talwani, M., 1973, Gravimetric Indian Ocean Geoid, Zeitschrift fur Geophysik, Band 39, Seite 167-187.

Khan, M.A., Woollard, G.P. and Daugherty, K.I., 1971, Statistical analysis of the relation of marine gravity anomalies to bathymetry, Hawaii Inst. Geophysics Rep., HIG-71-20, 141 p.

Leitao, C.D., McGoogan, J.T., 1975, SKYLAB radar altimeter: short-wave-length pertubations detected in ocean surface profiles, Science, 186, 1208-1209.

Lerch, F.J., Wagner, C.A., Richardson, J.A., and Brownd, J.E., 1974, Goddard Earth Models (5 and 6) Rep. X-921-74-145, Goddard Space Flight Center, Greenbelt, MD, 100 p.

Malahoff, A., and Woollard, G.P., 1968, Geophysical studies of the Hawaiian Ridge and Murray Fracture Zone, In: The Sea, v. 4, p. 73-90.

Marsh, J.G., and Vincent, S., 1974, Global detailed geoid computation and model analysis, Geophys. Surveys, 1, 481-511.

McGoogan, J.T., Leitao, C.D., Wells, W.T., 1975, Summary of SKYLAB S-193 altimeter altitude results, NASA technical memorandum, Rep. no. NASA TM X-69355, 323 p.

Rapp. R.H., 1973, Geoid information by wavelength, Bull, Geodesique, 110, 405-411.

Rose, J.C., and Belshe, J.C., 1975, Gravity and magnetic fields over the proposed Moho hole site north of Maui, Pacific Science, v. 19, 374-380.

Rose, J.C. and Tracy, R.W., 1971, Gravity results in the Solomon Islands region, aboard H.M.S. Dampier in 1965, Hawaii Inst. of Geophy. Data rep. No. 17.

Strange, W.E., Vincent, S.F., Berry, R.H., and Marsh, J.G., 1972, Detailed gravimetric geoid for the United States, In: The Use of Artificial Satellites for Geodesy, AGU, Washington, D.C., p. 169-176.

Talwani, M., Pappe, H.R. and Rabinowitz, P.D., 1972, Gravimetrically determined Geoid in the western North Atlantic, Sea Surface Topography from Space, v. 2, NOAA Tech. Rep., ERL-228-AOML 7-2, p. 1-34.

Tomada, Y., 1973, Maps of free-air and Bouguer gravity anomalies in and around Japan, Ocean Research Inst., Univ. of Tokyo Press.

Tomoda, Y., Kitazawa, K., and Koizumi, K., 1970, Measurement of gravity and magnetic force at sea during KH-68-4 Cruise, In: Preliminary report of the Hokuho Maru Cruise KH-68-4 (Southern Cross Cruise), Ocean Res. Inst., Univ. Tokyo, p. 80-102.

Tomoda, Y., Ozawa, K., and Segawa, J., 1968, Measurement of Gravity and Magnetic field on board a cruising vessel, Bull. Ocean Res. Inst., Univ. Tokyo, no. 3, p. 1-169.

Tomoda, Y., Segawa, J., and Takemura, T., 1973, Measurement of gravity, magnetic force and bathymetry, In: Preliminary Report Kakuho Maru Cruise KH 71-1, Ocean Res. Inst., Univ. Tokyo, 8-10.

U.S. Dept. of Commerce, 1964, International Indian Ocean Expedition, USC and GS Ship PIONEER, v. 1, Cruise narrative and scientific results, 139 p.

Von Arx, W., Bowen, D.C., Dean, J.P. and Haworth, R.T., 1971, Hudson 70 Gravity Observatory 62.9° to 575.5°N along 150°W, Woods Hole Oceanog. Inst. Rept. 71-68, 3, p.

Wagner, C.A., Lerch, F.J., Brownd, J.E., and Richardson, J.A., 1976, Improvement in the geopotential derived from satellite and surface data (GEM 7 and 8), Preprint X-921-76-20, Goddard Space Flight Center, Greenbelt, Md., 11 p.

Watts, A.B. and Talwani, M., 1974, Gravity anomalies seaward of deep-sea trenches and their tectonic implications, Geophys. J. R. Astr. Soc., 36, 57-90.

Watts, A.B. and Talwani, M., 1975, Gravity Field of the Northwest Pacific Ocean basin and its margin: Hawaii and vicinity, Geol. Soc. Amer. Spec. Map and Chart Series, MC-9.

Watts, A.B., 1975, Gravity Field of the Northwest Pacific Ocean basin and its margin: Aleutian Island Arc-trench System, Geol. Soc. Amer. Spec. Map and Chart Series, MC-10.

Watts, A.B., 1976a, Gravity Field of the Northwest Pacific Ocean basin and its margin: Philippine Sea, Geol. Soc. Amer. Spec. Map and Chart Series MC-12.

Watts, A.B., 1976b, Gravity and bathymetry in the Central Pacific Ocean, J. Geophys. Res., 81, 1533-1553.

Watts, A.B., Talwani, M., and Cochran, J.R., 1976, Gravity Field of the Northwest Pacific Ocean basin and its margin, In: Geophysics of the Pacific Ocean basin and its margin, AGU Monograph 19, 17-34.

Worzel, J.L., 1965, Pendulum gravity measurements at sea 1936-1959, J. Wiley & Sons, New York, London and Sydney, 422 p.

FIGURE CAPTIONS

Figure 1. Gravity measurements in the northwest Pacific ocean. The fine lines indicate ship's tracks along which continuous gravity measurements were obtained. The heavy dots indicate measurements obtained with a pendulum apparatus on board a submarine. The boxed areas indicate free-air anomaly map areas.

Figure 2. 1 x 1° free-air anomaly average map of the northwest Pacific ocean. The physiographic names on this and subsequent maps are based on Chase (1975). Selected 1 x 1° free-air anomaly values are shown to illustrate the behavior of the field between contours. A complete list of 1 x 1° averages is presented in Table 1. The 1 x 1° averages have been referred to the International Reference Ellipsoid (flattening 1/297.0).

Figure 3. 10 x 10° free-air anomaly averages compared to the GEM 6 gravity field model (Lerch et al., 1974). Both field have been referred to the International Reference Ellipsoid (flattening 1/297.0).

Figure 4. 1 x 1° difference geoid obtained from difference gravity anomalies between the 1 x 1° free-air anomaly averages (Fig. 2) and the GEM 6 gravity field (Fig. 3) by using Stokes's formula. Heavy lines indicate selected ship's tracks which have been projected in Figures 5 and 6.

Figure 5. 1 x 1° difference geoid profile across the Philippine Sea (Fig. 4). Also shown is the observed free-air anomaly (flattening 1/297.0) and topography profile obtained on V2405. The 2-D geoid is a computed profile obtained from the observed free-air anomaly using a simplified form of Stokes' formula on a plane. The structural fabric of the Philippine Sea trends generally N-S and the 1 x 1° difference geoid follows closely the computed 2-D geoid.

Figure 6. 1 x 1° difference geoid profile across the Hawaiian swell (Fig. 4). Also shown is the observed free-air anomaly (flattening 1/297.0) and topography profile obtained on C1209 and V2105. The computed 2-D geoid differs from the 1 x 1° difference in part due to the rapid variations in gravity anomalies observed along the Hawaiian ridge (Watts, 1976b).

Figure 7. The GEM 6 geoid (Lerch et al., 1974) referred to the best fitting reference ellipsoid (flattening 1/298.2).

Figure 8. Total geoid referred to the best fitting reference ellipsoid (flattening 1/298.2) obtained by adding the 1 x 1° difference geoid (Fig. 4) to the GEM 6 geoid (Fig. 7). The map is based on the 1 x 1° free-air anomaly averages in Table 1 and Figure 2. The thick lines indicate the tracks of SKYLAB-4 (McGoogan et al., 1975) and GEOS-3 (Stanley, personal communication) across the northwest Pacific.

Figure 9. Comparison of the total 1 x 1° gravimetric geoid with recent global Earth gravity models at Latitude 30°N and Longitude 170°E in the Northwest Pacific. The global Earth models used are GEM 6 (Lerch et al., 1974), GEM 8 (Wagner et al., 1976) and SE 3 (Gaposchkin, 1974).

Figure 10. Comparison of the total geoid (Fig. 8) to the SKYLAB-4 radar altimeter profile of the Northwest Pacific (McGoogan et al., 1975). Also shown by dashed lines is the detailed GEM 6 geoid of Marsh and Vincent (1974). The open triangle indicates the geoid height measured on the GEOS-3 altimeter profile (Stanley, personal communication) which intersected the SKYLAB-4 profile south of the eastern Aleutian trench (Fig. 8).

Figure 11. Comparison of the total geoid (Fig. 8) with the GEOS-3 radar altimeter profile (Stanley, personal communication) across the Aleutian island arc-trench system at about longitude 165°W.

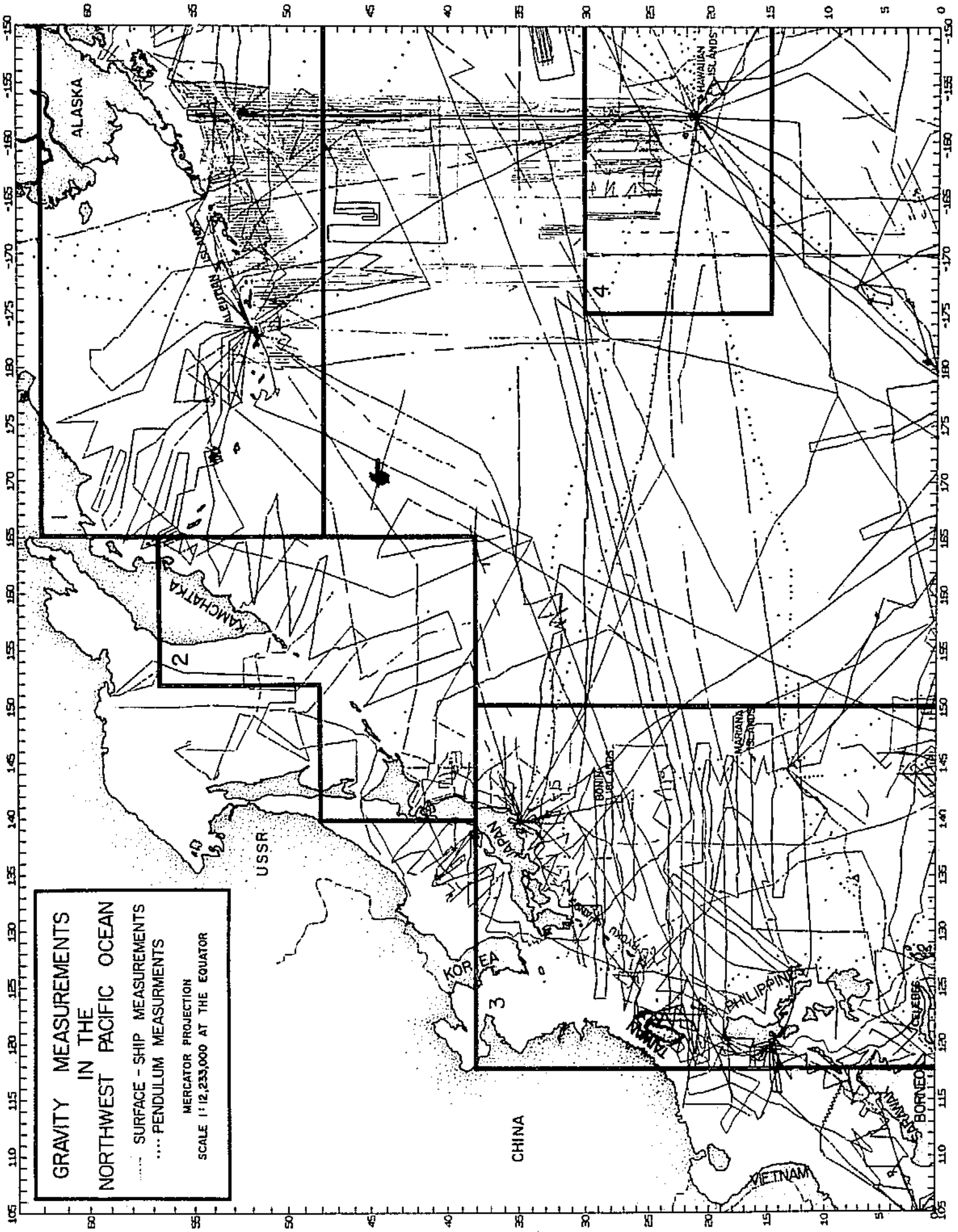
GRAVITY MEASUREMENTS
IN THE
NORTHWEST PACIFIC OCEAN
SURFACE - SHIP MEASUREMENTS
PENDULUM MEASURMENTS
MERCATOR PROJECTION
SCALE 1:12,233,000 AT THE EQUATOR
ALASKA
ALEUTIAN ISLANDS
HAWAIIAN ISLANDS
KAMCHATKA
USSR
CHINA
KOREA
JAPAN
BONIN ISLANDS
MARIANA ISLANDS
PHILIPPINES
TAIWAN
CELEBES
BORNEO
VIETNAM
1
2
3
4
5

Figure 1

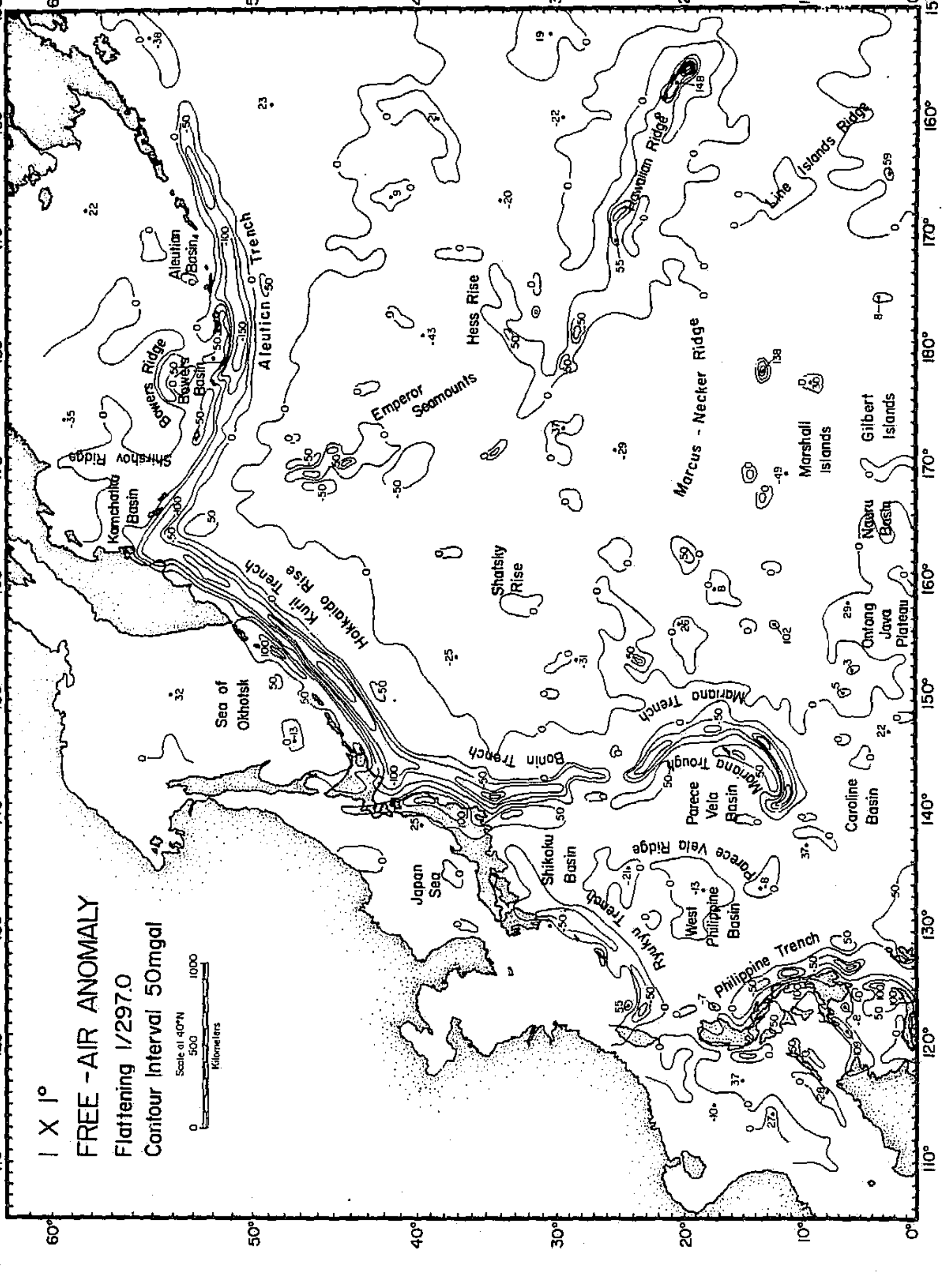
1 X 1°
FREE-AIR ANOMALY
Flattening 1/297.0
Contour Interval 50mgal
Scale at 40°N
0
500
1000
Kilometers
Sea of Okhotsk
Japan Sea
Kamchatka Basin
Shirshov Ridge
Bowers Ridge
Bowers Basin
Aleutian Basin
Aleutian Trench
Kuril Trench
Hokkaido Rise
Emperor Seamounts
Hess Rise
Shatsky Rise
Hawaiian Ridge
Line Islands Ridge
Marcus - Necker Ridge
Marshall Islands
Gilbert Islands
Nauru Basin
Ontong Java Plateau
Mariana Trench
Mariana Trough
Bonin Trench
Parece Vela Basin
Parece Vela Ridge
Shikoku Basin
Ryukyu Trench
West Philippine Basin
Philippine Trench
Caroline Basin
148
138
102
59
55
-150
-100
60°
50°
40°
30°
20°
10°
0°
110°
120°
130°
140°
150°
160°
170°
180°
150°

Figure 2

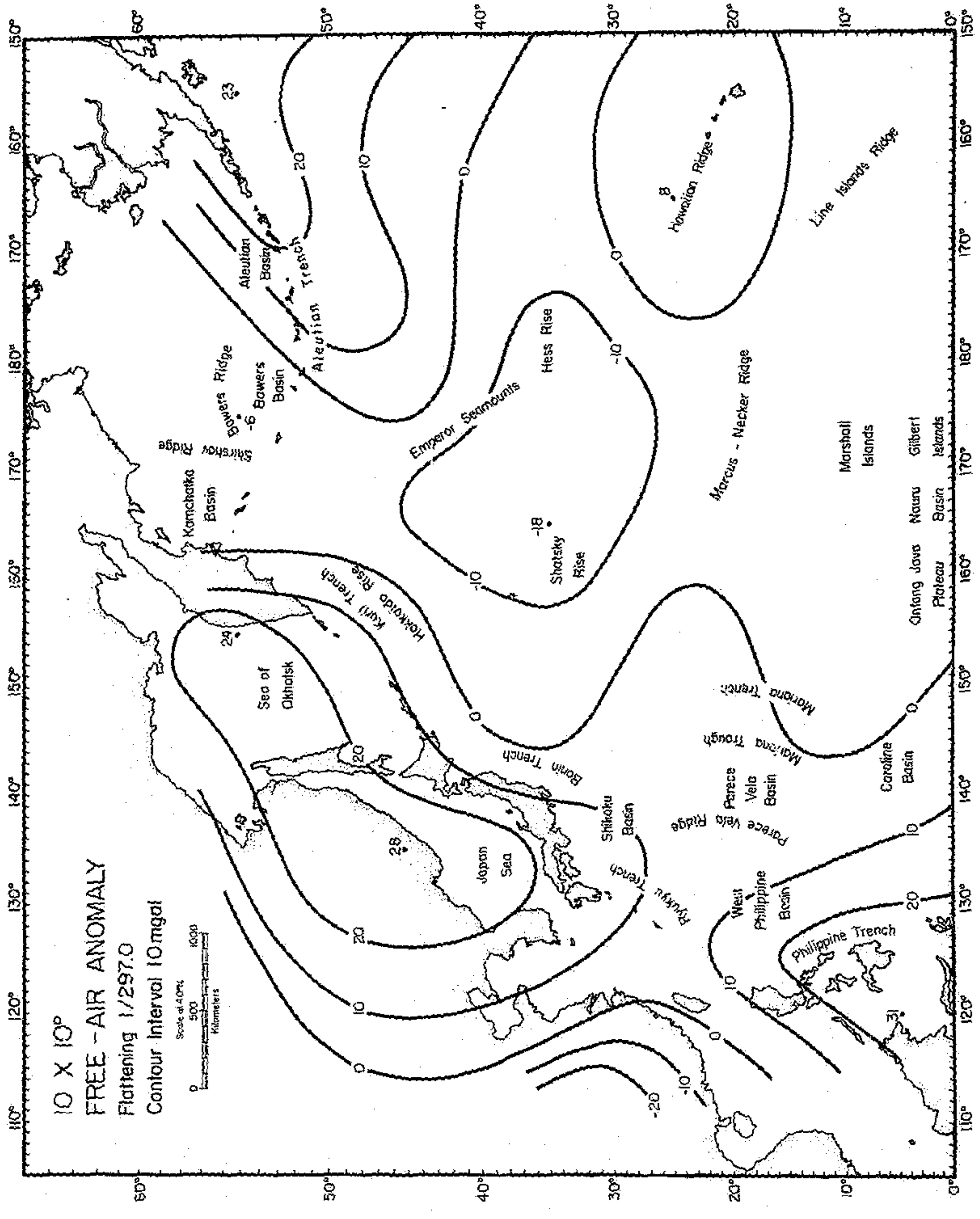
10 X 10°
FREE - AIR ANOMALY
Flattening 1/297.0
Contour Interval 10 mgal
Scale at 40°N
0
500
1000
Kilometers
Aleutian Trench
Aleutian Basin
Bowers Ridge
Bowers Basin
Shirshov Ridge
Kamchatka Basin
Emperor Seamounts
Hess Rise
Hawaiian Ridge
Line Islands Ridge
Marcus - Necker Ridge
Shatsky Rise
Marshall Islands
Gilbert Islands
Nauru Basin
Ontong Java Plateau
Hokkaido Rise
Kuril Trench
Sea of Okhotsk
Japan Sea
Bonin Trench
Mariana Trench
Mariana Trough
Caroline Basin
Parece Vela Basin
Parece Vela Ridge
Shikoku Basin
Ryukyu Trench
West Philippine Basin
Philippine Trench
23
-6
8
-18
24
28
48
31
20
10
0
-10
-20
110°
120°
130°
140°
150°
160°
170°
180°
0°
10°
20°
30°
40°
50°
60°

Figure 3-A

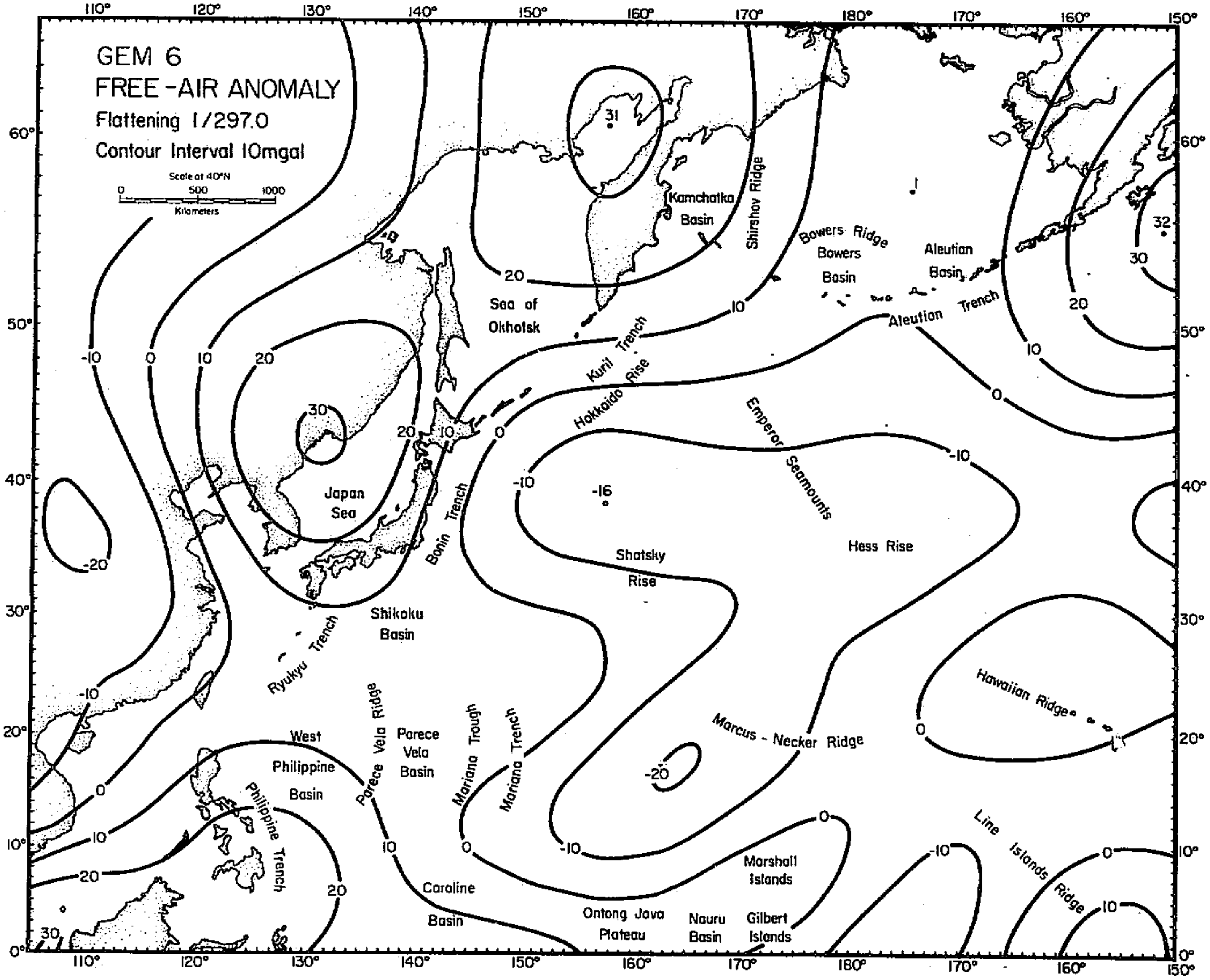
GEM 6
FREE-AIR ANOMALY
Flattening 1/297.0
Contour Interval 10mgal
Scale at 40°N
0
500
1000
Kilometers
110°
120°
130°
140°
150°
160°
170°
180°
170°
160°
150°
60°
50°
40°
30°
20°
10°
0°
Sea of Okhotsk
Kamchatka Basin
Shirshov Ridge
Bowers Ridge
Bowers Basin
Aleutian Basin
Aleutian Trench
Kuril Trench
Hokkaido Rise
Emperor Seamounts
Hess Rise
Shatsky Rise
Japan Sea
Bonin Trench
Shikoku Basin
Ryukyu Trench
West Philippine Basin
Philippine Trench
Parece Vela Ridge
Parece Vela Basin
Mariana Trough
Mariana Trench
Marcus - Necker Ridge
Hawaiian Ridge
Line Islands Ridge
Marshall Islands
Gilbert Islands
Nauru Basin
Ontong Java Plateau
Caroline Basin
31
32
30
20
10
0
-10
-16
-20

Figure 3-B

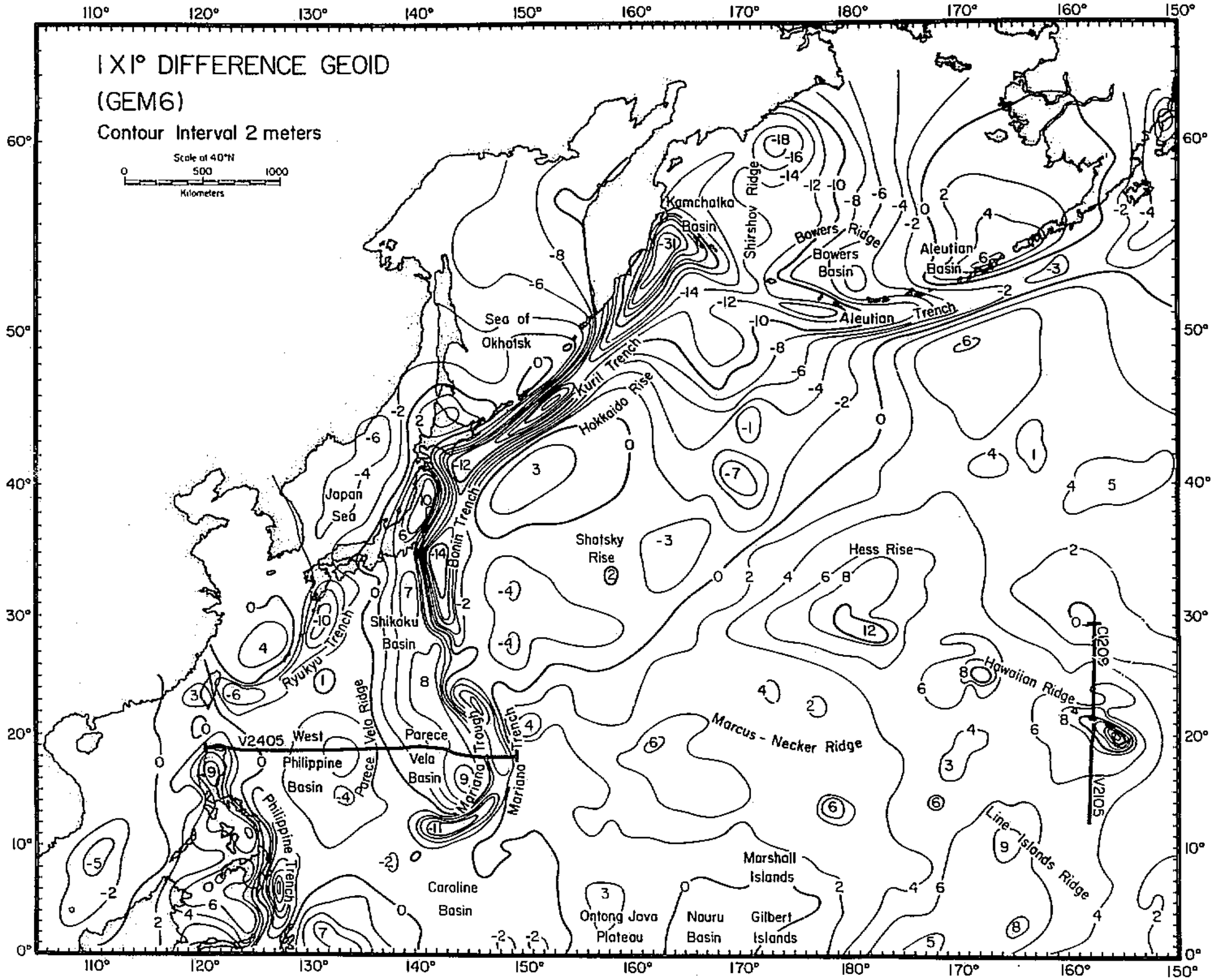
1X1° DIFFERENCE GEOID
(GEM6)
Contour Interval 2 meters
Scale at 40°N
0
500
1000
Kilometers
110°
120°
130°
140°
150°
160°
170°
180°
170°
160°
150°
60°
50°
40°
30°
20°
10°
0°
Sea of Okhotsk
Kamchatka Basin
Shirshov Ridge
Bowers Ridge
Bowers Basin
Aleutian Basin
Aleutian Trench
Kuril Trench
Hokkaido Rise
Japan Sea
Bonin Trench
Shatsky Rise
Hess Rise
Shikoku Basin
Ryukyu Trench
Parece Vela Ridge
Parece Vela Basin
Mariana Trough
Mariana Trench
West Philippine Basin
Philippine Trench
Caroline Basin
Ontong Java Plateau
Nauru Basin
Marshall Islands
Gilbert Islands
Marcus - Necker Ridge
Hawaiian Ridge
Line Islands Ridge
V2405
C1209
V2105

Figure 4

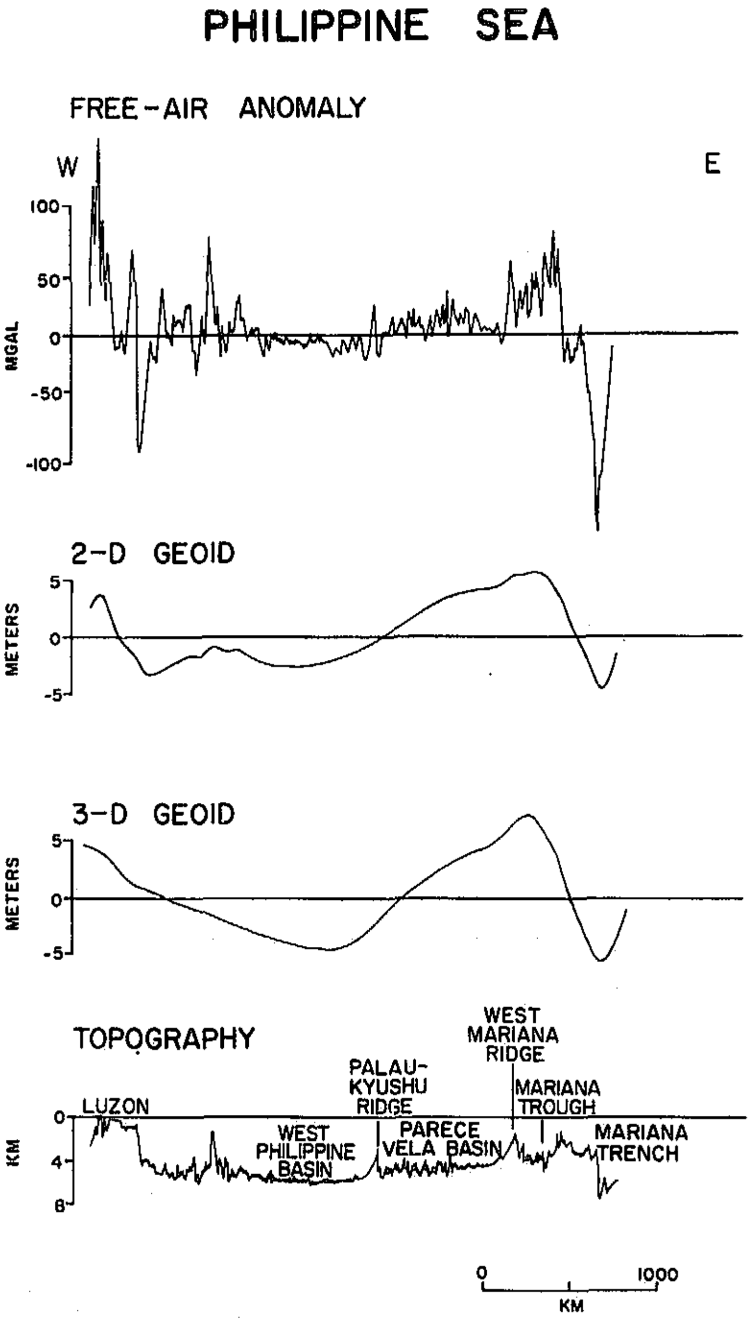
PHILIPPINE SEA
FREE-AIR ANOMALY
W
E
100
50
0
-50
-100
MGAL
2-D GEOID
5
0
-5
METERS
3-D GEOID
5
0
-5
METERS
TOPOGRAPHY
0
4
8
KM
LUZON
WEST PHILIPPINE BASIN
PALAU-KYUSHU RIDGE
PARECE VELA BASIN
WEST MARIANA RIDGE
MARIANA TROUGH
MARIANA TRENCH
0
1000
KM

Figure 5

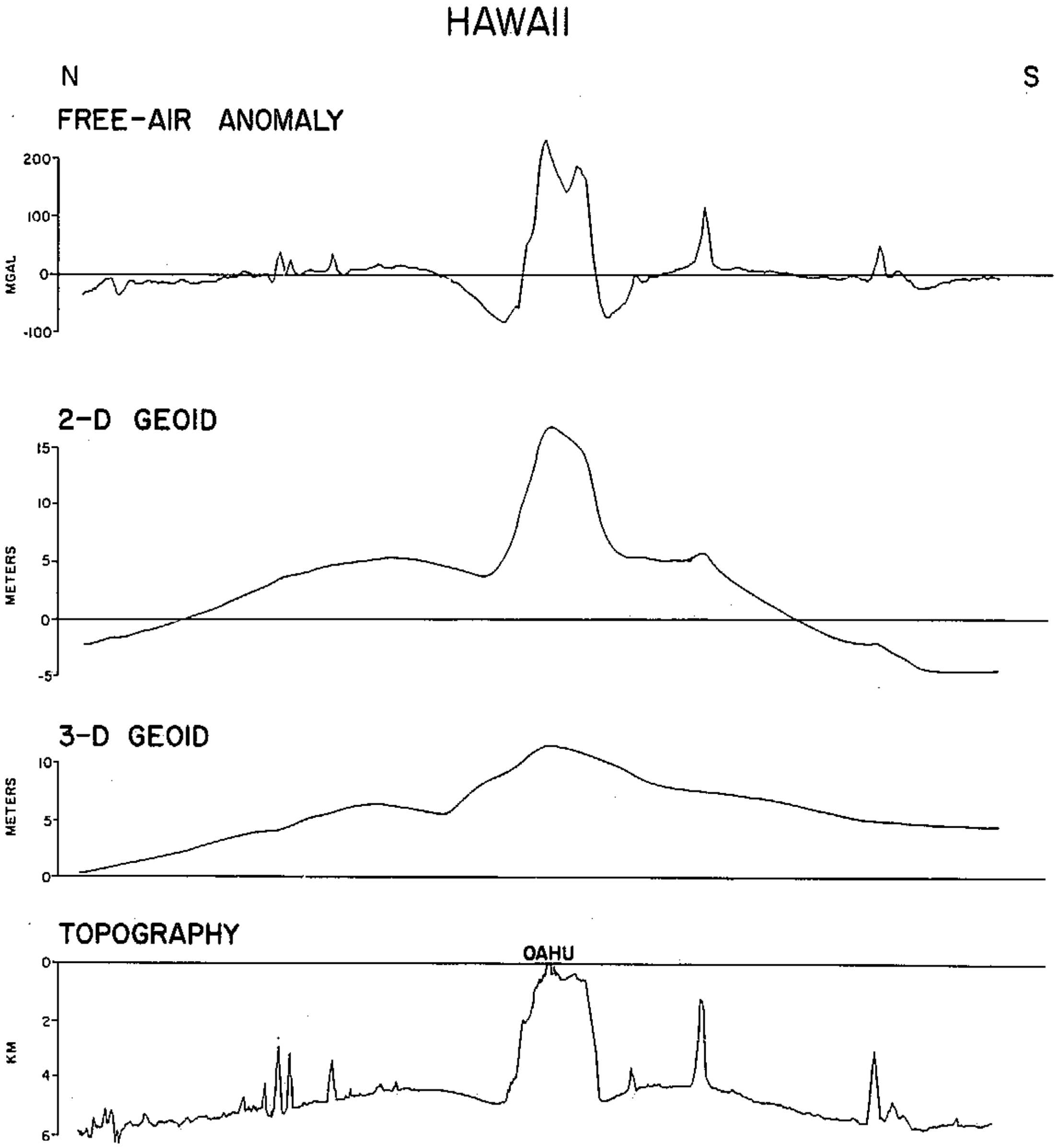
HAWAII
N
S
FREE-AIR ANOMALY
200
100
0
-100
MGAL
2-D GEOID
15
10
5
0
-5
METERS
3-D GEOID
10
5
0
METERS
TOPOGRAPHY
OAHU
0
2
4
6
KM

Figure 6

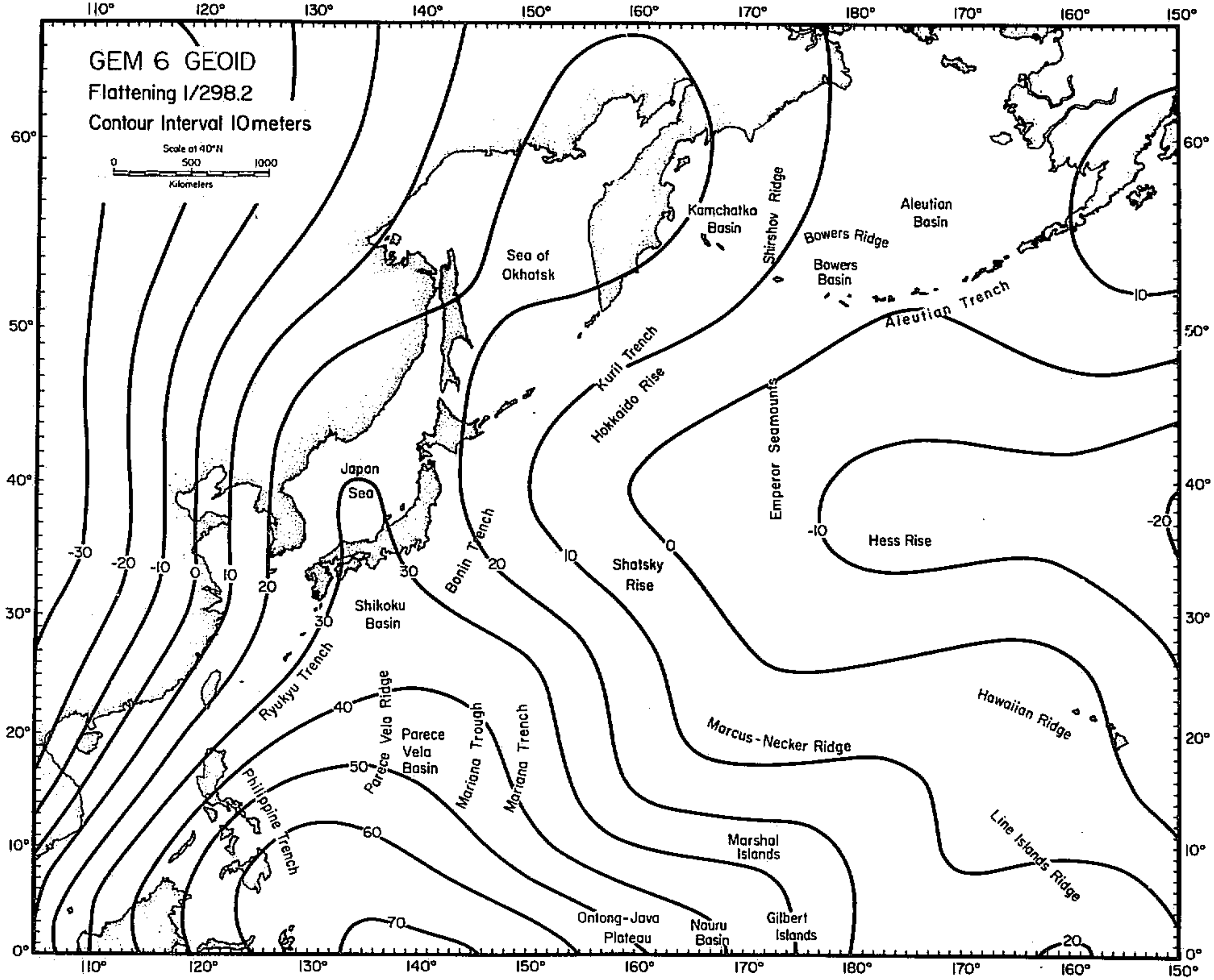
GEM 6 GEOID
Flattening 1/298.2
Contour Interval 10 meters
Scale at 40°N
0 500 1000
Kilometers
110° 120° 130° 140° 150° 160° 170° 180° 170° 160° 150°
0° 10° 20° 30° 40° 50° 60°
-30
-20
-10
0
10
20
30
40
50
60
70
-20
-10
0
10
20
-20
Sea of Okhotsk
Kamchatka Basin
Shirshov Ridge
Bowers Ridge
Bowers Basin
Aleutian Basin
Aleutian Trench
Kuril Trench
Hokkaido Rise
Emperor Seamounts
Hess Rise
Japan Sea
Shatsky Rise
Bonin Trench
Shikoku Basin
Ryukyu Trench
Parece Vela Ridge
Parece Vela Basin
Mariana Trough
Mariana Trench
Philippine Trench
Marcus-Necker Ridge
Hawaiian Ridge
Line Islands Ridge
Marshal Islands
Ontong-Java Plateau
Nauru Basin
Gilbert Islands

Figure 7

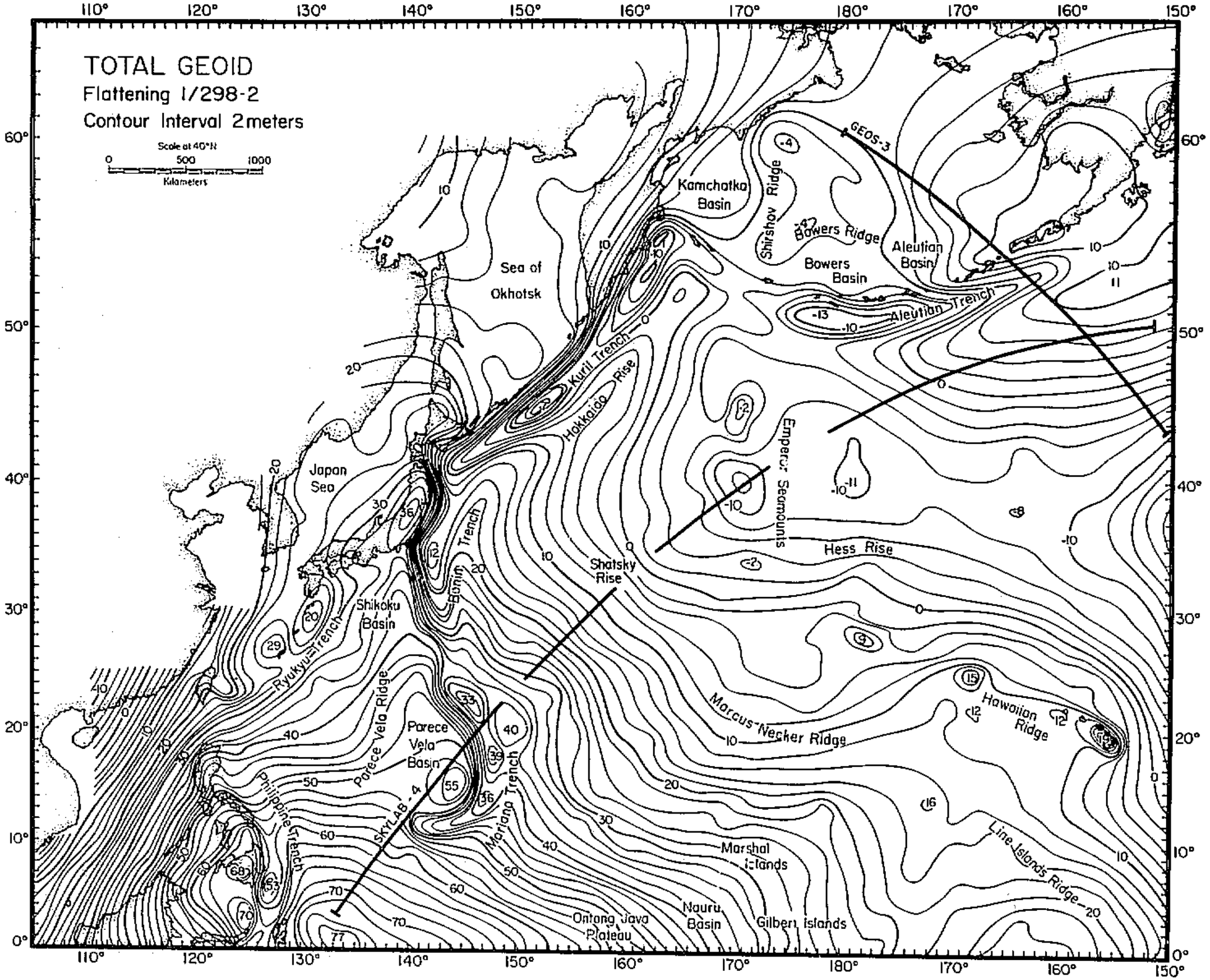
TOTAL GEOID
Flattening 1/298-2
Contour Interval 2meters
Scale at 40°N
0 500 1000
Kilometers
Sea of Okhotsk
Japan Sea
Kamchatka Basin
Shirshov Ridge
Bowers Ridge
Bowers Basin
Aleutian Basin
Aleutian Trench
GEOS-3
Kuril Trench
Hokkaido Rise
Emperor Seamounts
Hess Rise
Shatsky Rise
Bonin Trench
Shikoku Basin
Ryukyu Trench
Parece Vela Ridge
Parece Vela Basin
SKYLAB-4
Mariana Trench
Philippine Trench
Marcus-Necker Ridge
Hawaiian Ridge
Line Islands Ridge
Marshal Islands
Nauru Basin
Gilbert Islands
Ontong Java Plateau
110°
120°
130°
140°
150°
160°
170°
180°
170°
160°
150°
0°
10°
20°
30°
40°
50°
60°

Figure 8

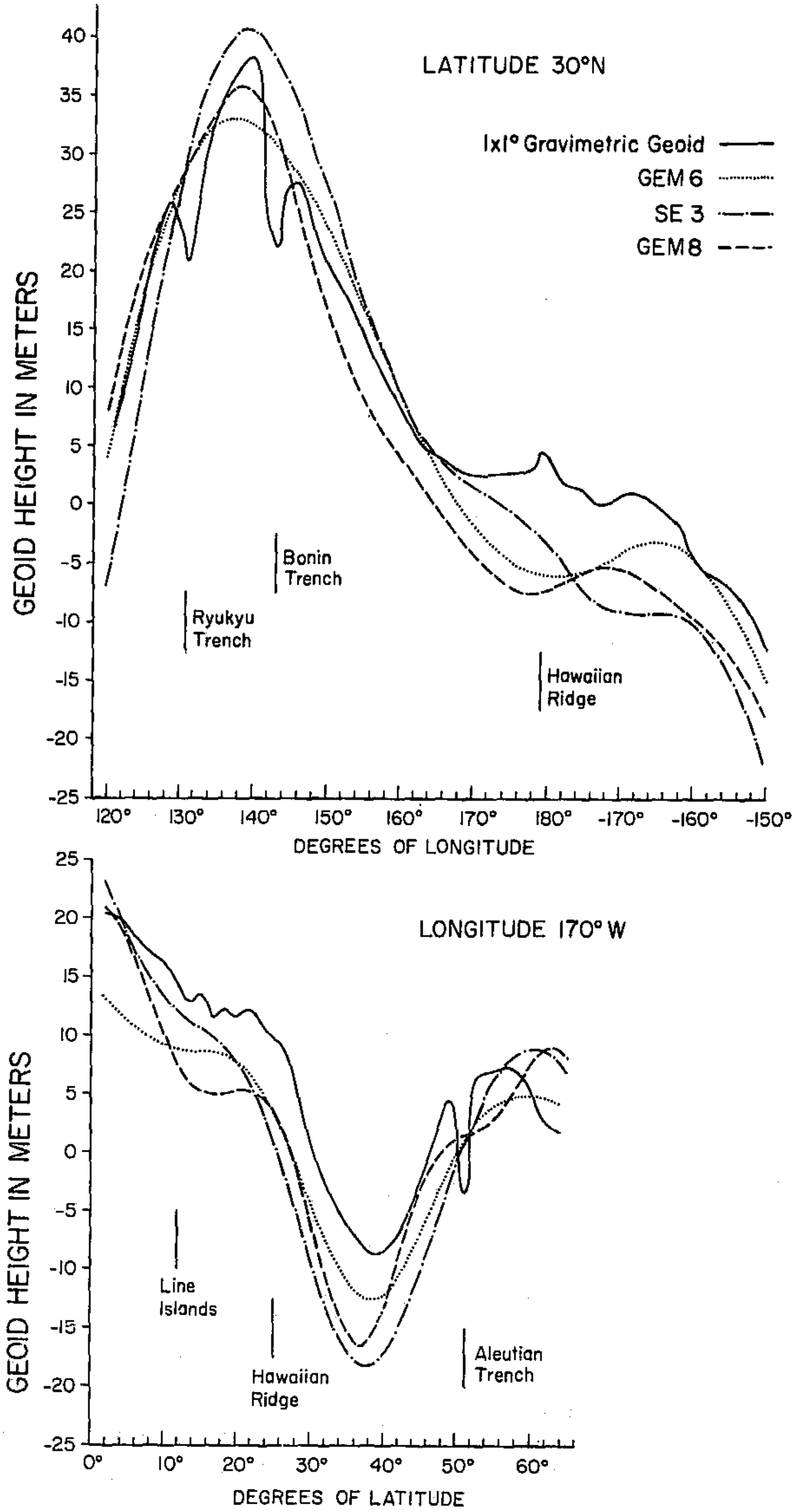
LATITUDE 30°N
1x1° Gravimetric Geoid
GEM 6
SE 3
GEM 8
GEOID HEIGHT IN METERS
40
35
30
25
20
15
10
5
0
-5
-10
-15
-20
-25
Bonin Trench
Ryukyu Trench
Hawaiian Ridge
120°
130°
140°
150°
160°
170°
180°
-170°
-160°
-150°
DEGREES OF LONGITUDE
LONGITUDE 170° W
GEOID HEIGHT IN METERS
25
20
15
10
5
0
-5
-10
-15
-20
-25
Line Islands
Hawaiian Ridge
Aleutian Trench
0°
10°
20°
30°
40°
50°
60°
DEGREES OF LATITUDE

Figure 9

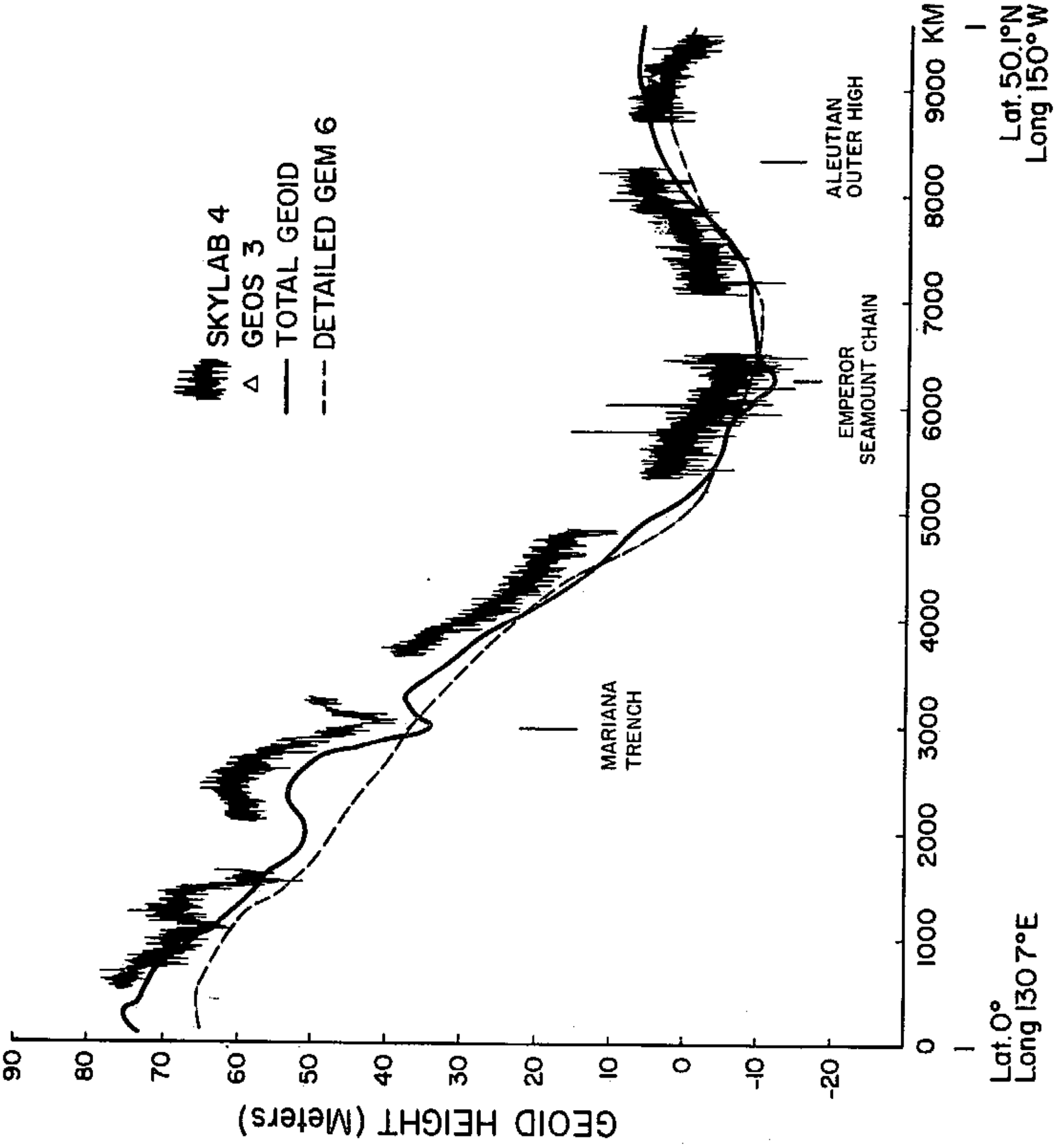
GEOID HEIGHT (Meters)
90
80
70
60
50
40
30
20
10
0
-10
-20
0
1000
2000
3000
4000
5000
6000
7000
8000
9000 KM
Lat. 0°
Long 130.7°E
Lat. 50.1°N
Long 150°W
SKYLAB 4
GEOS 3
TOTAL GEOID
DETAILED GEM 6
MARIANA TRENCH
EMPEROR SEAMOUNT CHAIN
ALEUTIAN OUTER HIGH

Figure 10

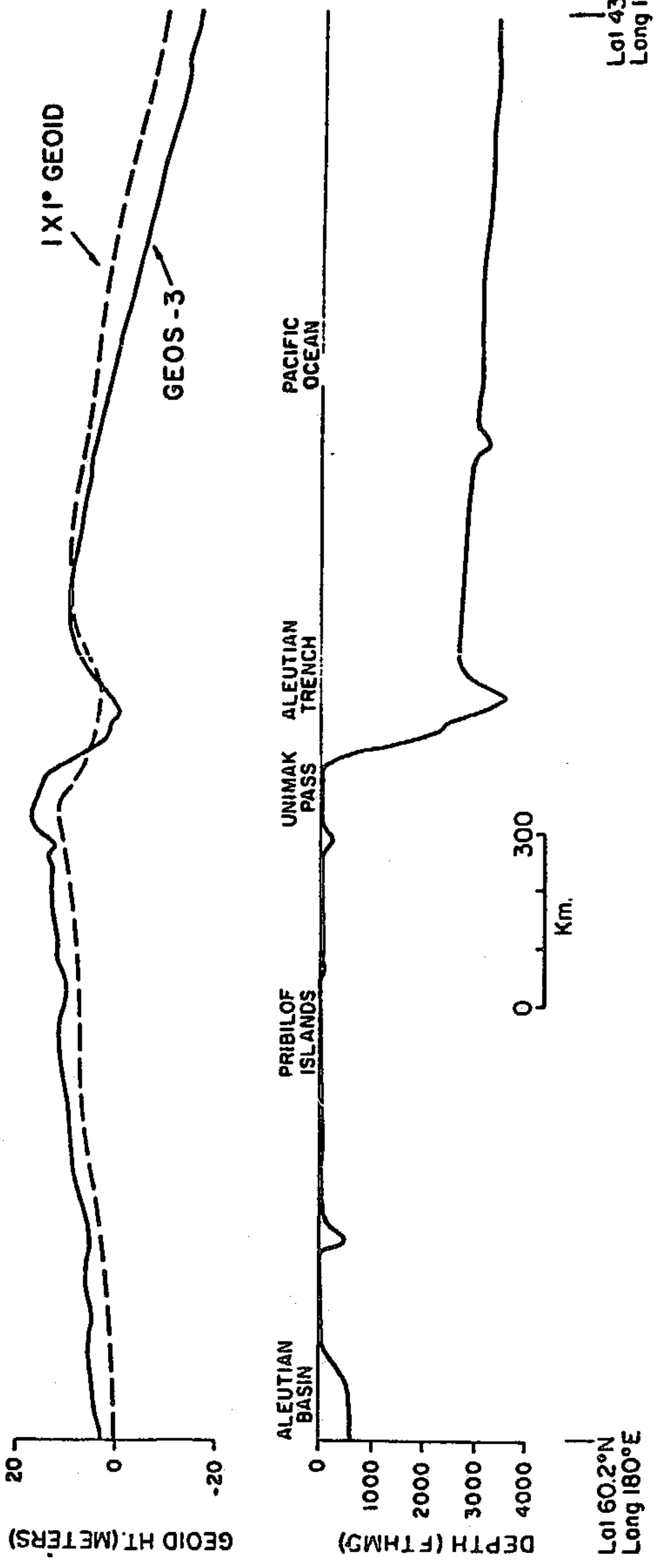
GEOID HT.(METERS)
20
0
-20
1X1° GEOID
GEOS-3
DEPTH (FTHMS)
0
1000
2000
3000
4000
ALEUTIAN BASIN
PRIBILOF ISLANDS
UNIMAK PASS
ALEUTIAN TRENCH
PACIFIC OCEAN
0
300
Km.
Lat 60.2°N
Long 180°E
Lat 43.3°N
Long 150.3W

Figure 11

TABLE 1. 1 x 1° free-air anomaly values (mgal) in the northwest Pacific ocean referred to International Reference Ellipsoid (flattening 1/297.0).

	105					110					115				120
60															
50															
40															
30															
															5
														13	30
										-13	-24	-8	3	15	20
										-25	-2	-2	5	-2	-5
										-4	3	11	17	10	11
20															
								0	-10	-20	1	-8	-5	-2	1
								-15	-4	-15	-2	0	14	9	-26
								-16	-3	-10	-7	5	4	5	-15
									-11	9	-3	7	1	24	30
									-11	-12	-3	7	37	33	-25
										0	6	8	17	11	63
										-1	1	15	16	22	-39
									15	27		9	5	24	17
								-7	-18				11	11	45
							-25	-8					-3	25	52
10															
						-20	-23						-10	47	-9
					2	-13					-21	-28	47	-2	27
				10	-7	2	2		25		-12			38	23
			32	16	9	10	3	16	-7	36	30			48	12
				17	10	15	23	30	5	36	32			77	55
				10	10	15	19	24	34	39			42	56	73
	12	25	25	6	17	22	21					38	28	6	24
	20	32	24	25	28	23							36		-3
	25	25												54	-32
	25	35	30				43					34	56	60	-12
0															
	105					110					115				120

	120					125					130				135
60															
50															
															95
														55	36
															3
													-7	-5	6
40															
													-1	23	21
													-3	20	2
						6	21	12	42	10	5	11	16	13	-9
							20	24	34	25	-19	7	6	37	22
							12	29	26	8	9	9	19	33	20
							22	40	20	17	3	11	7	27	11
							24			21	24	9	4	31	38
										28	30	-13	-11	38	-6
									9	11	31	-52	-32	-20	-5
								28	19	26	12	-78	-13	13	14
30															
							23	25	22	20	-64	-76	12	24	12
					3	19	36	27	21	-1	-56	-78	23	10	18
					20	47	33	45	42	-46	-57	-3	15	-2	0
				12	27	43	28	64	14	-53	-9	28	-3	-5	-15
	-5	-3	14	23	22	31	-18	-33	-55	-15	27	23	26	27	-2
	1	-46	-35	55	36	18	4	-45	-7	18	28	55	-10	-15	-18
	55	50	-99	-105	-74	-54	-25	4	9	17	1	11	12	9	8
	14	30	-4	-25	-9	7	11	9	24	7	-5	-2	10	6	15
	-20	16	0	7	17	15	13	19	18	4	1	9	6	3	4
	-38	36	0	7	11	7	7	11	5	-1	-1	1	-2	-3	-4
20															
	-39	39	13	-1	18	5	2	4	7	-2	-4	-1	-4	-5	-7
	39	66	12	6	9	8	7	11	12	-2	0	-5	-6	-13	-10
	78	35	48	-7	23	24	18	7	8	9	2	4	-5	-12	-12
	80	70	72	5	34	25	13	10	9	12	5	1	-2	-1	4
	74	81	-33	-20	-6	13	15	11	10	4	12	8	9	5	11
	51	48	61	-17	-3	-27	26	20	13	9	10	13	4	-5	8
	9	32	45	55	33	-88	25	28	17	11	13	4	3	-8	-12
	44	61	37	34	67	-20	-25	28	26	19	22	15	6		
	48	48	41	58	74	106	-103	41	39	24	18	11	12	8	4
	52	22	31	46	70	161	-106	26	43	34	20	13	13		
10															
	31	3	11	42	9	103	-29	-7			24	12	12		
	30	7	-4	50	60	59	19	-62			23	14			
	12	12	107	50	82	44	71	-99			21				15
	28	109	45	-8	144	70	-57	-118	66	50	25				29
	80	39	30	35	-34	10	-52	-180	52	30	18				70
	29	43	48	54	27	90	-7	-32	-28	47	37	18	23	24	33
	33	29	41	53	60	128	-36	-33	-27	48	55	33	23	24	44
	33	28	39	55	63	97	-35	-35	6	53	77	65			
	-3		-25	18	101	52	-80	81		37	67	68	58		52
			-78	49	51	-43	-21	50					68	62	81
0															
	120					125					130				135

135 140 145 150

60															
															23
															21
															45
										-25	26	32	26		35
										-4	-7	-10			
										-1	4	6	13	30	
												6	18	29	20
												4	9	11	19
												11	4	2	22
50															
											21	4	15	39	41
											11	9		22	24
												-13	-1	6	33
								35	51			12	12	18	50
				17	28	34	31	49	50	9	9	11	21	13	
		-7	1	34	31	54	45	86	85	25	11	78	68	75	-89
	-13	-15	5			58	25	64	39	121	108	50	-90	-162	-160
	-5	-3	13	8		75	23	-1	3	-25	-76	-132	-130	-36	21
	12	2	-1	2	15	73	41	-143	-111	-116	-103	-34	28	35	35
	34	13	23	3	6	72	112	17	-47	-119	4	35	27	26	22
40															
	34	11	13	25	31	86	153	57	-56	-73	36	28	20	18	10
	6	9	19	25	58	88	131	44	-64	-57	35	30	20	13	8
	-4	42	11	23	89	115	91	-26	-97	-25	24	21	11	0	-9
	11	27	17	64	71	117	-3	-120	-47	19	15	19	6	0	-10
	28	1	31	79	27	33	-83	-97	-10	3	16	0	-1		-13
	44	49	27	25	75	-15	-227	-86	11	7	-7	-12			
	39	-12	3	18	91	131	-121	-106	24	16	37	6	-7	-22	-7
	-34	-7	13	34	89	98	-68	-136	35	19	5	5	-19	-23	-27
	22	26	20	41	80	56	-34	-136	25	25	6	4	-11	-23	-28
	24	24	7	42	71	68	-4	-138	23	27	18	9	5	-3	-11
30															
	10	19	28	27	54	34	-32	-122	-63	26	28	17	0	-5	-2
	7	11	8	16	37	37	29	75	-82	11	25	14	-10	-18	-17
	4	2	18	14	33	48	-1	193	111	24	24	16	-3	-25	-20
	-3	-9	5	16	13	42	-5	74	-66	53	20	9	-23	-19	-18
	10	10	20	32	19	50	50	30	15	16	-6	8	11	34	-2
	-21	13	2	17	24	38	73	39	-82	53	47	12	12	10	-15
	0	6	7	19	28	19	69	9	-106	-94	4	32	31	32	-12
	-3	13	25	17	39	41	50	68	20	-58	-134	-46	27	43	27
	-4	20	22	24	16	24	30	46	51	52	-46	-108	-3	42	10
	-11	9	11	18	15	19	17	35	42	44	38	-62	-42	27	15
20															
	-11	8	4	12	3	11	9	13	30	41	29	-22	-52	56	19
	-7	1	7	6	15	17	11	10	38	45	31	-7	-83	-20	10
	2	0	2	14	8	10	6	15	30	40	50	-4	-113	-30	-14
	12	9	0	6	8	18	20	25	39	46	72	40	-77	-8	-12
	10	8	13	13	-4	5	9	28	43	50	103	8	-60	35	24
	3	1	6	10	-1	4	7	14	35	52	96	-57	-94	11	-4
	11	5	0	0	0	0	0	29	48	94	34	-181	-31	15	9
		0	1	25			-25	52	50	-105	-133	-38	37	10	-1
	22	16	5	38	14	-12	-170	-159	-134	-96	-6	14	8	2	18
		6	10	-19	11	19	-46	-18	8	43	41	1	-8	-6	-14
10															
		1	37	-20	50	36	22	67	28			13	1	6	
		13	17	-30	8	12	10					22			6
	3	7	-13	14		18	2	2				33			
	9	3			5	0	24					-10			
	10				3					-3	1				-20
					1			11		-2	-2	9			-24
														4	4
					20	10	20		3	7		9	22	9	42
						11	22	16	24	13	6	13	24	-21	21
	62	35					9	18	23	9	14	2	6	-5	16
0															

135 140 145 150

150 155 160 165

60															
	39	43													
	41	29	4											0	-38
	24	15	1	7	11										13
			8	-3	19									29	-26
	32			21									-182	-169	-100
	32		26	28								39	-138	-133	-28
	14		25								-8	-110	-174	-6	66
	15	16	31	33	35						-145	-152	-62	28	58
	18	15	23	15	45					-120	-153	-28	23	36	37
	13	13	28	29	30	80	90	-24	-100	-117	-26	24	23	23	18
50															
	29	38	21	55	80	100	1	-133	-105	-4	27	27	20	13	2
	27	51	17	66	158	-22	-175	-68	21	26	28	20	13	7	4
	47	35	138	49	-18	-156	-30	35	33	30	25	22	3	-2	-5
	70	90	20	-198	-179	3	36	29	28	24	22	15	4	0	-2
	150	-150	-247	-141	28	38	32	21	22	20	15	7	1	-5	-10
	-238	-199	-55	22	32	19	10	14	15	15	12	5	-7	-10	-10
	-49	36	41	30	17	10	12	5	10	12	10	2	-15	-17	-17
	51	46	37	20	9	-2	-3	-1	-3	-3	-5	-7	-15	-20	-17
	33	26	20	12	2	-10	-13	-6	-6	-8	-15	-12	-13	-16	-20
	20	5	2	4	-1	-10	-8	-4	-3	-5	-12	-20	-20	-19	-18
40															
	17	1	-6	-5	-6	-8	-8	-10	-10	-12	-15	-18	-12	-17	-21
	0	-8	-8	-3	-10	-9	-15	-11	-12	-10	-7	-6	0	-10	-20
	-15	-17	-10	-9	-25	-12	-20	-20	-8	-2		-23	10	-4	-22
			-10						0	-18	-37			-14	-26
				-9								-36	-28	-17	-27
				-12	-12				-1	-6	-6	-17	-24	-36	-28
	-11	-2	-8	-10	-14	-23	-11	4	7	-6		-20	-27	-33	-19
	-21	-18	-9	1	-4	-8	-7	8	4	-16	-14	-20	-31	-25	-37
	-4	-1		-17	4	-4	0	-2	1	-4	-11		-22		
	4	-8	2	-11	-10	-11	-8	-15	-7	-1	-6	-13	-19	-8	-2
30															
	-5	-7	-3	23	-1	0	-16	0	-14	-16		-20			
				-31	-27	-27	-20	-9	-18	-22	-8	3	2	2	-11
							-14	-18	-15	-5	-18	-10	-13	-12	1
			5	1	-2	1	-3	-4	2	3	0	-12	5	-9	-19
	8	15	28	8	1	-6	-8	-2	4	-9	-6	13	10	3	-12
	1	11	-2	33	28	10		7	12	-1	-6	0			
	14	-3	9	100	-13	9	3		-9						
	29	21	0					-8					-14	-9	
	4						-14	-22	-19	-17		-16			
	137	-12	-2	-6	42		26							3	-1
20															
			7				22					10	57		
			-16			2	-2			-1	-18	-8			
				-17		-4			1	8	4				
					-26	-37					0	-12	-16	-33	-21
	25				-2			-34	1	-40	-24	-35	16	11	3
	0	-13	-16	-6	-16	-39	-59		-20			-23			
	-1	-3	10	-3		-12	-13	-23	-2	-1				3	-20
	-5	-9	-10	-3			102	-43			-17	15	-22		
		-5	-11					-19							
	-23	-19	-15						-6						
10															
		-21	-9							-12	-31				
	-16	-31		-17						-24	-13	-16			
	-11	-17	-10	3	1						-10	-11	4		
	5	-8			-6	12	5					-6		1	-4
			3		-7	11	20	14	29			-9	-3		-2
			-12	-9		2		14	8	-7			12		
	6				23		25		27	1				3	
	-5					1	28		9	7	0	11	5	0	-10
	-3	3	5	-6			13	18		5	-5	0	2	3	0
	1	-13	-19	11	12	21	14	2	9	-1	14	-3			4
0															

150 155 160 165

165 170 175 180

										-11					
								-96	-57	-65	-58	-40			
60															
	29	28	-26	-48	-36	35	-17	-62	-44	-35	-28	-18	-17	-22	-24
	-28	-23	-3	-3	5	44	14	-40	-17	-12	-10	-8	-6	-10	-2
	25	17	10	-11	14	50	43	-7	6	5	3	-1	-5	-3	4
	18	22	26	26	10	18	0	-9	3	1	-5	-15	-15	-12	0
	34	49	14	6	1	3	-13	8	6	-13	-41	-43	-39	-37	-39
	-109	-122	-7	35	21	15	-26	-16	-24	-22	-11	64	39	63	57
	45	-8	-79	-89	-2	34	38	18	12	2	9	9	-5	-12	29
	60	40	24	9	-23	-51	-56	25	43	74	68	55	14	26	54
	31	14	29	20	24	29	2	-58	-48	-71	-60	-90	-26	-120	83
	10	-18	21	-11	-10	5	32	22	35	10	-24	-93	-85	-120	-152
50															
	-9	-17	-26	-20	-30	5	11	-7	0	13	21	25	26	39	35
	-10	-17	-25	-25	-37	-38	-10			4	3	8	12	20	23
	2	-3	-39	-36	25	-55	-10	6	-6	-14	-7	-5	-2	1	-4
	-10	-15	-25	-60	60	-65	-20	-11	-18	-16	-14	-12	-4	-13	
				-73	-47	40	89	-14			-6	-20	-12		
			3	-26	16	129	-41	-4		-24			-13		
	-17	-7	-5		-7	3	8		3	-15	-33	5			
			-7	-11		43			7		-21		0		
			-12		-60			-28		-18	-23				
		-18	-13	-60	-76		-64			-5					
40															
		-7		-35		-72	-64		-2						
	-11	19	4			-17		-30							
	-19	-24	-21	-22	-27	-43	-49	-49							
	-16	-21	-10	-8	-28						11				
	-23	-26	-19					0				-12	6	-7	-16
	-33			-6	-28	-32	84		-16	-2	-4				-4
	-3														10
		-24	15	-42	-29					-26	11	12	3	1	9
	-7	-9				-1	1	5	2	-15	4	-1	8	-8	-7
30															
	0	-2	1	-3	-2	5	4	-5	37	-3	8	-6	-11	12	74
	-6	2	2	-3	17	-9	-18	-7	6	0	-1	21	12	0	-20
	-12	-19	-13	-7	-14	-5	-8	-16	-12	-15	-7				-8
	-10	-12	-6	-8	-13	-14						-21	-4	-2	
	2		-11	-7			-29	-24	-25	-19	-25	-27			
					-15	-13	-6	-9	-14			-21	-27	-15	-12
					-18	-16	-12	1	3	-15	-31	-4	-2	-19	-10
			-9	-24	-11						7	-49	-42	-28	6
	-5	-11	-7												
	-6														
20															
														8	-27
							-29	-15	3	-19	-18	-1	-44	9	-3
			19	-21	-9	-17	-13		-3	-14	-7	-17			-19
				-6	-10	-6	-4	-29							-9
	20	-19	-21		53										-27
	-4		58											138	-2
				-1	-11									-4	
					-49	-18	14	0	4					5	
								1	12	8				-1	
10															
									0		6	-7	30	-6	-7
									-1	-5		0	15	-1	
									4	3	-6			-17	
	-9	-9						-28	-4	-3			-2		
	-9	-25					-26	26	-7	-9			-9		
	1	-12	0			3			-23	-3	-10	-32	-26	-12	
	-5	-5	-8	-11	1	-9	-10	-38	-18	-6		10		-7	
	5	5	-11	-4						10	-12			-9	
	3	9		9	-30					6	-2			-19	
	-4	-2	-3		-26	2				-10	1	-14		-10	-14
0															

165 170 175 180

180 -175 -170 -165

											9		27	15
										18	16			
60															
	-23	34					15	17	20	28	25	21	14		
	-13	-66	16	6	12	16	22	20	18	16	10	21	22	15	
	2	-3	-14	-20	-24		50	40	27	19	23	20	18	15	
	5	3	-1	-12	-20	-19	5	31	22	45	50	30	26	30	33
	-8	2	1	5	5	4	1	5	-10	-3	-1	20	38	28	20
	-49	-12	8	13	13	11	9	10	1	30	23	15	26	29	32
	32	35	4	6	6	1	-4	9	10	18	35	80	120	124	31
	31	-16	-5	6	10	8	41	86	95	93	61	-12	-60	-120	-121
	24	87	26	55	-37	-100	-90	-84	-101	-136	-125	-87	-30	18	40
	-155	-152	-143	-121	-105	-72	-47	-39	-5	14	33	48	47	46	40
50															
	37	46	47	45	40	50	50	45	45	44	40	37	30	33	36
	18	20	19	12	19	29	29	35	32	29	25	19	22	21	23
	-1	5	10	10	8	12	16	33	14	15	15	14	15	14	18
	-16	-2	-2	-2	-1	-2	8	24	10	12	15	9	11	14	16
	-15					-9	-5	4	2	-13	9	10	10	11	13
	-17	-6				-5		4	3	-3	9	9	7	11	12
		-25					-2	2	-4			6	-4	-12	-6
		-36		-5			-23	5	4	-9	-8	-6	-6	6	-15
				8			-18	-8	-4	-14	-5	-2		9	3
		-43	11					-4	-1	-13	-2	2	-4	0	3
40															
		-43								-14		-23			
		-1						-1	7	-14			-2		
		-13						-15	6						
		6	-6					-15	2				-5	-10	-32
			-1					-14	1	-6	-7	-8			-7
	-24		17			6	4	0	-2	-11					-20
		65	-2	37	8	2		-14	-11	-14		1	-2		
	1	-4	-4		-22	-10	-16	-8	-7			-7	-7		-13
	45	-4	-3	8	-9	12	4	-10		-9	-8	-7	-11	-9	-8
	-16	-12	-6	-16	-10	-14	-14	-14	-12	-11		-2	-6		
30															
	-17	-30	-33	-9	-6	-22	-4	1	-20	0	3	1	0	0	-4
	15	120	65	34	1	-18	-7	4	16	2	10	16	11	8	2
	-22	-6	7				-12	-12		14	8	9	13	16	15
			-9				-30	-48	-16	-23	-29	-16	-5	10	18
			-9					42	39	55	22	125	79	-40	-7
	-5	2	-3						0	-22	-44	34	71	4	0
	-24	-16	-9	5	5	12	11	7	25	33	3	-20	-22		
	5	-10				-6			7	15	23	16	15	10	11
		-7	-6	-11	-7	-1	3	-1		10	-19			6	7
	1					-5	0	-14	20	3				7	2
20															
	-4				51	-23	20	14	9	-8	-24	-28	-7	-5	-2
	25	-21	-13	-5	-15						17			0	-8
	-6	-24								-37					-13
										-38			13	5	18
										10					
									35	-11	-17	7	3	2	-24
							-5	3	32	-31	-24	-21	7	-9	
					2	0	-24			-4	-19	1	5	-6	-1
				-4	1				-5	-15	-11	-7	2	18	6
		3	-8					-18	-15	-4	23			1	25
10															
	-15	-7	-2	0	-6	-9	-11	-18	-4	-7	-1	2	-2	0	38
							-28	-14	-8	4			5	-3	-9
						-34	-34	-18	-7	5	0	-6	-13		
					-16	-15	7	-16	3	-1	-3	-9			
				-8	-6	-31	-14	-22	-8	-14	7	8			5
			-21	-10	-2	-16	-23	-12	-6	-5	15		4	-7	1
			-18	-6	8		0	-12		-4	12		9		-1
	-8	-5	-17	-8	6	-4	13		-13	-7	5			8	4
	-14	-10	-4	-12	-1					5	-10			0	9
	7	-7	-1	94						18	-11		16	17	17
0															

180 -175 -170 -165

-165 -160 -155 -150

	15	23	24	15	29	36	30	19	3	27				-52	-94
			13	30	43								74	-95	-34
60															
				38	63	48	34	33	37	39	35	17	-5	6	10
			40			31	25	29	40	46	43	-4	4	6	10
							21	22	52	0	14	27	27	-3	-2
	25	24	25	30	14	18	42	31	20	-21	24	55	39	3	-24
	28	24	31	60	72			30	59	67	47	-6	-38	-12	12
	84	106	76	37	36	26	13	11	-18	-30	-12	-30	30	40	76
	44	-49	-105	-96	-62	-26	-5	20	42	39	40	25	27	20	25
	-71	-10	11	36	42	42	35	37	39	33	37	30	25	28	
	46	39	42	47	46	46	38	38	24	23					
	33	28	26	25	22	20	27	26	27	22					
50															
	23	24	14	20	14	12	23	24	26						
	15	19	11	15	18	23	13	16	22						
	14	17	14	16	15	11	13	13	19						
	14	12	14	16	14	3	10	11	23						
		5	8	4	4	0	8	3	17						
	-4	-8	-2		12	3	5	5	13	9					
	-7	-45			5	0	0	-1	8		6	4			
	-7	-44			-5	-1	0	-8	2				3	11	-6
	-18	-28	-26	-4	-1	3	6	-3	1					20	14
	-1	-8	-8	-1	-5	-2	7	0	-1	11	12	7	14	11	5
40															
	-10	-20	-23	-26	-13		9	0	7	12	8		-10		
	2	9	-33	-10	2	21	-7	-15	-2	4		-5			
	7	4	20	6	15	-4	-8	-14	-10						-20
	-21	-8	-9		-14	-5	-3	-6	-4						
	-13	-5	-8	-10	-11	-13	-10	-13	-10	4	1				
	-10	-4	-6	-13	-14	-20	-13	-6	-8	4	-2		-12	-14	-11
	-15	-4	-3	-11	-10	-7	-8	-10	-15		2	-2	-5	-4	-4
	-13	-11	-8	-7	-6	-19	-10	-11	-9		4	2	3	4	0
	-24	-5	-11	-4	-5	-14	-12	-16	0		7	4	3	7	4
		-7	-3	-9	-10	-18	-11	-14	-1		1	3	19		3
30															
	-6	-12	7	3	-7	-22	-18	-9	-3	-15	-15	-10	6	6	0
	4	8	3	8	-5	-13	-1	-4	-1	-15	-15	5	5	-2	-8
	11	4	13	19	1	-4	13	-2	-1	-15	-15	-10	-6	-6	-10
	24	15	12	13	7	-5	20	3	5	-5	-3	2	4	-4	-5
	7	8	8	18	6	4	18	17	14	2	0	-3	-3	-3	-2
	-15	-16	-12	-1	-3	2	19	31	27	15	12	4	-1	-2	-2
		19	26	35	-19	-35	0	15	27	31	27	7	0	-15	-15
	16	2	11	21	22	69	-36	-39	-15	-8	15	17	3	-3	-12
	0	13	11	-2	41	37	49	114	-2	-80	-27	9	6	-1	-10
	12	10	15	7	-2	-14	-21	7	148	88	-37	4	1	-3	-7
20															
	0	-1	2	8	13	12	10	-8	-34	331	39	0	0	-6	-8
	3	-3	-9	0	9	19	16	-8	-18	-19	-35	0	1	1	-8
	4	-3	-11	2	4	17	1	5	9	-2	-8	-3	0	4	-5
	-3	-15	-3	3	0	-2	-7	-6	2	11	6	0	-5	-7	-11
				5	4	0	-8	-9	-5	-3	-5	-7	-12	-9	-6
		2	-7	-1	-3		-9			-10	-18	-18	-14	-16	-4
		3		4			-9				-11	-17			-13
	0	-7	-5	-7	-14	-6	-3				-6	-8			-1
	18	1									-6		-8		-3
	-3										-4			0	-5
10															
										-1				2	-7
								-2	0					-9	-3
	10							10	17					-5	
	2	-10	19					29	18			-5	-7		
	5				4		13	17				-4			
	1		30	10	9	-8	18				5				
	5	18	27			38	15	22	10	3	9	20			
	59	12	5	8					-6				1	0	17
	14			5	10	9	25	29							
	13					5	18	6							
0															

-165 -160 -155 -150

TABLE 2

Comparison of total geoid with gravity models SE 3 (Gaposchkin, 1974), GEM 6 (Lerch et al., 1974) and GEM 8 (Wagner et al., 1976) along selected profiles (Fig. 9).

Earth model	RMS difference meters
SE 3	±6.6
GEM 6	±4.6
GEM 8	±5.7

DETAILED 1° x 1° GRAVIMETRIC INDIAN OCEAN GEOID

A. Introduction

A comprehensive set of data on the variation of the sea surface height has been obtained in the past three years by means of the GEOS-3 satellite carrying a radar altimeter. With knowledge of the satellite's position and after corrections for oceanographic effects, one obtains along-track variations of the geoidal height over the world's oceans. These measured undulations of the geoid are extremely valuable for geophysical interpretations because they provide, in part, information about density inhomogeneities in the earth's upper mantle. The distribution of the density inhomogeneities reflected in the geoid will hopefully provide information on convection within the mantle or on other possible driving forces of the earth's lithospheric plates.

Consequently, it is of special interest to determine and study the geoid on a worldwide scale. In the past, the only way to compute the geoid over oceanic areas was to apply Stokes' integral to the gravity anomalies observed over the earth's surface. Gravimetric geoids over oceanic areas have been computed in this way in the western North Atlantic (TALWANI, POPPE and RABINOWITZ, 1972), in the Indian Ocean (KAHLE and TALWANI, 1973) and in the Northwest Pacific (WATTS and LEEDS, 1977).

The knowledge of the geoid derived from surface gravity is essential in order to calibrate the radar altimeter, test its performance and possibly suggest optimum locations at which the altimeter measurements should be performed. Eventually, it will be desirable to compute a gravimetric geoid independent of satellite altimetry in order to obtain the dynamic sea surface height, the slight discrepancy between the geoid and sea surface being important in ocean dynamics.

In turn, there are techniques to recover gravity anomalies from GEOS-3 measurements of the sea surface height (e.g. KAHN, SIREY, BROWN and AGRAWAL, 1976). The method for obtaining gravity anomalies on the basis of satellite radar altimetry can be very useful for determining the gravity field in remote areas such as in the southern hemisphere where ship measurements are scarce. In order to test this method and define its accuracy it is necessary to compare the results with independently obtained gravity values from surface ship gravity measurements in surveyed regions.

It is the purpose of this paper to compile a new set of 1° x 1° mean free-air gravity anomalies in the Indian Ocean by using all the gravity data available up to 1976, compute the corresponding gravimetric geoid and compare the results with GEOS-3 altimeter derived geoid profiles (in the Southwest and Northeast Indian Ocean).

B. Sea Gravity Data in the Indian Ocean

Fig. 1 shows the location of the submarine pendulum observations (VENING MEINESZ, 1948; GIRDLER and HARRISON, 1957; TALWANI, 1962) as well as the ship's tracks along which continuous gravity measurements were obtained.

At present, there are about 100,000 gravity data available in the Indian Ocean.

The data used in this study were obtained by

a) Lamont-Doherty Geological Observatory of Columbia University during VEMA cruises 18, 19, 20, 22, 24, 29 and 33 and during CONRAD cruises 8, 9, 11, 12, 14 and 17.

b) Institute of Geophysics and Planetary Physics of the University of California at Los Angeles and Scripps Institution of Oceanography, San Diego, during ARGO cruises "Monsoon" and "Lusiad" (HELFER, CAPUTO and HARRISON, 1963; CAPUTO, MASADA, HELFER and HAGER, 1964).

c) Department of Geodesy and Geophysics, Cambridge University, during OWEN cruises 611 through 619, 621 through 626, 110, 111 and during DISCOVERY cruises 671 and 672 (HYDROGRAPHIC DEPARTMENT, 1963, 1966; WILLIAMS, 1968).

d) ESSA (now NOAA) during PIONEER and OCEANOGRAPHER Cruises (U.S. DEPARTMENT OF COMMERCE, 1969, 1970).

e) Bundesanstalt für Bodenforschung, Hannover, West Germany, during METEOR cruise (PLAUMANN, 1965, personal communication).

f) Woods Hole Oceanographic Institution, U.S.A., during CHAIN cruise 100 (BOWIN, 1973, and BOWIN, personal communication).

The data obtained prior to 1971 are included in the gravity maps (TALWANI and KAHLE, 1975) of the International Indian Ocean Expedition (IIOE) Atlas of Geology and Geophysics (UDINTSEV, 1975) as well as in the previous Indian Ocean geoid paper (KAHLE and TALWANI, 1973). During recent Lamont cruises (1974, 1977) a considerable amount of data of greater accuracy have been accumulated which made it desirable to recompile the entire set of 1° x 1° mean gravity data. The main areas of substantial improvements in the surface gravity field of the Indian Ocean are the Central Indian Basin including the prominent Indian Ocean gravity low as well as the South-West Indian Ocean covering the pronounced South-West Indian Ocean gravity high. In the West Pacific we incorporated 1° x 1°

mean free-air anomalies compiled by WATTS and LEEDS (1977). For the Indian peninsula we used a set of 1°x 1° anomalies by WOOLLARD (1970) and values for Madagascar were provided by the International Gravity Bureau, Paris (CORON, 1972, personal communication).

The new set of 1° x 1° free-air anomalies for the Indian Ocean is listed in Table 1. The gravity values are referred to the International Reference Ellipsoid ($f = 1/297$).

The 1° x 1° averages were obtained from revised free-air anomaly contour maps by dividing each 1° x 1° square into nine smaller squares. The values at the centers of these smaller squares were visually interpolated and averaged to give a value for the 1° x 1° square. In areas such as the southwest Indian Ocean the 1° x 1° values were determined by averaging along individual ship's tracks.

C. Method of Geoid Computation

The following method - proposed and used by many authors including STRANGE, VINCENT, BERRY and MARSH (1972) and TALWANI, POPPE, and RABINOWITZ (1972) - has been adopted in computing the gravimetric geoid for the Indian Ocean:

1) Calculation of the free-air anomalies based primarily on the satellite derived gravity field, in this case the GEM-6 potential field model which includes harmonics up to $n = 16$ (LERCH et al., 1974; SMITH et al., 1976).
2) Subtraction of the GEM-6 free-air anomalies from the new set of 1° x 1° mean gravity data (: Difference anomalies $\delta\Delta g$).
3) Computation of the difference geoid ΔN (Fig. 2) by applying Stokes' integral to the difference anomalies $\delta\Delta g$.
4) Summation of the GEM-6 geoid N_{GEM-6} (Fig. 3) and the difference geoid ΔN (: Gravimetric geoid $N = N_{GEM-6} + \Delta N$) (Fig. 4).

The advantage of this procedure is that Stokes' integration (HEISKANEN and MORITZ, 1967)

$$\Delta N = \frac{1}{4\pi g R} \int S\ (\Psi)\ \delta\Delta g\ da \qquad (1)$$

has to be carried out only over the Indian Ocean because outside this area the difference anomalies $\delta\Delta g$ are assumed to be zero.

We recognize that we are ignoring the difference anomalies outside the Indian Ocean, which will give rise to some errors particularly near the boundaries of our area of integration, these errors however are less than 1 meter (STRANGE et al., 1972). In parts of the Indian Ocean, where gravity averages could not be obtained by the procedure described above - because of scarcity of data - we assumed the difference anomaly $\delta\Delta g$ to be zero. As we shall see in a later section, this gives rise to errors in regions of no ship gravity measurements, but this procedure is still superior to procedures in which gravity values are truncated after a certain radius.

In Equation (1)ΔN = Difference geoid, R = mean earth's radius, g = mean earth's gravity, ψ = angular distance between the element of area da (at which $\delta\Delta g$ is given) and the point of calculation, $S(\psi)$ = Stokes' function. Stokes' function $S(\psi)$ is defined as

$$S(\psi) = \frac{2}{\sin\psi} \quad F(\psi) \qquad (2)$$

where $F(\psi) = \cos\frac{1}{2}\psi + \frac{1}{2}\sin\psi(1-5\cos\psi - 6\sin\frac{1}{2}\psi - 3\cos\psi\ln(\sin\frac{1}{2}\psi + \sin^2\frac{1}{2}\psi))$

Since S (ψ) changes strongly near $\psi=0°$ the effect of a square very close to the computation point cannot be calculated by simply using $S(\psi)$ with ψ being the distance to the center of the square. For this reason the squares close to the computation points were subdivided into smaller squares in such a way that the percentage error in calculating $S(\psi)$ is below 1% (TALWANI et al., 1972).

D. The GEM-6 Geoid, Difference Geoid and 1° x 1° Gravimetric Geoid

In subtracting the GEM-6 free-air anomalies (n=16) from the 1° x 1° surface data and applying Stokes' integral to the difference anomalies, a difference geoid is obtained which reflects mainly the contributions of harmonics $16 < n < 180$. The order n=180 corresponds to a wavelength of 2 degrees which is approximately represented by the 1° x 1° mean free-air anomalies. As such, the difference geoid containing wavelengths between about 220 km and 2500 km can be interpreted as a filtered version of the total geoid. This range is of special interest for geophysicists because mass inhomogeneities associated with sea-floor spreading and lithospheric motions may produce geoid anomalies of such wavelengths. Fig. 2 shows the computed difference geoid.

The aereal average of the difference gravity anomalies $\delta\Delta g$ is -.54 mgal and that of the difference geoid ΔN is -.47m. Thus, the systematic error in geoid height corresponding to this difference is negligible and may not be considered further. The general pattern of the difference geoid can be characterized by the zero meter contour line, indicated by the heavy line on Fig. 2. The entire Northwest Indian

Ocean including the major basins such as the Somali and Arabian Basins are associated with a negative difference geoid reaching -18 m over the Arabian Basin. Another large area with negative difference geoidal undulation is the Northeast Indian Ocean covering the southern Central Indian Basin, the West Australian Basin and the Indonesian deep sea trench with lowest values over the Sunda Trench (-22 m) and Timor Trough (-30 m).

The northern Central Indian Basin, the major part of the Bay of Bengal (Ganges Cone) and the entire Southwest Indian Ocean is characterized by a pronounced difference geoid high with highest values over the Madagascar Ridge (+20 m). While the major actively spreading ridges are not well expressed in the difference geoid, the triple junction of the three Indian Ocean ridge branches at 25°S, 70°E clearly stands out as a positive feature (+8 m). Also aseismic ridges including the Madagascar Ridge, the Mascarene Plateau, the Ninetyeast Ridge (+14 m) and the Afanasy Nikitin Seamount chain are associated with a positive difference geoid.

The total 1° x 1° geoid obtained by adding the difference geoid to the GEM-6 geoid (Fig. 3) is shown in Fig. 4. While the difference geoid reflects wavelengths between 220 and 2500 km, the total geoid reveals information with all wavelengths greater than 220 km. As might be expected, the long wavelength features are still present in the total geoid. The prominent Indian Ocean geoid low (-130 m) as well as the geoid highs in the Southwest Indian Ocean and over the western Pacific are clearly expressed in the 1° x 1° total gravimetric geoid. In addition the short and intermediate wavelength features such as the Mozambique Ridge and Basin, the Madagascar Ridge and Mascarene Plateau, the Triple Junction, the Ninetyeast Ridge and the Sunda Trench are evident by the bending of contours around those structures. The minimum south of India has shifted towards the northeast and has decreased in amplitude by 8 m. The Somali Basin low appears to connect with the Arabian Basin low.

E. GEOS-3 Profiles in the Indian Ocean

Classically the geoid height has been determined by the Stokes' integration of gravity values, as demonstrated in the previous section. The altimeter in the GEOS-3 satellite now makes it possible to directly measure the elevation of the satellite over the ocean surface. When combined with precise orbital tracking one obtains the height of the ocean surface relative to an earth ellipsoid. The sea surface is not at a constant gravitational potential; nongravitational forces can cause slight deviations between the geoid and sea surface. Dynamic topography due to ocean currents can be 100 cm in amplitude (DEFANT, 1941), tidal heights in the deep ocean can also be 50 cm in amplitude (SCHWIDERSKI, 1977). After correction for such deviations, measurements of the geoid height may be obtained along the sub satellite track.

While this procedure for obtaining geoid heights from altimeter measurements is valid, it is subject to certain errors. An extensive error analysis has been made for GEOS-3 measurements in the calibration area between Florida and Bermuda (MARTIN and BUTLER, 1977), this showed an average noise level of .72 m in the intensive mode and 1.81 m in the global mode for cumulative altitudes every .1 seconds. Additionally, bias values of -5.3 m (intensive mode) and -3.55 m (global mode) were discovered for altitude determinations by the altimeter. Accuracy of the sea surface height measurements is primarily limited by the orbit computations. Long wavelength errors in orbital height can be between 1-2 m rms and 10 m rms depending upon the method of tracking (H.R. STANLEY, personal communication). In constructing a consistent set of altimeter tracks a least square reduction of crossover errors can be utilized, such a technique effectively eliminates any long wavelength orbital errors (RUMMEL and RAPP, 1977). In this paper we are primarily interested in comparing original GEOS-3 data (from NASA Wallops Flight Center) with a gravimetric geoid in the Indian Ocean to see the influence of such errors. The orbit numbers and dates for the satellite tracks are listed in Table 2.

Operation of the altimeter is conceptually simple, a radar pulse is transmitted downward and the return pulse is received after reflection from the sea surface. As there is a finite beam width, the instrument measures the sea surface height over a limited area, with a 14.3 km radius for global mode and 3.6 km radius for intensive mode. Operation of the altimeter is in one of two modes; global mode or intensive mode during which measurements are made every .01024 seconds. This is a sampling rate of approximately every 65.5 meters. During data processing the sea surface height measurements are averaged over a finite time, this is a low pass filtering operation. In this paper we only use time averaged data usually over a 2.048 second interval, consequently the resultant datum is an average measurement of the sea surface height over an area of 14.3 by 13.4 km (global mode) or 3.6 by 13.4 km (intensive mode). Knowledge of the beam footprint and the altimeter accuracy is necessary in understanding the utility and ultimate resolution of GEOS-3 measurements.

The geoid measurements made by the radar altimeter are shown in Figure 5 and 6. The sub satellite track is plotted on a Mercator projection, the geoid height is plotted perpendicular to the track with positive values on the north side. An arbitrary constant offset has been subtracted from each profile because we are only interested in the relative changes of the geoid. Figure 5 is the Indonesian Island arc region and Figure 6 is the Southwest Indian Ocean.

Three GEOS-3 tracks, all approximately perpendicular to the Java Trench, are illustrated in Figure 5. Each profile shows a steep long wavelength increase in the geoid height of 90 m over a distance of approximately 2400 km, with highest values towards the northeast. Not being symmetric about the trench axis, the geoid continues to increase across the trench until leveling off in the Philippine Sea (Fig. 4). Directly over the Java Trench the profiles indicate a geoid low of -10 m amplitude and 250 km wavelength. Analagous with the gravity low over deep sea trenches (WATTS and TALWANI, 1974), this geoid low is primarily caused by the bottom topography.

While the principal features of the Northeast Indian Ocean are deep sea trenches and an island arc, the Southwest Indian Ocean is the location of a seismically active spreading center - the Southwest Indian Ridge. Topographically high, it is associated with a 6 m positive geoid anomaly, 500 km wide (Figure 6 and 7, especially tracks G0219 and G0224). Additionally a longer wavelength geoid gradient exists, increasing towards the southeast and leveling off at the ridge axis (Figure 4 and 6).

F. Comparison of gravimetric geoid with GEOS-3 altimeter measurements

Being a new scientific instrument, the accuracy and precision of the GEOS-3 altimeter must be determined. Obviously a useful test would be the comparison of the gravimetric Indian Ocean geoid with geoid heights measured directly by the GEOS-3 radar altimeter. In making the comparison characteristics of each method must be understood. The gravimetric geoid contains information from the GEM-6 gravity model up to $n = 16$, the higher harmonics (to $n = 180$) being dependent upon the accuracy and availability of ship gravity data. Resolution of features with wavelengths less than about 200 km cannot be expected in the gravimetric geoid due to our averaging procedure over 1° x 1° squares. With the GEOS-3 altimeter sea surface features with wavelengths of 1.31 km can technically be resolved (with average values every 655 m), however with the averaged data we utilized resolution is limited to 28 km. Also inaccurate orbit determinations result in constant and very long wavelength errors in the altimeter measurements. Consequently we only make comparisons of geoid information with wavelengths shorter than several thousand km.

GEOS-3 measurements of geoid height are referred to an ellipsoid with flattening $f = 1/298.255$ and semi-major axis $a = 6378145$ m, thus the gravimetric geoid was converted to this ellipsoid prior to comparison. Linear interpolation of the gravimetric geoid with the nearest three geoid values was used in order to compute the gravimetric geoid height along the sub satellite track. Results of this comparison are in Figure 7, each track location is plotted in Figure 5 or 6 and the track designation (e.g. G0195) is at the start of the pass (time = 0 seconds).

Obviously the radar altimeter cannot measure the geoid over land, thus such measurements have been deleted (e.g. Madagascar). GEOS-3 measurements in Figure 7 are indicated by the thin line and the gravimetric geoid by the thick line. An obvious feature of this comparison is the offset values of up to 25 m, probably due to error in orbit determination. These profiles indicate a great similarity (except for a constant shift) between GEOS-3 data and the gravimetric geoid wherever good gravimetric control exists (see e.g. G0242). In some areas (south of 39°S in SW Indian Ocean) only few sea gravity measurements exist. Consequently, in this area the gravimetric geoid contains little information for wavelengths shorter than n = 16 (2500 km). This is seen in tracks G0224 and G0219 between 0 and 120 seconds over the Southwest Indian Ridge. The GEOS-3 data indicate a clear anomaly over the ridge while the gravimetric geoid does not. As there is poor gravity control in this area and the anomaly is seen on both tracks, we conclude the gravimetric geoid is incorrect along this part of profiles G0224 and G0219, whereas GEOS-3 measures the true geoid anomaly over the Southwest Indian Ridge.

In finer detail, the GEOS-3 altimeter has greater resolution than the 1° X 1° gravimetric geoid (of this paper), due to a smaller sampling interval for the altimeter. Over the Java Trench (tracks G0195, G0193 in Figure 7) the effect of the averaging procedure for the calculation of the gravimetric geoid is clear: GEOS-3 data indicate a 250 km wide low, 10 m deep, the gravimetric geoid barely defines the low. Due to the information content in wavelengths shorter than about 200 km, it is understandable that the GEOS-3 altimeter with a smaller sampling interval would measure the geoid more accurately in this region.

G. Conclusions

On the basis of marine gravity measurements in the past three decades, we have compiled and listed in Table 1 1° x 1° mean free-air gravity anomalies for the Indian Ocean. These values are useful in geoid computations and as a test for techniques of gravity recovery from GEOS-3 geoid measurements. Utilizing these 1° x 1° averages we have computed a difference and total gravimetric geoid for the region.

The difference gravimetric geoid contains information with wavelengths between about 200 km and 2500 km, such wavelengths being determined by lateral density inhomogeneities within the crust and upper mantle. Anomalies of -18 m in the difference geoid exist over the Arabian Basin, another large area with negative values is the Northeast Indian Ocean with lowest values over Sunda Trench (-22 m) and Timor Trough (-30 m). Over the Madagascar Ridge there is a 20 m difference geoid high, another positive feature is the triple junction of the three Indian Ocean ridges, +8 m amplitude. Aseismic ridges such as Madagascar Ridge, Ninetyeast Ridge and Afanasy Nikitin seamount chain are also associated with a positive difference geoid.

The total gravimetric geoid contains information on all wavelengths down to about 200 km; thus it has both long and intermediate wavelength features. Over the Central Indian basin is the most prominent long wavelength feature, the -130 m Indian Ocean geoid low. Steep geoidal gradients exist over the Indonesian Island Arc up to a flat region of the geoid in the Phillipine Sea. Another level portion of the geoid exists south of the Crozet Plateau. Intermediate wavelength anomalies in the total geoid are over the same features as in the difference geoid.

GEOS-3 profiles of geoid height show anomalies across topographic features in the Indian Ocean. Over the Southwest Indian Ridge there is a 6 m positive geoid anomaly, 500 km wide. Across the Java Trench there is a steep increase in the geoid of 90 m over a distance of 2400 km, with highest values towards the northeast. Directly over the Java Trench there is a -10 m geoid low, 250 km wide. If this relative low is removed, an overall geoid high remains. This is an interesting result because it might shed some light on the density inhomogeneities associated with the descending Indian lithospheric plate. In part, this pronounced geoid high - verified in the GEOS-3 profiles - can be explained by the positive density contrast of the cold lithosphere with respect to the less dense adjacent asthenosphere. On the basis of gravity data Watts and Talwani (1974) concluded this effect is not the only component because unrealistically high density values would have to be postulated to explain both the "outer gravity high" and the overall high. It is further interesting to note that in our GEOS-3 profiles an "isolated" outer geoid high does not exist. The increase in geoid height seaward of the Indonesian Trench appears to be a portion of the overall long-wavelength high - only interrupted by the relative small-wavelength low over the trench proper. Another possible source for part of this long-wavelength geoid high may be associated with the downwarped isotherms caused by the cold sinking lithosphere. If the temperature is lowered at the Olivine-Spinel transition zone (at depths between 300 and 400 km) this phase change migrates upwards, thus providing a positive density contrast of about 0.2 gm/cm^3 (BOTT, 1971; RINGWOOD, 1976). To explain this long wavelength geoid anomaly at the Java Trench, a detailed modeling study should be undertaken; only then will the cause of this anomaly be better defined.

Comparisons of GEOS-3 data with the gravimetric geoid show a great similarity where good gravimetric control exists. Due to the shorter sampling interval (14 km versus about 100 km averaging for the gravimetric geoid) for the altimeter the GEOS-3 satellite can better detect short wavelength features such as the low over the Java Trench. On the basis of these comparisons we conclude the GEOS-3 altimeter is an accurate and highly useful instrument for mapping the geoid at sea.

REFERENCES

Bott, M.H.P., 1971. The mantle transition zone as a possible source of global gravity anomalies, Earth and Planetary Science Letters, 11, 28.

Bowin, C., 1973. Origin of the Ninety-East Ridge from studies near the equator, J. Geophys. Res., 78, 6029.

Caputo, M., Masada, R., Helfer, M.D., and Hager, C.L., 1964. Gravity measurements in the Atlantic, Pacific and Indian Oceans, May 1962 - August 1963, R/V ARGO. Interim Report, Univ. of Calif, Inst. of Geophysics and Planetary Physics.

Defant, A., 1941. Quantitative Untersuchungen zur Statik und Dynamik des Atlantischen Ozeans, Die relative Topographie einzelner Druckflächen in Atlantischen Ozean, Deutsche Atlantische Exped. Meteor, 1925-1927, Wiss. Erg., VI, 183.

Girdler, R.W. and Harrison, J.C., 1957. Submarine gravity measurements in the Atlantic Ocean, Indian Ocean, Red Sea and Mediterranean Sea. Proc. Roy. Soc., A 239, 202.

Heiskanen, W.A. and Moritz, H., 1967. Physical Geodesy, W.H. Freeman and Co., San Francisco, Calif.

Helfer, M.D., Caputo, M. and Harrison, J.C., 1963. Gravity measurements in the Pacific and Indian Oceans, MONSOON Expedition 1960-1961. Interim Rept., Univ. of Calif., Inst. of Geophysics and Planetary Physics.

Hydrographic Department, Admiralty, 1963, 1966: Bathymetric, magnetic and gravity investigations H.M.S. OWEN 1961-1962, 1962-1963, Admiralty Marine Sci. Publ., no. 4, parts 1, 2; no. 9, parts 1, 2.

Kahle, H.G. and Talwani, M. 1973. Gravimetric Indian Ocean Geoid. Z. für Geophysik, 39, 167 and 491.

Kahn, W.D., Sirey, J.W., Brown, R.D. and Agrawal, B.B., 1976. Gravity anomaly determination by means of GEOS-3 altimetry data. (Abstract only) EOS, 57, 901.

Lerch, F., Wagner, C.A., Richardson, F.A., Brown, F.E., 1974. Goddard Earth Models 5 and 6 Rep. X-921-74-145, Goddard Space Flight Center, Greenbelt, Md.

Martin, C.F. and Butler, M.L., 1977. Calibration results for the GEOS-3 altimeter, NASA Contractor Report CR-141430.

Ringwood, A.E., 1976. Phase transformations in decending plates and implications for mantle dynamics, Tectonophysics, 32, 129.

Rummel, R. and Rapp, R., 1977. Undulation and anomaly estimation using GEOS-3 altimeter data without precise satellite orbits, Bull. Geod., 51, 73.

Schwiderski, E.W., 1977. Ocean tides and GEOS-3, Trans., A.G.U., 58, 370 (Abstract only).

Smith, D.E., Lerch, F.J., Marsh, J.G., Wagner, C.A., Kolenkiewicz, R., and Kahn, M.A., 1976. Contributions to the National Geodetic Satellite Program by Goddard Space Flight Center, J. Geophys. Res., 81, 1006.

Strange, W.E., Vincent, S.F., Berry, R.H. and Marsh, J.G., 1972. Detailed gravimetric geoid for the United States, In: The Use of Artificial Satellites for Geodesy, S. Henriksen, A. Mancini, and B. Chovitz (eds.), Washington, D.C., 169.

Talwani, M., 1962. Gravity measurements on H.M.S. ACHERON in South Atlantic and Indian Oceans, Geological Society of America Bull., 73, 1171.

Talwani, M., Poppe, H. and Rabinowitz, P., 1972. Gravimetrically determined geoid in the western North Atlantic. In: Sea surface topography from space, NOAA Tech. Rept. ERL-228 - AO ML 7-2, 34p.

Talwani, M. and Kahle, H.-G., 1975. Maps of free-air gravity anomalies in the Indian Ocean, In: The International Indian Ocean Expedition Geological - Geophysical Atlas of the Indian Ocean, G. Udintsev (ed.), Moscow, 87.

Udintsev, G. (ed.), 1975. The International Indian Ocean Expedition Geological - Geophysical Atlas of the Indian Ocean, Moscow.

U.S. Department of Commerce, Environmental Science Services Administration, 1969. International Indian Ocean Expedition USC & GS Ship PIONEER, 1964, v. 1 & 3. Washington.

U.S. Department of Commerce, Environmental Science Services Administration, 1970. Technical Report ERL 152-OD 4. Global Expedition USC & GS Ship OCEANOGRAPHER - 1967 Cruise Narrative and Scientific Program. Boulder.

Vening Meinesz, F.A., 1948. Gravity expedition at sea 1923-1938, v.IV, Publ. Neth. Geod. Commission, Delft.

Watts, A. B. and Talwani, M., 1974. Gravity anomalies seaward of deep-sea trenches and their tectonic implications, Geophys. J. Roy. Astr. Soc., 36, 57.

Watts, A.B. and Leeds, A., 1977. Gravimetric geoid in the Northwest Pacific Ocean, Geophys. J. Roy. Astr. Soc., 50, 249.

Williams, C., 1968. R.R.S. DISCOVERY cruise 16 Indian Ocean 1967, bathymetric, gravity and magnetic data report.

Woollard, G.P., 1970. 1° x 1° square free-air gravity averages in India, Publ. Hawaii Inst. of Geophys.

FIGURE CAPTIONS

Figure 1. Location of gravity measurements in the Indian Ocean. Lines are surface ship data, dots are submarine pendulum observations.

Figure 2. Difference 1° x 1° Geoid. This is the result of the Stokes' integration of the difference gravity.

Figure 3. GEM-6 geoid, referred to the International Ellipsoid.

Figure 4. Gravimetric 1° x 1° geoid, referred to the International Ellipsoid.

Figure 5. GEOS-3 profiles in the Indonesian Island Arc region. Sub satellite track is dotted line, track designation (e.g. G0193) is at start of the pass. Geoid height is plotted perpendicular to track, positive values are northwards and the scale is indicated. An arbitrary constant was removed from each track.

Figure 6. GEOS-3 profiles in the Southwest Indian Ocean. Sub satellite track is dotted line, track designation (e.g. G0154) is at start of pass. Geoid height is plotted perpendicular to track, positive values are northwards and the scale is indicated. An arbitrary constant was removed from each track.

Figure 7. Comparison of gravimetric geoid with GEOS-3 altimeter measurements. GEOS-3 measured geoid height is plotted as a function of time from start of each pass, track locations are shown in Figures 5 and 6. The dark line is the gravimetric geoid height, referred to an ellipsoid 1/f = 298.255. The distance scale is indicated.

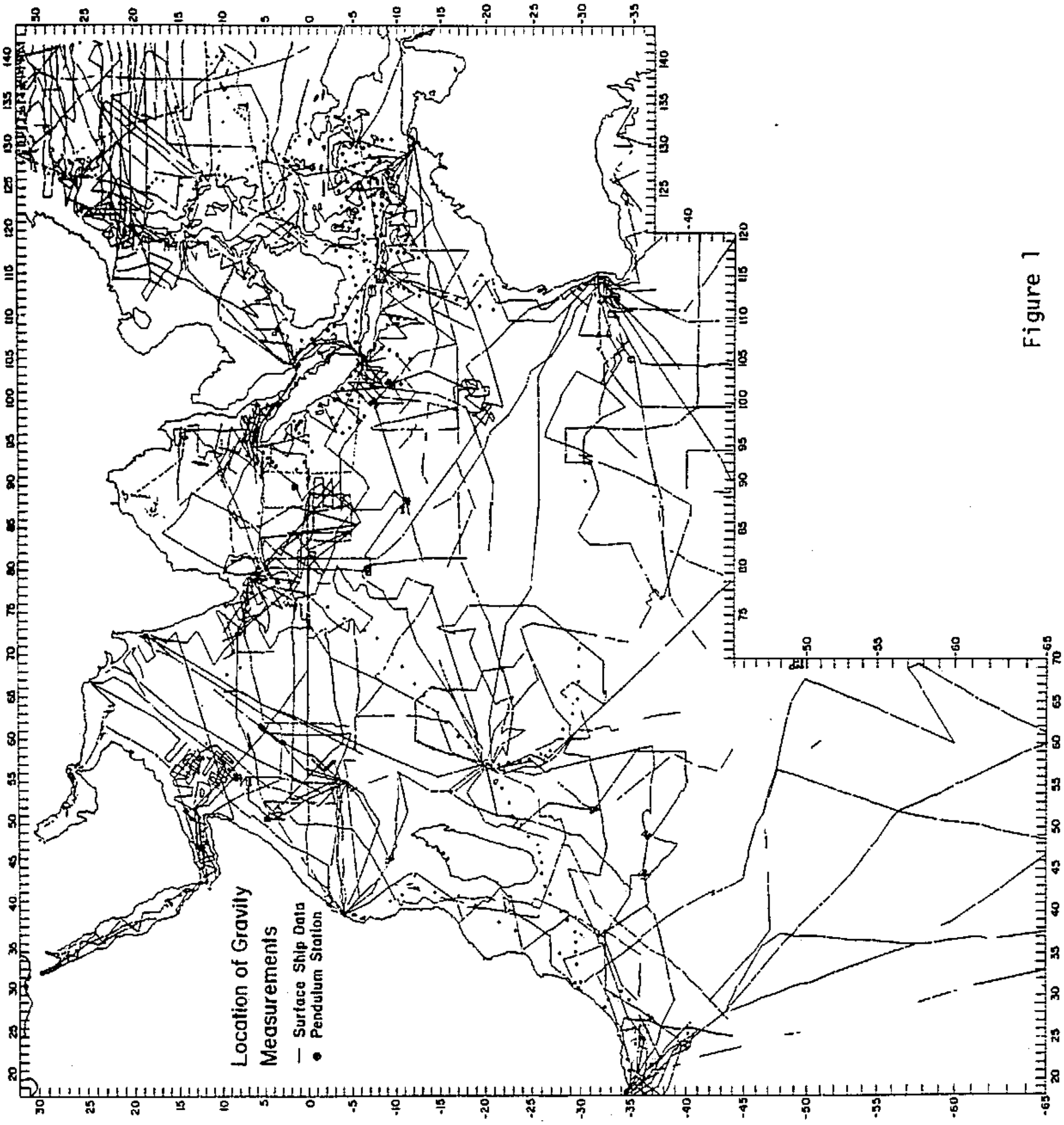
Location of Gravity Measurements
— Surface Ship Data
• Pendulum Station

Figure 1

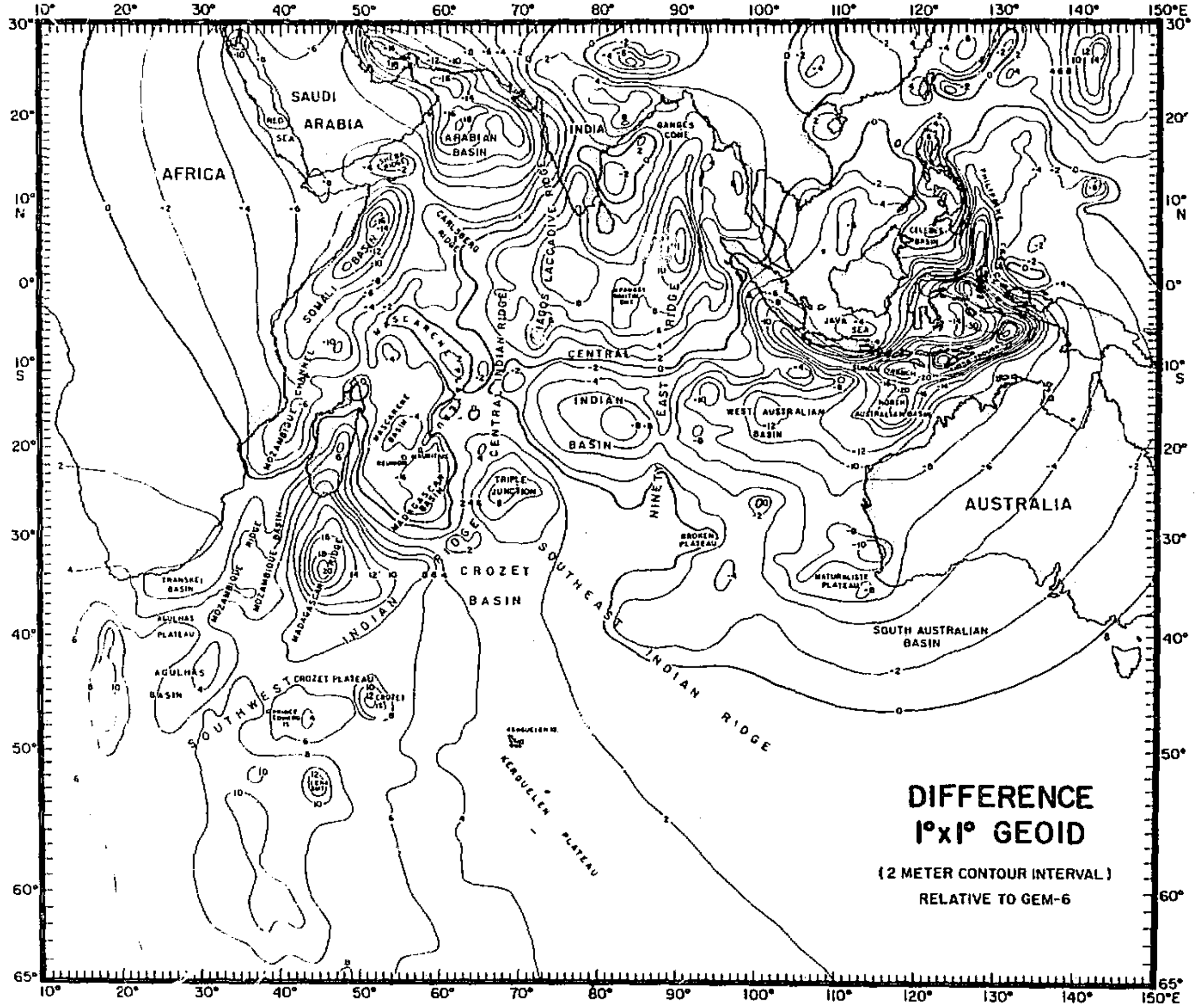
DIFFERENCE
1°x1° GEOID
(2 METER CONTOUR INTERVAL)
RELATIVE TO GEM-6
AFRICA
SAUDI ARABIA
RED SEA
ARABIAN BASIN
INDIA
GANGES CONE
AUSTRALIA
SOMALI BASIN
CARLSBERG RIDGE
LACCADIVE RIDGE
CHAGOS
CENTRAL INDIAN RIDGE
MASCARENE
MASCARENE BASIN
MOZAMBIQUE CHANNEL
MADAGASCAR BASIN
MADAGASCAR RIDGE
MOZAMBIQUE BASIN
MOZAMBIQUE RIDGE
TRANSKEI BASIN
AGULHAS PLATEAU
AGULHAS BASIN
SOUTHWEST INDIAN RIDGE
CROZET PLATEAU
CROZET BASIN
TRIPLE JUNCTION
CENTRAL INDIAN BASIN
NINETYEAST RIDGE
SOUTHEAST INDIAN RIDGE
KERGUELEN PLATEAU
BROKEN PLATEAU
WEST AUSTRALIAN BASIN
NORTH AUSTRALIAN BASIN
JAVA SEA
CELEBES BASIN
PHILIPPINE TRENCH
NATURALISTE PLATEAU
SOUTH AUSTRALIAN BASIN
10° 20° 30° 40° 50° 60° 70° 80° 90° 100° 110° 120° 130° 140° 150°E
30° 20° 10° N 0° 10° S 20° 30° 40° 50° 60° 65°

Figure 2

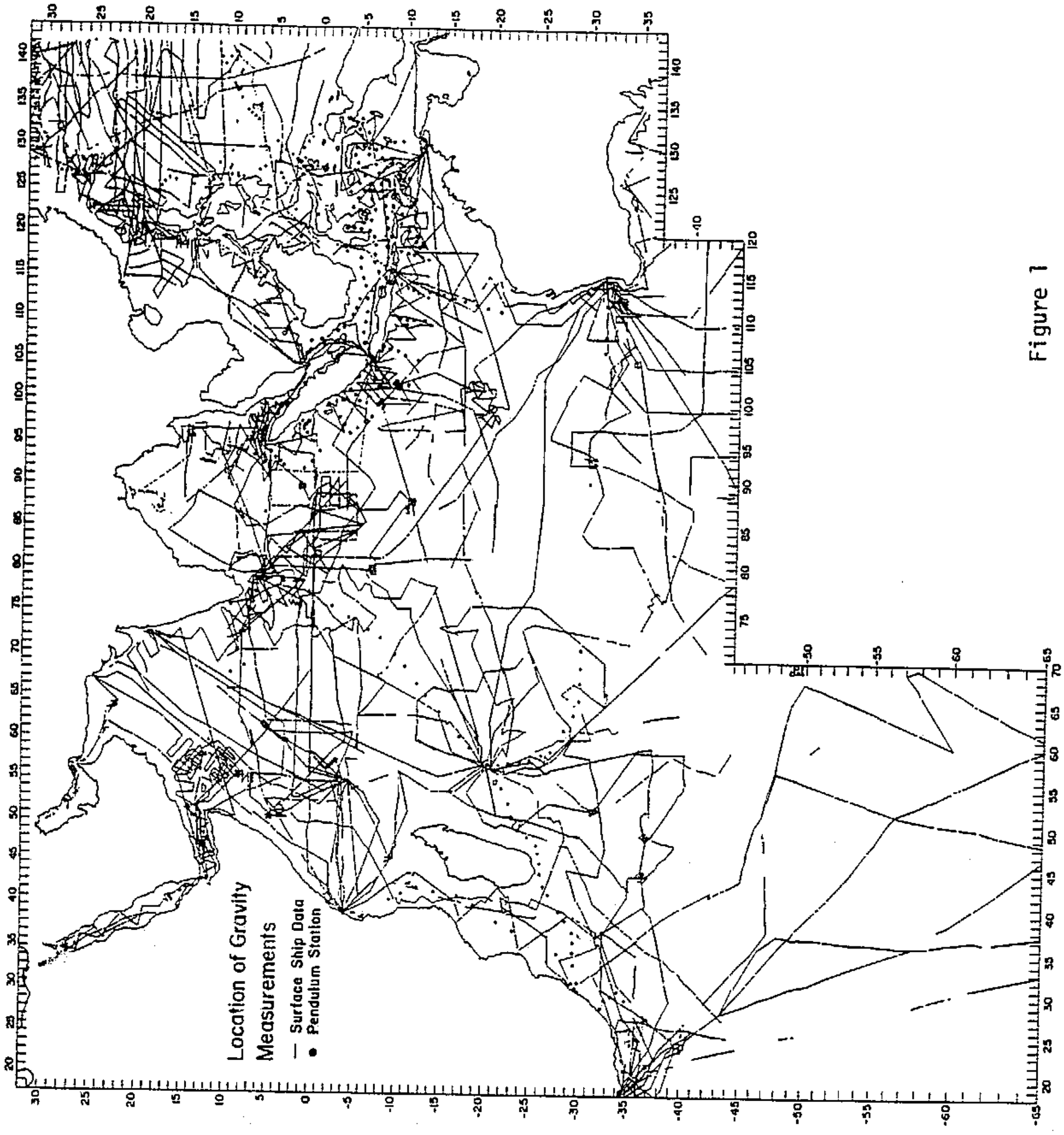
Location of Gravity Measurements
— Surface Ship Data
● Pendulum Station

Figure 1

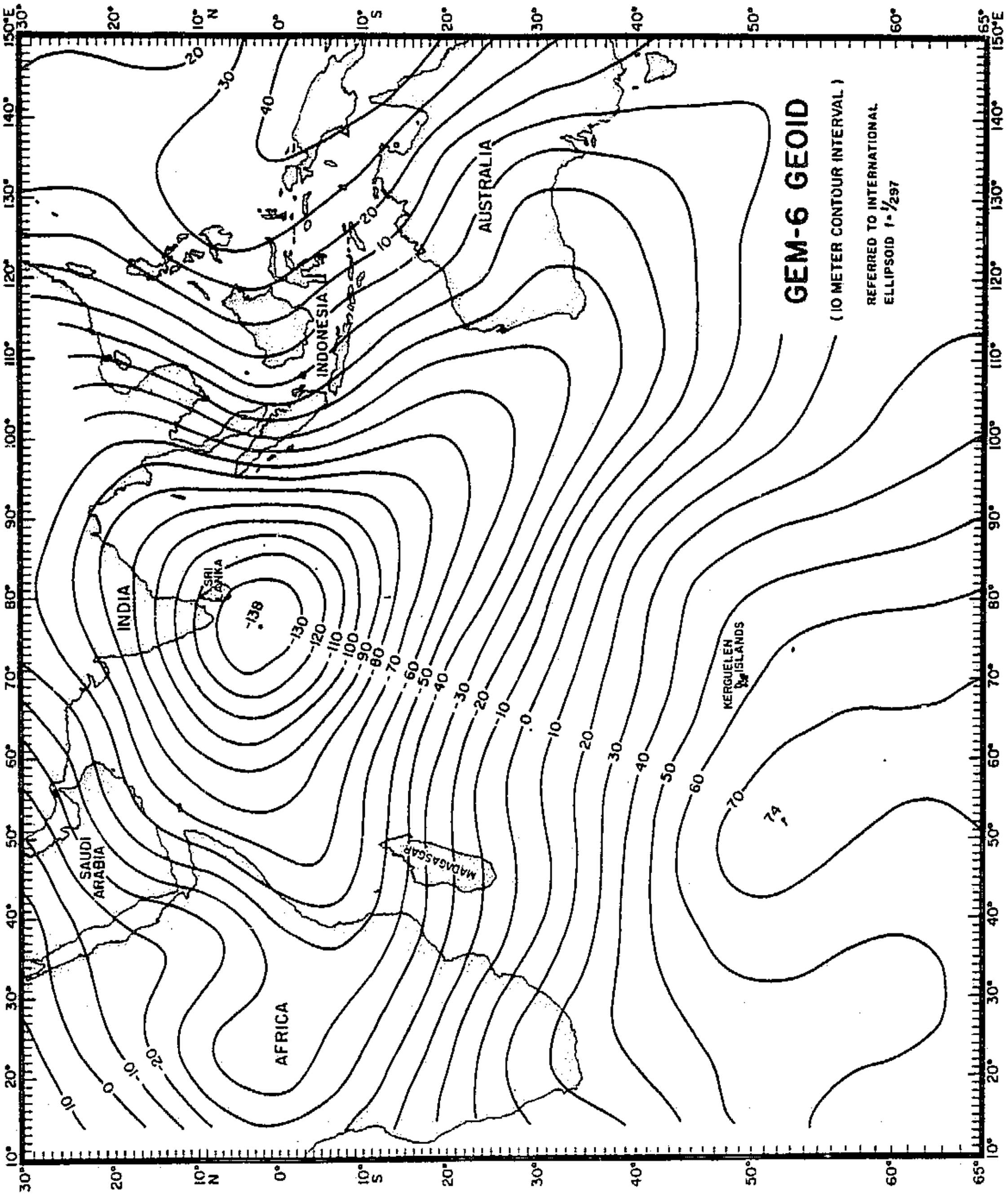
GEM-6 GEOID
(10 METER CONTOUR INTERVAL)
REFERRED TO INTERNATIONAL ELLIPSOID f=1/297
AFRICA
SAUDI ARABIA
INDIA
SRI LANKA
INDONESIA
AUSTRALIA
MADAGASCAR
KERGUELEN ISLANDS
-138
-130
-120
-110
-100
-90
-80
-70
-60
-50
-40
-30
-20
-10
0
10
20
30
40
50
60
70
74
150°E
140°
130°
120°
110°
100°
90°
80°
70°
60°
50°
40°
30°
20°
10°
30°
20°
10° N
0°
10° S
20°
30°
40°
50°
60°
65°

Figure 3

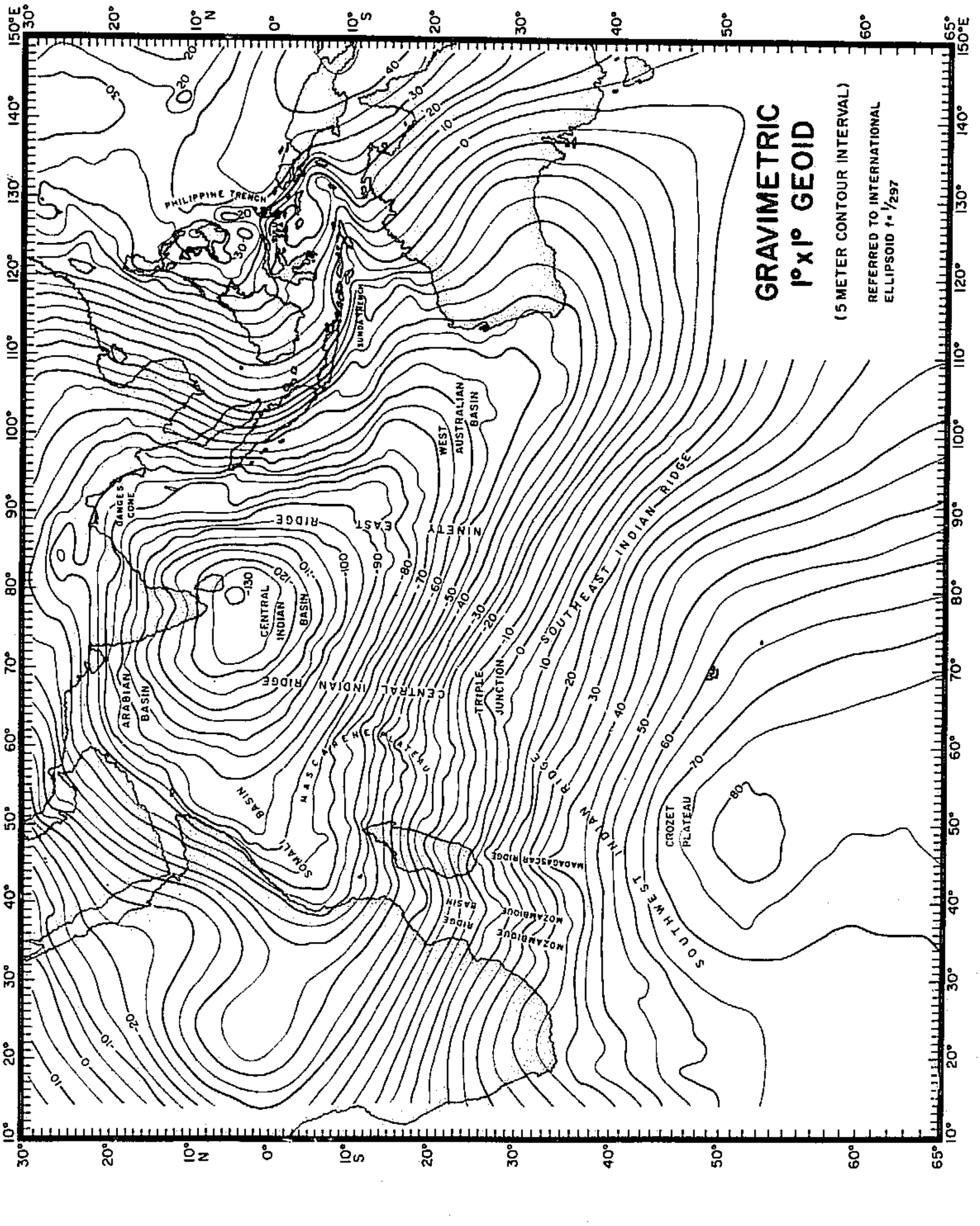
GRAVIMETRIC
1°x1° GEOID
(5 METER CONTOUR INTERVAL)
REFERRED TO INTERNATIONAL ELLIPSOID f = 1/297
PHILIPPINE TRENCH
SUNDA TRENCH
WEST AUSTRALIAN BASIN
NINETY EAST RIDGE
GANGES CONE
CENTRAL INDIAN BASIN
ARABIAN BASIN
SOMALI BASIN
MASCARENE PLATEAU
CENTRAL INDIAN RIDGE
TRIPLE JUNCTION
SOUTHEAST INDIAN RIDGE
SOUTHWEST INDIAN RIDGE
CROZET PLATEAU
MADAGASCAR RIDGE
MOZAMBIQUE RIDGE
MOZAMBIQUE BASIN
-130
-120
-110
-100
-90
-80
-70
-60
-50
-40
-30
-20
-10
0
10
20
30
40
50
60
70
80
150°E
140°
130°
120°
110°
100°
90°
80°
70°
60°
50°
40°
30°
20°
10°
30°
20°
10° N
0°
10° S
20°
30°
40°
50°
60°
65°

Figure 4

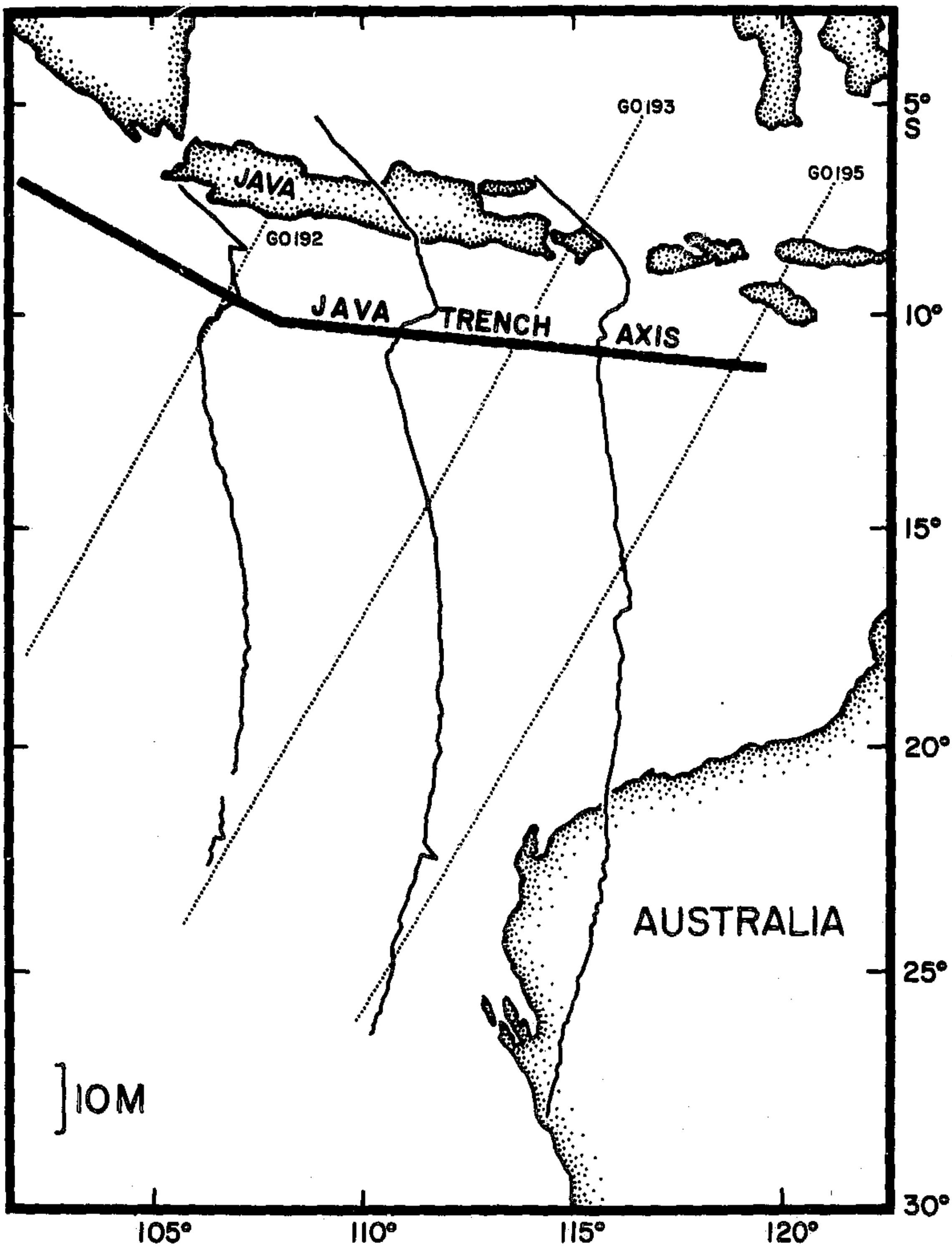
G0193
G0195
JAVA
G0192
JAVA TRENCH AXIS
AUSTRALIA
10M
5° S
10°
15°
20°
25°
30°
105°
110°
115°
120°

Figure 5

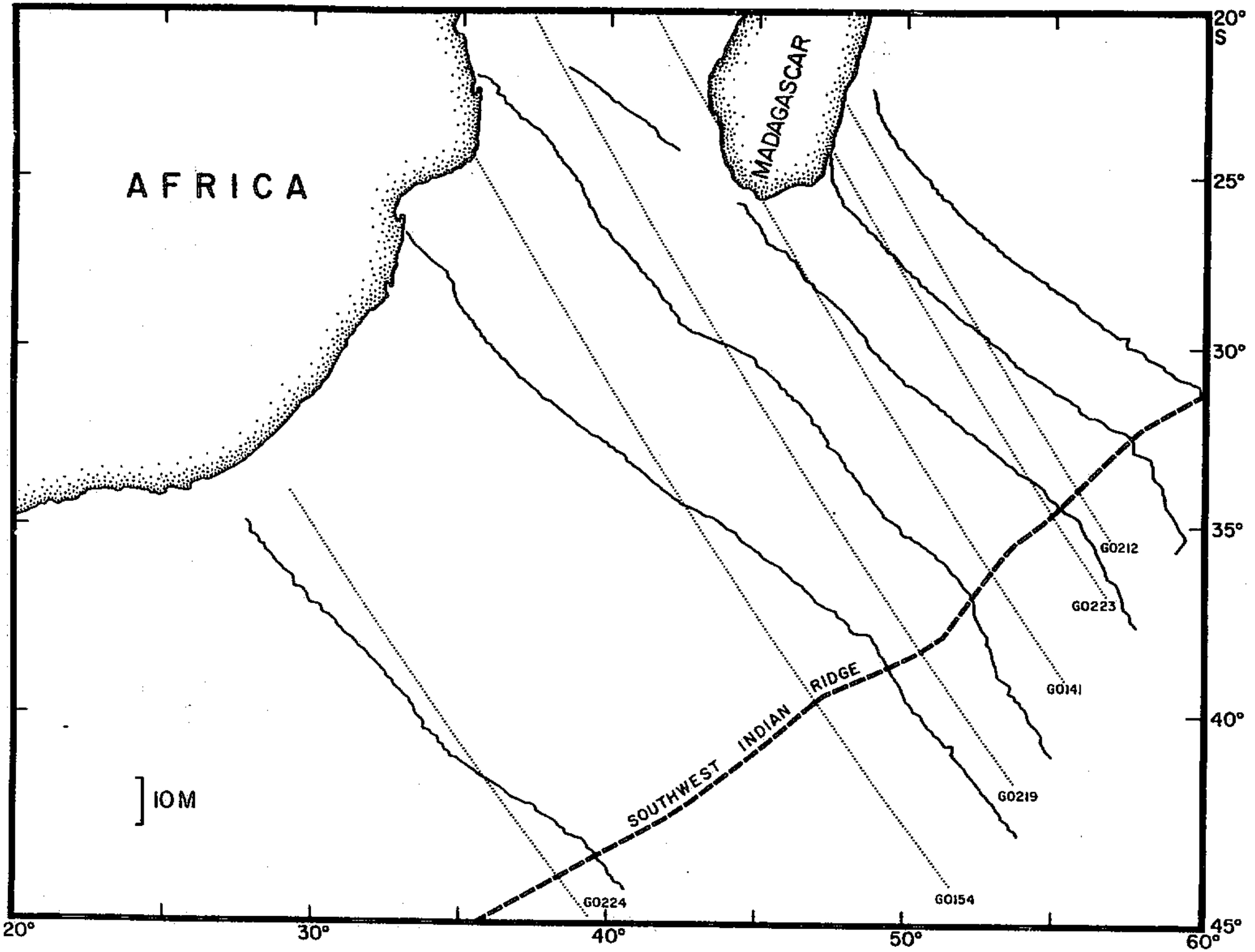
AFRICA
MADAGASCAR
SOUTHWEST INDIAN RIDGE
G0212
G0223
G0141
G0219
G0154
G0224
10M
20°
30°
40°
50°
60°
20° S
25°
30°
35°
40°
45°

Figure 6

COMPARISON OF GRAVIMETRIC GEOID WITH GEOS-3 ALTIMETER MEASUREMENTS

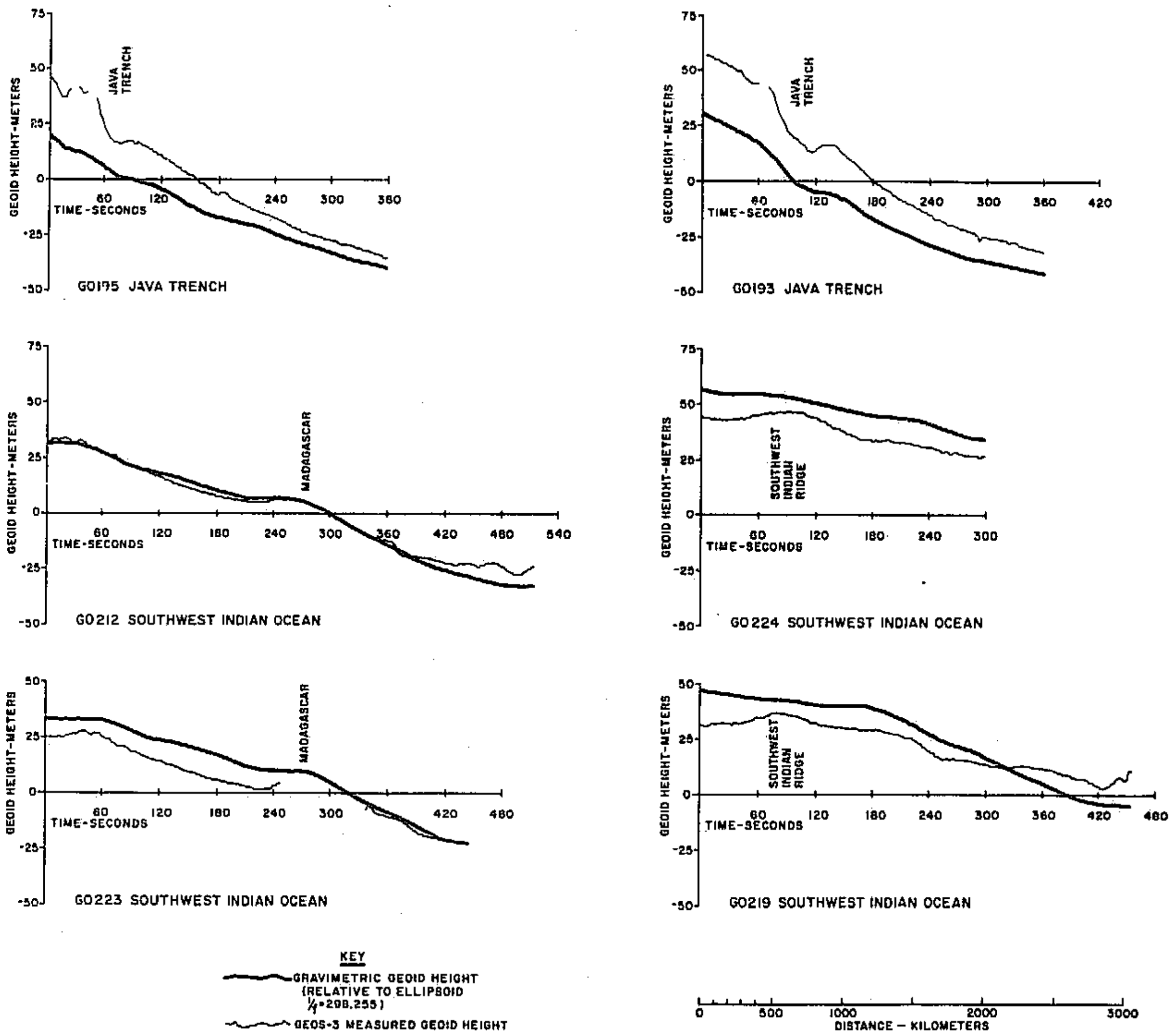

Figure 7

Table 1. 1° x 1° Averages of Free-Air Gravity, referred to the International Ellipsoid

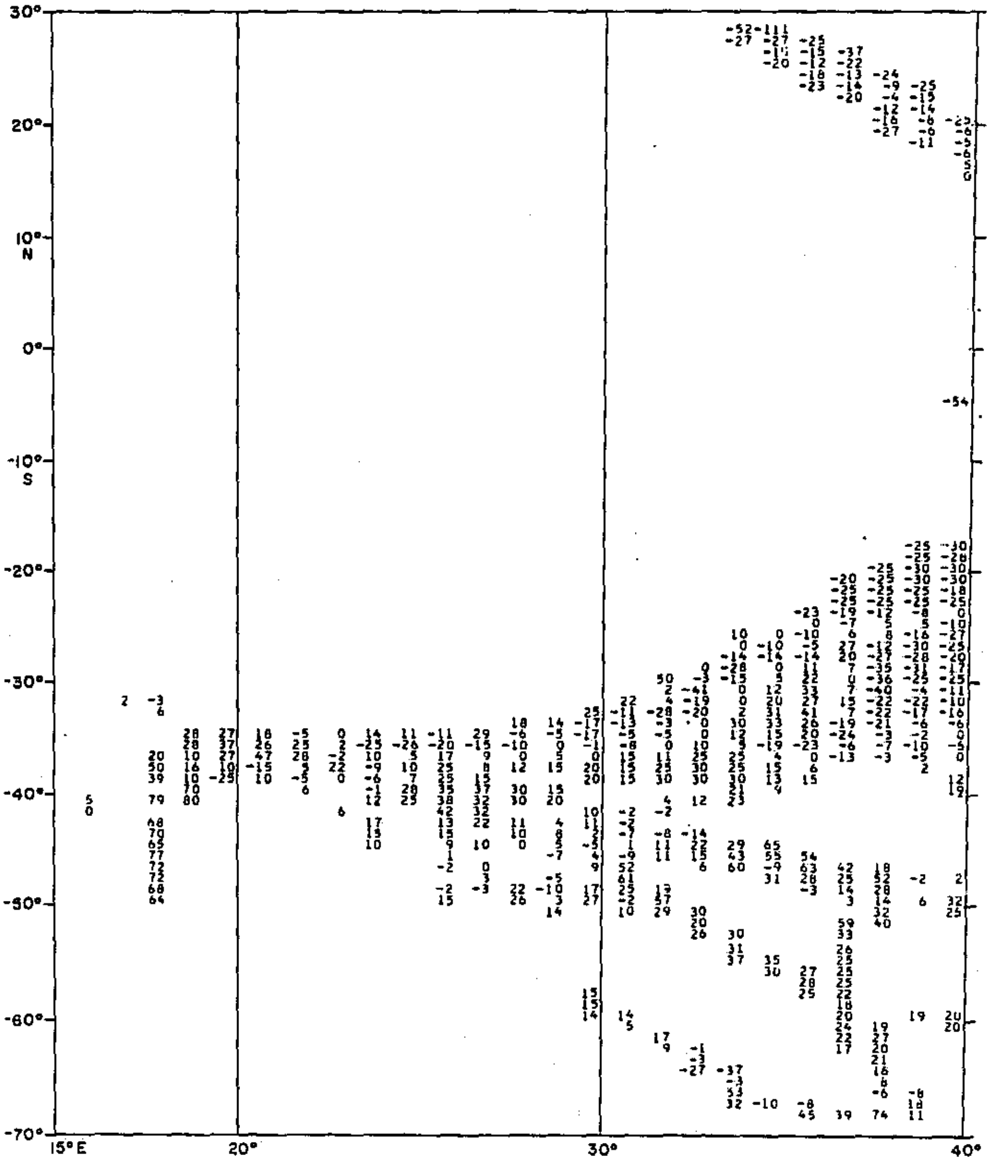

ORIGINAL PAGE IS
OF POOR QUALITY

Table 1. Continued.

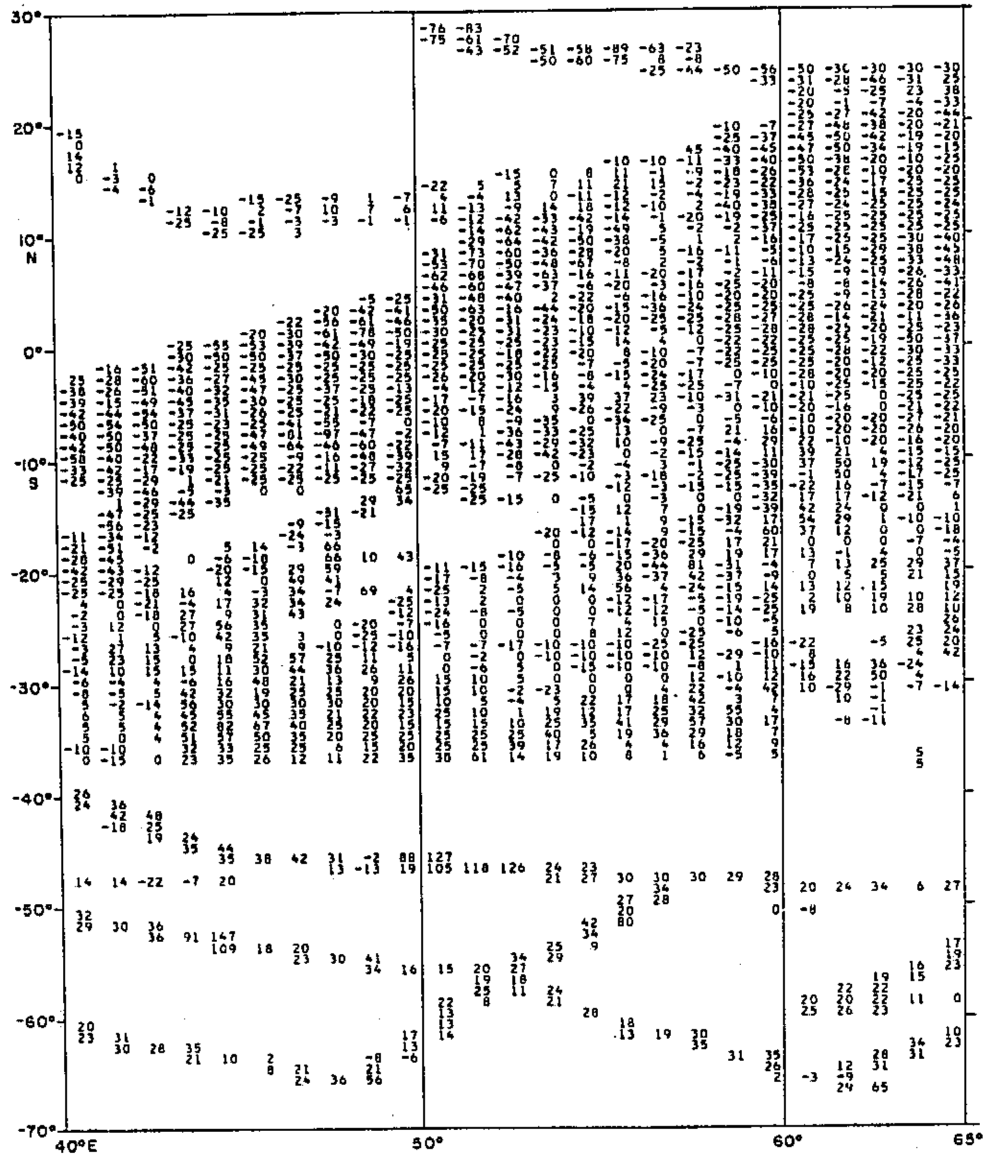

Table 1. Continued.

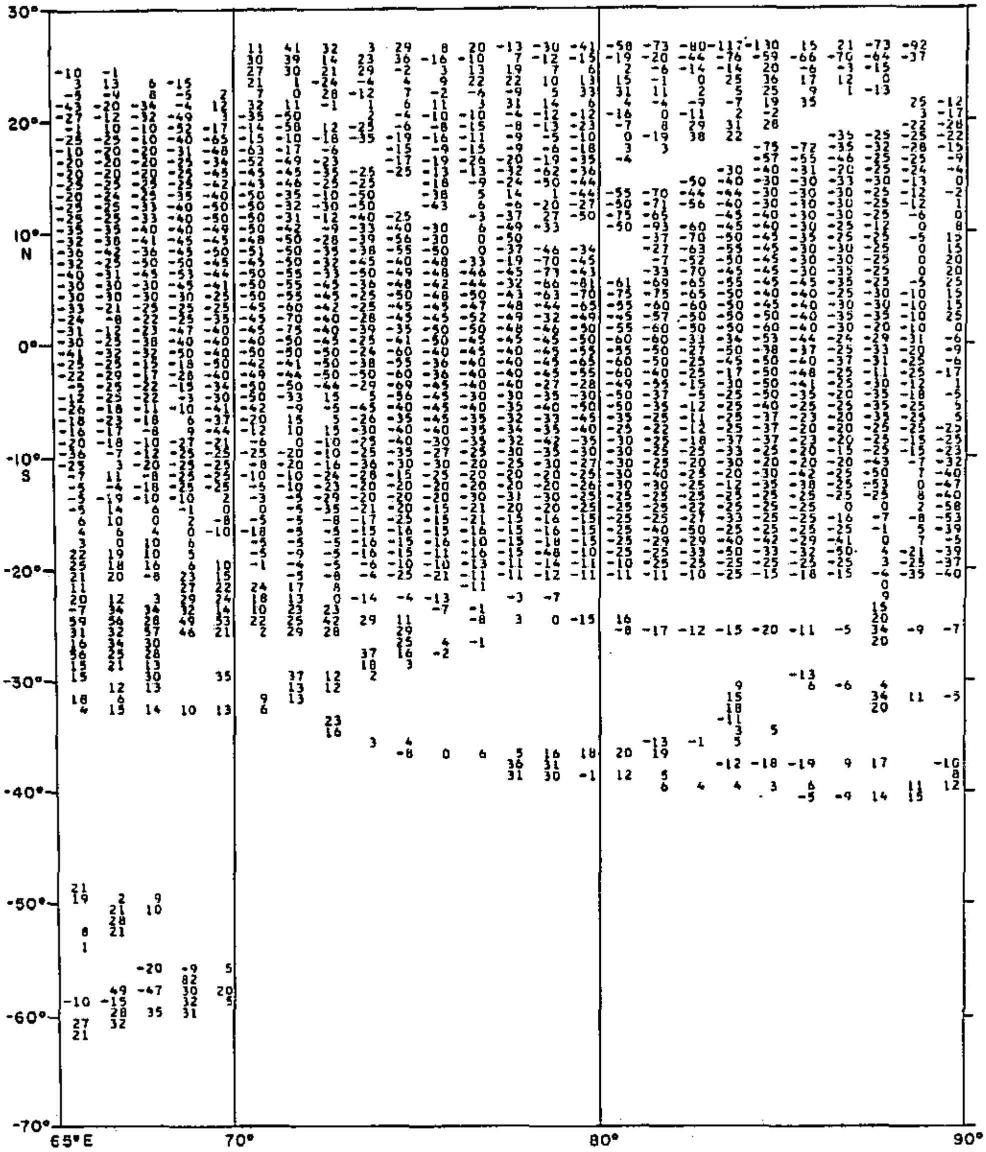

Table 1. Continued.

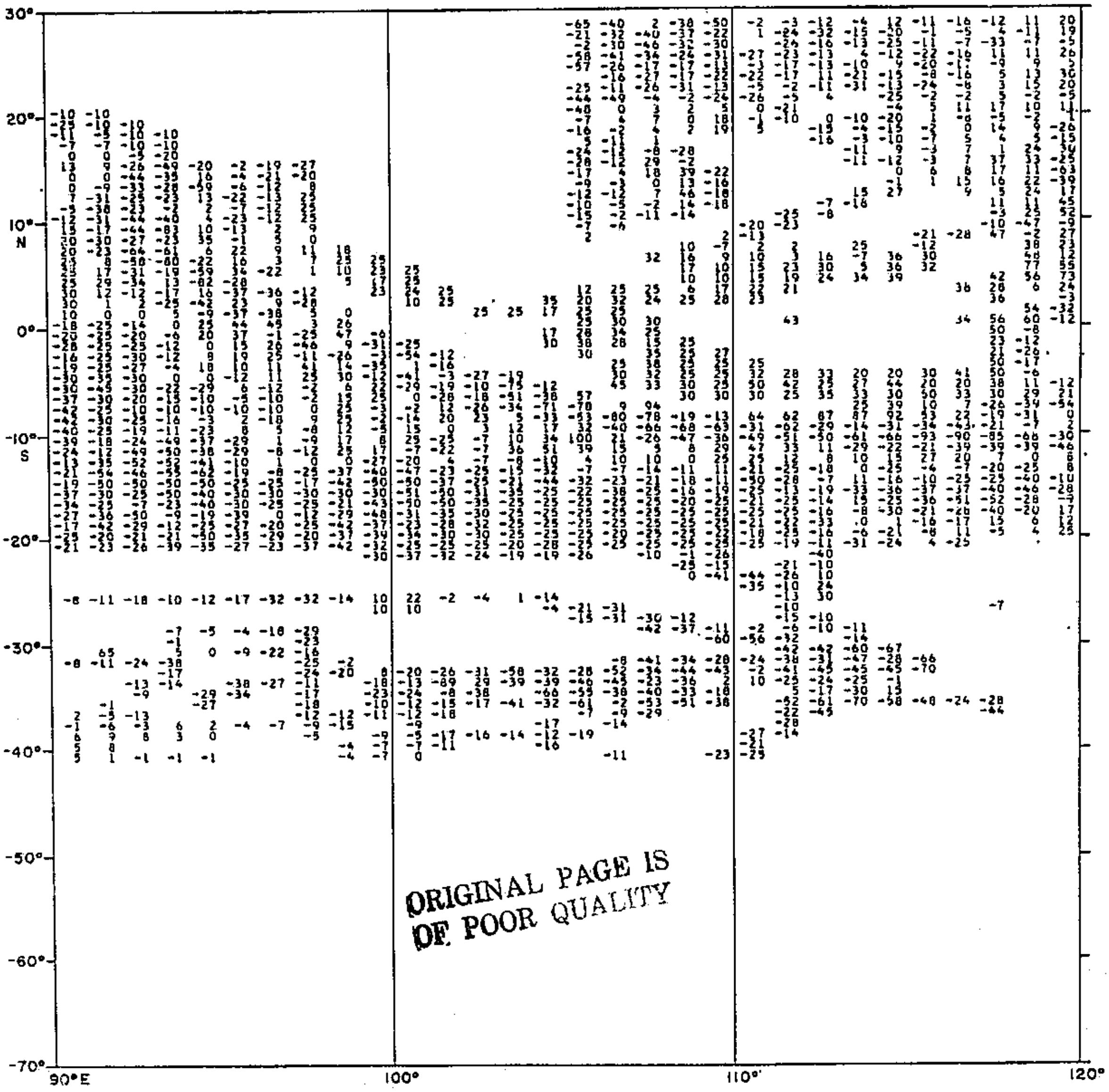

Table 1. Concluded.

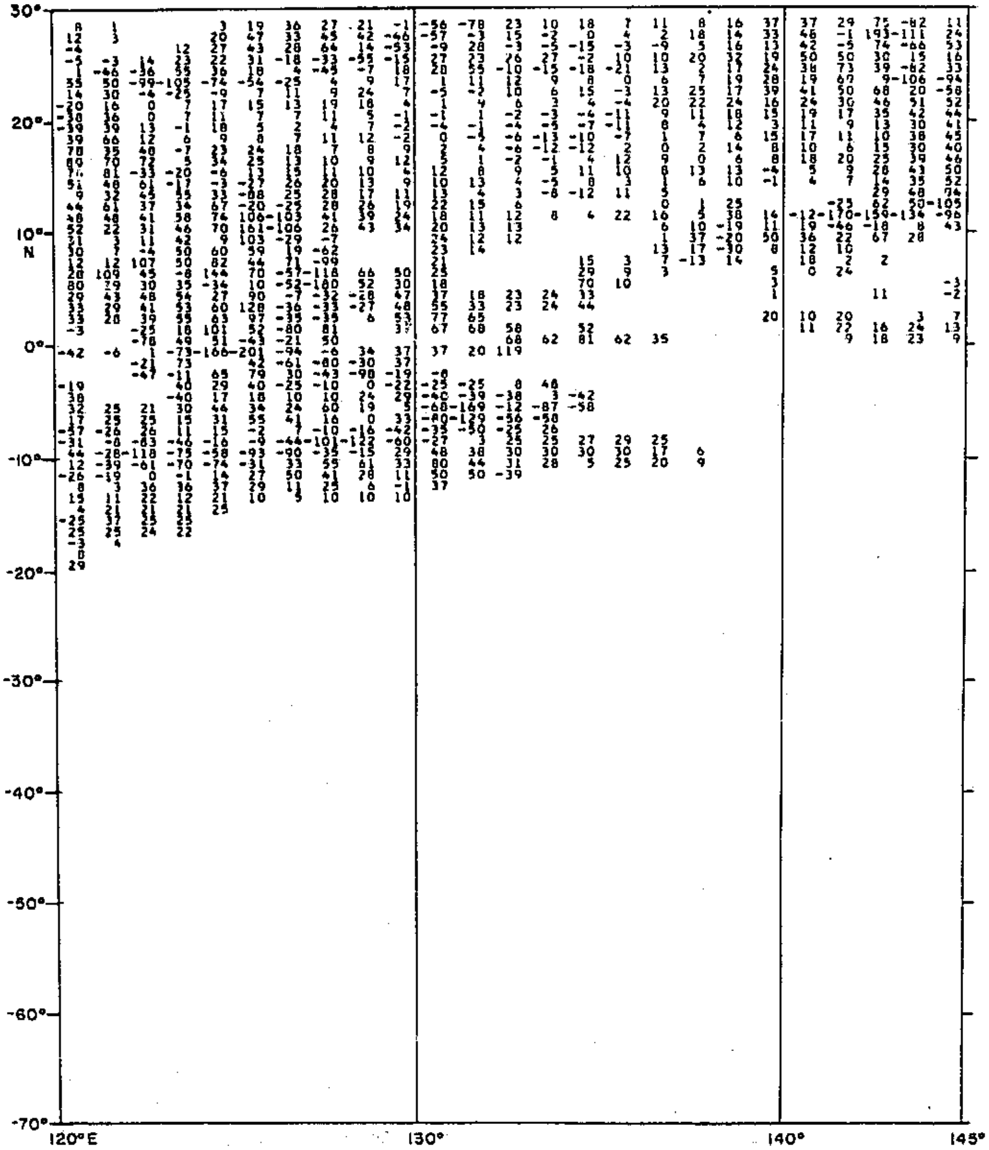

Table 2. Orbits and Dates for Satellite Tracks

Track Designation	Orbit Number	Day	Year	Altimeter Mode	Orbital Accuracy
G0141	1194	184	1975	Global	A
G0154	1237	187	1975	Intensive	A
G0192	1647	216	1975	Intensive	J
G0193	1653	216	1975	Global	D
G0195	1667	217	1975	Intensive	D
G0212	2061	245	1975	Intensive	D
G0219	2104	248	1975	Intensive	D
G0223	2189	254	1975	Intensive	D
G0224	2190	254	1975	Intensive	D

A	10^{+}m rms
D	3 - 10m rms
J	3m rms

COMPARISON OF GRAVIMETRIC GEOIDS WITH GEOS-3 ALTIMETER

INTRODUCTION

With the aid of a radar altimeter mounted on board the GEOS-3 satellite it is now possible to rapidly determine the shape of the ocean surface. This information can be used to provide an estimate of the marine geoid. However, because the altimeter is a new instrument, it is of considerable interest to compare such measurements with other types of data. Thus we examine how well GEOS-3 estimates of geoid height compare with data from independently determined gravimetric geoids.

GRAVIMETRIC GEOIDS

On land the geoid may be constructed using astrogeodetic methods; or alternatively utilizing gravimetric methods and Stokes' integration of the measured values of gravity. At sea direct determination of deflection of the vertical is a difficult task, consequently only about 20 measurements have ever been made (Von Arx, 1966). Due to this difficulty only with measurements of gravity at sea can geoid computations be performed. This technique for oceanic geoid construction was initially demonstrated in the western North Atlantic Ocean (Talwani, et al, 1972). Subsequent studies have involved construction of oceanic geoids in the Indian Ocean (Kahle and Talwani, 1973), Northwest Pacific (Watts and Leeds, 1977) and an updated Indian Ocean geoid (Kahle, Chapman and Talwani, 1978).

Basically our technique of geoid construction involved a series of computational steps:

1. Compilation of marine gravity data and averaging over a specified area - in this case 1° x 1° averages.

2. Calculation of free air anomalies on the basis of a certain gravitational potential model; our computations utilized the GEM-6 model (Smith et al., 1976).
3. Subtraction of the calculated free-air anomalies (GEM-6) from the areal averages of measured gravity; this is the set of difference gravity anomalies.
4. Application of Stokes' integral to these difference gravity values to obtain the difference geoid.
5. Addition of this difference geoid to the geoid of the gravitational potential model (GEM-6) to obtain the total gravimetric geoid.

Computationally this procedure is efficient because it eliminates the need for calculation of Stokes' integral over the entire earth. As the integration is done only over the area of study, this is equivalent to utilizing GEM-6 gravity values outside the area of computation. Some errors can be introduced especially near the boundaries, however such errors are less than 1 meter (Strange et al., 1972).

Due to this procedure there are several inherent characteristics of these gravimetric geoids. Outside a certain region the values of gravity due to a satellite model are utilized, consequently the long wavelength (roughly $N \leq 16$) components in these geoids are determined by that particular gravity model. In our case the long wavelength components of the gravimetric geoids are determined by the GEM-6 field. Another property of these geoids results from the initial procedure of averaging gravity values over a finite region. Averaging over a certain interval and subsequent decimation of data corresponds to a low pass filter operation with a gradual cutoff band. In our gravimetric geoids this procedure would eliminate most wavelengths shorter than 2° which is twice the sampling period. At a latitude of 23° then one could state that our 1° x 1° gravimetric geoids do not contain much information in the wavelengths shorter than about 200 km. Another characteristic of the present marine geoids is that in some regions where there are few ship tracks there is difficulty in obtaining average gravity values. As Stokes' function is most sensitive to adjacent locations, it would be expected that in regions where gravity averages are poorly determined, the geoid would likewise not be accurately calculated.

For purposes of comparison in this study we utilize gravimetric geoids in the Indian ocean (Kahle, Chapman and Talwani, 1978) as shown in Figure 1, Northwest Pacific (Watts and Leeds, 1977) in Figure 2, and North Atlantic (Talwani and Leeds, in preparation) in Figure 3. Prior to our comparisons these geoids were changed to be relative to an ellipsoid with 1/f = 298.255 and semimajor axis 6378145 m.

GEOS-3 ALTIMETER

Several characteristics of the GEOS-3 radar altimeter have a bearing on our study. On board the satellite there are two transmitters, one designated the global mode and the other termed intensive mode. Both measure the height of the satellite above the sea surface every .01 seconds. In practice it has been found that the global mode results in a signal with higher noise, consequently this mode was little used after the initial stages of the mission (H.R. Stanley, personal communication). During computer processing of this data an average measurement is determined; for the low rate telemetry format this is a 2.048 second average and for the high rate telemetry format a 3.277 second average. At an average ground track speed of 6.55 km/sec this results in a measurement every 14.3 km (low rate) or 21.5 km (high rate). Due to this averaging procedure most wavelengths shorter than 28.6 km (low rate) or 43 km (high rate) will be eliminated from our GEOS-3 measurements.

After the radar altimeter measures the altitude of the spacecraft, orbit calculations are utilized to locate the satellite relative to the center of mass of the earth. During the orbit computation a satellite derived gravity field is used, thus the long wavelength components of the orbit reflect the gravity field which was assumed. For the GEOS-3 satellite this was GEM-8 or an NWL model. Consequently long wavelength components of the GEOS-3 sea surface height measurements are dependent upon these gravity models. Additionally due to range errors there are errors in the constant level of GEOS-3 sea surface height data.

After altitude measurement and orbit calculation the sea surface height is determined. To obtain an estimate of geoid height, tidal corrections should be made. Our GEOS-3 data was corrected with the tide model of Hendershott (1973).

COMPARISON OF GRAVIMETRIC GEOIDS WITH GEOS-3 ALTIMETER

Using GEOS-3 altimeter estimates of geoid height, we have made comparisons with the gravimetric geoids presented in the previous section. In order to do this the gravimetric geoids were first transformed to be relative to an ellipsoid with radius 6378145 m and $1/f = 298.255$ which is the ellipsoid to which altimeter data is also referenced. Then the gravimetric geoids were interpolated at the point of altimeter measurement; interpolation was linear relative to the nearest three gravimetric geoid values. A track chart of the location of altimeter measurements, and the extent of the gravimetric geoids is shown in Figure 4; a listing of orbit numbers for each track is in Table 1.

In Figure 5 there is a comparison of data with the Indian Ocean geoid, the altimeter data is plotted as a function of time of acquisition from the first data point. The first obvious fact from this comparison is that GEOS-3 data often differs from the gravimetric geoid by a constant level. RMS differences between the two sets of data are in the range 3.69 m to 13.27 m as listed in Table 2. There are three main causes for this discrepancy; bias in altitude determination (Martin and Butler, 1977), radial orbit errors, and differences in the long wavelength components of the gravimetric geoid and altimeter data. To test the effect of bias the corrections for this error (Martin and Butler, 1977) were made and the rms differences recomputed; results are also listed in Table 2. In general this bias correction often increases the rms differences. This shows that in our comparisons the GEOS-3 values are mostly lower than the gravimetric geoid, and the bias correction enlarges this difference. Thus bias errors in altitude determination are not the cause of the large constant offsets. Another possible reason for this discrepancy could be differences in the long wavelength components of the gravimetric geoid and altimeter data. As stated previously this would be due to differences between the GEM-6 model on which our gravimetric geoids are based, and the GEM-8 or NWL model by which altimeter data is determined. It is doubtful that these long wavelength differences can explain more than a few meters of discrepancy in constant values. Radial errors in orbit determination are the most probable cause of the constant offsets between the gravimetric geoids and altimeter data. A priori estimates of rms orbital errors are listed in Table 2; thus track G0106 has an a priori error of greater than 10 m rms while the rms discrepancy between the gravimetric and altimetric geoid is 4.78 m. In other cases the actual rms difference exceeds the a priori estimates.

These large constant offsets indicate the need for high quality orbital computations, and analysis of internal consistency of the data. By analyzing altimeter data at crossover locations and least square reduction of crossover errors, Rummel and Rapp (1977) were able to obtain rms crossover discrepancies of .78 m for intensive mode operation. Our comparisons indicate the need for this type of crossover analysis and error reduction.

Comparisons of the altimeter data and the Northwest Pacific gravimetric geoid are shown in Figure 6. In this the influence of the transmitter mode is evident. Tracks G0242 and G0230 are relatively smooth and were collected in the intensive mode, tracks G0235 and G0266 have high frequency noise and were made in the global mode. In general all of the figures show that the intensive mode has less high frequency noise than the global mode of acquisition.

Another aspect of our comparison study involves the question of what are the shortest wavelengths in the geoid and how well does the gravimetric geoid and altimeter data record such wavelengths. To understand the short wavelength (less than several hundred kilometers) components of the geoid it is necessary to examine their origin. Any geoid anomaly is due to the anomalous potential caused by a mass heterogeneity. On the basis of potential theory it would be expected that short wavelength components of the geoid would be caused by the nearest mass anomalies; this would be topography of the ocean floor and moho which are large, adjacent mass inhomogeneities. To see this mathematically consider the relationship between the fourier transform of gravity and bathymetry, the admittance.

$$Z(k) = \mathcal{F}[g(k)] \,/\, \mathcal{F}[b(k)] \qquad (1)$$

For an Airy model of two dimensional crust this function would be (McKenzie and Bowin, 1976)

$$Z(k) = 2\pi G\,(\rho_c - \rho_w)\,e^{-kd}\,(1 - e^{-kt}) \qquad (2)$$

where G is the gravitational constant

and ρ_c, ρ_w, are density of crust and water respectively

k is wavenumber in radians/km

d is depth of the water layer

t is the thickness of crustal layer

Utilizing the transfer function between the fourier transform of gravity and geoid (Chapman, 1978; A. Leeds, personal communication) we can obtain the admittance between the fourier transform of geoid and bathymetry for two dimensional Airy isostasy:

$$\mathcal{F}(N)/\mathcal{F}(b) = \frac{2\pi G}{|k|\gamma}\,(\rho_c - \rho_w)\,e^{-kd}\,(1 - e^{-kt})$$

where $\mathcal{F}(N)$ is the fourier transform of geoid height

γ is normal gravity : 980 cm/sec

What this equation shows is that topography of the ocean floor will give rise to undulations of the geoid which have identical frequencies but amplitude decreasing with an increase in frequency. Any other model of compensation would also have identical frequencies but a different amplitude function. This relationship is important in our comparison study because it indicates that topographic features will generate undulations of the geoid with similar frequencies. In the case of the Hawaiian ridge this has been proven in a quantitative manner by Watts (1978).

As an example of this relation between bathymetry and geoid consider the Aleutian trench (Figure 7). At the trench axis there is a topographic depression which is approximately 100 km wide, it has a gravity anomaly of similar width. Assuming two dimensionality it is possible to compute what the geoid anomaly is from the gravity anomaly (Talwani et al, 1972; A. Leeds, personal communication).

$$N(x) = \left(\frac{-1}{\pi r}\right) = \int_{-\infty}^{+\infty} g(x') \log [x - x'] \, dx' \qquad (4)$$

This is a convolution integral and is the spatial equivalent of the transfer function between the fourier transform of gravity and geoid (Chapman, 1978). Utilizing this formula and the observed gravity across the Aleutian trench, a two dimensional geoid profile has been computed and is also shown in Figure 7. Additionally a GEOS-3 profile and corresponding gravimetric geoid is shown. From this it is clear that above the trench there is a two dimensional geoid minimum with similar frequencies as the bathymetry. In both amplitude and wavelength this is identical to the observed minimum GEOS-3 data. However the trench low as seen in the 1° x 1° gravimetric geoid is much broader and shallower. On the basis of the relation between geoid and bathymetry having identical frequencies, and our computation of the two dimensional geoid it is clear that above the narrow Aleutian trench there is a geoid anomaly with similar frequency components. As the GEOS-3 altimeter records a signal similar in shape to the two dimensional geoid, it is reasonable to assume that the altimeter is faithfully measuring the geoid signal. In the 1° x 1° gravimetric geoid the trench low is much broader and shallower; in comparison to the GEOS-3 data and two dimensional geoid, the gravimetric geoid has less high frequencies and more energy in the medium frequency (wavelengths approximately 200 km) range. This is aliasing of the geoid signal and is due to our procedure in geoid construction of averaging gravity values over 1° squares.

This analysis of geoid height over the Aleutian trench indicates a limitation of 1° x 1° gravimetric geoids. In certain regions there can be energy in the geoid for wavelengths shorter than are resolved by averaging over 1° squares. In such areas it is necessary to construct gravimetric geoids by first averaging gravity values over smaller regions, perhaps 10' or 5' squares. Prior to averaging these values, it is possible to estimate how much high frequency information exists in the geoid. This can be done by multiplication of the fourier transform of bathymetry and the admittance function. This gives an estimate of what the geoid heights would be at the shorter wavelengths. Another technique to estimate the high frequency geoid heights would be to first compute the fourier transform of gravity values. After multiplication by the transfer function for a plane earth this gives the fourier transform of geoid height. This gives an estimate of the geoid height at the highest frequencies.

Data from the North Atlantic region are compared in Figure 8. Again the same features are noted as before, constant offsets and noisy altimeter data when the global mode is utilized. However, track G0096 exhibits another feature, there is a tilt of the altimeter measurements relative to the gravimetric geoid. Because this is such a long wavelength difference, and does not appear in the other regions of the North Atlantic we suspect it is due to very long wavelength errors in the computed satellite orbit. For this reason, Rummel and Rapp (1977) in correcting GEOS-3 data removed both a long wavelength orbital tilt in addition to constant offsets. Such a procedure is both justified and necessary in order to obtain good geoid estimates from the GEOS-3 altimeter.

In an effort to overcome such long wavelength differences, several tracks of GEOS-3 altimeter data were adjusted by requiring that they agree with each other at crossover locations and with the GEM-6 geoid. To do this adjustment the technique of Rummel and Rapp (1977) was utilized; this minimizes in a least square sense discrepancies due to bias and tilts. A comparison of these adjusted GEOS-3 geoid estimates with the Northwest Pacific gravimetric geoid is shown in Figure 9. For each track the GEOS-3 data and gravimetric geoid are both shown, directly above this the difference in height between the two is shown at a different scale. Thus for track G0266 agreement is quite good except at the Bonin trench; the rms discrepancy is 2.07 m (Table 3). For all of these tracks major disagreements of up to 10 m occur above the trench systems such as the Bonin, Mariana, Ryukyu, and Philippine trench. As discussed previously for the Aleutian trench, this discrepancy is due to inadequate resolution of the gravimetric geoid.

Other broad regions of difference occur; on track G0565 (Figure 9) southeast of the Mariana trench there is a broad disagreement of up to 5 meters. Because this area does not have the same quantity of gravimetric data as other regions, we suspect this is due to errors in the gravimetric geoid. When making detailed comparisons though, it becomes exceedingly difficult to ascertain whether there are slight errors in orbital computation or geoid calculation, or simply one could be seeing the effect of transient sea surface topography in the altimetry data. With gravimetric geoids what is needed are finer resolution grids and detailed error analysis of their quality; in orbit determination the best calculations should be made to reduce radial errors to less than 1 meter.

The primary mission of the GEOS-3 satellite was to determine information about the gravitational field of the earth; our comparisons indicate that GEOS-3 estimates of geoid height are no better than the orbital computations which are utilized. Specifically at the very long wavelengths there can be errors in GEOS-3 data. Thus altimetry data cannot give any new information about the earth's gravitational field for wavelengths with order n less than approximately 10. This is obvious because a gravitational field model is necessary for the orbit determination; these longest wavelength elements of the gravitational field are best determined by satellite tracking. A question exists though as to what are the shortest wavelengths at which the altimeter can yield new information about the gravitational field. In our comparison of the GEOS-3 data with the two dimensional geoid over the Aleutian trench it was clear that the altimeter could record information with wavelengths on the order of 50 kilometers. But does the altimeter obtain better information than a marine gravimeter at short wavelengths? The answer to this can be found by examining the relative properties of the geoid and gravity field and the comparative accuracies of altimeters and gravimeters.

Consider hypothetical measurements of geoid and gravity on a plane two dimensional earth. Geoid height is determined by an altimeter with a noise level of 1 meter; gravity is measured by a gravimeter with a noise level of 10 mgals. (Both somewhat arbitrary and conservative estimates.) Assume that water is 5 km deep and the crust is 6 km thick in Airy isostatic equilibrium; additionally suppose the amplitude spectra of topography is white with amplitude of 3 km. Then on the surface of the water the amplitude spectrum of gravity is obtained from equation 2 and spectrum of geoid is obtained from equation 3. A plot of these functions is in Figure 10. The vertical scale has been adjusted so that 10 mgals is equivalent in height to 1 meter. Thus whenever one function is plotted higher than the other, it indicates the higher function has a larger signal to noise ratio. From this plot we see that for wavelengths longer than 628 km, an altimeter will have a higher signal to noise ratio. For wavelengths shorter than 628 km a marine gravimeter will record with a better signal to noise ratio. What this analysis indicates is that altimeters measuring the geoid are best utilized to record information on the gravitational field for wavelengths longer than approximately 628 km; while gravimeters are best utilized to record information in the wavelengths shorter than 628 km. At the very longest wavelengths ($n \leq 10$) satellite tracking is the best method to determine the earth's gravitational field. While the actual accuracies of altimeters and gravimeters may vary, it is a basic principle that measuring the geoid more accurately determines wavelengths longer than several hundred kilometers (in this example 628 km) and measuring the gravity field determines the shorter wavelengths with better accuracy. As in our example over the Aleutian Trench, an altimeter obviously still records the short wavelength information, but the gravimeter measures it with a higher signal to noise ratio.

SUMMARY AND CONCLUSIONS

In comparing the GEOS-3 geoid estimates with the gravimetric geoids over the different oceans, several features emerge. Constant offsets and tilts cause large-scale discrepancies of up to 24m rms (Table 1). Such errors are probably due to inaccurate orbit determination and possible due to differences between the gravity field used for orbit calculation and geoid computations. Over large scale topographic features such as the Aleutian Trench there can be a large geoid signal with wavelengths shorter than can be resolved by 1° X 1° gravimetric geoids.

In regions where there is good coverage of marine gravity data, and sufficient energy in the geoid at shorter wavelengths (less than 200 km) then more detailed gravimetric geoids should be utilized. Examination of the topography and techniques utilizing the admittance between geoid and bathymetry should be useful in estimating the geoid signal at these short wavelengths.

After elimination of long wavelength differences, adjusted GEOS-3 data still show discrepancies with the gravimetric geoids. Over the trench systems of the western Pacific there were differences of up to 10 m, this is due to averaging gravity data over too large an area. In other regions there are discrepancies of several meters. Such differences indicate the need for estimation of the errors in geoid computations, and the best possible orbital determinations for the GEOS-3 satellite.

Although some difficulties exist with orbital errors, the GEOS-3 altimeter is an excellent instrument for acquiring measurements of the shape of the ocean surface. After correcting for orbital errors, it can be used for a global mapping of the marine geoid, with resolutions much greater than are easily achievable with gravimetric geoids. In utilizing this instrument, it will be most useful in studying features in the gravitational field with wavelengths $N>10$ and larger than approximately 628 kilometers. Marine gravimeters will record the shorter wavelengths with a better accuracy. In the medium wavelength range the GEOS-3 altimeter gives a promise to yield new information on the gravimetric field of the earth.

REFERENCES

Chapman, M.E., Techniques for interpretation of geoid anomalies. J. Geophys. Res., this volume, 1978.

Hendershott, M.C., Tide model ocean tides. Trans. A.G.U., 54, 76-86 1973.

Kahle, H.G., M. Chapman, and M. Talwani, Detailed 1° X 1° gravimetric Indian Ocean geoid and comparison with GEOS-3 radar altimeter geoid profiles. Geophys. J. Roy. astr. Soc., in press, 1978.

Kahle, H.G., and M. Talwani, Gravimetric Indian Ocean geoid. Z. für Geophysik, 39, 167-187, 1973.

Martin, C.F. and M.L. Butler, Calibration results for the GEOS-3 altimeter. NASA Contractor Report, NASA CR-141430, 86pp., 1977.

McKenzie, D. and C. Bowin, The relationship between bathymetry and gravity in the Atlantic Ocean. J. Geophys. Res., 81, 1903-1915, 1976.

Rummel, R. and R. Rapp, Undulation and anomaly estimation using GEOS-3 altimeter data without precise satellite orbits. Bull. Geod., 51, 73-88, 1977.

Smith, D.E., F.J. Lerch, J.G. Marsh, C. A. Wagner, R. Kolenkiewicz, and M.A. Khan, Contributions to the National Geodetic satellite program by Goddard Space Flight Center. J. Geophys. Res., 81, 1006 1026, 1976.

Strange, W.E., S.F. Vincent, and R.H. Berry, Detailed gravimetric geoid for the United States. In: The Use of Artificial Satellites for Geodesy, ed. by S. Henriksen, A. Mancini, and B. Chovitz, Washington, D.C., 169pp., 1972.

Talwani, M., H. Poppe, and P. Rabinowitz, Gravimetrically determined geoid in the western North Atlantic. In: Sea surface topography from space, NOAA Tech. Rept. ERL-228-AOML 7-2, 2, 1-34, 1972.

Von Arx, W.S., Level-surface profiles across the Puerto Rico trench. Science, 154, 1615-1654, 1966.

Watts, A.B., A preliminary analysis of geoid heights derived from GEOS-3 altimeter data along the Hawaiian-Emperor seamount chain. J. Geophys. Res., this volume, 1978.

Watts, A.B. and A. Leeds, Gravimetric geoid in the Northwest Pacific Ocean. Geophys. J. Roy. astr. Soc., 50, 249-278, 1977.

FIGURE CAPTIONS

Figure 1	1° X 1° gravimetric geoid in the Indian Ocean, after Kahle, Chapman, and Talwani, 1978. Referred to in ternational ellipsoid.
Figure 2	1° X 1° gravimetric geoid in the Northwest Pacific, after Watts and Leeds, 1977. Referred to the best fit ellipsoid with flattening 1/298.25.
Figure 3	1° X 1° gravimetric geoid in the North Atlantic, after Talwani and Leeds, in preparation. Contour interval is 2 meters.
Figure 4	Location of GEOS-3 tracks utilized in this study. Track designations are the L-DGO numbers, orbit numbers for each track are listed in Table 1. Outlines of each region covered by each gravimetric geoid are also shown.
Figure 5	Comparison of Indian Ocean gravimetric geoid with GEOS-3 estimates of geoid height. Geoid height is plotted as a function of time of acquisition from first point. The subsatellite point travels at an average but not constant speed of 6.55 km/sec, so the distance scale is approximate. Gravimetric geoid height is the smooth thick line, altimetric geoid height is the rougher and thinner line. Both geoid heights are relative to an ellipsoid with flattening 1/298.255.
Figure 6	Comparison of Northwest Pacific gravimetric geoid with GEOS-3 geoid height. GEOS-3 data are rougher line and are labeled by the Lamont track number, gravimetric geoid heights are the smooth line.
Figure 7	Geoid height and bathymetry across the Aleutian trench. Bathymetry profile is at bottom and is from a ship track; the gravity profile is also from Conrad cruise 1109. Utilizing this gravity profile which is projected normal to the trench axis, and formula 4, a two dimensional geoid, was calculated and is shown. This compares well with the GEOS-3 altimetry data; however the 1° X 1° gravimetric geoid has a wider and shallower low above the trench axis. A sketch map of the location of the projected ship track and GEOS-3 profile is also shown.
Figure 8	Comparison of North Atlantic gravimetric geoid with GEOS-3 altimeter estimates of geoid height. Rough line is altimeter data and is labeled GEOS-3; smoother line is gravimetric geoid heights.

Figure 9 Comparison of Northwest Pacific gravimetric geoid with adjusted GEOS-3 estimates of geoid height. For each profile the gravimetric and altimetric measurements are shown in the lower plot, above them at a different scale the difference in height is indicated.

Figure 10 Comparative accuracies of an altimeter and gravimeter in detecting the gravitational field on a plane earth. This is a plot of the geoid and gravity amplitude spectrum as a function of wave number; the signal is caused by two dimensional topography in Airy isostasy with a white spectrum 3 km in amplitude. Vertical scales have been adjusted to indicate the signal to noise ratio in measuring the field, whose scale is also shown. Thus far an altimeter has a higher signal to noise ratio, for shorter wavelengths a gravimeter records the signal better.

a.2

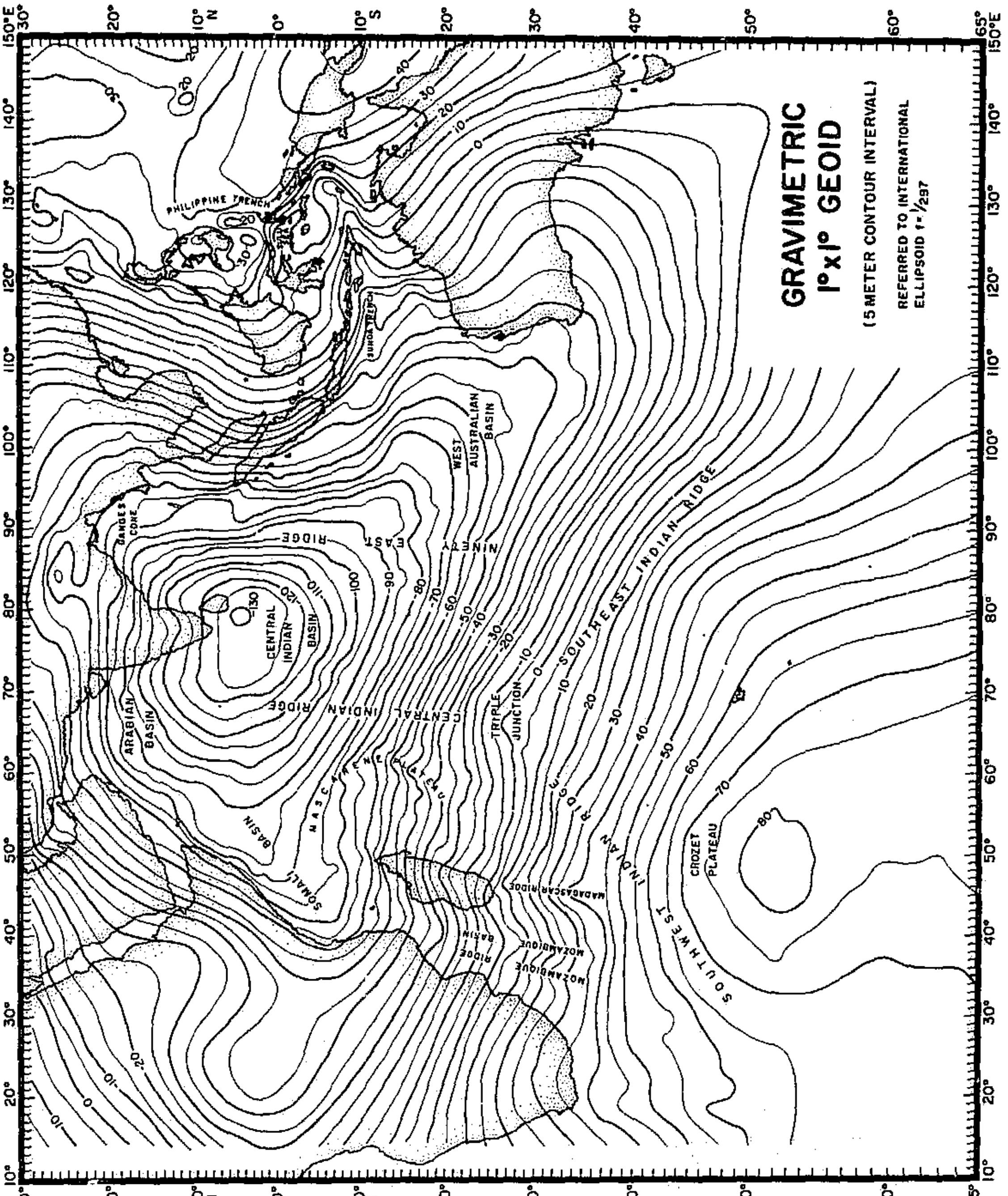

Figure 1

ORIGINAL PAGE IS
OF POOR QUALITY

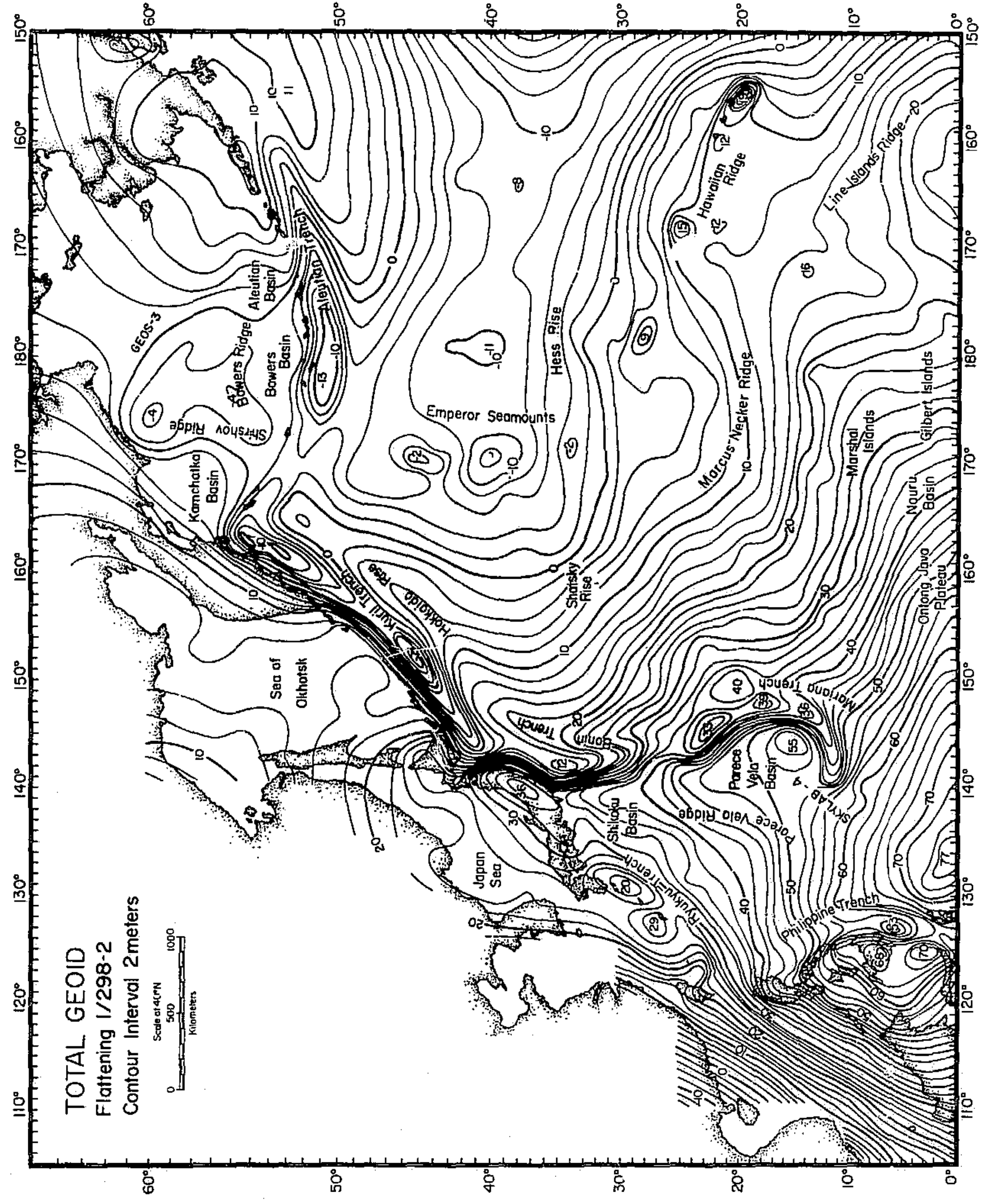
TOTAL GEOID
Flattening 1/298-2
Contour Interval 2meters
Scale at 40°N
0
500
1000
Kilometers
Sea of Okhotsk
Japan Sea
Kamchatka Basin
Shirshov Ridge
Bowers Ridge
Bowers Basin
Aleutian Basin
GEOS-3
Aleutian Trench
Kuril Trench
Hokkaido Rise
Emperor Seamounts
Hess Rise
Shatsky Rise
Bonin Trench
Shikoku Basin
Ryukyu Trench
Parece Vela Ridge
Parece Vela Basin
SKYLAB-4
Mariana Trench
Philippine Trench
Marcus-Necker Ridge
Hawaiian Ridge
Line Islands Ridge
Marshall Islands
Gilbert Islands
Nauru Basin
Ontong-Java Plateau
110°
120°
130°
140°
150°
160°
170°
180°
0°
10°
20°
30°
40°
50°
60°

Figure 2

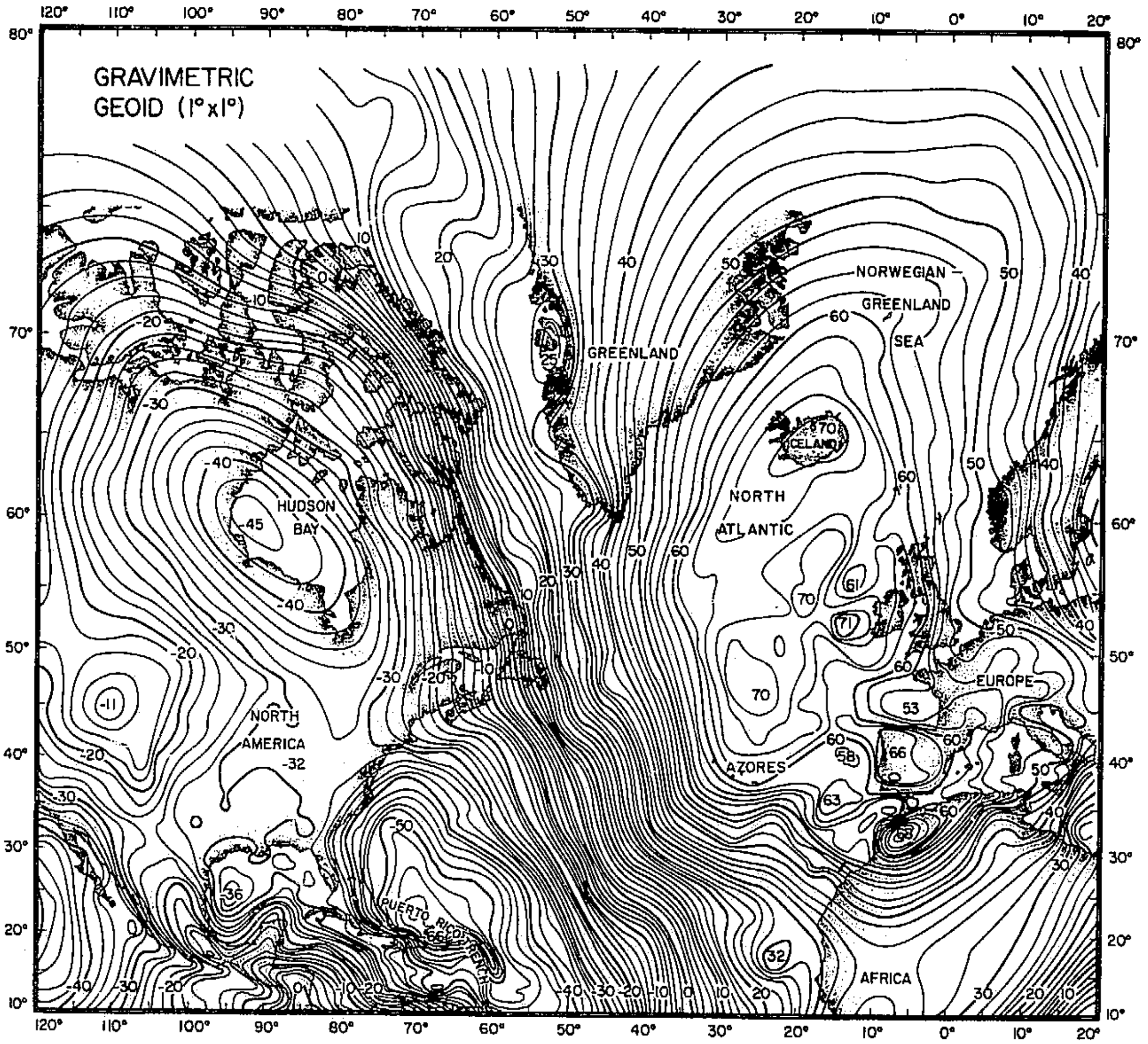
GRAVIMETRIC
GEOID (1°x1°)
HUDSON
BAY
NORTH
AMERICA
GREENLAND
NORWEGIAN
GREENLAND
SEA
ICELAND
NORTH
ATLANTIC
AZORES
EUROPE
AFRICA
PUERTO RICO TRENCH
-45
-40
-30
-20
-11
-32
-36
-50
66
70
71
61
53
58
63
66
32
120°
110°
100°
90°
80°
70°
60°
50°
40°
30°
20°
10°
0°
10°
20°
80°
70°
60°
50°
40°
30°
20°
10°

Figure 3

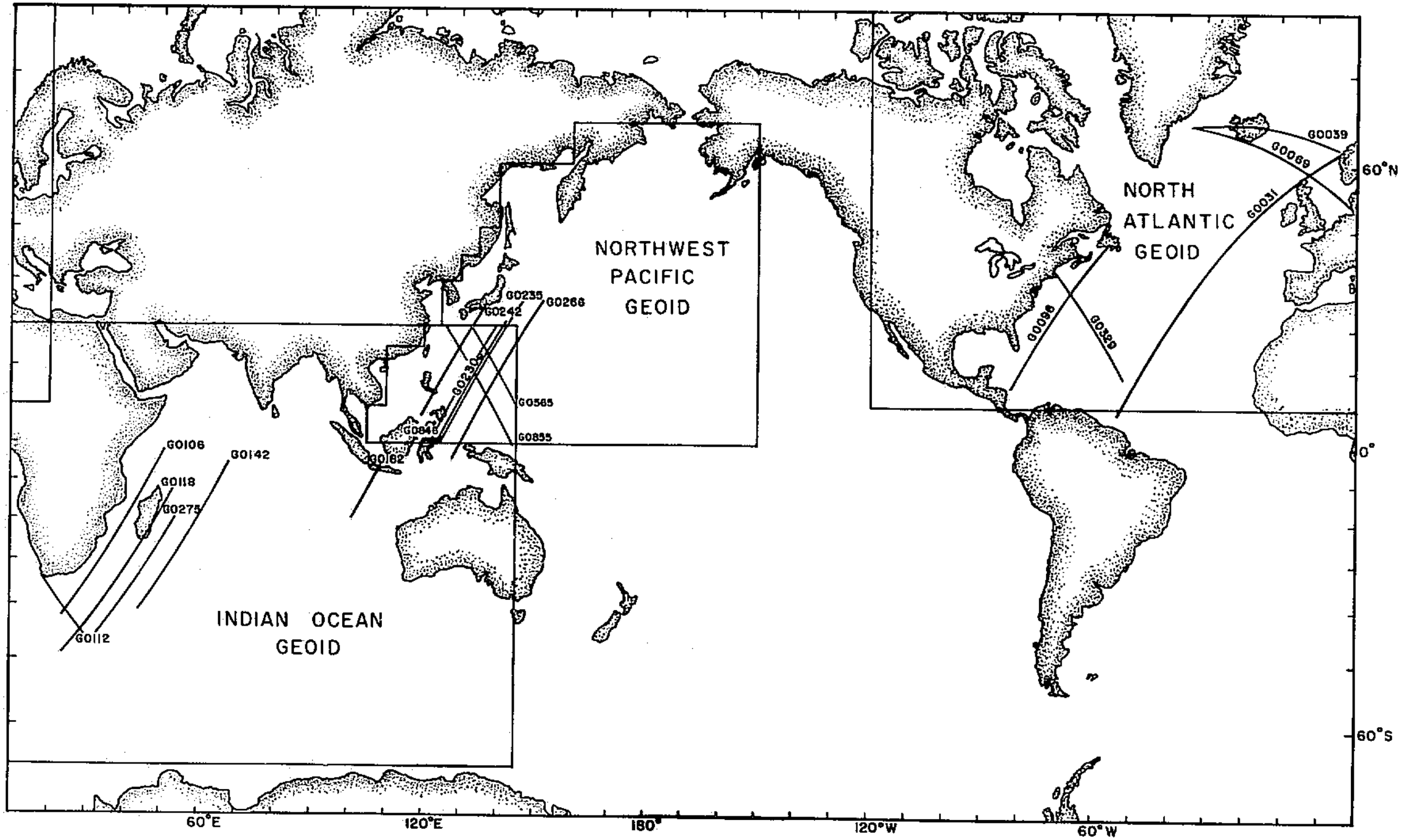
NORTH ATLANTIC GEOID
NORTHWEST PACIFIC GEOID
INDIAN OCEAN GEOID
G0039
G0069
G0031
G0096
G0329
G0235
G0266
G0242
G0230
G0565
G0855
G0848
G0162
G0106
G0142
G0118
G0275
G0112
60°N
0°
60°S
60°E
120°E
180°
120°W
60°W

Figure 4

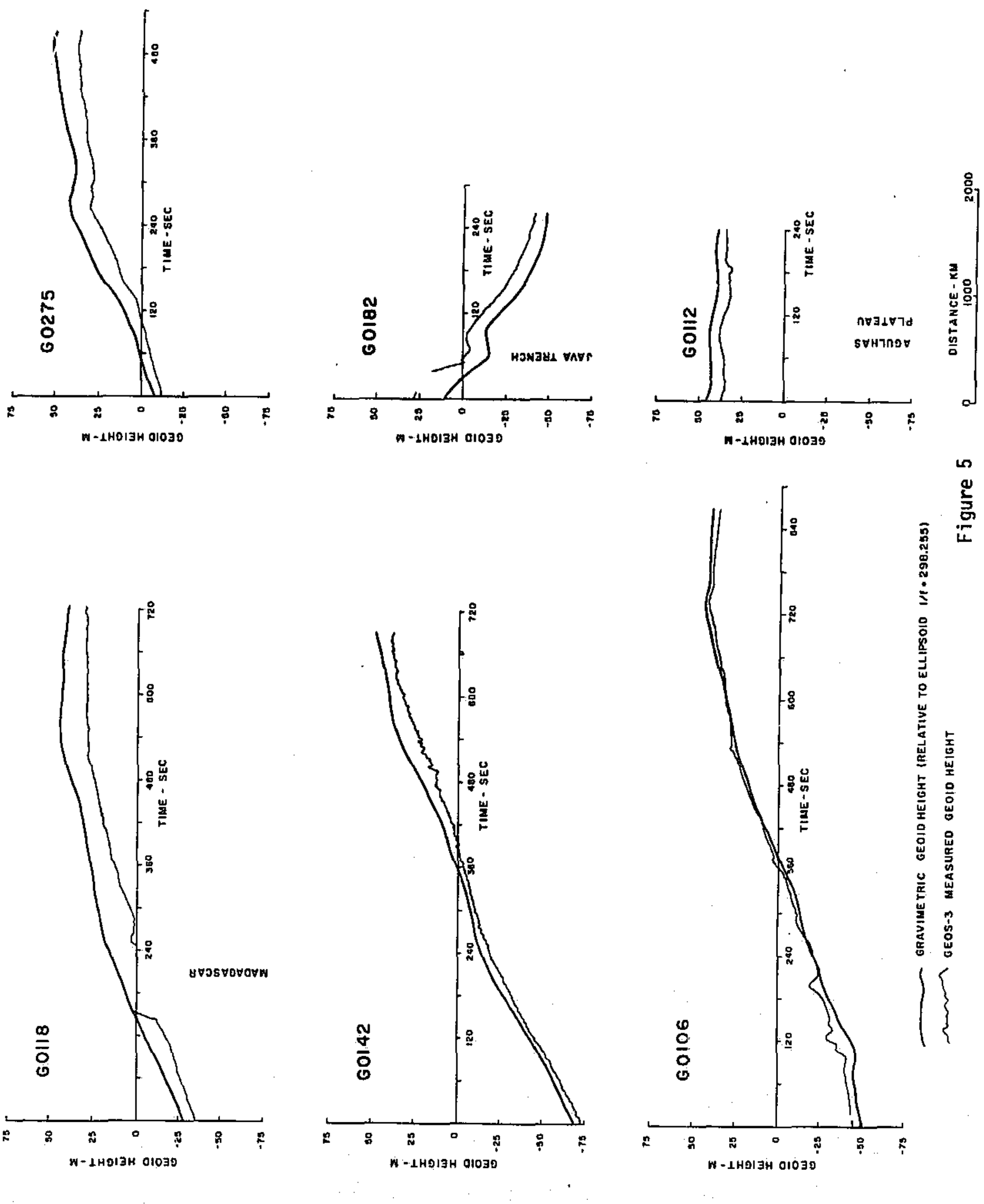
GO118
MADAGASCAR
GO142
GO106
GO275
GO182
JAVA TRENCH
GO112
AGULHAS PLATEAU
GEOID HEIGHT - M
75
50
25
0
-25
-50
-75
TIME - SEC
120
240
360
480
600
720
840
DISTANCE - KM
0
1000
2000
GRAVIMETRIC GEOID HEIGHT (RELATIVE TO ELLIPSOID 1/f = 298.255)
GEOS-3 MEASURED GEOID HEIGHT

Figure 5

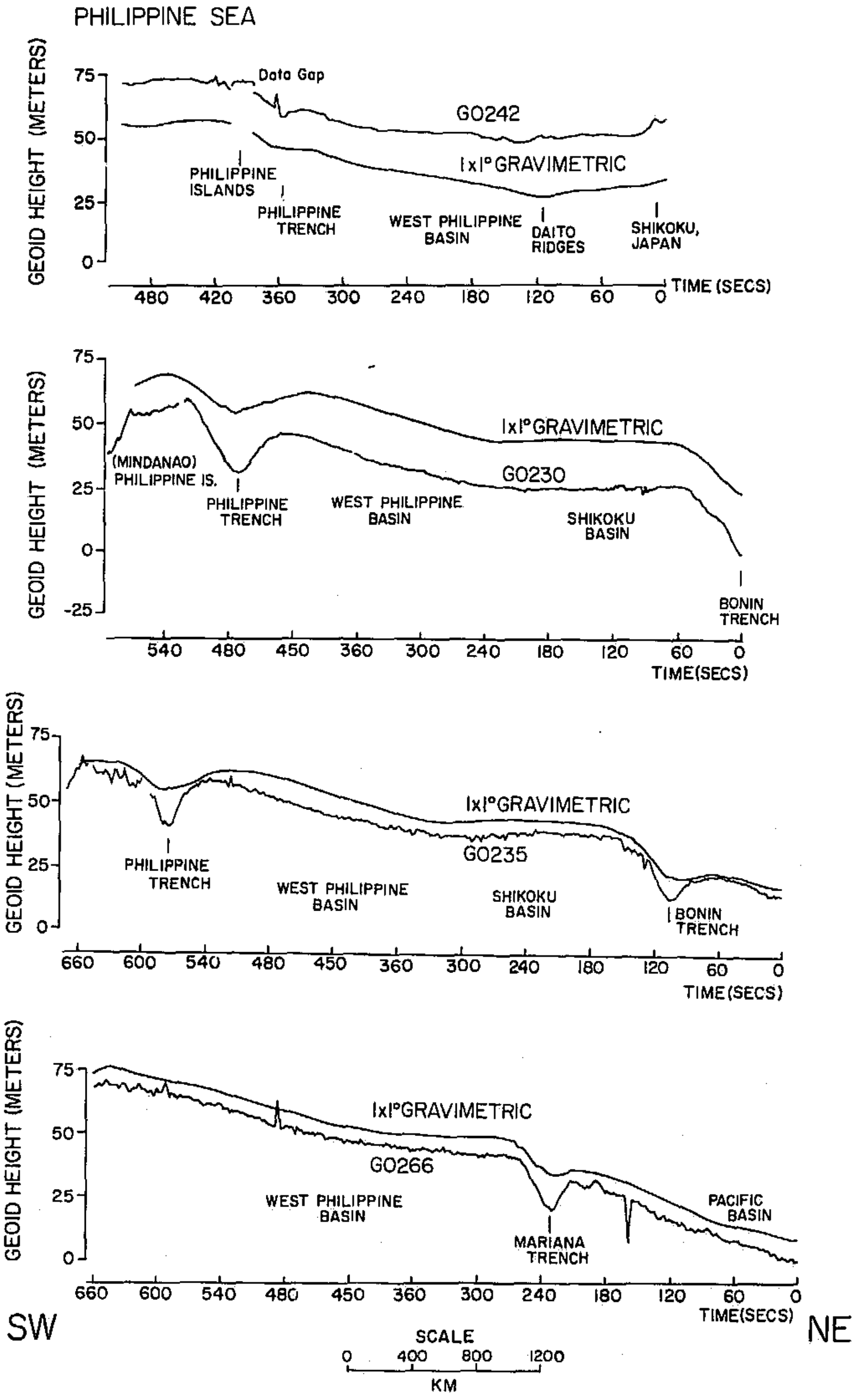
PHILIPPINE SEA
GEOID HEIGHT (METERS)
75
50
25
0
Data Gap
G0242
1x1° GRAVIMETRIC
PHILIPPINE ISLANDS
PHILIPPINE TRENCH
WEST PHILIPPINE BASIN
DAITO RIDGES
SHIKOKU, JAPAN
480 420 360 300 240 180 120 60 0
TIME (SECS)
GEOID HEIGHT (METERS)
75
50
25
0
-25
1x1° GRAVIMETRIC
G0230
(MINDANAO) PHILIPPINE IS.
PHILIPPINE TRENCH
WEST PHILIPPINE BASIN
SHIKOKU BASIN
BONIN TRENCH
540 480 450 360 300 240 180 120 60 0
TIME(SECS)
GEOID HEIGHT (METERS)
75
50
25
0
1x1° GRAVIMETRIC
G0235
PHILIPPINE TRENCH
WEST PHILIPPINE BASIN
SHIKOKU BASIN
BONIN TRENCH
660 600 540 480 450 360 300 240 180 120 60 0
TIME(SECS)
GEOID HEIGHT (METERS)
75
50
25
0
1x1° GRAVIMETRIC
G0266
WEST PHILIPPINE BASIN
MARIANA TRENCH
PACIFIC BASIN
660 600 540 480 450 360 300 240 180 120 60 0
TIME(SECS)
SW
NE
SCALE
0 400 800 1200
KM

Figure 6

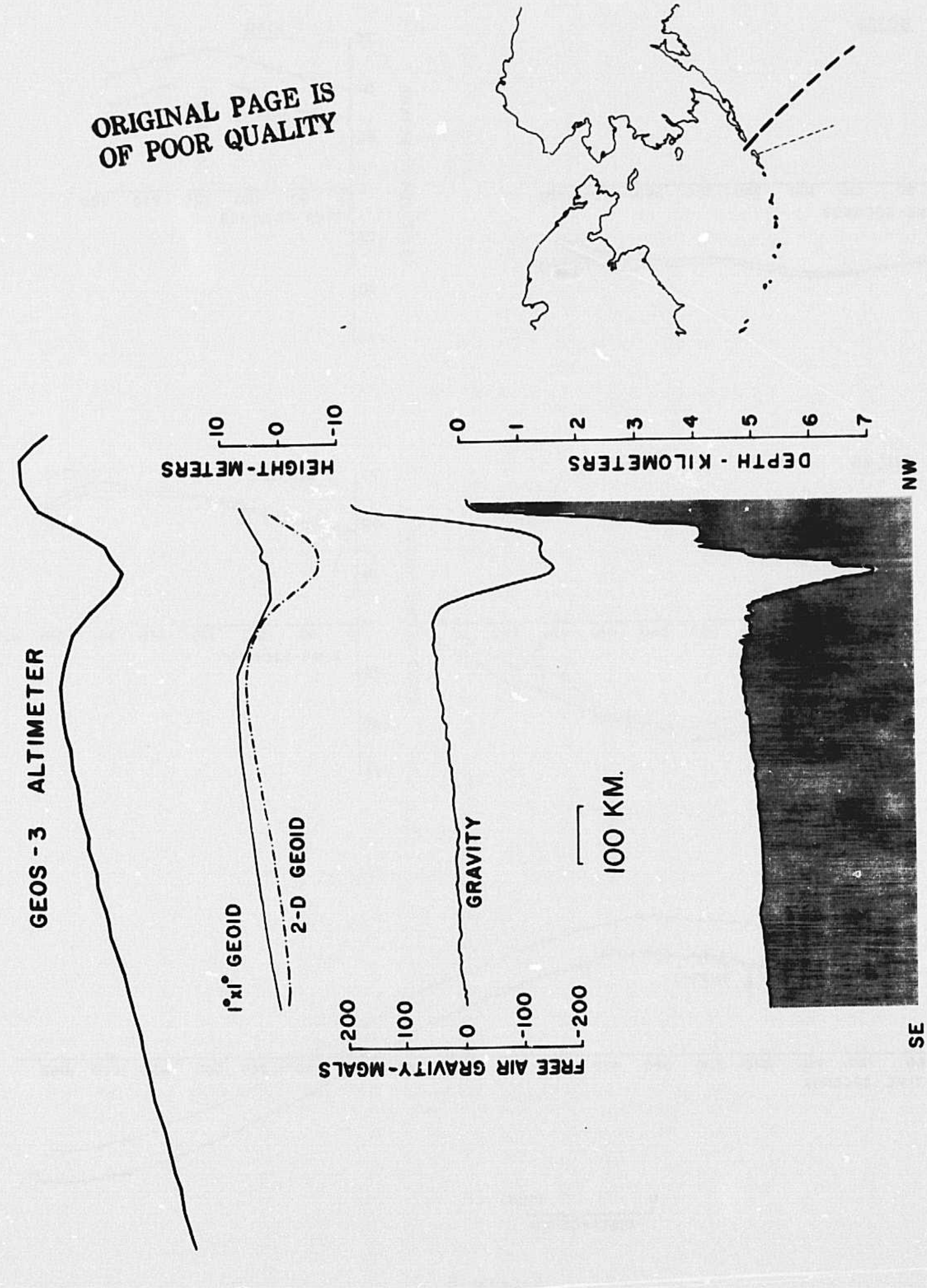
GEOS-3 ALTIMETER
HEIGHT-METERS
20
10
0
-10
-20
1°x1° GEOID
2-D GEOID
HEIGHT-METERS
10
0
-10
GRAVITY
FREE AIR GRAVITY-MGALS
200
100
0
-100
-200
100 KM.
DEPTH - KILOMETERS
0
1
2
3
4
5
6
7
ALEUTIAN TRENCH
SE
NW

Figure 7

COMPARISON OF GRAVIMETRIC GEOID WITH GEOS-3 ALTIMETER

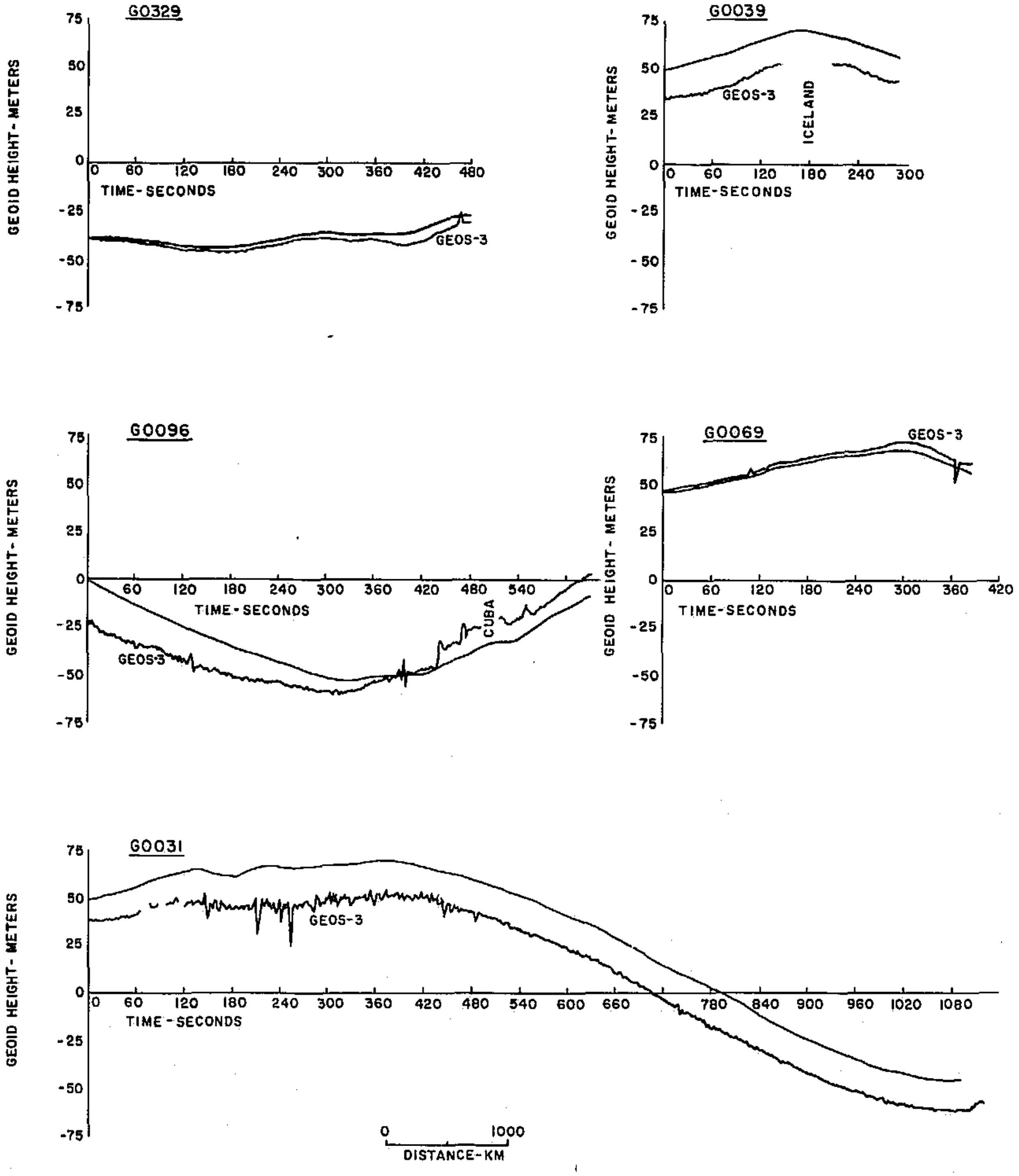

Figure 8

COMPARISON OF GRAVIMETRIC GEOID WITH ADJUSTED GEOS-3 ALTIMETER MEASUREMENTS

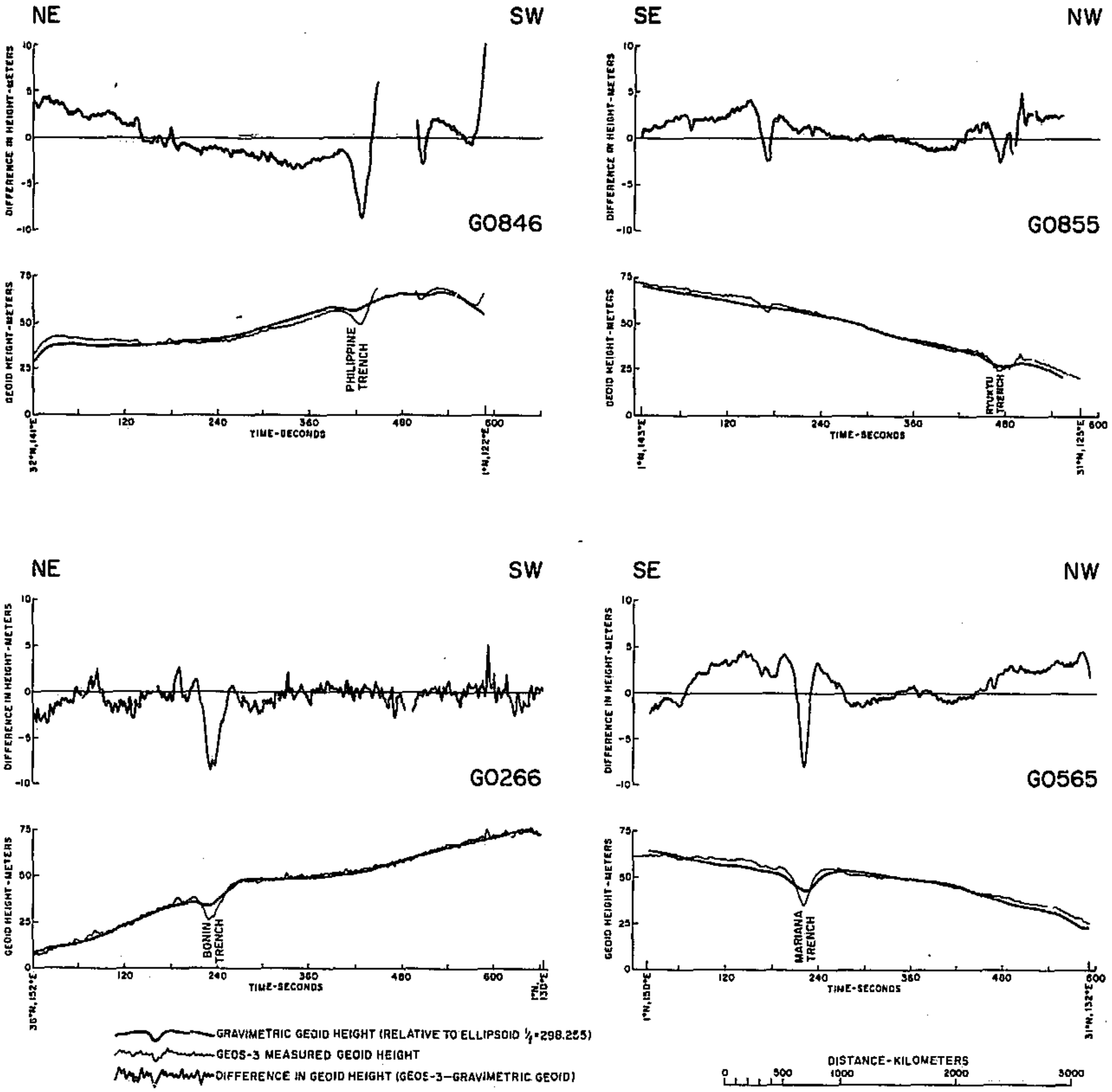

Figure 9

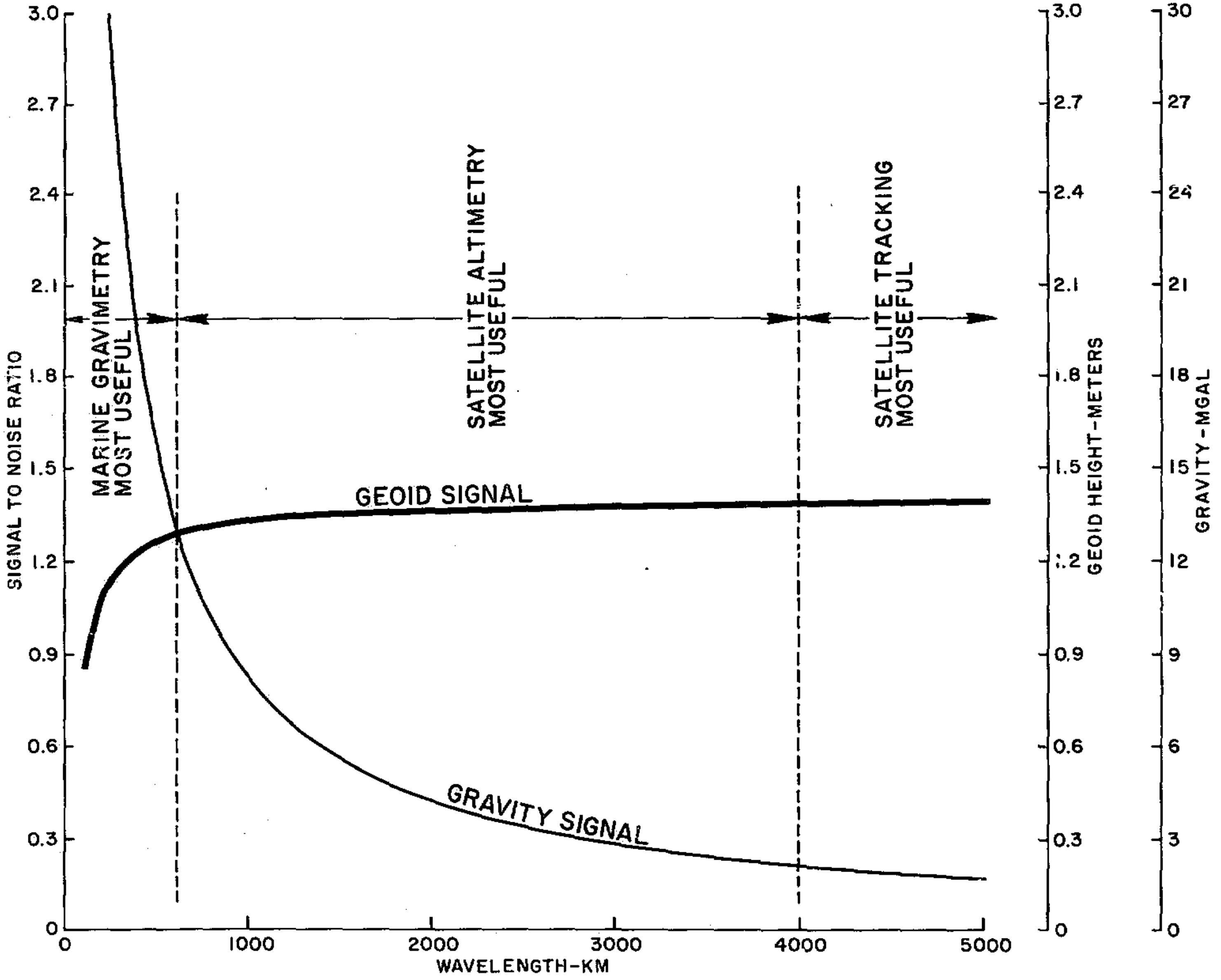
SIGNAL TO NOISE RATIO
3.0
2.7
2.4
2.1
1.8
1.5
1.2
0.9
0.6
0.3
0
WAVELENGTH-KM
0
1000
2000
3000
4000
5000
GEOID HEIGHT-METERS
3.0
2.7
2.4
2.1
1.8
1.2
1.5
0.9
0.6
0.3
0
GRAVITY-MGAL
30
27
24
21
18
15
12
9
6
3
0
MARINE GRAVIMETRY MOST USEFUL
SATELLITE ALTIMETRY MOST USEFUL
SATELLITE TRACKING MOST USEFUL
GEOID SIGNAL
GRAVITY SIGNAL

Figure 10

TABLE 1

Track no.	Orbit	Telemetry mode	Transmitter mode
G0118	646	Low	Intensive
G0275	461	Low	Intensive
G0142	1200	Low	Global
G0182	1568	Low	Intensive
G0106	362	High	Intensive
G0112	584	Low	Intensive
G0242	2037	Low	Intensive
G0230	1795	Low	Intensive
G0235	416	Low	Global
G0266	430	Low	Global
G0329	3245	Low	Intensive
G0039	184	Low	Global
G0096	325	Low	Global
G0069	398	High	Intensive
G0031	210		
G0846	1724	Low	Intensive
G0855	1616	Low	Intensive
G0565	2028	Low	Intensive

TABLE 2

RMS discrepancies between gravimetric geoids and GEOS-3 estimates of geoid

Track no.	RMS difference	RMS difference after bias correction	A priori orbital error
G0106	3.69 meters	4.78 meters	10^+ meters
G0112	6.99	12.26	10
G0118	13.27	18.37	10
G0142	6.67	10.01	10
G0275	10.84	16.02	10
G0182	11.15	6.46	3
G0242	17.87	15.87	3
G0230	18.00	23.61	3-10
G0235	5.86	11.07	10
G0266	6.82	10.27	10
G0031	18.99		
G0039	23.93	37.23	10
G0069	13.18	15.65	10
G0096	13.18	15.65	3-10
G0329	3.07	8.05	3

TABLE 3

RMS discrepancies between gravimetric geoids and adjusted GEOS-3 data

Track no.	RMS difference before adjustment	RMS difference after adjustment
G0846	12.34 meters	2.67 meters
G0855	4.82	1.69
G0565	4.00	2.36
G0266	10.27	2.07

TECHNIQUES FOR INTERPRETATION OF GEOID ANOMALIES

Introduction

When a new scientific instrument is developed and utilized for the study of the earth, there are always new and exciting discoveries. Such an instrument is the GEOS-3 radar altimeter, this has been used to make measurements of the shape of the sea surface over most of the worlds oceans. After corrections for errors and oceanographic effects this data is a determination of the marine geoid.

Given the shape of this gravitational equipotential surface inferences can be made about the density inhomogeneities within the earth which cause geoid undulations. Prior to satellite altimetry determination of the geoid was the primary goal. Now with geoid measurements via satellite altimetry new questions can be asked. Why does the geoid have its particular shape and what are the structures within the earth which cause geoid anomalies? In order to utilize altimetry data in studying the earth's interior mathematical techniques are necessary. For this reason we have developed several new analytic techniques for interpretation of geoid anomalies.

Our procedure is to initially compute formulas for the geoid anomaly over idealized bodies, these serve to demonstrate various properties of geoid anomalies. Then formulas are developed for computing the geoid anomaly over an arbitrary two dimensional body. Most general procedures require the calculation of geoid anomalies over three dimensional bodies. In order to understand the relationship between the gravity anomaly and the geoid, techniques in the frequency domain are developed. Finally, as practical examples, calculations of the geoid anomaly across continental margins and over seamounts are compared with actual geoid measurements.

Basic Formulas and Ideal Bodies

In dealing with geoid anomalies we are concerned with the computation of the shape of an equipotential surface, this surface is primarily ellipsoidal with small undulations due to an anomalous potential. If we know the anomalous potential, then the geoid anomaly is given by Brun's formula (Heiskanen & Moritz, 1967).

$$N = \frac{T}{\gamma} \tag{1}$$

Where N is geoid height, T is the anamolous potential, and γ is normal gravity - 980 cm/sec^2. A point mass will have an anomalous potential of

$$T = \frac{G\,M}{R} \tag{2}$$

where G is the Newtonian constant 6.678 10^{-8} cm^3/gm sec^2, M is the mass, and R is the distance between the point mass and the observation point. This expression has two conventions, potential is zero at infinity and positive everywhere else. Thus an excess mass corresponds to positive potential and positive geoid height. Our basic problem then is how to compute the geoid anomaly due to an assemblage of point masses.

$$N(x',y',z') = \frac{G}{\gamma}\iiint \frac{\rho \quad d\,x\,dy\,dz}{\sqrt{(x-x')^2 + (y-y')^2 + (z-z')^2}} \tag{3}$$

Primed coordinates indicate the observation point, unprimed coordinates are the integration variable, and ρ is density. Initially we compute the geoid over ideal bodies; lines, sheets, and rectangles in both two and three dimensions.

A finite horizontal line located at y_0, z_0 with linear density λ (gm/cm) has a corresponding geoid anomaly of (Figure 1a)

$$N = \frac{G}{\gamma}\int_{x_1}^{x_2} \frac{\lambda\; dx}{\sqrt{(x-x')^2 + (y_0-y')^2 + (z_0-z')^2}} \tag{4}$$

This, when integrated becomes

$$N = \frac{G\lambda}{\gamma} \log_e \left\{ \frac{(x_2-x') + \left[(x_2-x')^2 + (y_0-y')^2 + (z_0-z')^2\right]^{1/2}}{(x_1-x') + \left[(x_1-x')^2 + (y_0-y')^2 + (z_0-z')^2\right]^{1/2}} \right\} \qquad (5)$$

Figure 1B shows a plot of this function, the geoid height is always positive and decays to 0 in the limit as $|y|$ goes to infinity.

If the finite horizontal line is integrated along the z axis, one obtains the geoid anomaly over a finite vertical sheet (Figure 2a). This integral is (see appendix for details)

$$N = \frac{G\sigma}{\gamma} \left\{ G_1\,(x_2,z_2) - G_1\,(x_2,z_1) - G_1\,(x_1,z_2) + G_1\,(x_1,z_1) \right\} \qquad (6)$$

where σ is the surface density (gm/cm^2) and

$$\begin{aligned} G_1\,(x,z) = {} & (z-z') \log_e \left[(x-x') + \sqrt{(x-x')^2 + (y_0-y')^2 + (z-z')^2}\right] \\ & - (z-z') + (x-x') \log_e \left[(z-z') + \sqrt{(x-x')^2 + (y_0-y')^2 + (z-z')^2}\right] \qquad (7) \\ & + \left|y_0-y'\right| \sin^{-1} \left[\frac{-(x-x')^2 - (y_0-y')^2 - (x-x')\sqrt{(x-x')^2 + (y_0-y')^2 + (z-z')^2}}{\left|(x-x') + \sqrt{(x-x')^2 + (y_0-y')^2 + (z-z')^2}\right| \sqrt{(x-x')^2 + (y_0-y')^2}} \right] \end{aligned}$$

and restricting $(z-z') > 0$

A plot of this function is in Figure 2B. While always positive, the geoid height decays at a slower rate than the finite horizontal line.

Our next ideal body is an infinite horizontal line, while the actual integration is quite simple we utilize a slightly longer derivation in order to show the relationship between gravity, deflection of the vertical, and the geoid. This is also the basis for a later derivation in the frequency domain. In the two dimensional geoid calculations a complication arises, this involves the zero reference level. Calculation of the geoid anomaly over the infinite horizontal line will illustrate this complexity.

Due to an infinite horizontal line located at $y=0$, $z=z_0$, the horizontal component of gravity on the $z = o$ plane is

$$F_g^h = -2 G \lambda \frac{y \hat{y}}{(y^2 + z_0^2)} \quad (8)$$

Deflection of the vertical is defined to be the angle between a vertical line and the local direction of gravity (Figure 3). On a plane earth the gravitational attraction has a vertical component of $\gamma + Fg^V$, where γ is normal gravity and Fg^V is the vertical component of the gravity anomaly due to anomalous mass. The horizontal component is simply Fg^h, thus

$$\tan \delta = \frac{Fg^h}{\gamma + Fg^V} \quad (9)$$

where δ is deflection of vertical.

Because $Fg^V < < \gamma$, and $\delta \doteq 0$

$$\delta = \frac{Fg^h}{\gamma} = \frac{-2G\lambda}{\gamma} \frac{y}{(y^2 + z_0^2)} \quad (10)$$

Deflection of the vertical is just the slope of the geoid.

$$\delta = +\frac{\partial N}{\partial y} = \frac{-2G\lambda}{\gamma} \frac{y}{(y^2 + z_0^2)} \quad (11)$$

Solving for geoid height N we obtain:

$$N = -\frac{G \lambda}{\gamma} \log_e (y^2 + z_0^2) \Big|_{y_0}^{y} \quad (12)$$

where y_0 is an arbitrary constant of integration.

With the two dimensional potential the usual procedure is to let the potential be zero at unit distance, or when $(y_0^2 + z_0^2) = 1$. This has two effects; it causes the absolute amplitude of N to depend upon the units used, and it introduces both positive and negative geoid heights for a positive mass. In dealing with two dimensional bodies it is necessary to ignore this arbitrary constant level.

$$N = -\frac{G\lambda}{\gamma}\log_e (y^2 + z_0^2) \tag{13}$$

When the infinite horizontal line is integrated along the z axis, one obtains the geoid anomaly over a two dimensional vertical sheet.

$$N = -\frac{G\sigma}{\gamma}\int_{z_1}^{z2} \log_e [(y_0-y')^2 + (z-z')^2]\, dz \tag{14}$$

and after integration

$$N = -\frac{G\sigma}{\gamma}\left\{(z-z')\log_e [(y_0-y')^2 + (z-z')^2] - 2z + 2\left|y_0-y'\right| \mathrm{Tan}^{-1}\frac{(z-z')}{\left|y_0-y'\right|}\right\}\Bigg|_{z_1}^{z_2} \tag{15}$$

This anomaly is shown in figure 2c, for comparison purposes in figure 2b there is a geoid anomaly over a finite vertical sheet. Obviously they are quite similar in shape. This shows that two dimensional methods might approximate three dimensional ones in spite of the arbitrary height difference.

A two dimensional rectangle is obtained by an integration of the mass line over both the y and z axis.(Figure 4a).

$$N = -\frac{G\sigma}{\gamma}\int_{z_1}^{z_2}\int_{y_1}^{y_2} \log_e [(y-y')^2 + (z-z')^2]\, dy\, dz \tag{16}$$

after integration (see appendix for details)

$$N = -\frac{G\sigma}{\gamma}[G_2 (y_2, z2) - G_2 (y_1, z_2) - G_2 (y_2, z1) + G_2 (y_1, z_1)] \tag{17}$$

where

$$G_2\,(y,\,z) = (y-y')\,\{(z-z')\,\log_e\,[(y-y')^2 + (z-z')^2] - 2\,z + 2\,\left|\,y-y'\right| \cdot \mathrm{Tan}^{-1}\,\frac{(z-z')}{|y-y'|}\,\}\ \ -2\,y\,z + [(z-z')^2 + (y-y')^2]\ \ \mathrm{Tan}^{-1}\,\frac{(y-y')}{(z-z')} + (z-z')\,(y-y') \tag{18}$$

assuming $(z-z') > 0$

In Figure 4b there is a plot of this anomaly. Over the rectangle the geoid is not flat, it is always concave downwards until a point of inflection above the edge of the body. The implication of this curvature is that in constructing geoid models the anomalous mass must integrate to zero, otherwise there will be a long wavelength curvature of the geoid anomaly. To make the anomalous mass sum to zero, both negative and positive densities are utilized.

Integral Formulas For Two Dimensional Bodies

While analytic solutions for ideal bodies have an initial utility in understanding properties of geoid anomalies and verifying other formulas they are of limited utility in learning about the earth. Better models of the earth involve specifying densities of bodies of arbitrary shape and computing the resultant geoid anomaly. In order to achieve this result we have developed several techniques for the computation of geoid anomalies over bodies which are polygons in either two or three dimensions. These enable the models of virtually any shape to be calculated, the desired accuracy in shape only limited by the number of specified sides.

A simple numerical solution to computing geoid anomalies was originally developed by Talwani, Poppe and Rabinowitz (1972) in order to compute the geoid across a two dimensional structure from the gravity. For a given polygon in two dimensions the horizontal component of gravity is computed with the line integral method of Talwani et al. (1959), then after division by normal gravity the deflection of vertical is obtained.

$$\delta = \frac{Fg^h}{\gamma} \tag{19}$$

As in our previous derivation for the infinite line, this is the slope of the geoid

$$\delta = \frac{dn}{dy} \tag{20}$$

so finally

$$N = \int_{y_0}^{y} \delta\ (y)\ dy \tag{21}$$

This final integration is done with the trapezoidal rule or else Simpson's formula. Although it is a numerical solution it produces very accurate results in excellent agreement with exact analytic solutions.

For geophysical interpretation of two dimensional bodies of arbitrary shape a method has been developed to directly compute the geoid anomaly over a polygon in two dimensions. In this technique the body is specified by the location of each vertex and the density of the body, as in Figure 5a. For any arbitrary two dimensional body the geoid anomaly is

$$N = -\frac{G\ \lambda}{\gamma} \iint_S \log_e \left[(y-y')^2 + (z-z')^2\right]\ dy\ dz \tag{22}$$

To obtain a direct analytic solution for a two dimensional polygon we utilize Stokes' theorem to convert this surface integral to the following line integral:

$$N = -\frac{G\ \lambda}{\gamma} \oint \{(y-y')\ \log_e \left[(y-y')^2 + (z-z')^2\right] - 2\ y + 2\ (z-z') \bullet \operatorname{Tan}^{-1} \frac{(y-y')}{(z-z')}\}\ d\ z \tag{23}$$

and restricting $(z-z') > 0$

With a polygonal approximation each side is defined by the formula:

$$z = m_i\ y + b_i$$

then the contribution to the geoid anomaly due to the ${}_i$th line segment is: (see appendix for details)

$$\begin{aligned}
n_i = \Bigg[& m_i \frac{(y-y')^2}{2} \log_e [(y-y')^2 + (z-z')^2] - m_i \frac{(y-y')^2}{2} \\
& + \frac{m_i^2 A_2}{(1+m_i^2)} (y-y') - \frac{m_i\ (m_i^2-1)\ A_2^2}{2(1+m_i^2)^2} \log_e [(y-y')^2 + (z-z')^2] \\
& -2 \frac{m_i^2 A_2^2}{(1+m_i^2)^2} \operatorname{Tan}^{-1} \left[\frac{(1+m_i^2)\ (y-y') + m_i A_2}{A_2} \right] \\
& - m_i (y-y')^2 + z^2 \operatorname{Tan}^{-1} \frac{(y-y')}{z} \\
& \frac{-c_i\ D_i^2}{(1+c_i^2)^2} \log_e \left[\frac{(1 + c_i^2)\ Z^2 + 2\ c_i\ D_i\ Z + D_i^2}{D_i^2} \right] \\
& + \\
& + \frac{D_i\ Z}{(1+c_i)^2} + \frac{(1-c_i^2)\ D_i^2}{(1+c_i^2)^2} \operatorname{Tan}^{-1} \left(\frac{y-y'}{z} \right) \Bigg] \Bigg|_{y_{i-1}}^{y_i}
\end{aligned} \tag{24}$$

with $A_2 = m_i\ y' + B_i - z'$

$c_i = 1 / m_i$

$D_i = -B_i/m_i - y'$

m_i = slope of line segment

B_i = intercept of line segment

$Z = m_i\ y + b_i$

thus the total geoid anomaly is

$$N = \frac{-G\,\sigma}{\gamma} \sum_{i=1}^{L} n_i \qquad L = \text{number of segments} \tag{25}$$

Due to singularities in the integral formula the following special cases need also be considered:

a) $m_i = 0$ then $n_i = 0$ (slope of line segment is zero)

b) $c_i = 0$ then (slope of line segment is infinite)

$$\begin{aligned} n_i = \{ &(y_i-y')\,[(z-z')\log_e[(y_i-y')^2 + (z-z')^2] - 2(z-z') \\ &+ 2\left|y_i-y'\right| \mathrm{Tan}^{-1}\frac{(z-z')}{\left|(y_i-y')\right|}] - 2\,(y_i-y')\,z \\ &+ [(y_i-y')^2 + (z-z')^2]\ \mathrm{Tan}^{-1}\frac{(y_i-y')}{(z-z')} \\ &+ (y_i-y')\,(z-z')\} \Bigg|_{z_{i-1}}^{z_i} \end{aligned} \tag{26}$$

c) $B_i/m_i + y' = 0$ then (the extension of line segment passes through observation point)

$$n_i = \{\frac{z^2}{2m_i}\log_e[(1+\frac{1}{m_i^2})\,z^2] - \frac{3z^2}{2m_i} + z^2\ \mathrm{Tan}^{-1}\,(\frac{1}{m_i})\}\Bigg|_{z_{i-1}}^{z_i} \tag{27}$$

assuming $z' = 0$, $z > 0$

For a given geophysical model a number of individual bodies are specified by their respective densities and shape as defined by a number of vertices of a polygon. For each body the geoid effect is calculated using either the numerical technique in formula (21) or the analytic technique of formula (24), after summation over all bodies the total geoid height due to the model is obtained. In practice both of these mathematical techniques yield identical results. In Figure 5b there is a sample computation of geoid and gravity over a pentagonal body. The geoid has a shape similar to the gravity anomaly but is much wider, the geoid anomaly decays with distance at a slower rate.

In modeling two precautions are necessary, first the d.c. level of the geoid height must be ignored. This is because of the arbitrary location of zero potential for a two dimensional body. A second precaution concerns the specification of densities. In geoid calculations the anomalous density must be utilized rather than the total density, this is because Brun's formula (formula (1)) requires anomalous potential rather than total potential. If a given model is in isostatic equilibrium this second precaution requires that the sum of the anomalous masses in a given column be zero. This requirement is different than in standard gravity models, if the total mass did not sum to zero then a d.c. gravity value could always be subtracted from calculated gravity to obtain the gravity anomaly. In geoid computations this procedure does not work, the reason being that a two dimensional rectangle (as discussed previously) does not have a flat geoid anomaly above it. Whereas in gravity calculations a two dimensional rectangle, except for edge effects, has a flat gravity anomaly.

As a practical example of the utility of these methods we consider the study of an Atlantic type continental margin. In the transition between the deep sea and the continental margin of Nova Scotia in Eastern Canada, the ocean bottom changes in depth by five kilometers. In a likewise fashion the ocean surface changes in height by six meters (Figure 6), this change in geoid height has been determined from the GEOS-3 satellite. A natural question arises then, what is the cause of this change in geoid height? To help answer this question, a two dimensional density model of the Nova Scotia margin has been constructed (Figure 6). This is a simple three component model with water, crust, and mantle material. It is fully compensated in an Airy manner. Utilizing the two dimensional technique described in this section, we have calculated the geoid anomaly over this model. As Figure 6 indicates, the calculated geoid height is in good agreement with the observed GEOS-3 data. It can be concluded that a simple density model of the Nova Scotia margin which is in isostatic equilibrium is capable of successfully modeling the observed GEOS-3 data. Due to the noise level of the data a more elaborate model was believed unjustified.

Geoid Calculations For Three Dimensional Bodies

While the two dimensional approximation has a certain utility, more realistic geophysical modeling requires the computation of the geoid anomaly due to bodies of arbitrary shape and density in three dimensions. In the method now developed the shape of the body is prescribed to be a polyhedron. As this geometric form can be made in any configuration with many facets, virtually every shape can be modeled with this method. This same technique was developed in gravity modeling by Coggon (1976), Paul (1974), and Barnett (1976).

In Figure 7a we illustrate a polyhedron which is assumed to have constant density. To calculate the geoid height for this body the fundamental integral formula 3 has to be solved. Conceptually our method of solution is quite simple. This volume integral is converted to a surface integral by the divergence theorem. For each facet of the polyhedron this surface integral can be solved by conversion to a line integral via Stokes' theorem. Thus the total volume integral is calculated by a summation of surface integrals, one for each polygonal facet. Each surface integral is calculated by a summation of line integrals, one for each line segment on a given facet. This is an exact analytic technique, it is accurate for any shape which can be approximated as a polyhedron.

To derive our formula, we initially change the integration over the volume of the polyhedron, to become an integration over the surface of the polyhedron. If equation 3 is rewritten in the form

$$N = \frac{G\,\rho}{\gamma}\iiint_V \nabla \cdot \left(\tfrac{1}{2}\,\hat{r}\right) dv \qquad (28)$$

where $\hat{r}$ is the unit vector in the radial direction

$$\hat{r} = \frac{(x - x')\ \hat{y} + (y - y')\ \hat{y} + (z - z')\ \hat{z}}{[(x - x')^2 + (y - y')^2 + (z - z')^2]^{\frac{1}{2}}}$$

and ∇ is the vector del operator.

We see that it can be changed to a surface integral with the divergence theorem. Thus:

$$N = \frac{G\ \rho}{\gamma} \iint_s \frac{1}{2}\ \hat{r} \cdot \hat{u}_4\ ds \tag{29}$$

$$\text{or} = \frac{G\ \rho}{\gamma} \iint_s \frac{1}{2} \frac{[(x - x')\ u_{41} + (y - y')\ u_{42} + (z - z')\ u_{43}]\ ds}{[(x - x')^2 + (y - y')^2 + (z - z')^2]^{\frac{1}{2}}}$$

where $\hat{u}_4$ is a unit vector normal to the element of surface area ds, and has components (u_{41}, u_{42}, u_{43}).

This equation now is a surface integral and must be solved for each individual facet upon which the unit normal vector $\hat{u}_4$ is constant. After this integral is computed for each face, the results are summed for all facets thereby calculating the geoid anomaly due to the entire body. Thus

$$N = \sum_i I_i$$ where I_i is equation 29 evaluated for the ith facet of the polyhedron. (30)

Solution of this integral for each face of the polyhedron requires a coordinate transformation, this change rotates the facet until it is normal to one of the new axes. This technique was originally used for solving integrals in gravity and magnetic computations by Barnett (1976) and also Paul (1974).

This coordinate transformation involves a rotation and translation. To construct the necessary rotation matrix, three unit vectors must be first calculated. For a given facet (Figure 7b) these three vectors are determined in the following way. Each vertex in the facet is numbered in counter clockwise order when looking into the body. Unit vector $\hat{u}_1$ extends from point 1 to point

2, and unit vector $\hat{u}_2$ extends from point 2 to point 3. Given this numbering scheme $\hat{u}_1 \times \hat{u}_2$ (vector cross product) is the outward facing normal for the facet. With these vectors, two additional unit vectors can be calculated

$$\hat{u}_3 = \hat{u}_1 \times \hat{u}_2 \qquad \text{where } \hat{u}_3 \text{ is the}$$

$$\hat{u}_4 = \hat{u}_3 \times \hat{u}_1 \qquad \text{outward unit normal}$$

An orthogonal rotation matrix is constructed from these unit vectors.

$$|u| = \begin{vmatrix} u_{11} & u_{12} & u_{13} \\ u_{41} & u_{42} & u_{43} \\ u_{31} & u_{32} & u_{33} \end{vmatrix}$$

where u_{ij} is the jth component of the unit vector $\hat{u}_i$.

A coordinate translation is also applied so that the observation point (x', y', z') becomes located at the new zero origin. The complete coordinate transformation changes the (x, y, z) coordinates to a new (ζ, η, θ) system, in which (x', y', z') becomes (o, o, o,).

Thus

$$\begin{vmatrix} \zeta \\ \eta \\ \theta \end{vmatrix} = \begin{vmatrix} u_{11} & u_{12} & u_{13} \\ u_{41} & u_{42} & u_{43} \\ u_{31} & u_{32} & u_{33} \end{vmatrix} \begin{vmatrix} x \\ y \\ z \end{vmatrix} - \begin{vmatrix} \zeta' \\ \eta' \\ \theta' \end{vmatrix} \qquad (31)$$

where

$$\zeta' = u_{11} x' + u_{12} y' + u_{13} z'$$

$$\eta' = u_{41} x' + u_{42} y' + u_{43} z'$$

$$\theta' = u_{31} x' + u_{32} y' + u_{33} z'$$

After coordinate transformation the integral 29 for the i'th facet changes to the simpler form:

$$I_i = \frac{G\,\rho}{\gamma} \iint_S \frac{1}{2} \; \frac{\theta_i \, d\,\zeta \, d\,\eta}{[\,\zeta^2 + \eta^2 + \theta^2{}_i\,]^{\frac{1}{2}}} \qquad (32)$$

In order to solve this surface integral for the i'th face, we change it to a line integral over the sides of the polygonal facet via Stokes' theorem.

$$I_i = \frac{G\,\rho}{\gamma}\oint \frac{\theta_i}{2}\log_e\left[\zeta + \sqrt{\zeta^2 + \eta^2 + \theta_i^2}\,\right] d\eta \qquad (33)$$

where the integration is counter clockwise (when looking into the body) around the line segments bounding the i'th face of the polyhedron. It must be a closed contour.

Each side of the facet is a line segment with an equation

$$\zeta = m_j\eta + \zeta_j^o \qquad (34)$$

where m_j is the slope of the j'th line segment

$$m_j = \frac{\zeta_{j+i} - \zeta_j}{\eta_{j+i} - \eta_j}.$$

and also $\zeta_j^o = \zeta_j - m_j\,\eta_j$

Thus the total integral for the i'th facet is a sum of line integrals over all of the bounding line segments.

$$I_i = \sum_j L^i_j \qquad (35)$$

and

$$L^i_j = \frac{G\,\rho}{\gamma}\int_{\eta_j}^{\eta_{j+1}} \frac{\theta_i}{2}\log_e\left[(m_j\eta + \zeta_j^o) + \sqrt{(m_j\eta + \zeta_j^o)^2 + \eta^2 + \theta_i^2}\,\right] d\eta \qquad (36)$$

and L_j^i is the line integral for the j'th line segment of the i'th facet of the polyhedron.

This assumes that m_j is finite, if it is not then $d\eta$ is zero and consequently so is L_j^i. Also if θ_i is zero, then I_i is zero. After integration of equation

36 and summation over all line segments of all facets, the final result is obtained. (See appendix).

$$\begin{aligned} N = \frac{G\,\rho}{\gamma} \sum_{i} \frac{\theta_i}{2} \sum_{j} \Bigg\{ & \eta \log_e \Big[(m_j \eta + \zeta_j^\circ) + \sqrt{(m_j \eta + \zeta_j^\circ)^2 + \eta^2 + \theta_i^2} \Big] + \frac{\zeta_j^\circ}{\sqrt{1+m_j{}^2}} \log_e \Big[\sqrt{(m_j \eta + \zeta_j^\circ)^2 + \eta^2 + \theta_i^2} \\ & + \eta \sqrt{1 + m_j{}^2} + \frac{m_j \zeta_j^\circ}{\sqrt{1+m_j{}^2}} \Big] + \theta_i \operatorname{Tan}^{-1} \left[\frac{(m_j \theta_i^2 - \zeta_j^\circ \eta)}{\theta_i \sqrt{(m_j \eta + \zeta_j^\circ)^2 + \eta^2\, \theta_i^2}} \right] \Bigg\} \Bigg|_{\eta_j}^{\eta_{j+1}} \end{aligned} \tag{37}$$

This expression then, in conjunction with the coordinate transformation of equation 31, when evaluated, gives the geoid anomaly over an arbitrary polyhedron. As a practical matter, it is difficult to specify the coordinates of the body in the orderly manner required. To simplify matters all faces could be triangles and the body would be assembled in the manner described by Barnett (1976). Also it should be noted that both the two dimensional and three dimensional solutions to geoid anomaly modeling are exact analytic expressions. This is in contrast to the asymptotic expansion technique for geoid anomaly modeling developed by Ockendon and Turcotte (1977), which although easier to evaluate requires the body to be very thin. In many studies of geoid anomalies it will be necessary to compute the resultant anomaly on a spherical earth. The three dimensional method developed here can be utilized for that purpose, as long as it is realized that the connecting segments between points on the polygon are linear. An alternative approach would be to utilize the method developed by Johnson and Litehiser (1972), they give an expression for the potential due to a body on a spherical earth.

Their method in combination with Brun's formula would be a good numerical solution to geoid modeling on a spherical earth. Another numerical technique for computing geoid anomalies was developed and applied in a study by Bowin (1975).

As a geophysical example, this three dimensional modeling technique is utilized to study a geoid anomaly which has been observed above the Truk islands (part of the Caroline islands in the western Pacific). This geoid anomaly is 5 meters in amplitude and is above a seamount which is 4 km high . Quite simply this geoid high can be explained as due to the excess mass of the seamount itself, and the deficit mass of its compensating body. To model this anomaly the topography was digitized and a polyhedral body was constructed, in addition a polyhedral compensating mass was calculated. An Airy type crust with a compensation depth of 30 km was utilized. In Figure 8 a cross section of this model is depicted, along with both the calculated and observed geoid anomaly. From the good agreement of the two, it can be said that this geoid anomaly is explained by an isostatic model of this seamount.

Techniques in the Frequency Domain

A better understanding of the geoid can be learned in the frequency domain, this is done by examining the relationship between the Fourier transform of gravity and the Fourier transform of the geoid. In other words, what is the transfer function between gravity and the geoid? Our derivation is analagous to the derivation of formula 21, but is done in the frequency domain.

Given the vertical component of gravity due to a two dimensional body we go to the frequency domain via the Fourier transform.

$$\mathcal{F}(F_g^V) = \int_{-\infty}^{+\infty} F_g^V(y)\, e^{-iky}\, dy$$

To obtain the Fourier transform of the horizontal component of gravity we Hilbert transform $\mathcal{F}(F_g^V)$

$$\mathcal{F}(F_g^H) = \mathcal{F}(F_g^V) \cdot i \operatorname{sgn}(k)$$

where multiplication by i sgn (k) is the Hilbert transformation (Papoulis, 1962)

also $\operatorname{sgn}(k) = +1 \quad K > 0$ and $i = \sqrt{-1}$

$-1 \quad K < 0$

This procedure can be verified by comparing the Fourier transforms of the vertical and horizontal components of gravity due to an infinite mass line. After division by normal gravity we get the Fourier transform of the deflection of the vertical.

$$\mathcal{F}(\delta) = \frac{\mathcal{F}(F_g^H)}{\gamma} = \frac{\mathcal{F}(F_g^V) \cdot i \operatorname{sgn}(k)}{\gamma}$$

Utilizing the integration theorem in the frequency domain the Fourier transform of the geoid is obtained, this is because the geoid is the integral of deflection of the vertical.

$$\mathcal{F}(N) = \mathcal{F}(F_g^{\,v}) \cdot \frac{i\ \mathrm{sgn}\ (k)}{i\ \gamma\ k}$$

or

$$\mathcal{F}[N(y)] = \frac{1}{\gamma\ |k_y|}\ \mathcal{F}[F_g^{\,v}\ (y)]$$

Thus given the Fourier transform of gravity we multiply by a transfer function $S(k_y)$ to obtain the Fourier transform of the geoid. For the two dimensional case:

$$S(k_y) = \frac{1}{\gamma\ |k_y|}$$

This transfer function shows that a geoid anomaly over a body will have the same phase spectra as the gravity anomaly. In simpler words this is our previous observation, they have the same shape. However the geoid anomaly for a given wavelength is changed in amplitude by the factor $(1/|k_y|)$. Thus for long wavelengths $(k_y \ll 1)$ the geoid anomaly will be magnified, while at short wavelengths $(k_y \gg 1)$ diminished. This is our observation that geoid anomalies are "wider".

Conclusions

In this paper we have been concerned with developing the techniques necessary for the interpretation of geoid anomalies. These are mathemetical formulas which for a given geological model can be utilized to compute the resultant geoid anomaly. If the model is considered two dimensional then densities for a polygon in two dimensions are specified and using formulas 24 and 25 the geoid heights are calculated. In this method only the relative heights are important. Any geologic body can be modeled with a polyhedron shape in three dimensions. After specifying densities for this, formula 37 is utilized to calculate the resultant geoid anomaly. To understand geoid anomalies, it is seen that they basically have the same shape as gravity anomalies, but with the long wavelength components amplified. Techniques such as these are only tools, their real importance is in enabling the interpretation of observed geoid anomalies, such as are detected by GEOS-3.

APPENDIX

A) Finite Vertical Sheet

$$N = \frac{G\sigma}{\gamma} \int_{z_1}^{z_2} \left[\log_e (x-x') + \sqrt{(x-x')^2 + (y-y')^2 + (z-z')^2}\,\right] \Bigg|_{x_1}^{x_2} dz$$

This integral is of the form

$$\log_e \left(a + \sqrt{B^2 + x^2}\,\right)dx$$

letting $u^2 = B^2 + x^2$, restricting $u > o$ and integrating by parts we obtain

$$= \sqrt{u^2 - B^2}\ \log_e (a + u) - \int \frac{\sqrt{u^2 - B^2}}{a + u}\ du$$

and after integrating again

$$= \sqrt{u^2 - B^2}\ \log_e (a + u) - \sqrt{u^2 - B^2}$$

$$+ a \log_e \left(\sqrt{u^2 - B^2} + u\right) + \frac{(b^2 - a^2)}{\sqrt{b^2 - a^2}} \text{Sin}^{-1} \left[\frac{-1\ (b^2 + au)}{|a + u|\ |b|}\right]$$

or finally

$$\int \log_e \left(a + \sqrt{B^2 + x^2}\right) dx = x \log_e \left(a + \sqrt{b^2 + x^2}\right) - x$$

$$+ a \log_e \left(x + \sqrt{b^2 + x^2}\right) +$$

$$\sqrt{b^2 - a^2}\ \text{Sin}^{-1} \left[\frac{-1\ \left(b^2 + a\sqrt{b^2 + x^2}\right)}{\left|\left(a + \sqrt{b^2 + x^2}\right)\right|\ |B|}\right]$$

restricting $x > o$

B) Two dimensional rectangle

$$N = -\frac{G\sigma}{\gamma} \int_{z_1}^{z_2} \Bigg\{ (y - y') \log_e \left[(y - y')^2 + (z - z')^2\right] - 2y$$

$$+ 2\,|z - z'|\ \text{Tan}^{-1} \left[\frac{(y - y')}{(z - z')}\right] \Bigg\} \Bigg|_{y_1}^{y_2} dz$$

restricting $(z - z') > o$ (this is the same integral as used for the two dimensional sheet) and integrating

$$N = -\frac{G\,\sigma}{\gamma}\left\{ (y-y') \left[(z-z')\log_e\left[(y-y')^2 + (z-z')^2\right] - 2z + 2\left|y-y'\right| \operatorname{Tan}^{-1}\frac{(z-z')}{\left|y-y'\right|}\right] - 2\,y\,z + \int_{z_1}^{z_2} 2\,(z-z')\operatorname{Tan}^{-1}\frac{(y-y')}{(z-z')}\,dz \right\}\Bigg|_{y_1}^{y_2}$$

This last integral is of the form

$$\int z \operatorname{Tan}^{-1}\frac{a}{z}\,dz$$

Letting $w = \frac{a}{z}$ then integrating by parts we find

$$\int \frac{1}{w^3}\operatorname{Tan}^{-1} w\,dw = -\frac{1}{2}\left\{\left(1 + \frac{1}{w^2}\right)\operatorname{Tan}^{-1}(w) + \frac{1}{w}\right\}$$

so finally

$$N = -\frac{G\,\sigma}{\gamma}\left\{ (y-y') \left[(z-z')\log_e\left[(y-y')^2 + (z-z')^2\right] - 2z + 2\left|y-y'\right| \operatorname{Tan}^{-1}\frac{(z-z')}{\left|y-y'\right|}\right] - 2\,y\,z + \left[(z-z')^2 + (y-y')^2\right]\operatorname{Tan}^{-1}\frac{(y-y')}{(z-z')} + (z-z')\,(y-y')\right\}\Bigg|_{y_1}^{y_2}\Bigg|_{z_1}^{z_2}$$

C) Two dimensional polygon

For the ith side of the polygon we have

$$n_i = \int\left\{(y-y')\log_e\left[(y-y')^2 + (z-z')^2\right] - 2y + 2\,(z-z')\operatorname{Tan}^{-1}\frac{(y-y')}{(z-z')}\right\}dz$$

and we integrate along a linear line segment defined by $z = m_i\,y + b_i$ assuming m_i and $1/m_i$ are not zero we obtain

$$n_i = \int_{z_{i-1}}^{z_i} \Bigg\{ [(z-B_i)/m_i - y'] \log_e \left[\left(\frac{z-B_i}{m_i} - y' \right)^2 + (z-z')^2 \right]$$

$$-2\left(\frac{z-B_i}{m_i} - y' \right) + 2\,(z-z')\,\mathrm{Tan}^{-1}\left[\frac{\left(\frac{z-B_i}{m_i} - y' \right)}{(z-z')} \right] \Bigg\} dz$$

where $m_i = \dfrac{z_i - z_{i-1}}{y_i - y_{i-1}}$

$B_i = z_i - m_i\, y_i$

First part of the integral is of the form $\int x \log_e (a+bx+cx^2)\, dx$ and is a standard integral. Third part of the integral is of the form $\int x\, \mathrm{Tan}^{-1} [(Cx + D)/x]\, dx$. Letting $u = (Cx + D)/x$ and integrating by parts, this becomes

$$-\frac{D^2}{2} \left[-\frac{\mathrm{Tan}^{-1} u}{(u-c)^2} + \int \frac{du}{(u-c)^2\,(1+u^2)} \right]$$

After the final integration we find for the third part

$$\int x\, \mathrm{Tan}^{-1} [(Cx+D)/x] = \frac{1}{2} \Bigg\{ x^2\, \mathrm{Tan}^{-1} [(Cx+D)/x]$$

$$- \frac{C\,D^2}{(1+C^2)^2} \log_e \left[\frac{(1+C^2)\,x^2 + 2CDx + D^2}{D^2} \right]$$

$$+ \frac{D\,x}{(1+C^2)} + \frac{(1-C^2)\,D^2}{(1+C^2)^2} \mathrm{Tan}^{-1} [(Cx+D)/x] \Bigg\}$$

Thus formula 23 can be integrated to obtain formula (24).

In evaluating the line integral the following special cases are also important.

Case (a). If $m_i = 0$, then dz is zero and consequently n_i is also zero.

Case (b). If $1/m_i = 0$ then y is constant along the line segment and the line integral (23) is written as:

$$n_i = -\frac{G\lambda}{\gamma}\int_{Z_{i-1}}^{Z_i}\left\{(y_i-y')\log_e[(y_i-y')^2+(z-z')^2] -2(y_i-y')+2(z-z')\,\mathrm{Tan}^{-1}\frac{(y_i-y')}{(z-z')}\right\}dz$$

This is identical in form to the integral for the two dimensional rectangle and is solved in an identical fashion.

Case (c). If the extension of the line segment passes through the observation point (when $B_i/m_i + y' = 0$) then the line integral (23) is written as

$$n_i = -\frac{G\lambda}{\gamma}\int_{Z_{i-1}}^{Z_i}\left\{\frac{Z}{m_i}\log_e[(1+1/m_i^2)\,z^2] - 2\,z/m_i + 2\,Z\,\mathrm{Tan}^{-1}(1/m_i)\right\}dz$$

$$\text{assuming } Z' = 0,\ Z > 0$$

This is easily integrated to become equation (27).

Case (d). Three dimensional polyhedron. For the j'th line segment of the i'th facet we have, after integrating equation 36 by parts and rearranging

$$L_j^i = \frac{G\rho\theta_i}{2\gamma}\left\{\eta\log_e\left[(m_j\eta+\zeta_j^\circ)+\sqrt{(m_j\eta+\zeta_j^\circ)^2+\eta^2+\theta_i^2}\right]\Bigg|_{\eta_j}^{\eta_{j+1}} - \int_{\eta_i}^{\eta_{j+1}}\frac{\eta^2\,d\eta}{\eta^2+\theta^2} + \int_{\eta_i}^{\eta_{j+1}}\frac{\zeta_j^\circ\,d\eta}{\sqrt{(m_j\eta+\zeta_j^\circ)^2+\eta^2+\theta_i^2}}\right.$$

$$- \int_{\eta_i}^{\eta_{i+1}} \frac{(m_j\theta_i^2\eta + \zeta_j^\circ\theta_i^2)\ d\eta}{(\eta^2+\theta_i^2)\sqrt{(m_j\eta+\zeta_j^\circ)^2 + \eta^2+\theta_i^2}} \Bigg\}$$

The first integral is independent of the path of integration, thus when L_j^i is summed over all line segments for a closed path this integral will sum to zero. Consequently, we ignore this term. The second integral is in a standard form. To solve the third integral the substitution is made.

$$\eta = \frac{m_j^2\ \theta_i^2 - \zeta_j^{\circ 2}\ \chi}{(m_j\ \zeta_j^\circ)\ (\chi+1)}$$

This will transform the last integral into

$$\sqrt{m_j^2\theta_i^2+\zeta_j^{\circ 2}}\ \ m_j^2\theta_i^2\zeta_j^\circ \int \frac{d\chi}{(\zeta_j^{\circ 2}\chi^2 + m_j^2\theta_i^2)\ \sqrt{\zeta_j^{\circ 2}\chi^2 + m_j^2\theta_i^2 + m_j^2\ (m_j^2\theta_i^2 + \zeta_j^{\circ 2})}}$$

which is a standard form and can be integrated. This same integral (36) has also been solved for gravity problems by Barnett (1976) and Paul (1974).

References

Barnett, C.T., 1976. Theoretical modeling of the magnetic and gravitational fields of an arbitrary shaped three-dimensional body, Geophysics, 41, 1353-1364.

Bowin, C., 1975. Catalogue of geoidal variations for simple seafloor topographic features, Woods Hole Oceanographic Institution Tech. Report,. WHOI-75-14.

Coggon, J.H., 1976. Magnetic and gravity anomalies of polyhedron, Geoexploration, 14, 93-105.

Heiskanen, W.A. and H. Moritz, 1967. Physical Geodesy, W.H. Freeman & Co., San Francisco.

Johnson, L.R. and J.J. Litehiser, 1972. A method for computing the gravitational attraction of three-dimensional bodies in a spherical or ellipsoidal earth, J. Geophys. Res., 77, 6999-7009.

Ockendon, J.R. and D.L. Turcotte, 1977. On the gravitational potential and field anomalies due to thin mass layers, Geophys. J. R. astr. Soc., 48, 479-492.

Papoulis, A., 1962. The Fourier integral and its applications, McGraw-Hill Book Co., New York.

Paul, M.K., 1974. The gravity effect of a homogeneous polyhedron for three-dimensional interpretation, Pure and Appl. Geophys., 112, 553-561.

Talwani, M., J. Worzel and M. Landisman, 1959. Rapid gravity computations for two-dimensional bodies with application to the Mendocino submarine fracture zone, J. Geophys. Res., 64, 49-59.

Talwani, M., H. Poppe and P.D. Rabinowitz, 1972. Gravimetrically determined geoid in the western North Atlantic, in "Sea surface topography from space", NOAA technical report, ERL-228-AOML. 7-2, 2, 1-34.

FIGURE CAPTIONS

Figure 1. Calculation of geoid anomaly over a finite horizontal line and its resultant geoid height.

Figure 2. Calculation of geoid anomaly over a vertical sheet. Resultant geoid heights for the three dimensional (finite) and two dimensional (infinite) vertical sheet are plotted.

Figure 3. Calculation of geoid anomaly over an infinite horizontal line. In B the horizontal attraction of gravity in F_g^h, the vertical attraction due to the line is F_g^v. Acceleration due to the earth is g, and deflection of the vertical is d.

Figure 4. Calculation of geoid anomaly over a two dimensional rectangle. Note that the geoid anomaly is never flat, rather it is always curving.

Figure 5. Calculation of geoid anomaly over a two dimensional polygon. Integration proceeds in a clockwise fashion when looking in the positive $\hat{x}$ direction. Integral is computed by evaluating formula 24 for the i'th line segment and summation over all segments with formula 25. Note the rapid decrease in gravity compared to the slow decay in the geoid anomaly.

Figure 6. Geoid anomaly across Nova Scotia margin, left end of GEOS-3 profile is at 44.5°N, 63.25°W and right end is at 40°N, 58.7°W. A simple crustal model is used which is in Airy isostatic equilibrium. Calculated values of geoid height agree quite well with GEOS-3 observed values.

Figure 7. Calculation of geoid anomaly over a three dimensional polyhedron. For a given facet with a vector normal $\hat{u}_4$, the surface integral is computed by rotation of the facet to a new (ζ, η, θ) coordinate system. Integration is then done as a line integral around each

bordering line segment, it must proceed in a counterclockwise fashion when looking in the $-\hat{\theta}$ direction.

Figure 8. Geoid anomaly over the Truk Islands in the western Pacific. Left end of GEOS-3 profile is at 151.3°E, 6.85°N, right end is at 152.0°E, 8°N. A simple three component model was used with a density of 1.03 gm/cm^3 for water, 2.85 gm/cm^3 for crust, and 3.3 gm/cm^3 for mantle. The body was a polyhedron, a cross section of this body is shown. This model was in Airy isostatic equilibrium with a crustal thickness of 4 km sediment and 6 km basement.

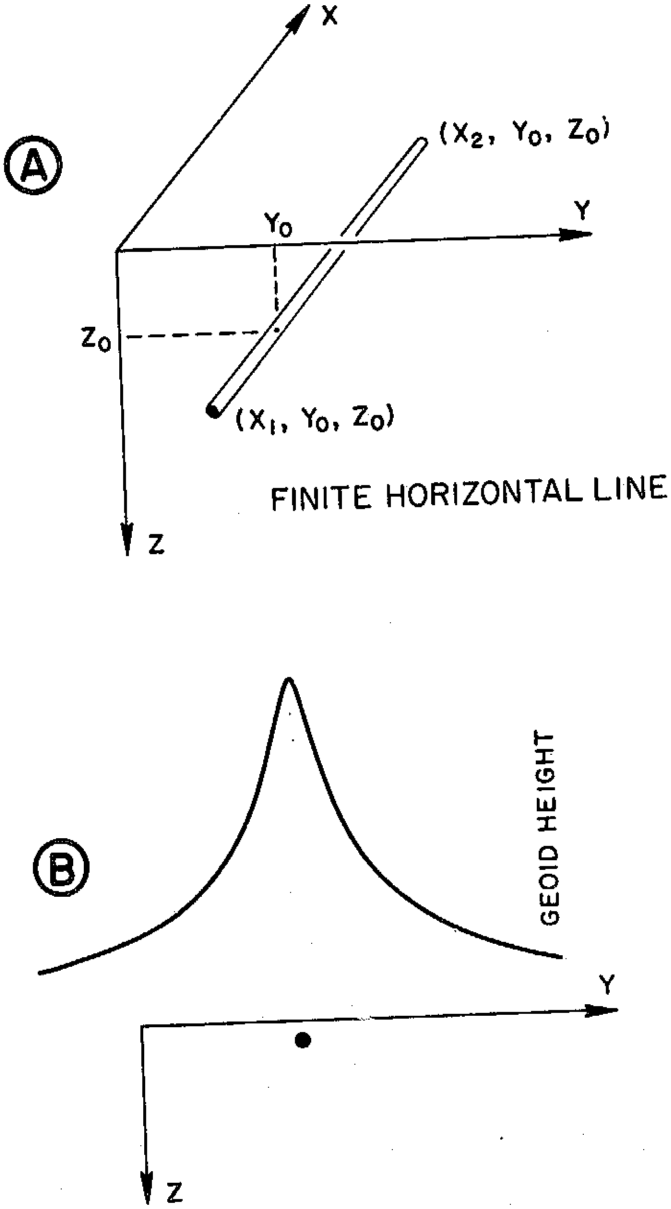
A
X
(X2, Y0, Z0)
Y
Y0
Z0
(X1, Y0, Z0)
FINITE HORIZONTAL LINE
Z
B
GEOID HEIGHT
Y
Z

Figure 1

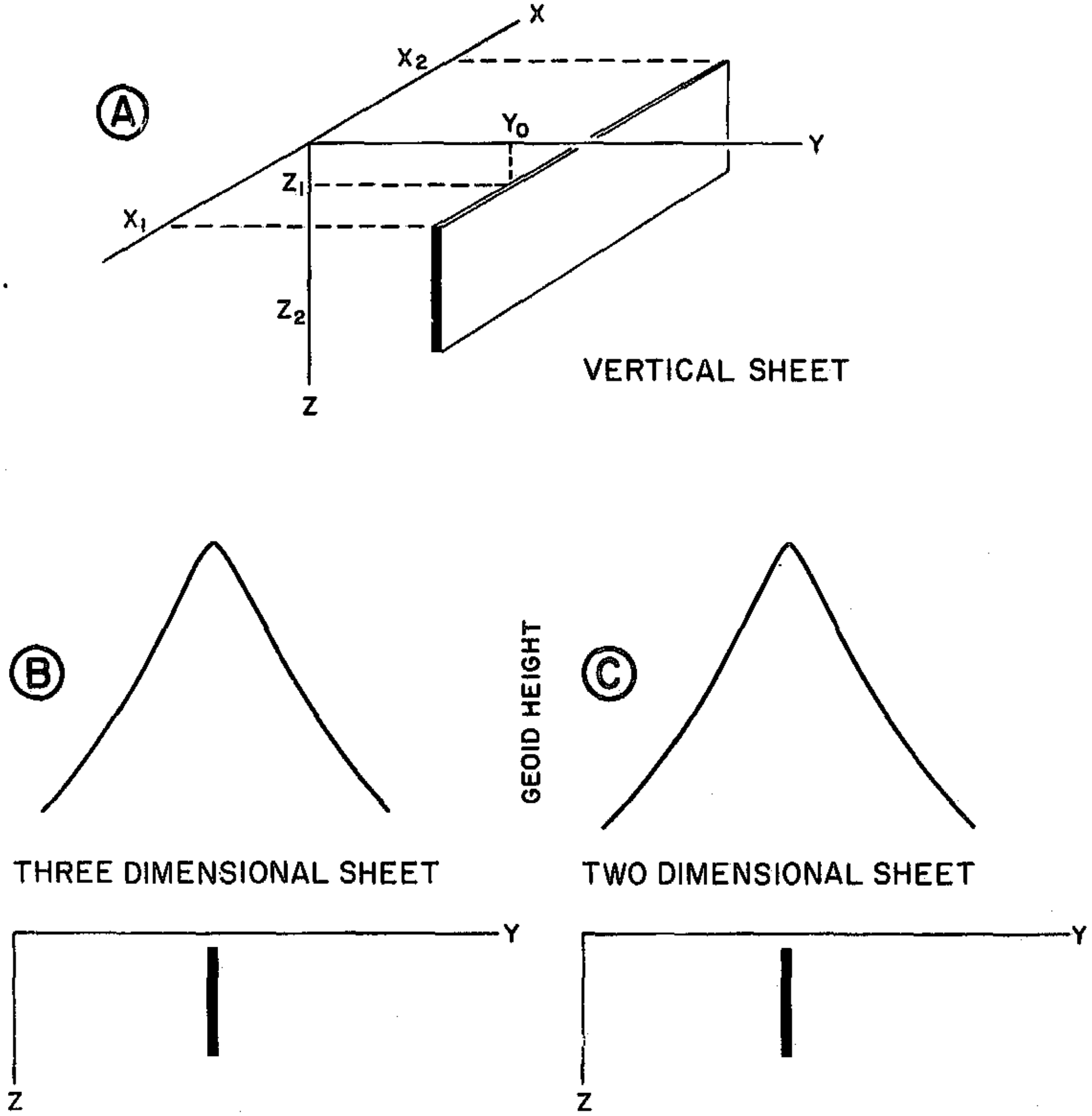
A
X
X_2
Y_0
Y
Z_1
X_1
Z_2
Z
VERTICAL SHEET
B
GEOID HEIGHT
C
THREE DIMENSIONAL SHEET
TWO DIMENSIONAL SHEET
Y
Z
Y
Z

Figure 2

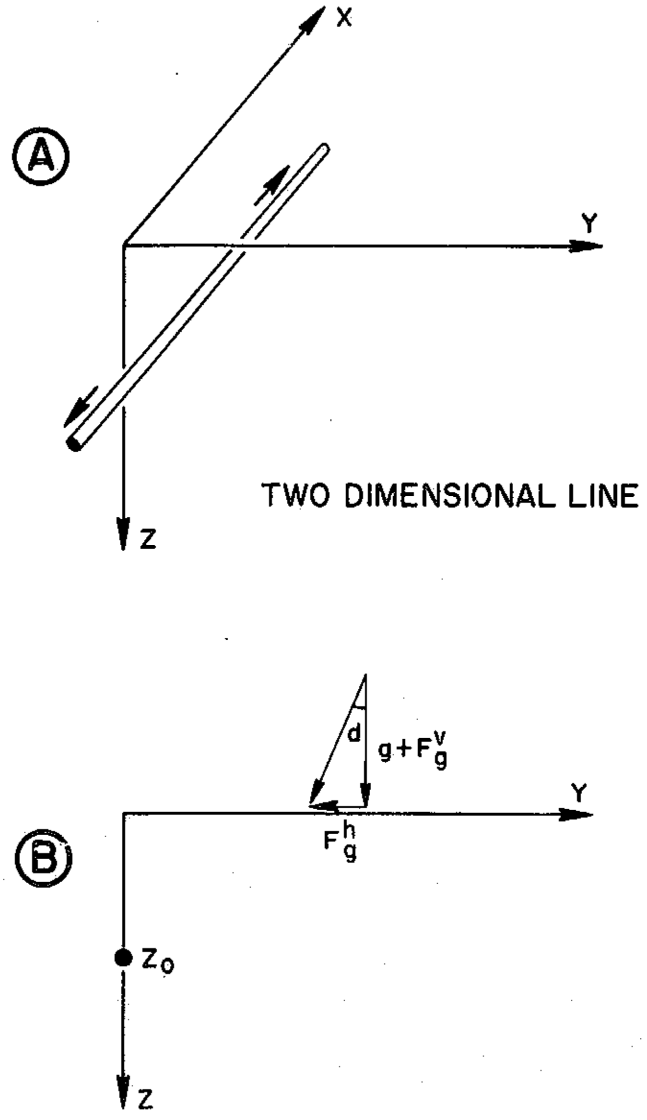

Figure 3

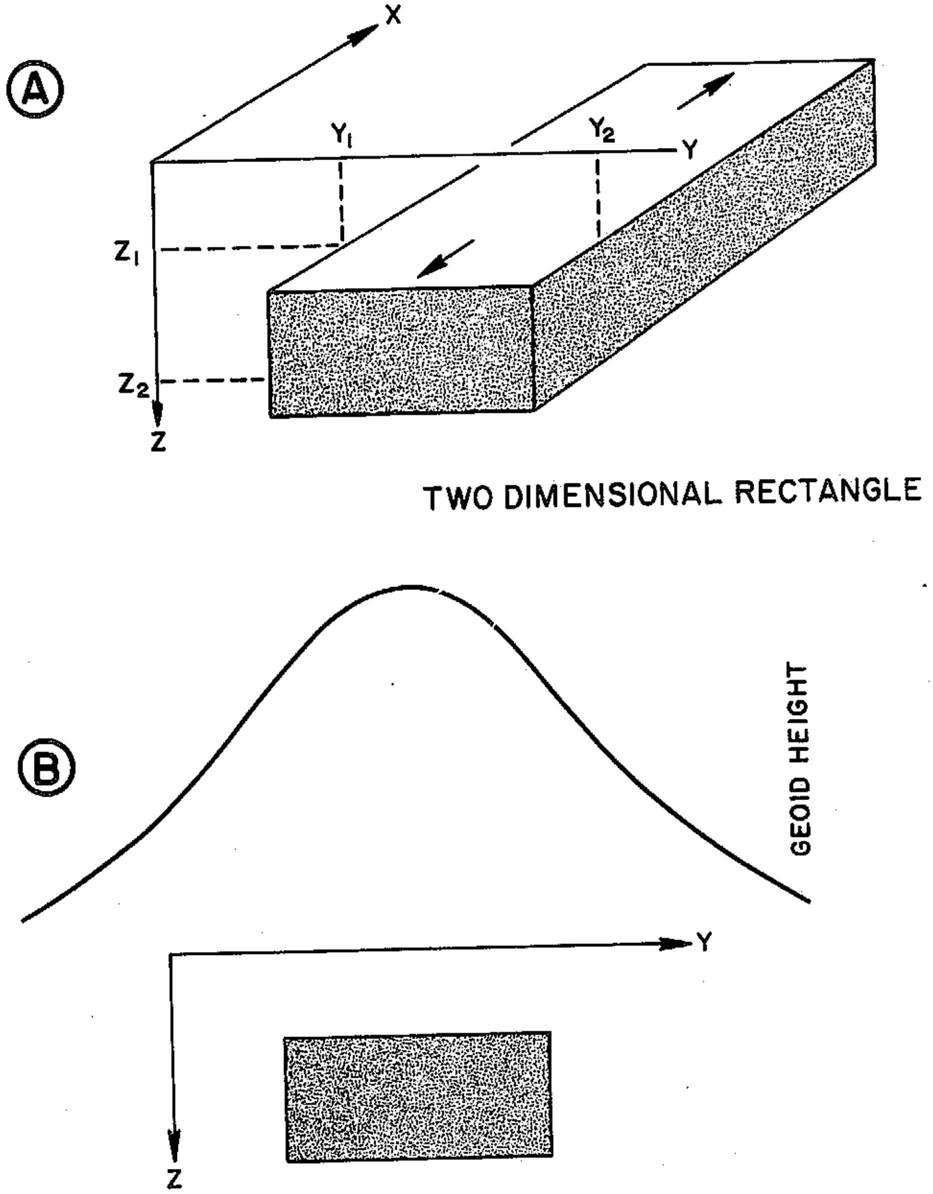

Figure 4

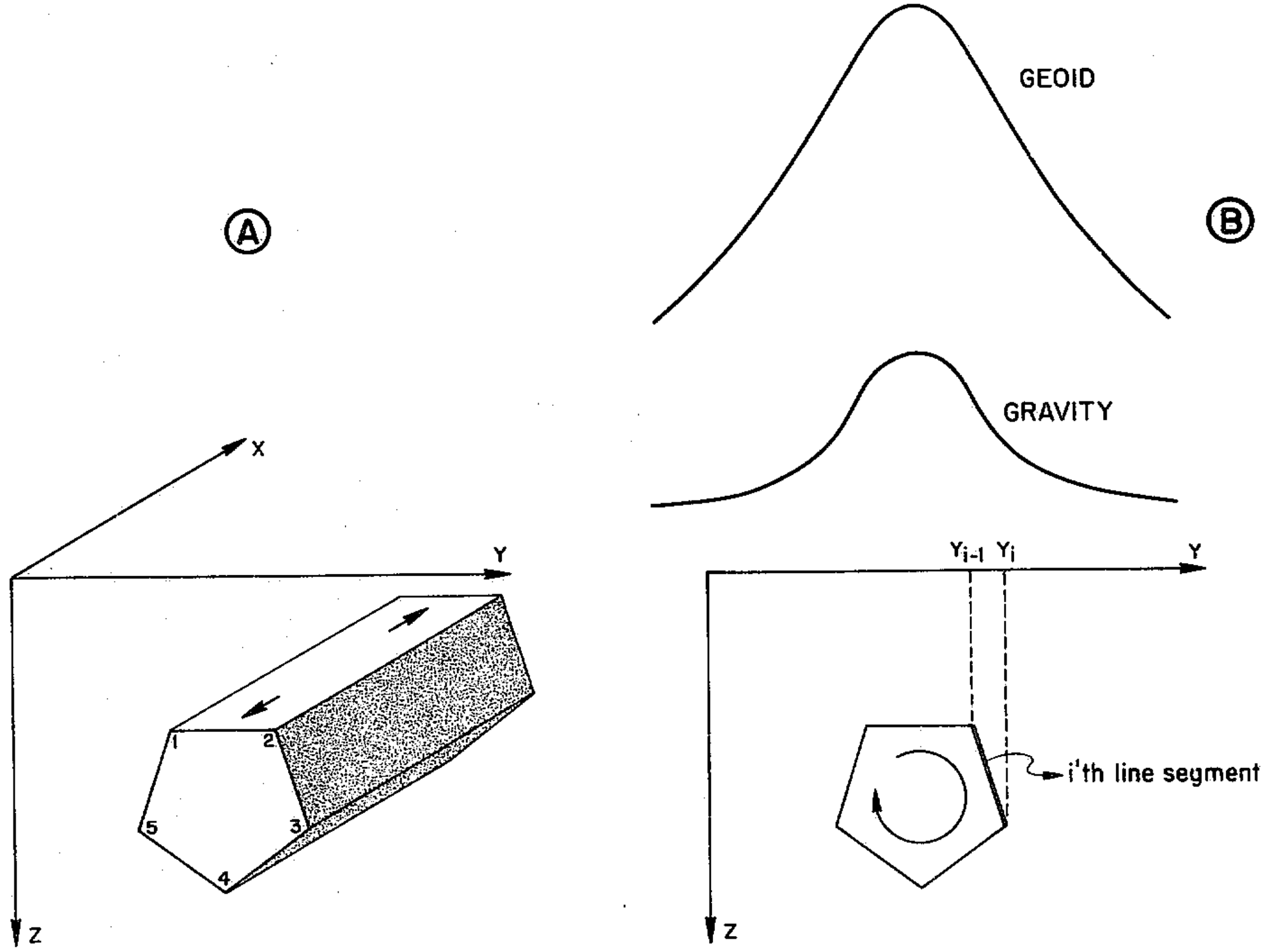

TWO DIMENSIONAL POLYGON

Figure 5

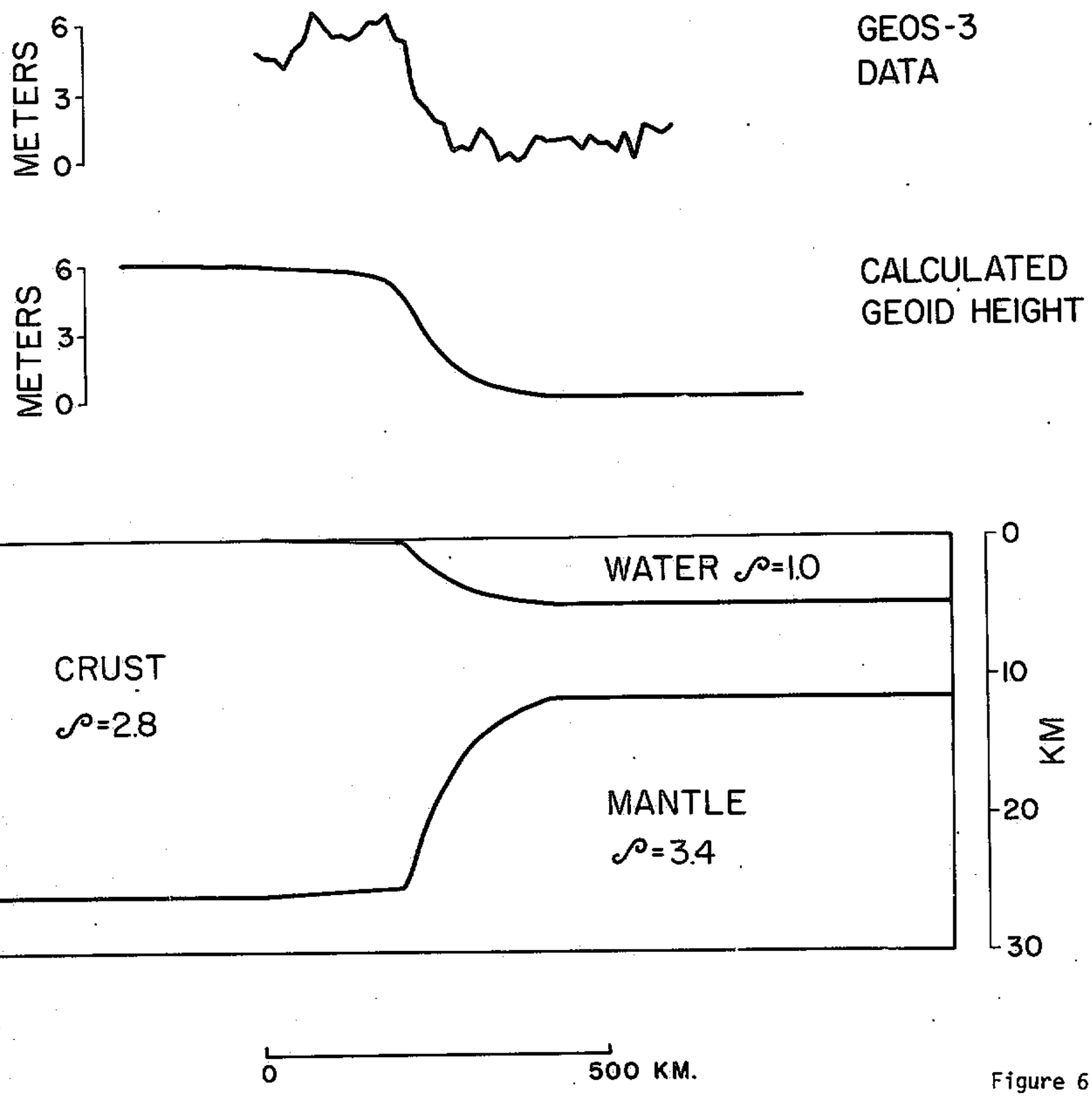
METERS
6
3
0
GEOS-3
DATA
METERS
6
3
0
CALCULATED
GEOID HEIGHT
WATER ρ=1.0
CRUST
ρ=2.8
MANTLE
ρ=3.4
0
10
20
30
KM
0
500 KM.

Figure 6

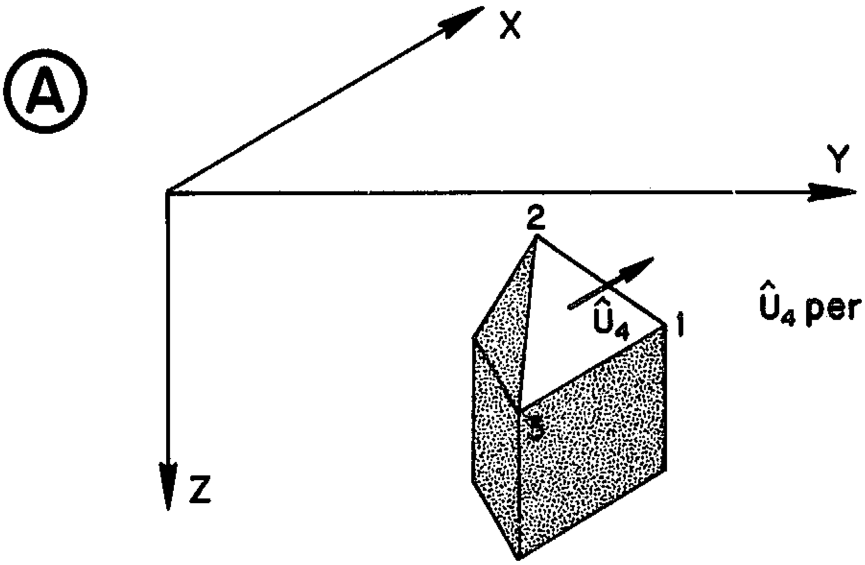

$\hat{U}_4$ perpendicular to facet

THREE DIMENSIONAL POLYHEDRON

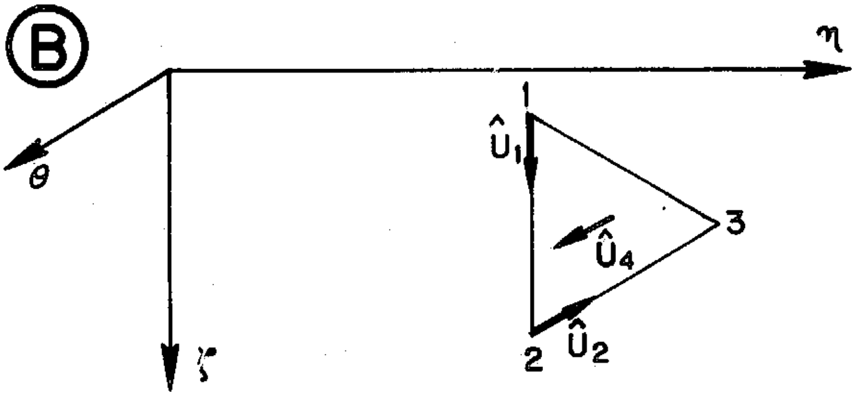

Figure 7

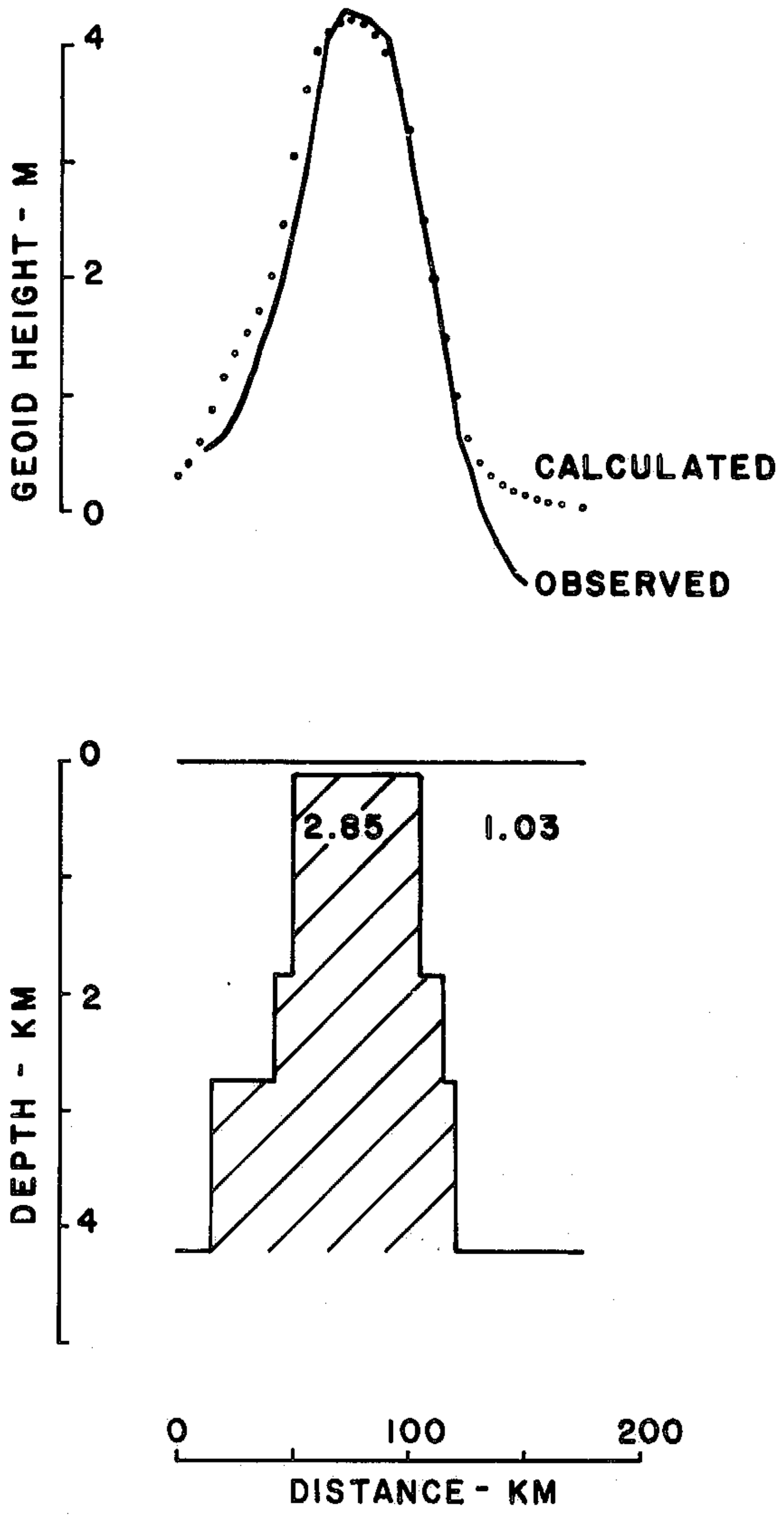
GEOID HEIGHT - M
4
2
0
CALCULATED
OBSERVED
DEPTH - KM
0
2
4
2.85
1.03
0
100
200
DISTANCE - KM

Figure 8

GEOID ANOMALIES OVER OCEANIC STRUCTURES

Radar altimeters mounted on an orbiting spacecraft have substantially enlarged the scope of marine geodesy. As the satellite orbits the Earth radar pulses are emitted, reflected from the sea surface and received by the altimeter (figure 1). These radar range measurements are utilized to obtain the sea surface height which to a very good approximation is the geoid height, the difference being less than 1 meter. After being corrected for a theoretical M-2 ocean tide such measurements are very accurate determinations of geoid height. Given the rapid speed of the satellite and the orbital motion it is possible to map the geoid on an unprecedented scale, in two years the GEOS-3 satellite has made extensive measurements over the world's oceans. This global mapping of the marine geoid has led to a greatly increased knowledge about the Earth's gravitational field over the world's oceans. In this paper we report on the geophysical results from the satellite altimetry program, and examine the future directions for scientific research in marine geodesy.

At the bottom of the ocean floor there are certain types of large structures, seamounts, continental margins, fracture zones, mid-ocean ridges, and deep sea trenches. Over each of these features there are characteristic undulations of the ocean surface; directly related to the density structure, these measured undulations can be utilized to infer the internal densities within the Earth. Using the GEOS-3 radar altimeter we have identified and modeled many of the geoid anomalies over these structures.

On the East Coast of the United States the sea surface has a 6 meter step across the continental margin (figure 2). In places it is quite distinct, as off Nova Scotia, further south the increase is quite gradual. The track over the Nova Scotia margin is modeled with a crustal model in isostatic equilibrium according to Airy isostasy (figure 3). This model quite clearly illustrates the 6 meter step in calculated geoid height, in good agreement with the GEOS-3 data. Other models of isostasy are also possible, the lithosphere can be considered to act as an elastic solid with a certain flexural rigidity and elastic thickness. As sediments are deposited on a continental margin, the crust would deform in such a manner as to keep the elastic lithosphere in mechanical equilibrium (figure 4). Various theoretical geoid profiles have been computed for continental margins, and show the geoid can be used to study the elastic properties of the lithosphere.

Over seamounts there is a geoid anomaly several meters high, 6 meters over Bermuda (figure 2) and 4 meters over the Caroline Islands (figure 5). At the Romanche Fracture Zone the geoid has a step of 4-5 meters (figure 6). In the Bismarck Sea the ocean surface forms a broad high, 450 km wide and 7 meters high (figure 7). This is a small marginal sea several kilometers shallower than the adjacent ocean.

In contrast to the high over the Bismarck Sea, the ocean surface forms deep valleys over oceanic trenches. The Mariana trench has a depression in the geoid of almost 20 m, over the Aleutian trench it is somewhat less shallow, about 13m deep. In the Aleutian profile there can be seen a long wavelength increase in the geoid towards the trench; it is concave downward and increases over the trench axis. Similarly the Java trench has a long wavelength increase in good height increasing towards the trench from the seaward side (figure 8). At this trench the long wavelength anomaly is concave upward. Adjacent to the Philippine Sea there are a number of trenches, a gravimetric geoid in figure 9 shows the depressions in the ocean surface. One of these trenches, the Mariana Island Arc-trench system has a characteristic geoid anomaly (figure 10). As this trench is approached from the Pacific side the geoid increases in height, then there is a 12 meter low directly above the trench axis followed by a continued increase in height over the island arc and Philippine Sea. Across the Philippine trench the geoid has a similar pattern, as the trench is approached from the seaward side the sea surface increases in height 15 meters over a distance of 800 kilometers (figure 11). Over the axis of the Philippine trench there is a 15 meter low which is 200 km wide. At the Bonin trench there is a 10 meter low above the axis and then a 12 meter high over the Bonin islands followed by an 8 meter low above the Bonin trough (figure 12). Utilizing the geoid profiles and gravity, topographic, and seismic data we constructed a cross section model of the Mariana trench region (figure 13). In constructing this model it was found that gravity data is very sensitive to crustal structure and insensitive to mantle densities, while geoid data is primarily sensitive to upper mantle structure. Thus as the depth of compensation was changed from 50 to 200 km the gravity only changed slightly, whereas the computed geoid changed significantly. In summary, these geoid profiles show three general characteristics, a long wavelength increase in height towards the trench, a narrow low over the trench axis of 10-20 meters deep and approximately 200 km wide, and finally a generally high level of the geoid behind the trench.

Mid-ocean ridges, where crustal accretion occurs, have a very broad geoid high. This anomaly is about 7 meters in amplitude and at least 1000 km wide. An example of this anomaly taken from the Southwest Indian ridge is shown in figure 14. The gravity and topography profiles are from a nearby ship track, the geoid data from the GEOS-3 satellite. Although gravity data shows little of a long wavelength anomaly, the geoid has a distinct anomaly centered over the ridge. Presumably this anomaly is the result of density anomalies due to the evolution and creation of the lithosphere at the ridge axis in what is considered to be a symmetric process, both sides of the ridge being created at equal rates. It is expected that the geoid and gravity anomaly would also be symmetric, thus the symmetric part of this anomaly was isolated and considered to be the ridge geoid anomaly over the southwest Indian ridge. Utilizing the thermal model of Sclater and Francheteau densities within the evolving lithosphere were computed and the consequent geoid anomaly calculated. Results of this are in figure 15, the computed geoid agrees very well with the observed anomaly.

Over the Hawaiian ridge there are two distinct anomalies, a broad swell over 1000 km wide and 3-4 meters high, and a narrow anomaly 7 meters high and 300-400 km wide (figure 16). In order to see this more clearly one of the profiles has been filtered with both a high and low pass filter (figure 17). The low pass filter isolates the broad geoid high which is over the Hawaiian swell, with the high pass filter the Hawaiian ridge anomaly is isolated. The narrow Hawaiian ridge anomaly has a distinct high bordered by two adjacent lows, this anomaly is characteristic of behavior of an elastic lithosphere deforming under the weight of the Hawaiian ridge. Modeling the crust in this manner we can obtain a good match to the geoid data (figure 18). With the longer wavelength anomaly, the origin is not yet clear.

With satellite measurements of the geoid short wavelength anomalies have been identified over seamounts, fracture zones, continental margins, the Hawaiian ridge, and the trench axis. Longer wavelength anomalies have been identified over the Bismarck Sea, seaward of trenches and over mid-ocean ridges and over the Hawaiian swell. In general the short wavelength anomalies are caused by inhomogeneous crust and uppermost mantle structure, the longer wavelength anomalies are caused by the mass distribution within the mantle. In studying the interior of the Earth the primary utility of satellite altimeters is in measuring the gravitational field in the wavelength band from approximately 5000 kilometers to 500 kilometers. Longer wavelengths are probably better defined by satellite tracking, shorter wavelengths by gravimetry. The reason for this is the properties of the geoid and gravity field. If a plane Earth were coated with a density layer with a white spectrum and the geoid and gravitational field measured above it, the geoid would have a drastically increasing signal at longer wavelengths (figure 19). Assuming an accuracy of satellite altimetry at 1 meter, and marine gravimetry at 10 mgals the relative utility of the instruments is calculated by adjusting the vertical scale so that 1 meter has the same height as 10 mgals. This shows that satellite altimeters have a better signal to noise ratio than marine gravimeters for wavelengths longer than 628 km, for shorter wavelengths marine gravimeters have better ratios. Obviously at the short wavelengths satellite altimeters still detect signals and are useful, however at these short wavelengths a marine gravimeter will have a better signal to noise ratio.

In considering the types of geoid anomalies which exist and the characteristics of altimeters versus gravimeters the future of satellite altimetry in studying the Earth can be discerned. Satellite altimeters can be used to identify short wavelength anomalies over seamounts, fracture zones and continental margins; however, ship gravimeters are a better instrument to use to study the causative density distribution. Maximum utility of satellite altimetry is in the identification and modeling of medium wavelength geoid anomalies over such features as mid ocean ridges, seaward of trenches, over marginal basins and over the Hawaiian swell. Future geophysical research with satellite altimeters should be concerned with these medium wavelength anomalies, locating, mapping and explaining these undulations of the ocean surface.

FIGURE CAPTIONS

Figure 1. Radar Range Measurement

Figure 2. East Coast of the United States

Figure 3. Nova Scotia Crustal Model in Isostatic Equilibrium According to Airy Isostasy

Figure 4. Geoid Profiles for Continental Margins

Figure 5. Caroline Islands Geoid

Figure 6. Romanche Fracture Zone Geoid

Figure 7. Bismarck Sea Geoid

Figure 8. Java Trench

Figure 9. 1° x 1° Gravimetric Geoid - Philippine Basin

Figure 10. Mariana Island Arc-Trench System

Figure 11. Philippine Island Arc-Trench System

Figure 12. Bonin Island Arc-Trench System

Figure 13. Mariana Island Arc-Trench System

Figure 14. Southwest Indian Ridge

Figure 15. Calculated Geoid - Southwest Indian Ridge

Figure 16. Hawaiian Ridge Geoid

Figure 17. Filtered Hawaiian Ridge Profile

Figure 18. Comparison of Modeled Crust and Geoid Data

Figure 19. Geoid Signal vs. Wavelength

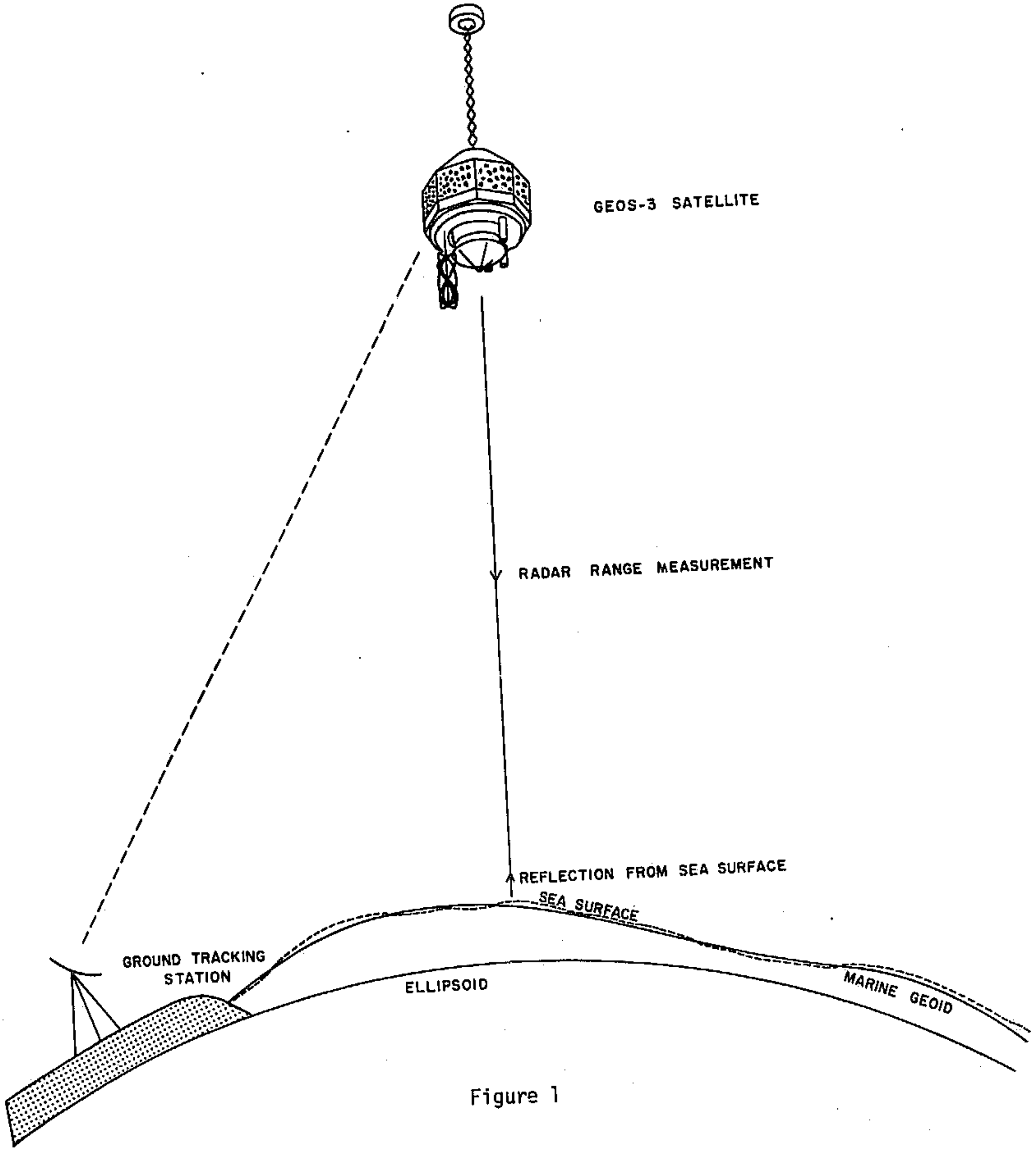

Figure 1

ORIGINAL PAGE IS
OF POOR QUALITY

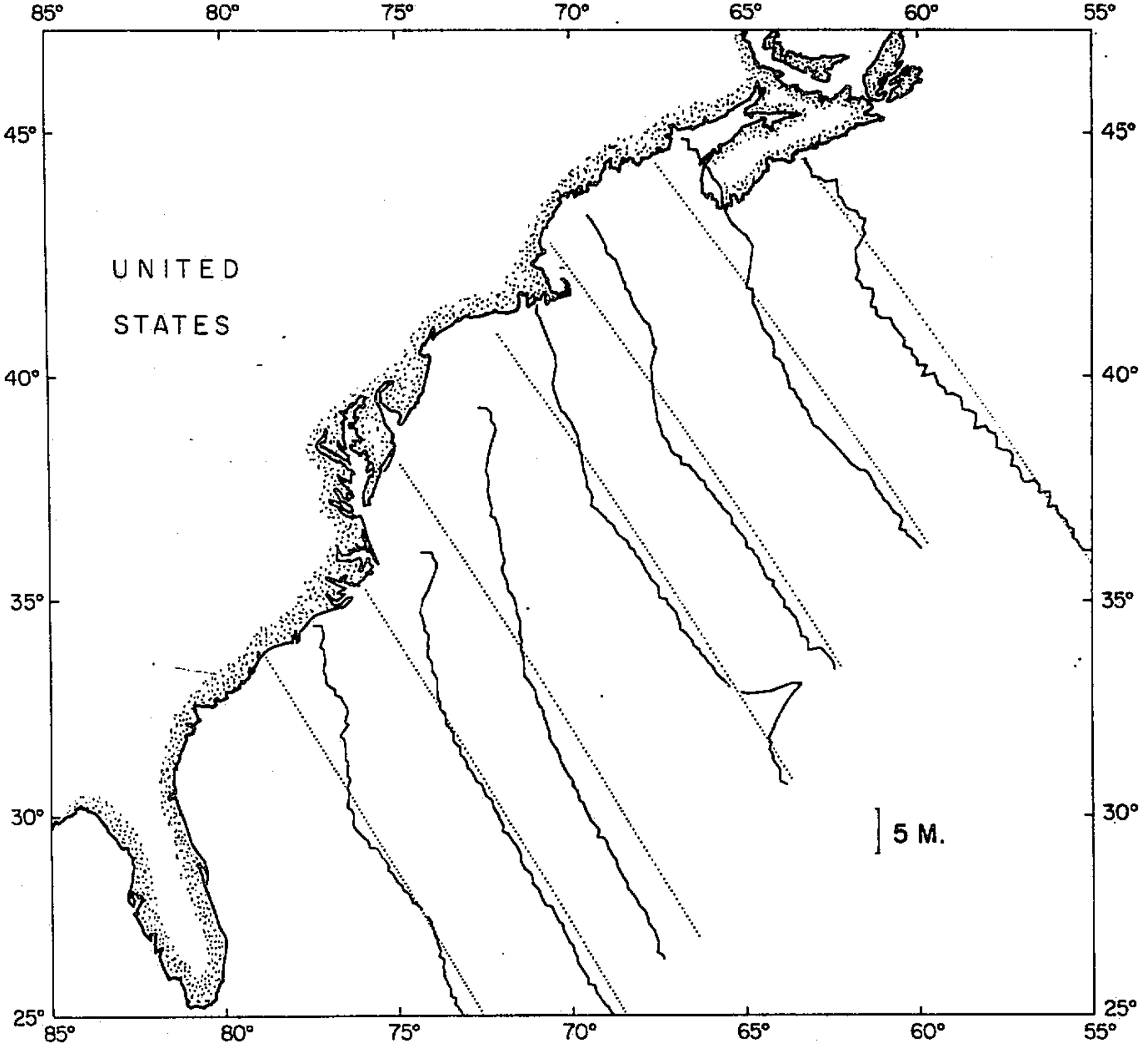

Figure 2

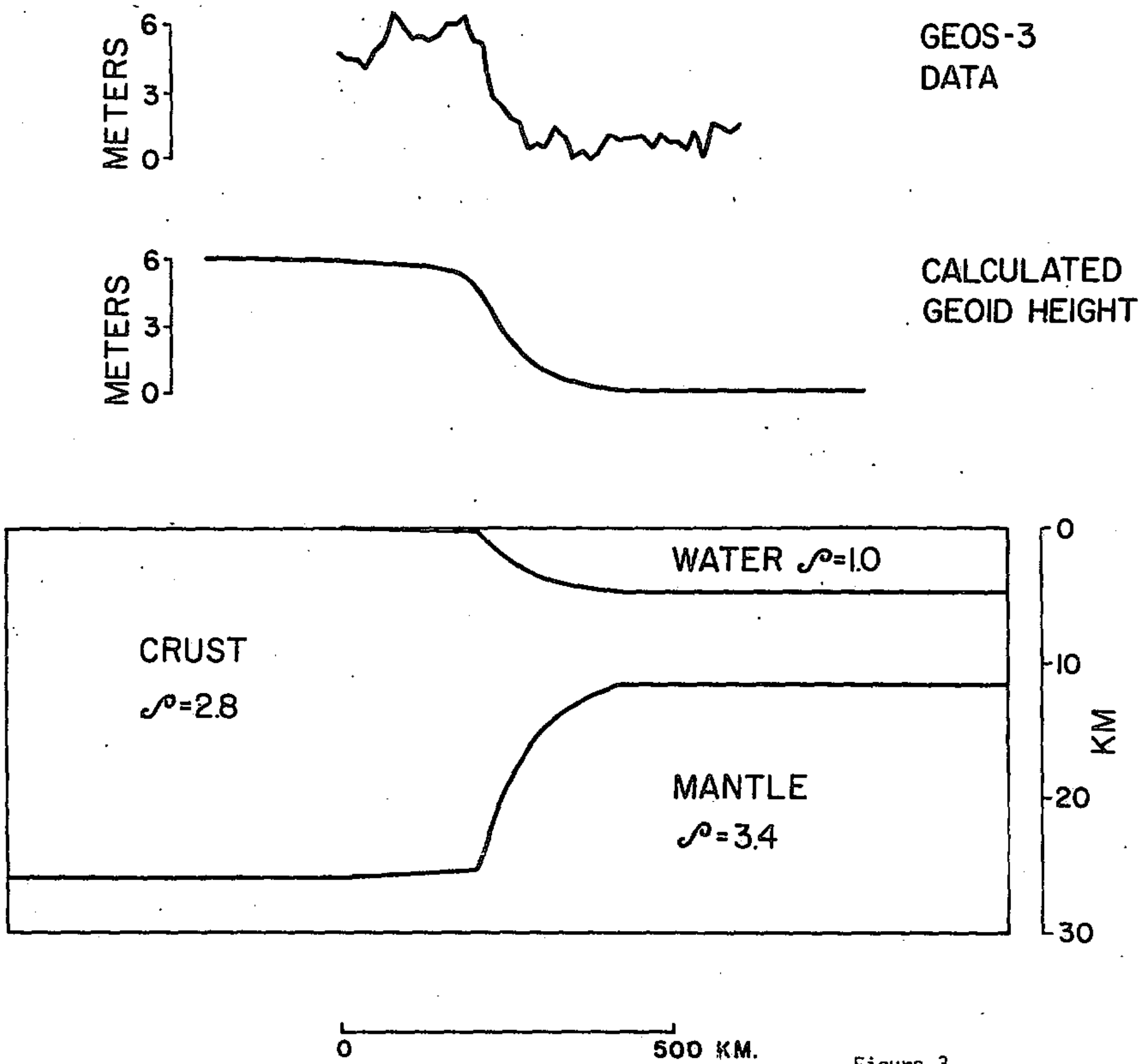
METERS
6
3
0
GEOS-3
DATA
METERS
6
3
0
CALCULATED
GEOID HEIGHT
WATER ρ=1.0
CRUST
ρ=2.8
MANTLE
ρ=3.4
0
10
20
30
KM
0
500 KM.

Figure 3

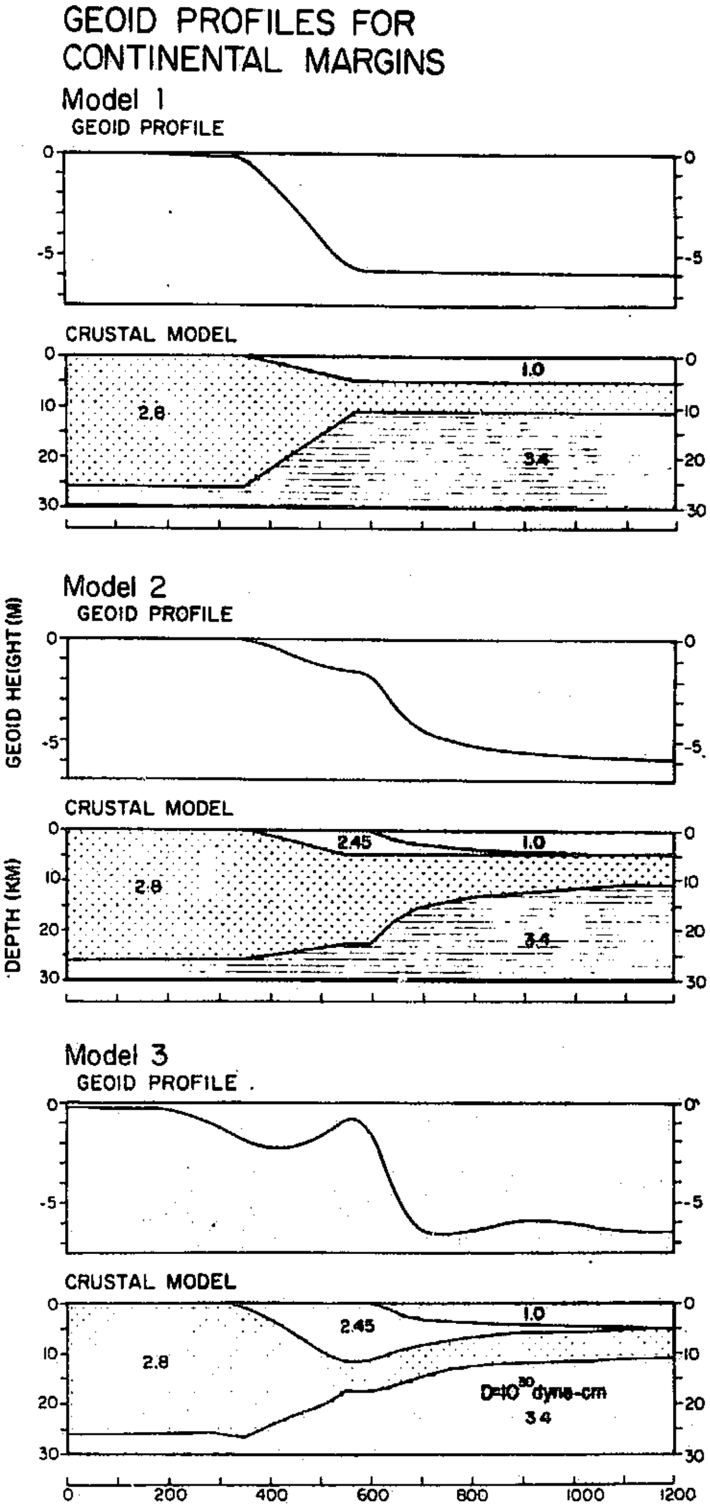
GEOID PROFILES FOR CONTINENTAL MARGINS
Model 1
GEOID PROFILE
0
-5
CRUSTAL MODEL
0
10
20
30
1.0
2.8
3.4
Model 2
GEOID PROFILE
GEOID HEIGHT (M)
DEPTH (KM)
2.45
1.0
2.8
3.4
Model 3
GEOID PROFILE
2.45
1.0
2.8
D=10^30 dyne-cm
3.4
0
200
400
600
800
1000
1200

Figure 4

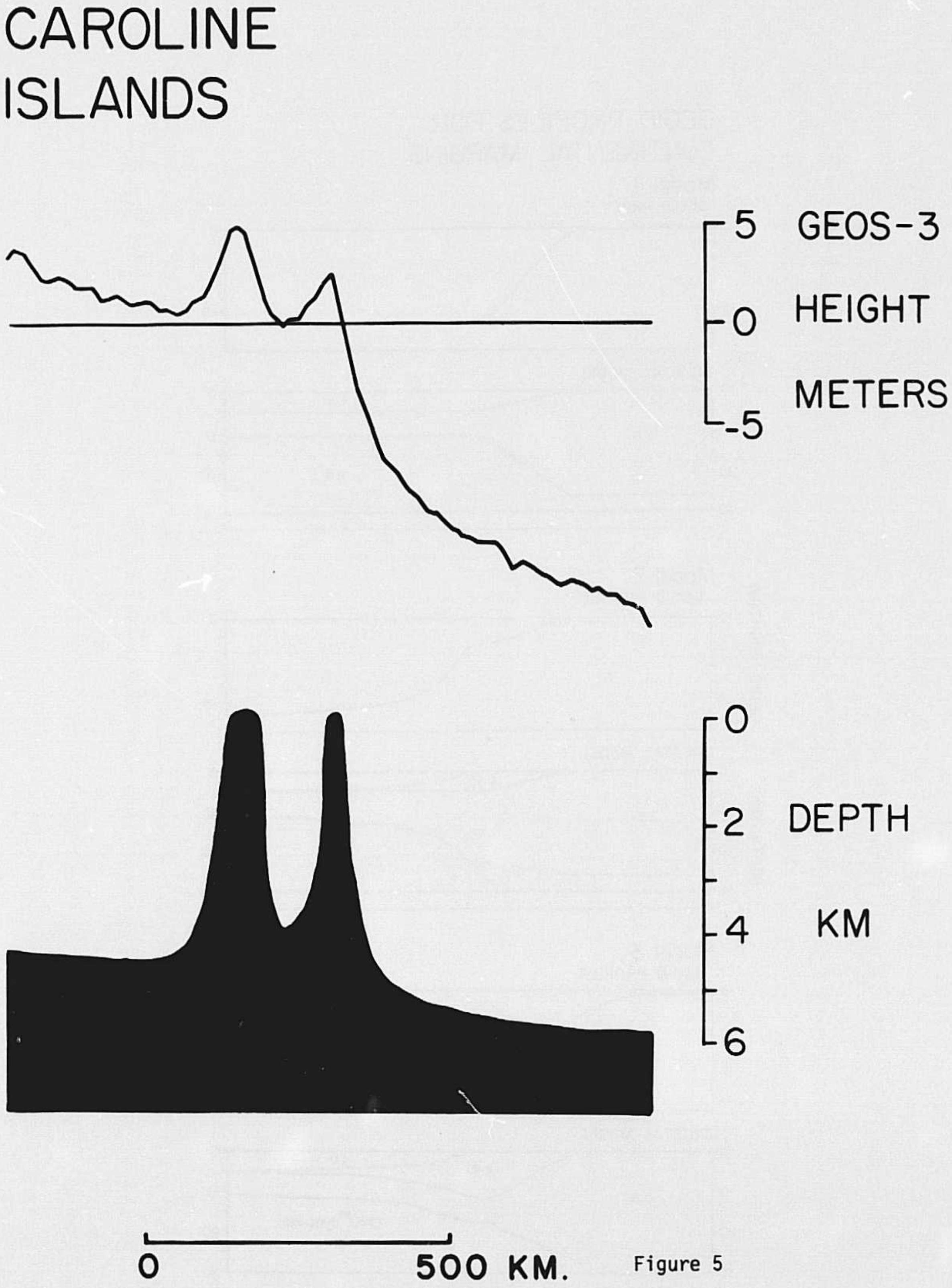
CAROLINE ISLANDS
5
0
-5
GEOS-3
HEIGHT
METERS
0
2
4
6
DEPTH
KM
0
500 KM.

Figure 5

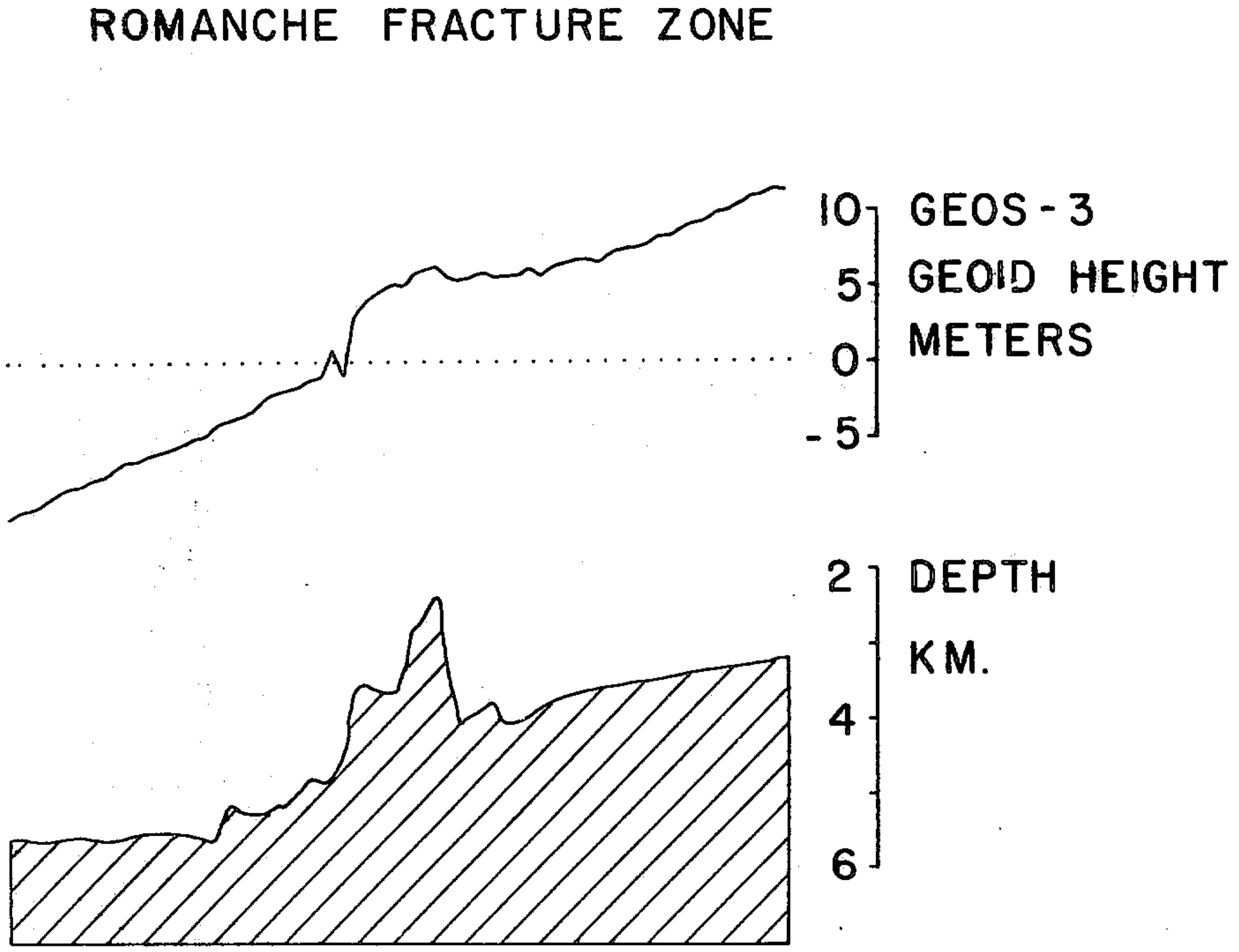
ROMANCHE FRACTURE ZONE
GEOS - 3
GEOID HEIGHT
METERS
10
5
0
-5
DEPTH
KM.
2
4
6

Figure 6

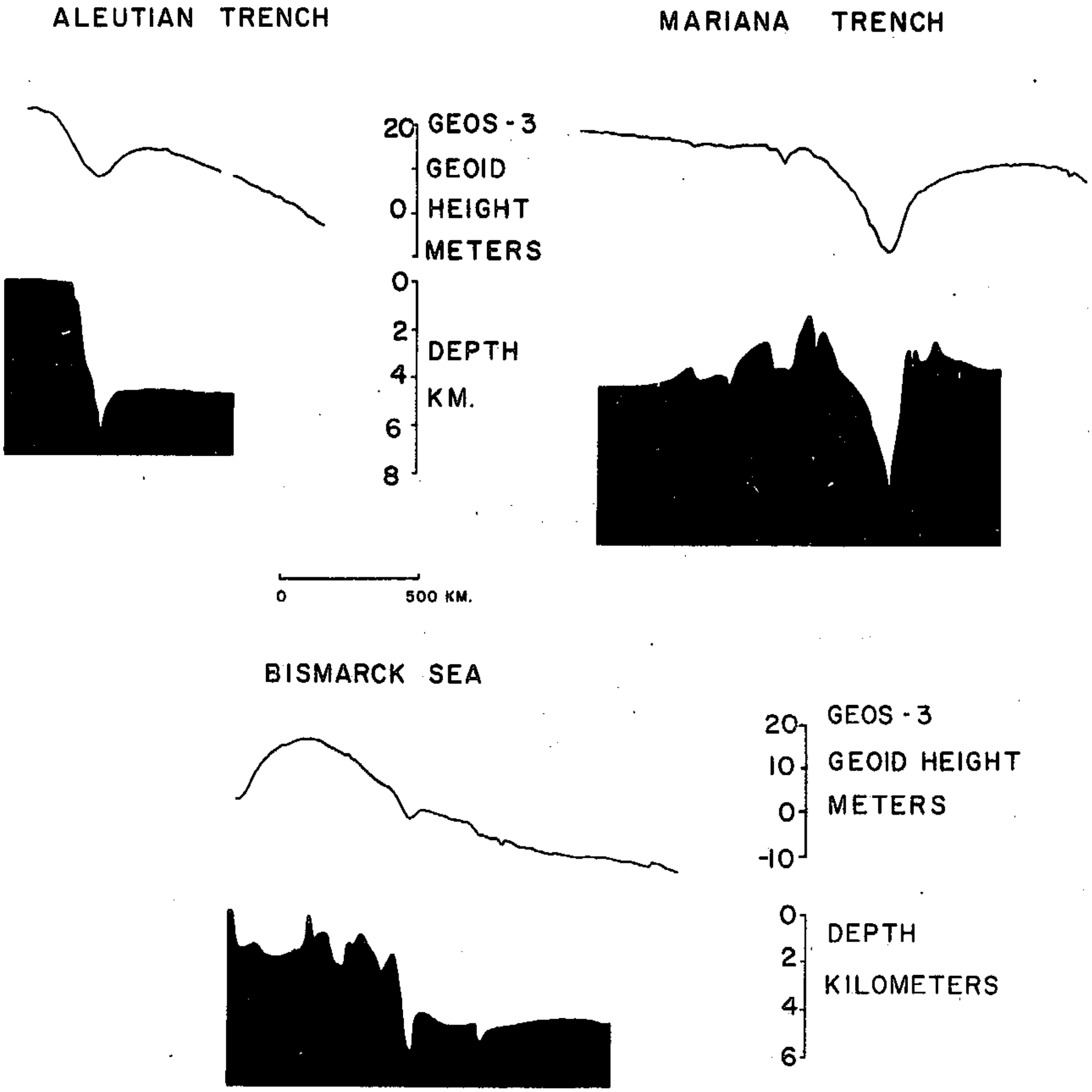
ALEUTIAN TRENCH
MARIANA TRENCH
20
0
GEOS - 3
GEOID
HEIGHT
METERS
0
2
4
6
8
DEPTH
KM.
0
500 KM.
BISMARCK SEA
20
10
0
-10
GEOS - 3
GEOID HEIGHT
METERS
0
2
4
6
DEPTH
KILOMETERS

Figure 7

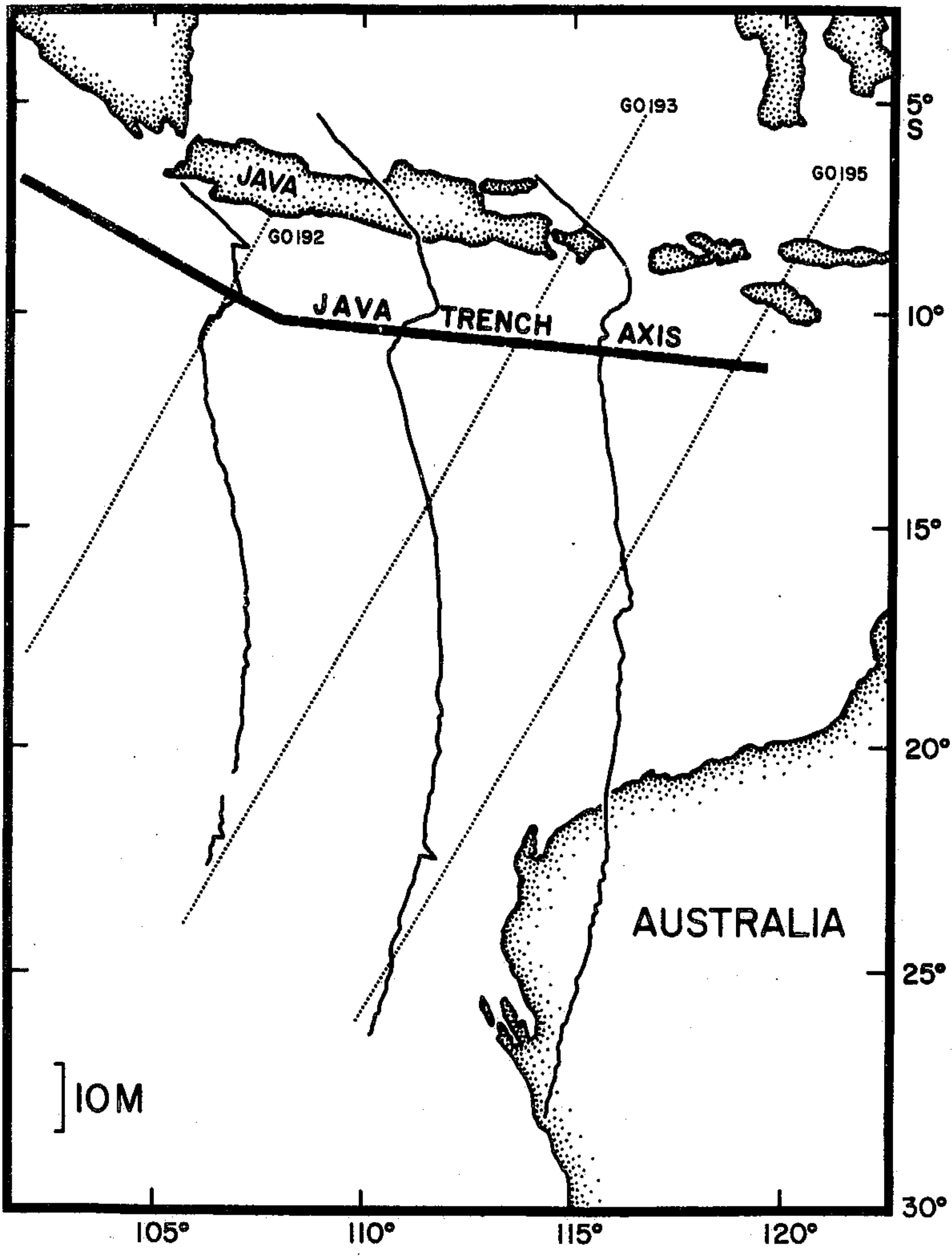
JAVA
GO192
GO193
GO195
JAVA TRENCH AXIS
AUSTRALIA
10M
5° S
10°
15°
20°
25°
30°
105°
110°
115°
120°

Figure 8

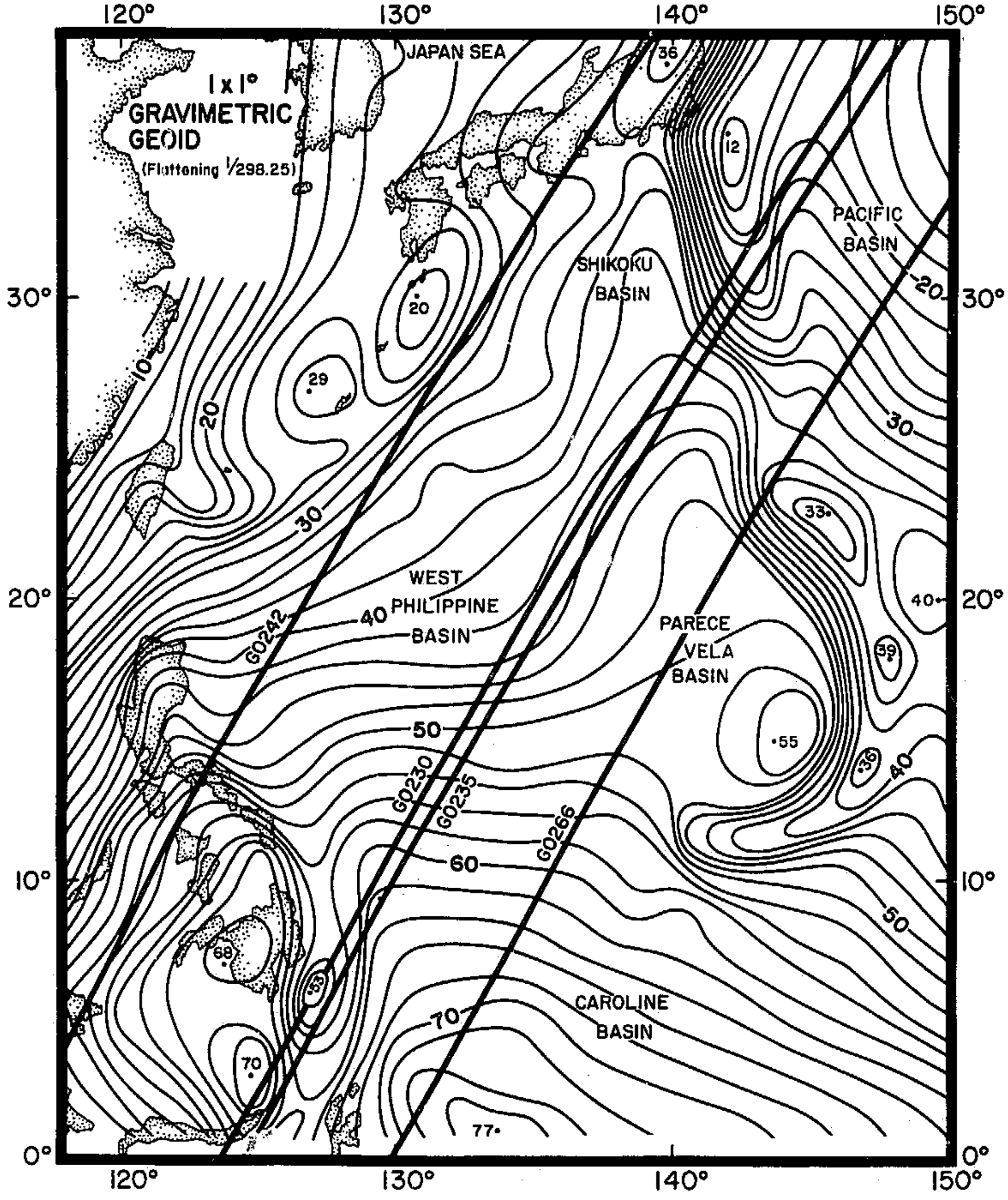
120°
130°
140°
150°
1x1°
GRAVIMETRIC
GEOID
(Flattening 1/298.25)
JAPAN SEA
36
12
PACIFIC
BASIN
SHIKOKU
BASIN
20
20
30°
29
10
20
30
30
33
WEST
PHILIPPINE
BASIN
40
G0242
20°
40
PARECE
VELA
BASIN
39
50
55
36
40
G0230
G0235
G0266
60
10°
50
68
53
CAROLINE
BASIN
70
70
77
0°

Figure 9

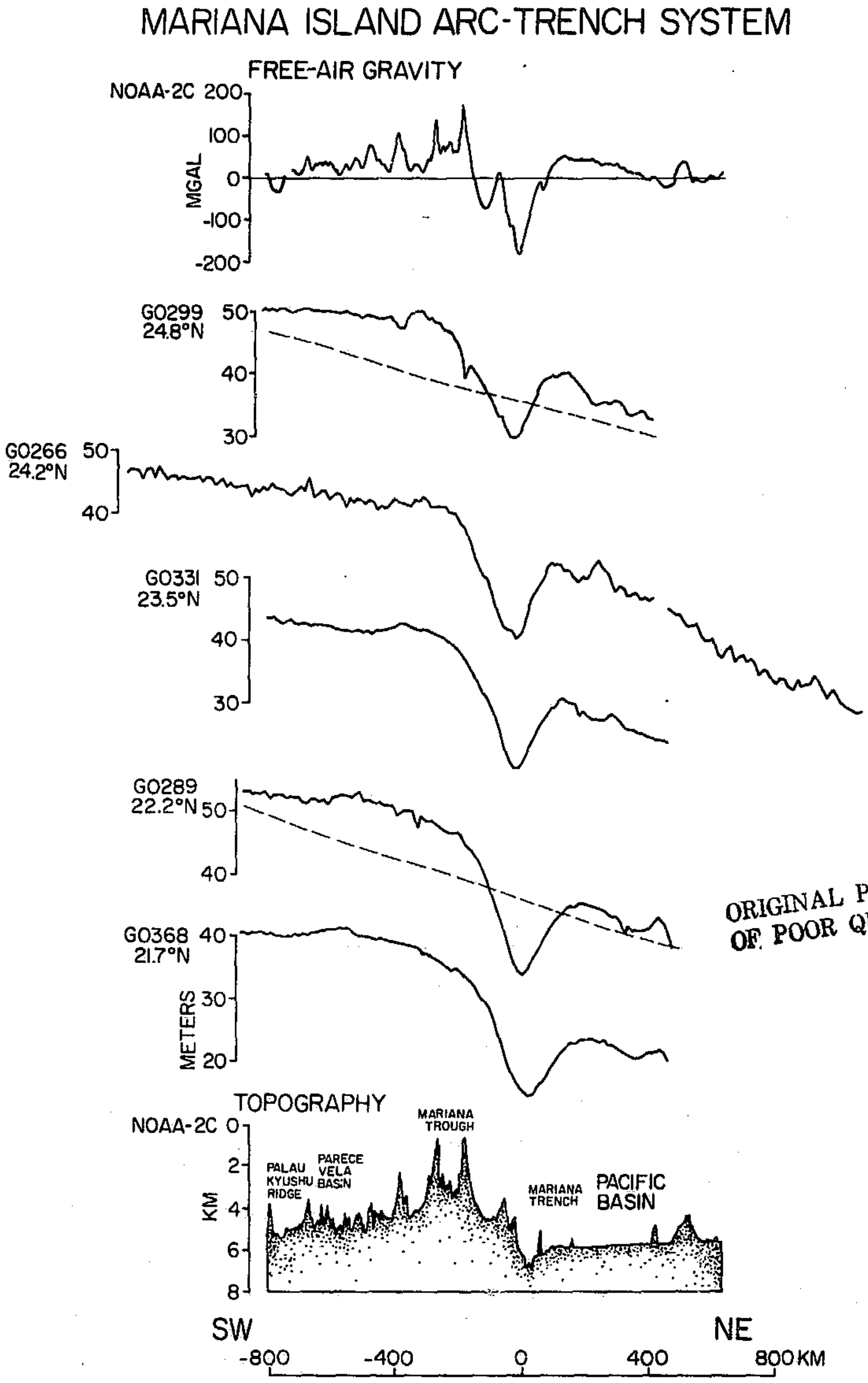
MARIANA ISLAND ARC-TRENCH SYSTEM
FREE-AIR GRAVITY
NOAA-2C
200
100
0
-100
-200
MGAL
G0299
24.8°N
50
40
30
G0266
24.2°N
50
40
G0331
23.5°N
50
40
30
G0289
22.2°N
50
40
G0368
21.7°N
40
30
20
METERS
TOPOGRAPHY
NOAA-2C
0
2
4
6
8
KM
PALAU KYUSHU RIDGE
PARECE VELA BASIN
MARIANA TROUGH
MARIANA TRENCH
PACIFIC BASIN
SW
NE
-800
-400
0
400
800 KM

Figure 10

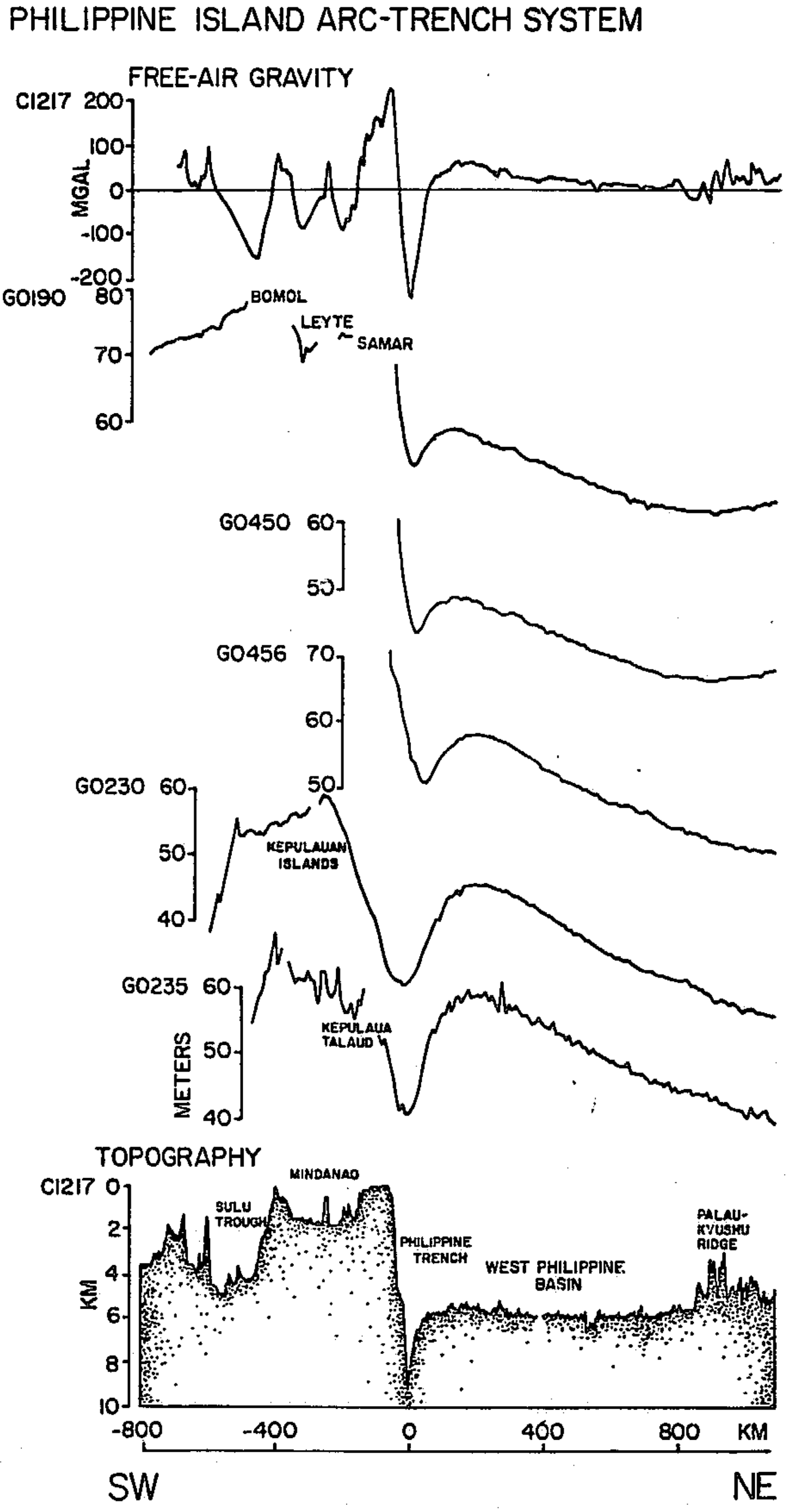
PHILIPPINE ISLAND ARC-TRENCH SYSTEM
FREE-AIR GRAVITY
C1217 200
100
0
-100
-200
MGAL
G0190 80
70
60
BOMOL
LEYTE
SAMAR
G0450 60
50
G0456 70
60
50
G0230 60
50
40
KEPULAUAN ISLANDS
G0235 60
50
40
METERS
KEPULAUA TALAUD
TOPOGRAPHY
C1217 0
2
4
6
8
10
KM
SULU TROUGH
MINDANAO
PHILIPPINE TRENCH
WEST PHILIPPINE BASIN
PALAU-KYUSHU RIDGE
-800
-400
0
400
800
KM
SW
NE

Figure 11

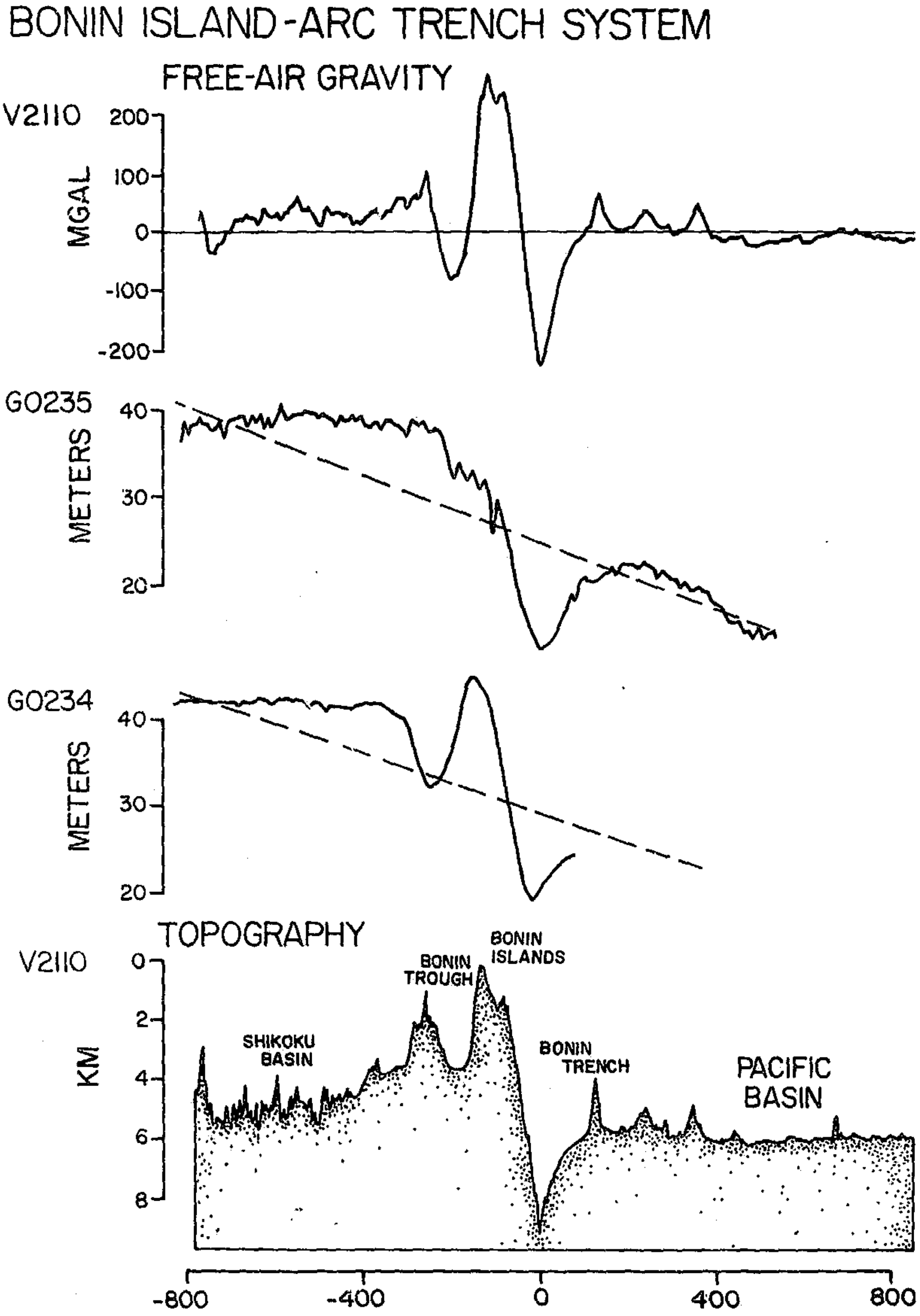
BONIN ISLAND-ARC TRENCH SYSTEM
FREE-AIR GRAVITY
V2110
MGAL
200
100
0
-100
-200
G0235
METERS
40
30
20
G0234
METERS
40
30
20
TOPOGRAPHY
V2110
KM
0
2
4
6
8
SHIKOKU BASIN
BONIN TROUGH
BONIN ISLANDS
BONIN TRENCH
PACIFIC BASIN
-800
-400
0
400
800

Figure 12

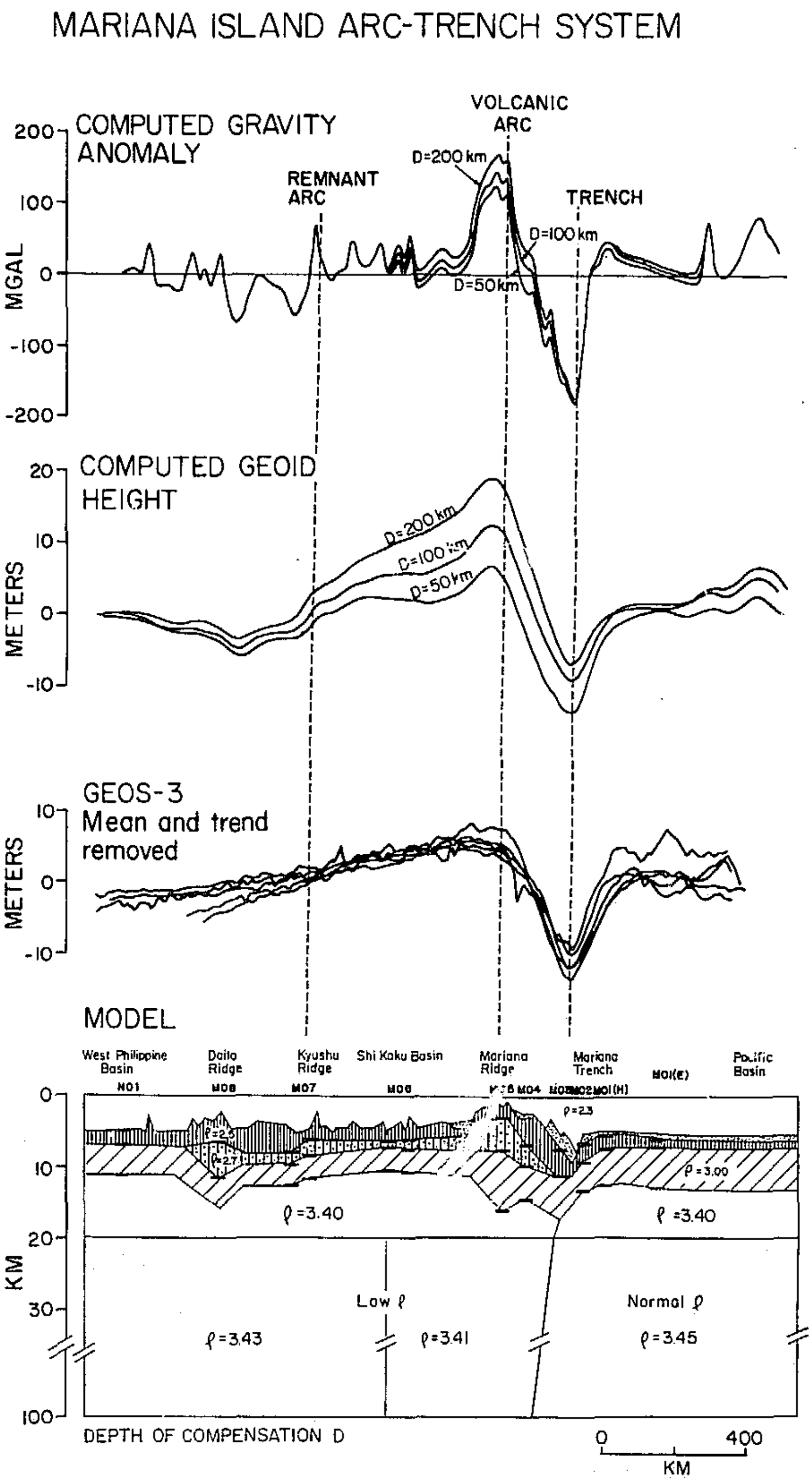
MARIANA ISLAND ARC-TRENCH SYSTEM
COMPUTED GRAVITY ANOMALY
MGAL
200
100
0
-100
-200
REMNANT ARC
VOLCANIC ARC
TRENCH
D=200 km
D=100 km
D=50 km
COMPUTED GEOID HEIGHT
METERS
20
10
0
-10
D=200 km
D=100 km
D=50 km
GEOS-3
Mean and trend removed
METERS
10
0
-10
MODEL
West Philippine Basin
Daito Ridge
Kyushu Ridge
Shi Koku Basin
Mariana Ridge
Mariana Trench
Pacific Basin
N01
M08
M07
M06
M04
M01(H)
M01(E)
ρ=2.5
ρ=2.7
ρ=2.3
ρ=3.00
ρ=3.40
ρ=3.40
Low ρ
Normal ρ
ρ=3.43
ρ=3.41
ρ=3.45
KM
0
10
20
30
100
DEPTH OF COMPENSATION D
0
400
KM

Figure 13

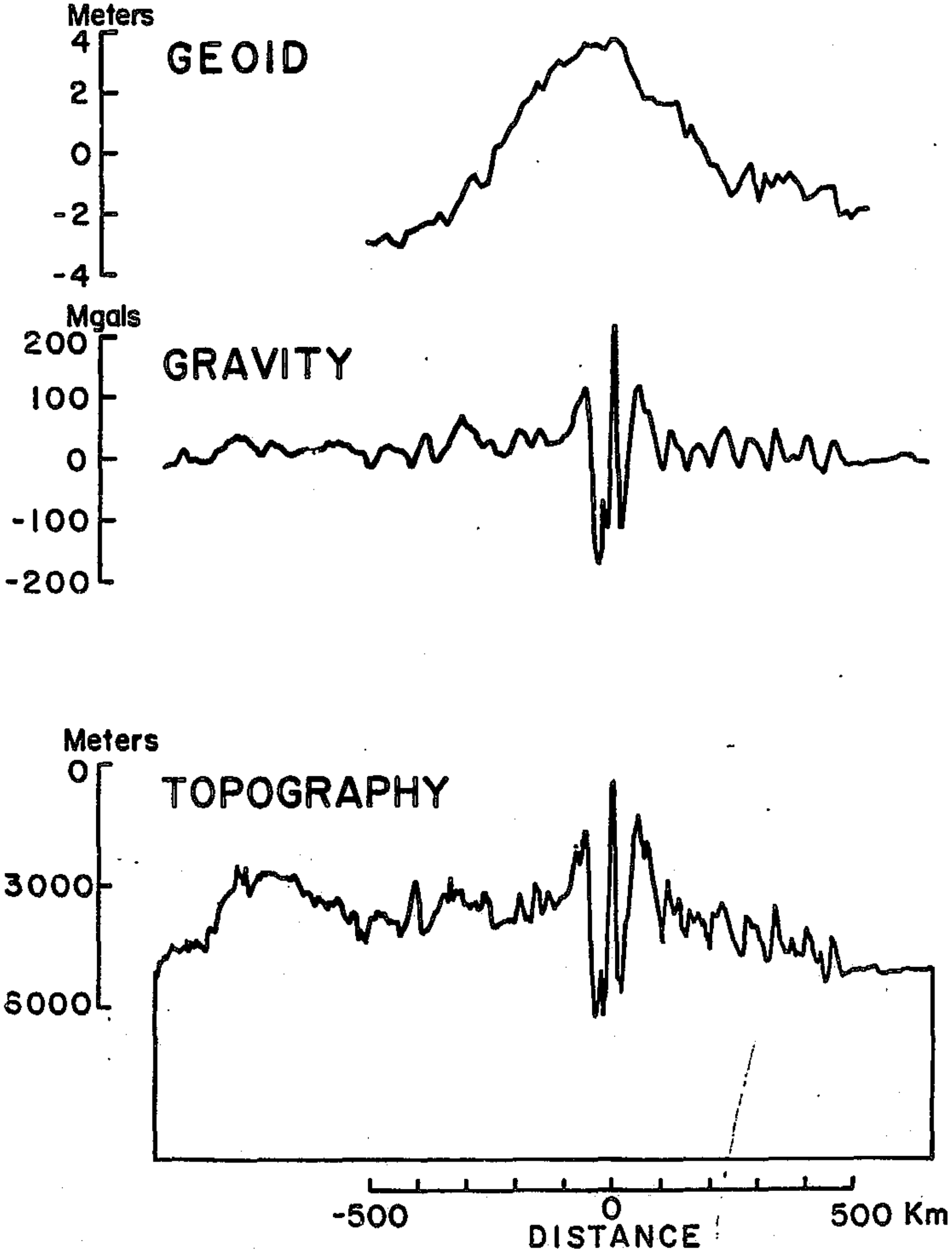
Meters
4
2
0
-2
-4
GEOID
Mgals
200
100
0
-100
-200
GRAVITY
Meters
0
3000
6000
TOPOGRAPHY
-500
0
500 Km
DISTANCE

Figure 14

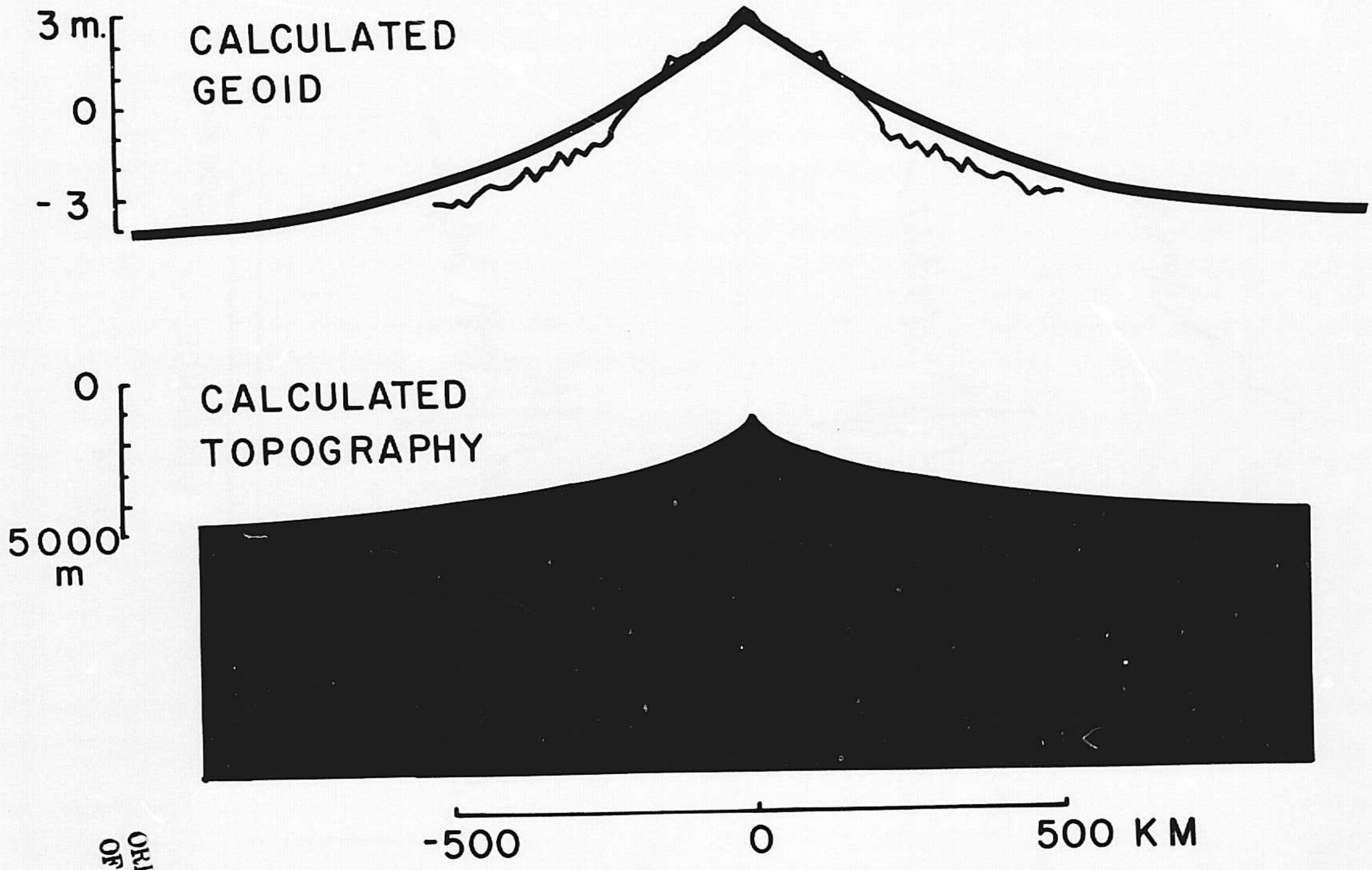
3 m.
0
- 3
CALCULATED
GEOID
0
5000
m
CALCULATED
TOPOGRAPHY
-500
0
500 KM

Figure 15

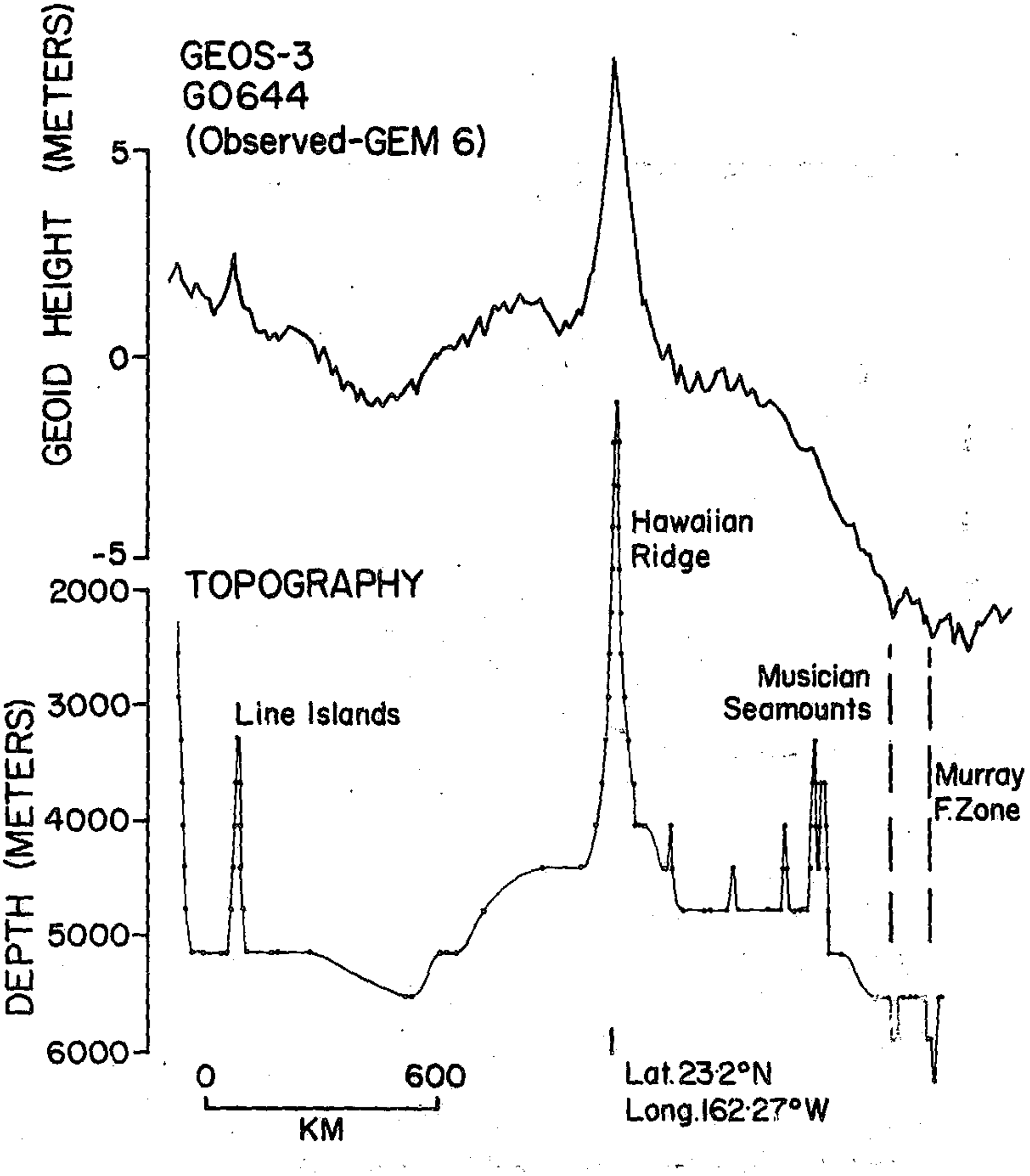
GEOS-3
GO644
(Observed-GEM 6)
GEOID HEIGHT (METERS)
5
0
-5
TOPOGRAPHY
DEPTH (METERS)
2000
3000
4000
5000
6000
Line Islands
Hawaiian Ridge
Musician Seamounts
Murray F.Zone
0
600
KM
Lat.23·2°N
Long.162·27°W

Figure 16

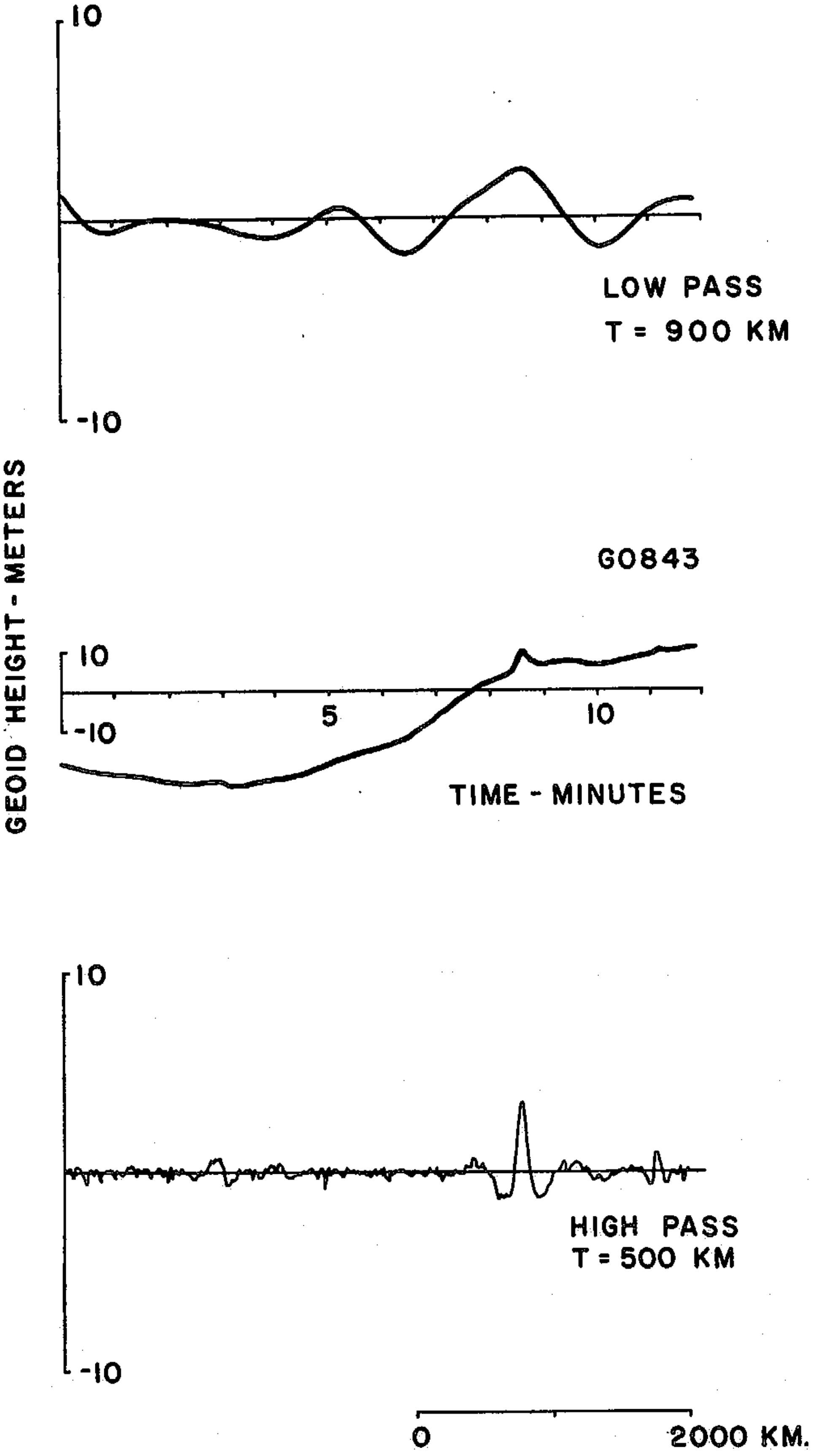
10
-10
LOW PASS
T = 900 KM
GEOID HEIGHT - METERS
G0843
10
-10
5
10
TIME - MINUTES
10
-10
HIGH PASS
T = 500 KM
0
2000 KM.

Figure 17

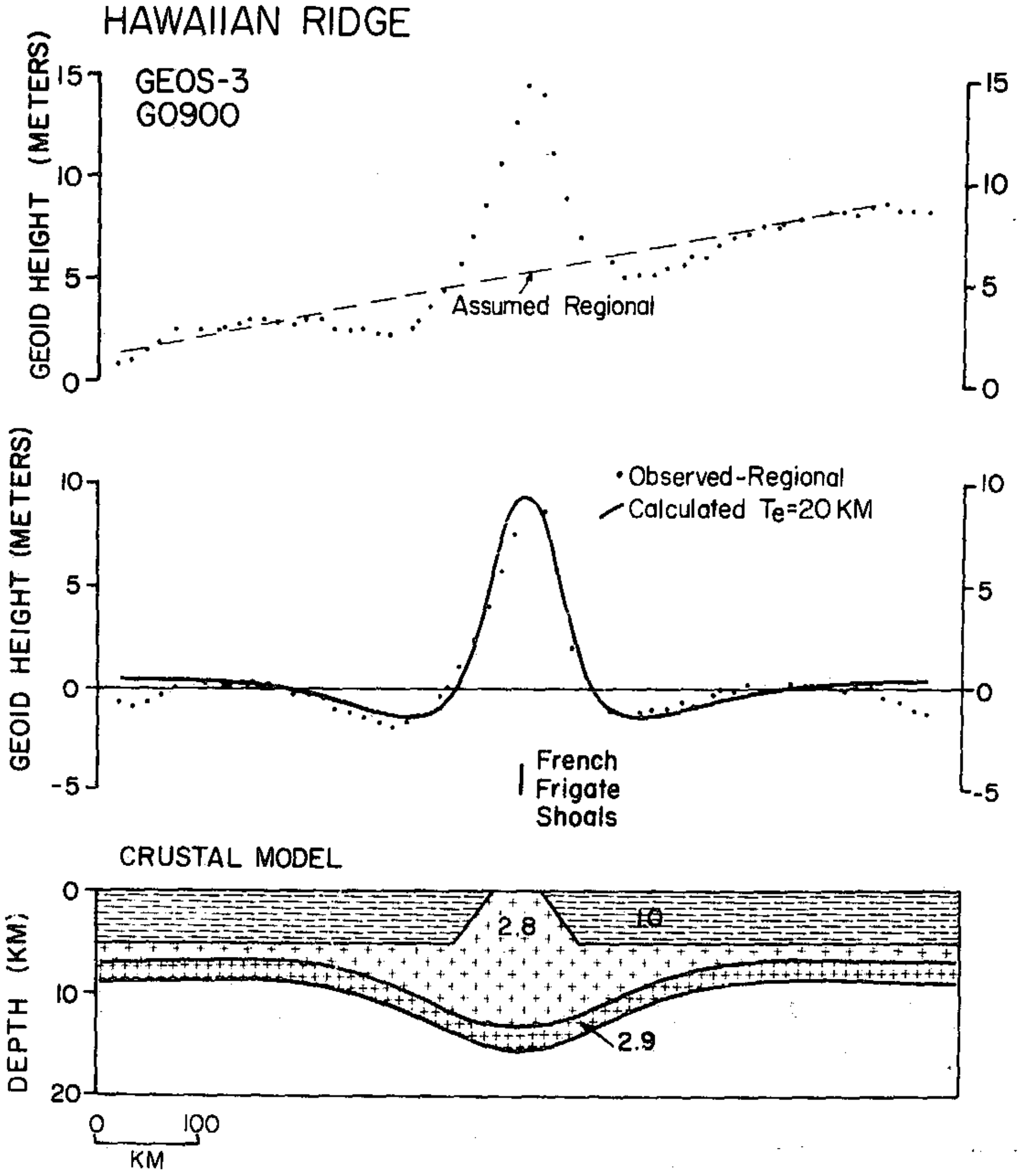
HAWAIIAN RIDGE
GEOS-3
GO900
GEOID HEIGHT (METERS)
15
10
5
0
Assumed Regional
GEOID HEIGHT (METERS)
10
5
0
-5
• Observed-Regional
Calculated T_e=20 KM
French
Frigate
Shoals
CRUSTAL MODEL
DEPTH (KM)
0
10
20
2.8
1.0
2.9
0
100
KM

Figure 18

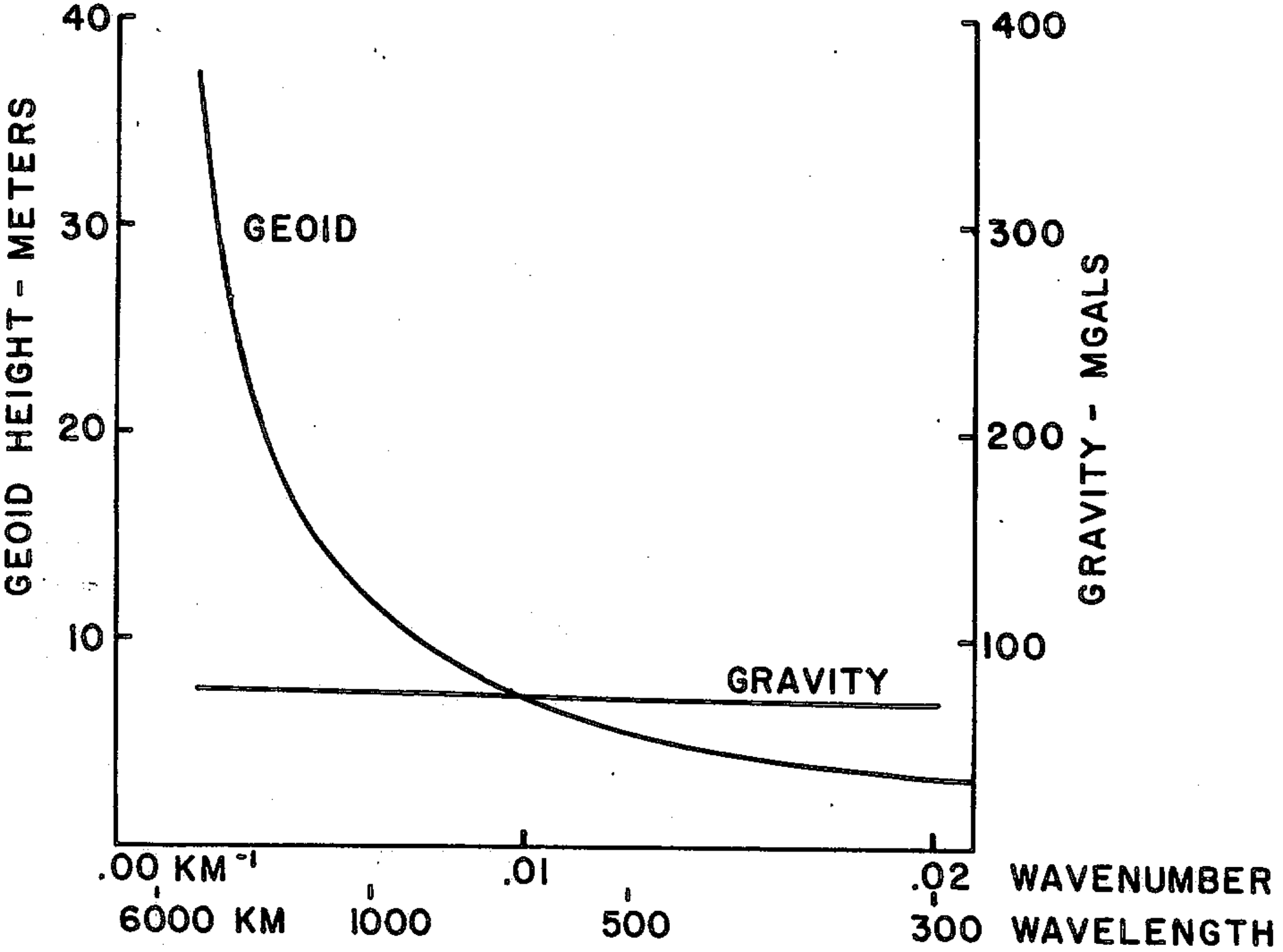
GEOID HEIGHT - METERS
40
30
20
10
GRAVITY - MGALS
400
300
200
100
GEOID
GRAVITY
.00 KM⁻¹
.01
.02
WAVENUMBER
6000 KM
1000
500
300
WAVELENGTH

Figure 19

A PRELIMINARY ANALYSIS OF GEOID HEIGHTS DERIVED FROM GEOS-3 ALTIMETER DATA ALONG THE HAWAIIAN EMPEROR SEAMOUNT CHAIN

Introduction

Studies of the Earth's gravity field have long been recognized as one of the principal means of deducing geological structure in oceanic regions. Since the development of plate tectonics two approaches to the interpretation of marine gravity anomalies have been carried out which have been proved useful. The first approach, based on pioneering studies of Vening Meinesz (1941) and Gunn (1943), uses relatively short-wavelength ($\lambda \sim 250$ km) gravity anomalies over surface-loads of long duration ($>10^6$ years) to determine information on the long-term mechanical properties of the lithospheric plates (for example, Watts and Cochran, 1974). The second approach uses the correlation between relatively long-wavelength ($\lambda \sim 2500$ km) gravity anomalies and bathymetry, which exists in some parts of the oceans (Sclater et al., 1975; Watts, 1976), to deduce information on the forces acting on the plates and which may ultimately drive them (for example, McKenzie, 1977).

The only global solutions of the Earth's gravity field, however, have come from combination solutions of terrestrial and satellite gravity data. One of the most recent Earth models, GEM 8 (Wagner et al., 1976), resolves information on the long-wavelength ($\lambda > 2600$ km) gravity field. Information on the short-wavelength ($\lambda < 2600$ km) field is based largely on surface measurements and these are generally sparse over the southern oceans.

There is therefore much geophysical interest in the recent NASA SKYLAB S-193 (Leitao and McGoogan, 1975; McGoogan et al., 1975) and GEOS-3 (Leitao et al., 1975) missions which attempt to determine the gravity field over the oceans with radar altimeters on orbiting satellites. Satellite altimeters when corrected for orbital and calibration errors measure directly the distance between the satellite and the mean ocean surface. The ocean surface, except for tidal and wind effects, follows the Earth's gravitational equipotential surface. The geoid height represents the departure of this equipotential surface from a reference ellipsoid. Thus if the height of the satellite above the reference ellipsoid and the tidal and wind effects are known, geoid heights may be estimated from the height of the satellite measured by the altimeter.

The GEOS-3 satellite (Leitao et al., 1975), which was launched in April 1975, currently provides the best means to estimate geoid heights in oceanic regions. The radar altimeter on this satellite operates by transmitting a pulse downward and receiving the reflection from the sea-surface. The instrument is operated either in an intensive or global mode. The sea-surface "footprint" of the instrument is about 4 km (intensive mode) or 14 km (global mode).

A number of ground truth studies have now been carried out to assess the performance of the altimeter. Chapman and Talwani (in preparation) have compared GEOS-3 altimeter data to 1 x 1° gravimetric geoids in the Atlantic, Indian and Pacific oceans. They conclude that although systematic differences in the geoids occur, the altimeter geoid has much better resolution than the 1 x 1° gravimetric geoid particularly over features such as island arcs, deep-sea trenches and Atlantic-type continental margins. Martin and Butler (1977) have compared the altimeter geoid to a 5 x 5' gravimetric geoid in the western North Atlantic. An average difference between the altimetric and gravimetric geoids of -4.33 meters was determined which they attributed to a bias in the altitude of the satellite. Marsh et al. (1977) have minimized the differences in the altimetric geoid at more than 19,000 track intersections over the western North Atlantic. They attributed the differences mainly to orbital uncertainties. The resulting altimetric geoid agreed closely with the 5 x 5' gravimetric geoid. The two geoids did not differ by more than 1 meter even over relatively short-wavelength features such as Bermuda and the Blake escarpment. Thus the altimetric geoid appears to be able to resolve features with wavelengths greater than about 40 km.

The geoid heights derived from the altimeter data, when corrected for orbital uncertainties and tidal effects, comprise three main effects. These are 1) geodetic, 2) oceanographic such as winds and 3) instrument noise. The separation of oceanographic effects from the altimetric geoid therefore requires knowledge of the geodetic portion. The main difficulty with this, however, is that with the possible exception of the western North Atlantic sufficiently accurate gravimetric geoids do not presently exist over the oceans.

A useful approach to the problem therefore is to establish whether geological features on the ocean floor are associated with geoid anomalies and then to establish simple models to interpret them. A number of studies have now been carried out which show there is a significant contribution of sea-floor topography to the gravity field between wavelengths of about 20 and 400 km (Talwani et al., 1972; McKenzie and Bowin, 1976; Watts, in preparation). The contribution is reduced at shorter wavelengths ($\lambda \lesssim 20$ km) because of instrument noise and at larger wavelengths ($\lambda \gtrsim 400$ km) because of the effects of isostatic compensation. It would therefore be expected that sea-floor topography should contribute to the geoid. For example, the gravity anomaly over the Hawaiian-Emperor seamount chain ($\lambda \sim 280$ km) is about +250 mgal. This anomaly is equivalent to a geoid height of about +11 meters. Thus if the noise level of geoid heights derived from GEOS-3 altimeter data is less than 1 meter (Martin and Butler, 1977) and if oceanographic effects are small it should be possible to separate the geoid undulation associated with the seamount chain from the altimetric geoid.

The main problem in accurately determining the geoidal undulations associated with geological features on the ocean floor, however, is that the bathymetry along a satellite track is poorly known. Although existing bathymetric maps in the oceans are sufficiently accurate to determine long-wavelength ($\lambda \gtrsim 50$ km) features on the sea-floor they are not, in general, accurate enough to resolve short-wavelength features.

The purpose of this paper is to present an interpretation of geoid heights derived from currently available GEOS-3 satellite radar altimeter data along the Hawaiian-Emperor seamount chain. An attempt is made to isolate that part of the altimetric geoid which is caused by the topography of the seamount chain and its compensation from that part due to other causes. These other causes include the effects of oceanographic and instrument "noise". The model of compensation which is used assumes that the seamount chain represents a load on a strong, rigid oceanic lithospheric plate. The altimeter data is used to estimate the elastic thickness of the plate and provide constraints on models for the long-term ($>10^6$ years) mechanical properties of the oceanic lithosphere.

GEOS-3 Altimeter Data

The geoid heights used in this study were derived from GEOS-3 altimeter data obtained between May and October 1975 over the central Pacific ocean (Table 1). The data was acquired while the instrument was operated in the intensive mode and has been smoothed over time frames of 2.2 or 3.2 sec. The smoothed data therefore resolves features in the mean ocean surface with wavelengths of 40 km and greater. The actual satellite tracks used are shown in Figure 1. The geoid heights have been corrected for the M-2 tidal model (Hendershott, 1973) and have been referred to an ellipsoid with flattening f = 1/298.255 and a semi-major axis a = 6378.145 km. An arbitrary constant was removed from each geoid profile prior to plotting the data normal to each satellite track.

The main features of the altimeter profiles are a relatively short-wavelength ($\lambda\sim280$ km) geoid high and low over the Hawaiian-Emperor seamount chain (Fig. 1). The geoid high reaches a maximum of about 12 meters near Molokai island and the geoid low reaches a maximum of about 3 meters north of the island. These short-wavelength geoid undulations on profiles G2676, G0843, G0644 and G1113 are superimposed on a relatively long-wavelength ($\lambda\sim2600$ km) geoid high of about 5 to 7 meters associated with the Hawaiian Swell (Betz and Hess, 1942; Watts, 1976). The long-wavelength geoid high is absent on profiles G0878 and G1695 which cross the Hawaiian Ridge west of 170°W.

The altimeter profiles of the Hawaiian Ridge shown in Figure 1 also show a broad ($\lambda\gtrsim6000$ km) increase in geoid from north to south. The increase is about 30 to 40 meters and corresponds to the northern gradient of the geoid high centered over the Fiji Plateau. This high is clearly seen in the GEM 6 combination solution (Lerch et al., 1974).

The relationship between altimeter profile G0644 (Fig. 1) and bathymetry is illustrated in Figure 2. This profile has had the detailed GEM 6 Earth model (Marsh and Vincent, 1974) subtracted from it. The purpose of removing this field is that this model describes the long-wavelength ($\lambda\gtrsim2600$ km) part of the geoid which does not appear to correlate with bathymetry. The bathymetry profile in Figure 2 has been constructed from available bathymetry maps of the central Pacific (Chase et al., 1970). The heavy dots on the profile represent the position of the intersection of a bathymetric contour with the satellite track. The main features of the profile are a short-wavelength ($\lambda\sim280$ km) geoid high of about 7 meters over the Hawaiian Ridge and a smaller amplitude geoid high of about 2 meters over the Line Islands. The Musician Seamounts and the Necker Ridge are not associated with a geoid high.

The geoid high over the Hawaiian Ridge is superimposed on a long-wavelength ($\lambda \sim 2600$ km) high associated with the Hawaiian Swell. There is an excellent correlation between the long-wavelength geoid high and bathymetry. A similar good correlation between gravity and bathymetry was observed by Watts (1976) over the Hawaiian Swell although it appears easier to distinguish the gravitational effect of the swell in the geoid than it is in gravity.

The relationship between altimeter profiles and bathymetry are shown for all satellite tracks used in this study in Figure 3. The profiles in this figure are observed altimeter profiles which have been projected normal to the local trend of the seamount chain (Table 1). Each profile extends 400 km either side of the crest of the seamount chain. Thus the Hawaiian Swell and its associated long-wavelength ($\lambda \sim 2600$ km) geoid high are not included in these profiles. The main feature of the observed profiles are short-wavelength ($\lambda \sim 280$ km) geoid highs of 5 to 12 meters over the crest of the seamount chain and geoid lows of 1 to 3 meters over flanking regions. The Musician Seamounts are not associated with a geoid high on profile G0843, in agreement with the observation on profile G0644 (Fig. 2).

The most likely explanation of the short-wavelength ($\lambda \sim 280$ km) geoidal undulations over the seamount chain (Figs. 1, 2 and 3) is that they are caused by topography of the seamount chain and its compensation. The source of these undulations is therefore believed to be located within the lithosphere. The explanation of the long-wavelength ($\lambda \sim 2600$ km) geoid high over the Hawaiian Swell (Fig. 1 and 2), however is presently unclear. Watts (1976) suggested the long-wavelength gravity anomaly over the swell could not be explained by the topography of the seamount chain and its compensation. Although the source of this long-wavelength anomaly is uncertain, Watts (1976) suggested it was located beneath the lithosphere.

Method of Analysis

The geoid anomaly caused by a given mass distribution in the Earth can be computed in an analogous manner to gravity anomalies (Leeds, personal communication, 1974; Bowin, 1975). For three dimensional distributions it is convenient to divide the body into a number of finite horizontal plane lamina. The potential due to a lamina of thickness dz is

$$V = G\rho dz \int [(r^2 + z^2)^{\frac{1}{2}} - z]\, d\psi \qquad (1)$$

where G is the gravitation constant, ρ is the density, z is the positive depth of the lamina, r is the distance in the plane of the lamina from a point on the boundary to the projection of the observation point, and the line integral is evaluated around the boundary of the lamina. For a polygonal boundary the line integral can be calculated exactly. Each body is described by a series of contours at various depths, and the total potential is found by numerical integration over z. The total potential T can be converted to a geoid height N by Bruns Formula.

$$N = \frac{T}{g} \qquad (2)$$

This method has been used to calculate the geoid undulations for a simplified "theoretical" seamount chain in Figure 4. The computations were carried out assuming long rectangular laminae. Corrections due to the curvature of the Earth have been neglected.

The crustal model in Figure 4 is based on the flexure or plate model for the compensation of surface features. In this model the seamount chain represents a load on a thin elastic plate which overlies a weak fluid substratum. This model has been widely used (Walcott, 1970; Watts and Cochran, 1974) to study lithospheric flexure caused by surface loads of long duration ($\geq 10^6$ years). The amplitude of flexure is determined by the flexural rigidity D which is a measure of the stiffness of the plate. Geoid profiles have been computed for different assumed values of D (Fig. 4). The amplitude and wavelength of these geoid heights are generally similar to the measured heights over the chain in Figure 3.

Figure 4 shows significant differences in the amplitude and wavelength of the geoid profiles for values of the flexural rigidity in the range 10^{29} to 10^{31} dyn-cm. It should therefore be possible to resolve these differences in measured profiles (Fig. 3) and estimate the best fitting flexural rigidity. Watts and Cochran (1974) determined the flexure of the lithosphere associated with seamount loads using equations given in Hetényi (1946). They then computed the combined gravity effect of the load and its compensation for different assumed values of the flexural rigidity. The best fitting rigidity was selected as that value which minimized the sums of the squares of the residuals between observed and calculated gravity anomalies.

A more convenient way to compute the geoid profile due to a topographic load and its compensation, however, is to use Fast Fourier transform techniques. In this approach theoretical transfer functions or filters are constructed for different assumed values of the flexural rigidity. The filters represent the geoid effect of a unit load on the surface of the plate. Thus by convolution of these filters with the observed bathymetry computed geoid profiles can be obtained for different values of rigidity and compared with the observed geoid.

McKenzie and Bowin (1976) and Watts (in preparation) have given expressions for the transfer function or admittance Z(k) which describes the relationship of gravity and bathymetry as a function of wavelength for the plate model.

The expressions differ only in the crustal structure assumed. The admittance $Z_g(k)$ which describes the relation of geoid undulation and bathymetry as a function of wavelength (for example, Chapman, this volume) can then be obtained from

$$Z_g(k) = \frac{Z(k)}{g\ k} \tag{3}$$

where $k = 2\pi/\lambda$ and the geoid filter is obtained by inverse Fourier transforming $Z_g(k)$. A theoretical filter for a flexural rigidity of 1.5×10^{30} dyn-cm, which corresponds to an elastic thickness $T_e = 25$ km is shown in Figure 5.

The Fast Fourier transform method of computing the geoid height compares well to the line-integral method used in Figure 4. The only difference between the two methods occurred over the crest of the seamount chain and at the ends of the profile. These differences do not exceed 1 meter and can be attributed to the method used to remove the mean from the bathymetry profiles and to tapering their ends.

Results

The GEOS-3 altimeter profiles in Figure 3 are compared to theoretical profiles based on the plate model in Figure 6 and 7. Theoretical filters were constructed for different values of the elastic plate thickness T_e and then convolved with the "observed" bathymetry. The trend and mean were then removed from each bathymetry profile and the ends tapered. The ends of each bathymetry profile were "padded" with zeros in order to prevent filter wrap around and possible distortion at the ends of the computed profiles. Theoretical or predicted geoid profiles were then obtained by convolving the filters with the "observed" bathymetry.

Figure 6 shows there is generally a good agreement between observed geoid profiles G2676, G0843, G0644 and G0878 and computed profiles based on the theoretical filters. The best fitting elastic thickness T_e was estimated as that value which minimized the RMS difference between observed and computed profiles. The best fitting estimates of the elastic thickness range from 25 to 37.5 km and the RMS difference does not exceed ±0.8 meters on any of the profiles (Fig. 6).

There is generally a poor agreement, however, between observed profiles G1695 and G1113 and computed profiles (Fig. 7). The main problem with profile G1113 is the large differences obtained over the Musician Seamounts and the Necker Ridge. Although an elastic thickness $T_e = 40$ km generally explains the amplitude and wavelength of the geoid high over the seamount chain it does not explain the absence of a geoid high over the Musician Seamounts and Necker Ridge. This suggests that smaller values of the elastic thickness, or the Airy model, may better explain observed data over these features. The main problem with profile G1695 is that although the amplitude of the observed geoid high can be explained for a plate thickness of $T_e = 30$ km, the wavelength cannot (Fig. 7). This difference is attributed to the assumption of two-dimensionality and to uncertainties in the observed bathymetry profile because profile G1695 intersects the steep flanks of the Emperor Seamounts at a high angle (Fig. 1).

The range of best fitting elastic thickness can also be estimated using linear transfer function techniques similar to those described by Lewis and Dorman (1970), Dorman and Lewis (1970) and McKenzie and Bowin (1976). The transfer function or admittance contains information on the mechanism of isostasy at a feature. The advantage of these techniques is that they use observational data and are not based on a particular model of isostasy. The admittance can, however, be interpreted in terms of different models of isostasy and in some cases may be used to distinguish between them.

The main problem is obtaining smooth estimates of the admittance from the observed data. McKenzie and Bowin (1976) determined smooth estimates by dividing their two long surface-ship gravity and bathymetry profiles, which crossed a number of geological features on the ocean floor, into a number of shorter profiles. They then averaged the spectra for each sub-profile for a particular wavelength. Watts (in preparation) has outlined a method more suitable for determining the admittance for a single geological feature. In this approach many surface-ship profiles over the same feature are used, each of which constitutes an independent estimate of the relationship between gravity and bathymetry. The spectra are then averaged for each profile for a particular wavenumber.

The altimeter and bathymetry profiles in Figure 6 were used to generate admittance values along the Hawaiian Ridge. The basic computational steps are similar to this described by Watts (in preparation) for gravity and bathymetry. Observed geoid and bathymetry profiles are linearly interpolated to obtain evenly spaced values. After the removal of the trend and mean the discrete Fourier transform is obtained by use of the Fast Fourier Transform. The two transforms are used to estimate the cross spectrum and power spectrum and to construct an average over the set of profiles. The admittance is given by the cross spectrum of the geoid and bathymetry divided by the power spectrum of the bathymetry. The altimeter and bathymetry profiles were used to obtain 4 independent estimates of the cross spectrum and power spectrum. The smoothed spectra were then used to compute the coherence γ^2, the phase of the admittance and the admittance (Table 3). The relative smoothness of the admittance values for $0.0078 < k < 0.0469$ (Table 3) is evidence that a similar signal was present in each profile and the smoothing procedure satisfactorily reduces noise. The phase of the admittance is approximately zero for these wavenumbers indicating the admittance is real. The coherence is high (>0.7) suggesting that for wavelengths longer than about 100 km a significant portion of the energy in the geoid can be attributed to bathymetry.

The observed admittance values are compared to calculated curves based on the plate model in Figure 8. The parameters assumed in the calculations are summarized in Table 2. The admittance curves increase for $300 > \lambda > 50$ km because short-wavelength topography is uncompensated. The curves decrease for longer wavelengths ($\lambda \gtrsim 300$ km) because of the effect of isostatic compensation.

Although there is some scatter (Fig. 8), the best fit for the observed admittance values is for plate thickness in the range 28 to 37 km. These estimates are therefore similar to those obtained with the theoretical filters in Fig. 6. The advantage of this approach, however, is that the admittance is obtained completely from the observed data. As more altimeter data is made available along the chain more reliable estimates for the admittance and, therefore, the elastic thickness may be made.

Tectonic Implications

Geoid heights derived from GEOS-3 satellite altimeter data have therefore been used to estimate the elastic thickness of the oceanic lithosphere along the Hawaiian Ridge. The best fitting values are in the range 25 to 37.5 km. In this section the tectonic implications of these values are examined.

The elastic thickness of the lithosphere determined from the altimeter data is not the actual thickness of the lithosphere. It is the thickness the lithosphere would have if it responded to long-term ($>10^6$ years) loads as an elastic plate overlying a weak fluid. The elastic thickness is much less than the seismic or thermal thickness of the lithosphere. Apparently in response to long-term loads only the upper part of the plate responds elastically.

Watts (in preparation) has suggested, based on gravity and bathymetry data in the Pacific ocean, that the elastic thickness acquired at long-term loads depends on the temperature gradient of the lithosphere at the time of loading. The elastic thickness is plotted against age of the lithosphere at the time of loading in Figure 9. The data from the Pacific (shown by open triangles) show there is an exponential decrease in the elastic thickness with decrease in age of the lithosphere at the time of loading. This decrease can be reasonably well fit by a simple model in which the elastic thickness represents the depth to the 450°C isotherm (Fig. 9). Apparently at temperatures less than about 450°C the lithosphere responds elastically on long-time scales.

The results from the altimeter data (Fig. 6) are shown as a solid triangle in Figure 9. The age of the lithosphere at the time of loading has been estimated from age data along the seamount chain (Clague and Jarrard, 1973) and from inferred age of the sea-floor based on magnetic lineations. The plot in Figure 9 shows the altimeter results are in substantial agreement with those from previous studies based on gravity and bathymetry data along the chain.

The altimeter data (Fig. 9) support the suggestion that the lithosphere is capable of supporting large loads on the surface of the plates for long periods of geological time (at least up to about 55 m.y.). The close fit of the elastic thickness estimates to the 450°C isotherm (Fig. 9) suggests there has been little or no relaxation of the deformation with time. Thus the oceanic lithosphere behaves elastically on long-time terms rather than visco-elastically as previously suggested by Walcott (1970).

The range of elastic thickness plotted in Figure 9 cannot, however, explain the measured geoid over features flanking the seamount chain such as the Musician Seamounts and Necker Ridge (Figs. 6 and 7). Apparently these features require much lower values of the elastic thickness. One possibility is that these features originated at a mid-oceanic ridge crest rather than in the interior of a relatively old lithospheric plate.

We have explained a significant part of the altimetric geoid in terms of the structure of the lithosphere beneath the chain. This result is important since this lithospheric effect can now be removed from the measured geoid height and residual profiles interpreted in terms of mass distributions either at depth within the lithosphere or beneath it. Of particular interest is the origin of the long-wavelength geoid high over the Hawaiian Swell (Fig. 2). Future studies which use GEOS-3 data over the Pacific Ocean should be able to establish the source of the geoid high and whether or not it is related to deep processes in the Earth such as mantle convection.

Conclusions

This analysis of geoid heights derived from available GEOS-3 satellite altimeter data along the Hawaiian-Emperor seamount chain allow the following conclusions to be made.

1. The GEOS-3 satellite altimeter has successively recovered short-wavelength ($\lambda \sim 280$ km) geoid highs of 5 to 12 meters over the Hawaiian-Emperor seamount chain and geoid lows of 1 to 3 meters over flanking regions.

2. These geoid undulations can be explained by a simple model in which the oceanic lithosphere supports the weight of the seamount chain for long periods of geological time (at least about 55 m.y.).

3. The best fitting elastic thickness of the oceanic lithosphere based on the altimeter data is in the range 25 to 37.5 km.

4. The differences between "observed" and calculated geoid heights based on these thicknesses is small and does not exceed an RMS discrepancy of ±0.8 meters on any of the profiles.

5. Sea-floor topography and its compensation contributes a significant part of the energy in the altimetric geoid for about $100 < \lambda < 800$ km. At shorter wavelengths other effects such as instrument and oceanographic "noise" probably

contribute the most energy.

6. The elastic thickness estimates deduced from the GEOS-3 altimeter data are in substantial agreement with values based on surface-ship gravity and bathymetry observations and provide further support for the hypothesis that the oceanic lithosphere is elastic, rather than viscoelastic, on long-time ($>10^6$ years) scales.

7. The short-wavelength geoid undulations associated with the seamount chain are superimposed on a long-wavelength ($\lambda \sim 2600$ km) geoid high associated with the Hawaiian Swell. This geoid high cannot be explained by the flexure model and is probably caused by mass distributions at depth in the lithosphere or beneath it.

References

Betz, F. and H.H. Hess, 1942. The floor of the North Pacific Ocean, Geogr. Rev., 32, 99-116.

Bowin, C., 1975. Catalogue of geoidal variations for simple seafloor topographic features, Woods Hole Oceanographic Institution Tech. Report WHOI-75-14.

Chapman, M., Techniques for interpretation of geoid anomalies, Submitted to J. Geophys. Res. (this issue).

Chapman, M. and M. Talwani, 1978. Comparison of gravimetric geoids with GEOS-3 altimeter, (in preparation).

Chase, T.E., H.W. Menard, and J. Mammerickx. 1970. Bathymetry of the North Pacific, Scripps Inst. of Oceanography and Inst. of Marine Res., Chart No. 5 and 6.

Clague, D.A. and R.D. Jarrard, 1973. Tertiary Pacific plate motion deduced from the Hawaiian-Emperor chain, Geol. Soc. Am. Bull. 84, 1135-1154.

Dorman, L.M. and B.T.R. Lewis, 1970. Experimental Isostasy 1. Theory of the determination of the Earth's response to a concentrated load, J. Geophys. Res. 75, 3357-3365.

Gunn, R., 1943. A quantitative evaluation of the influence of the lithosphere on the anomalies of gravity, J. Franklin Inst., v.236, 373-396.

Graf, A. and R. Schulze, 1961. Improvements on the sea gravimeter Gss2, J. Geophys. Res. 66, 1813-1821.

Hendershott, M.C., 1973. Tide model ocean tides, Trans. A.G.U., 54, 76-86.

Hetényi, M., 1946. Beams on elastic foundation, Ann Arbor: The Univ. of Mich. Press, 255 p.

Leitao, C.D. and J.T. McGoogan, 1975. Skylab Radar Altimeter: Short wavelength pertubations detected in ocean surface profiles, Science 186, 1208-1029.

Leitao, C.D., C.L. Purdy and R.L. Brooks, 1975. Wallops GEOS-C altimeter preprocessing report, NASA Technical Memorandum, NASA TM X-69357, 68p.

Lerch, F.J., C.A. Wagner, J.A. Richardson and J.E. Brownd, 1974. Goddard Earth models (5 and 6) Rep. X-921-74-145, Goddard Space Flight Center Greenbelt, Md.

Lewis, B.T.R. and L.M. Dorman, 1970. Experimental Isostasy 2. An isostatic model for the USA derived from gravity and topographic data, J. Geophys. Res. 75, 3367-3386.

Marsh, J.G. and S. Vincent, 1974. Global detailed geoid computation and model analysis, Geophysical Surveys, 1, 481-511.

Marsh, J.G., G.H. Wyatt, T.V. Martin, J.J. McCarthy and P.S. Choritz, 1977. Sea-surface estimation in the North Atlantic using GEOS-3 altimeter data, preprint.

Martin, C.F. and M.L. Butler, 1977. Calibration results for the GEOS-3 altimeter NASA contractor report, NASA CR-141430, 86p.

McGoogan, J.T., C.D. Leitao and W.T. Wells, 1975. Summary of SKYLAB S-193 altimeter altitude results, NASA Technical Memorandum, NASA TM X-69355, 323p.

McKenzie, D.P. and C. Bowin, 1976. The relationship between bathymetry and gravity in the Atlantic Ocean, J. Geophys. Res., 81, 1903-1915.

McKenzie, D.P., 1977. Surface deformation, gravity anomalies and convection, Geophys. J. R. astr. Soc. 48, 211-238.

Sclater, J.G., Lawver, L.A. and B. Parsons, 1975. Comparison of long wavelength residual elevation and free-air gravity anomalies in the North Atlantic and possible implications for the thickness of the lithospheric plate, J. Geophys. Res. 80, 1031-1052.

Talwani, M, H.R. Poppe and P.D. Rabinowitz, 1972. Gravimetrically determined geoid in the western North Atlantic in Sea Surface Topography from Space, 2, NOAA Tech. Report ERL-228-AOML 7-2, 1-34.

Vening Meinesz, F.A., 1941. Gravity over the Hawaiian Archipelago and over the Madiera area: conclusions about the Earth's crust, Proc. Kon. Ned. Akad. Wetensia, 44p.

Wagner, C.A., F.J. Lerch, J.E. Brownd and J.A. Richardson, 1976. Improvement in the geopotential derived from satellite and surface data (GEM-7 and 8). NASA/GSFC Doc. x-921-76-20, Greenbelt, Md.

Walcott, R.I., 1970. Flexural rigidity, thickness and viscosity of the lithosphere, J. Geophys. Res. 75, 3941-3954.

Watts, A.B. and J.R. Cochran, 1974. Gravity anomalies and flexure of the lithosphere along the Hawaiian-Emperor seamount chain, Geophys. J. R. astr. Soc. 38, 119-141.

Watts, A.B., 1976. Gravity and bathymetry in the Central Pacific Ocean, J. Geophys. Res. 81, 1533-1553.

Watts, A.B., An analysis of isostasy in the world's oceans: Part 1. Hawaiian-Emperor Seamount Chain, Submitted to J. Geophys. Res.

Worzel, J.L., 1965. Pendulum gravity measurements at sea 1936-1959, J. Wiley, New York, 422p.

Figure Captions

Figure 1. GEOS-3 satellite radar altimeter profiles of the Hawaiian-Emperor seamount chain used in this study. The "observed" geoid profiles are plotted along each satellite pass. An arbitrary constant value has been subtracted from each profile. The seamount chain is associated with a short-wavelength ($\lambda \sim 400$ km) geoid high of 5 to 12 meters and a flanking geoid low of 1 to 4 meters. These geoidal undulations are superimposed in profiles G2676, G0843, G0644 and G1113 on a long-wavelength ($\lambda \sim 2600$ km) geoid high of 4 to 7 meters associated with the Hawaiian swell (Betz and Hess, 1942). The bathymetry is at 1000 fathom intervals and is based on Chase et al. (1970).

Figure 2. Altimetry and topography profile G0644 (Fig. 1) of the Line Islands, Hawaiian Ridge and Murray Fracture Zone. The altimeter profile has had the GEM 6 Earth model (Wagner et al., 1976) subtracted from it. The topography profile has been constructed using contour maps of Chase et al. (1970). Heavy dots indicate the location of individual contours. The Hawaiian Ridge and Line Islands are associated with geoid highs of 6 and 2 meters respectively. The Musician seamounts and the Murray Fracture Zone, however, are not associated with prominent geoid highs or lows.

Figure 3. Projected altimetry and topography profiles of the Hawaiian-Emperor seamount chain. Each profile has been projected normal to the local trend of the ridge (Table 1) and extends 400 km either side of the ridge crest.

Figure 4. Theoretical geoid profiles over a 60 km wide seamount for different assumed values of the effective flexural rigidity of the lithosphere D. The profiles were computed using a line-integral method for the determination of the disturbing potential.

Figure 5. Theoretical filter for an effective elastic thickness T_e = 25 km. The filter was obtained by inverse Fourier trensforming the admittance Z(K) due to the plate model (McKenzie and Bowin, 1976). The parameters assumed in the computation are summarized in Table 2. The filter can be considered an impulse function representing the gravity effect of a line load. Therefore the filter peak represents the gravity effect of the load and the filter side lobes represent the effect of its compensation.

Figure 6. Difference geoid, "observed" geoid, filtered topography, and "observed" topography for profiles G2676, G0843, G0644 and G0878 of the Hawaiian Ridge (Figs. 1,3). The "observed" geoid and topography profiles are the observed profiles in Figure 3 with their mean and trend removed. The mean removed is indicated to the right of each profile in meters. The filtered topography is an estimate of the geoid produced by convolving theoretical filters (for example, Fig. 5) with each "observed" profile. The difference geoid is the difference between "observed" geoid and filtered topography. The elastic thickness T_e was estimated for each profile as that value which best minimized the difference geoid. The variance associated with the best fitting value is shown to the right of the difference geoid and does not exceed 80 cms on any of the profiles. The difference geoid therefore represents that part of the "observed" geoid which cannot be explained by the elastic plate model.

Figure 7. "Observed" geoid for profile G1695 of the Emperor Seamounts and profile G1113 of the Hawaiian Ridge compared to theoretical profiles. The fits between observed and calculated are poor, and these profiles could not be used to estimate a best fitting elastic plate thickness.

Figure 8. Observed admittance values Z(K) (solid dots) generated from altimetry and topography profiles 1, 2, 3 and 5 in Figure 6. The standard error on each estimate is computed from the coherence (Table 3) assuming a normal probability distribution for the ratio of true/sample admittance (Munk and Cartwright, 1966). The solid lines represent theoretical models based on the plate model for an assumed mean water depth of 4.335 km, density of topography of 2.80 g cm^{-3} (Watts, in preparation) and effective elastic thickness values of T_e = 20, 30 and 40 km.

Figure 9. Plot of isotherms for a simple cooling plate model. The assumed initial temperature is 1325°C, heat capacity is 0.3 Cal. g^{-1} $°C^{-1}$ and thermal conductivity is 7.5×10^{-3} Cal $°C^{-1}$ cm^{-1} s^{-1}. Lithospheric thickness estimates deduced from short period (20 to 200 sec) Rayleigh wave dispersion data summarized in Forsyth (1977). Unfilled triangles represent elastic thickness estimates determined from gravity and bathymetry studies in the Pacific ocean (Watts, in preparation). The filled triangle represents elastic thickness estimates based on Figure 6.

C-3

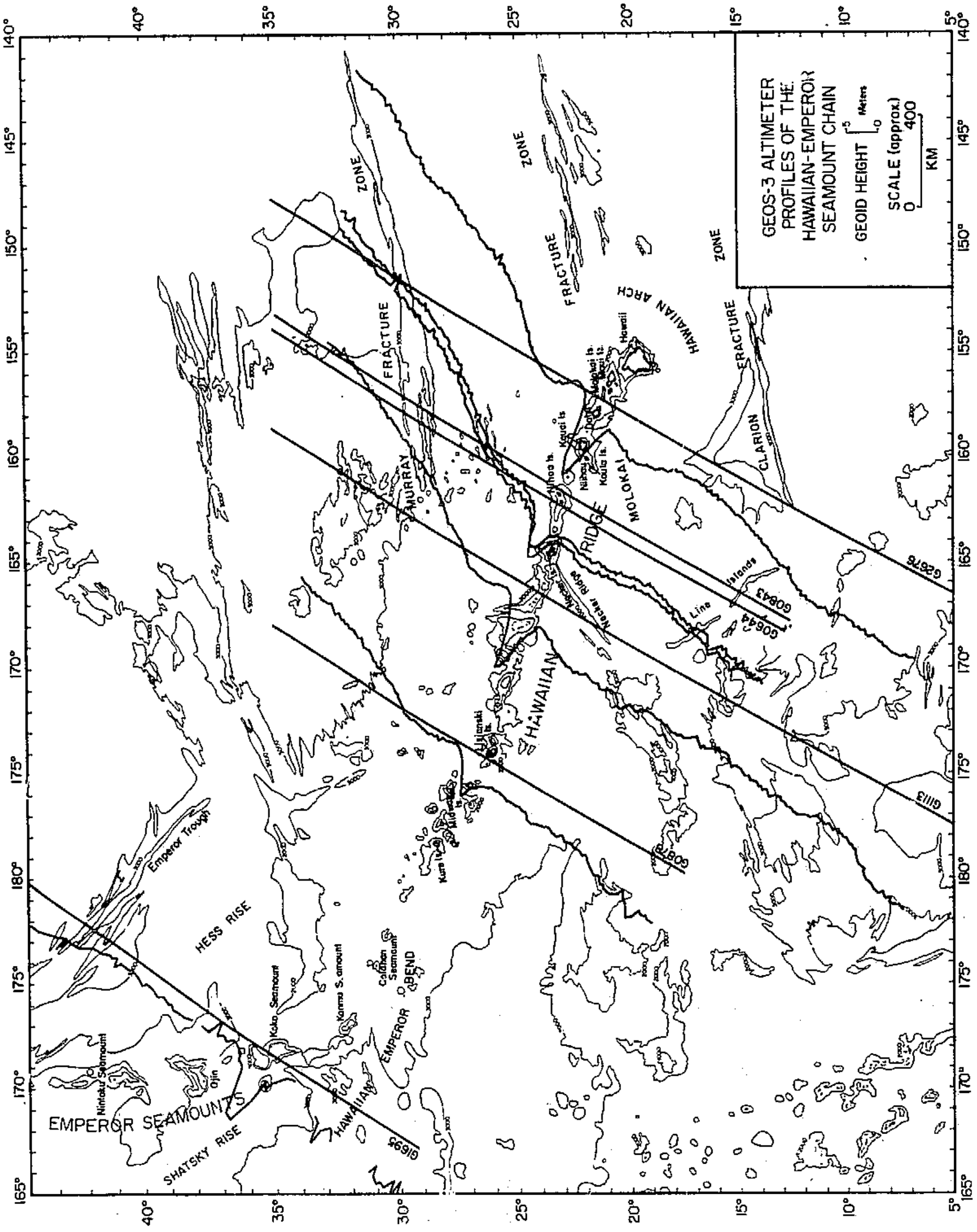
GEOS-3 ALTIMETER PROFILES OF THE HAWAIIAN-EMPEROR SEAMOUNT CHAIN
GEOID HEIGHT 5 Meters 0
SCALE (approx.) 0 400 KM
ZONE
FRACTURE
ZONE
FRACTURE
ZONE
FRACTURE
HAWAIIAN ARCH
Hawaii
Molokai Is.
Maui Is.
Oahu
Kauai Is.
Niihau Is.
Kaula Is.
Nihoa Is.
MOLOKAI
CLARION
MURRAY
RIDGE
HAWAIIAN
Necker Ridge
Line Islands
G2676
G0643
G0644
G1113
G0878
G1695
Lisianski Is.
Midway Is.
Kure Is.
Emperor Trough
HESS RISE
Koko Seamount
Kanmu Seamount
Colahan Seamount
BEND
EMPEROR
Ojin
Nintoku Seamount
EMPEROR SEAMOUNTS
SHATSKY RISE
HAWAIIAN
140°
145°
150°
155°
160°
165°
170°
175°
180°
175°
170°
165°
40°
35°
30°
25°
20°
15°
10°
5°

Figure 1

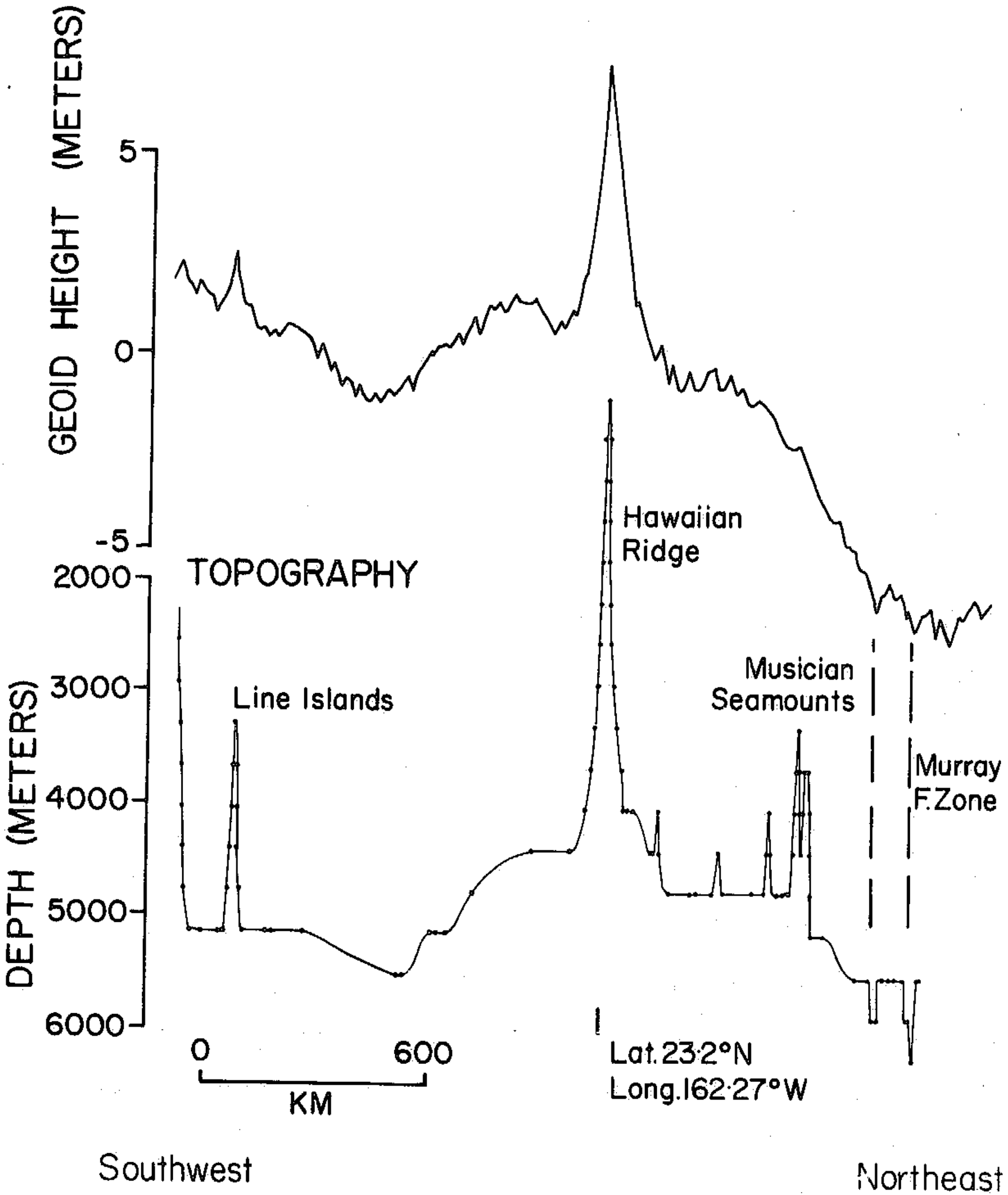
GEOID HEIGHT (METERS)
5
0
-5
TOPOGRAPHY
2000
3000
4000
5000
6000
DEPTH (METERS)
Line Islands
Hawaiian
Ridge
Musician
Seamounts
Murray
F.Zone
0
600
KM
Lat. 23.2°N
Long. 162.27°W
Southwest
Northeast

Figure 2

[redacted]

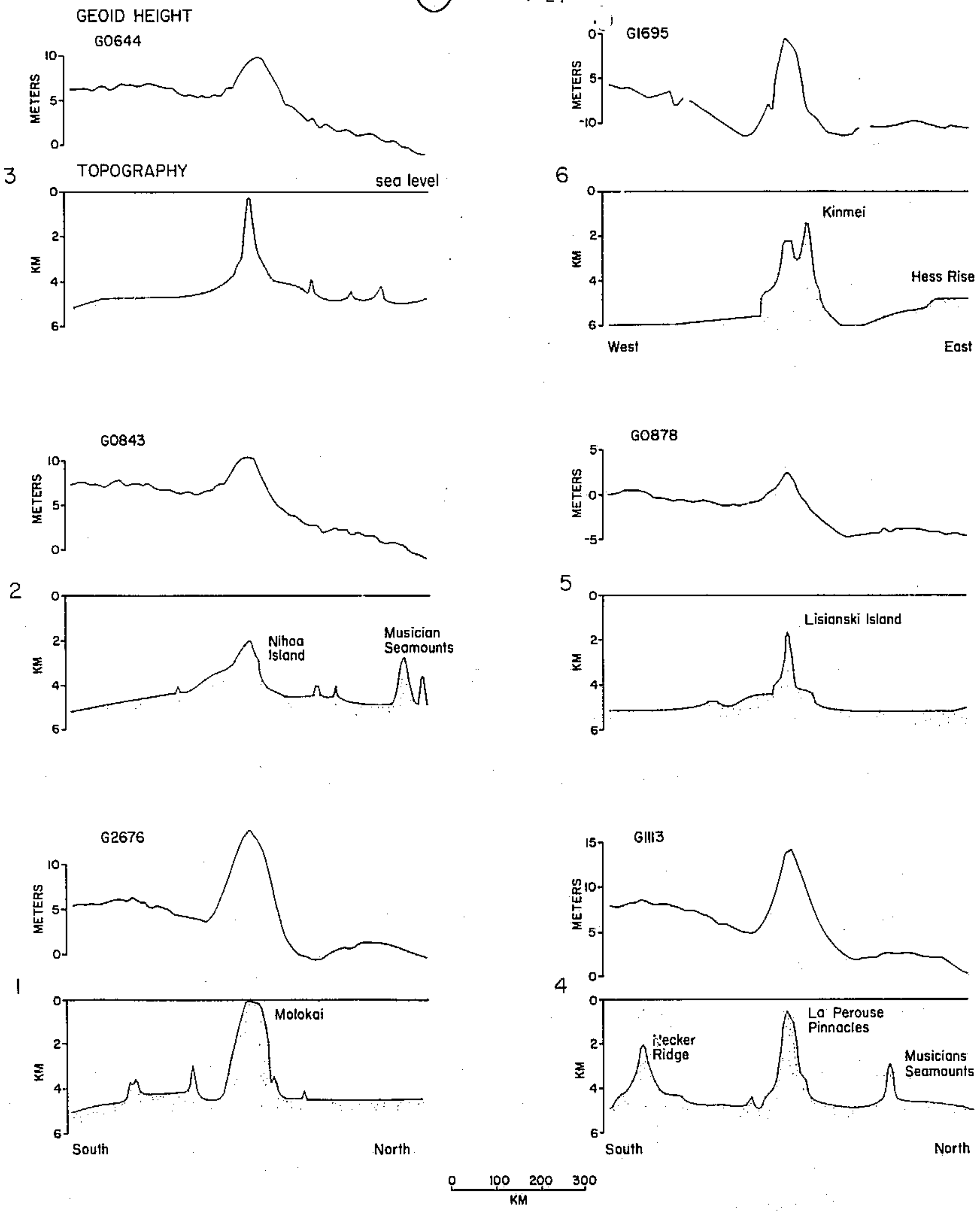

Figure 3

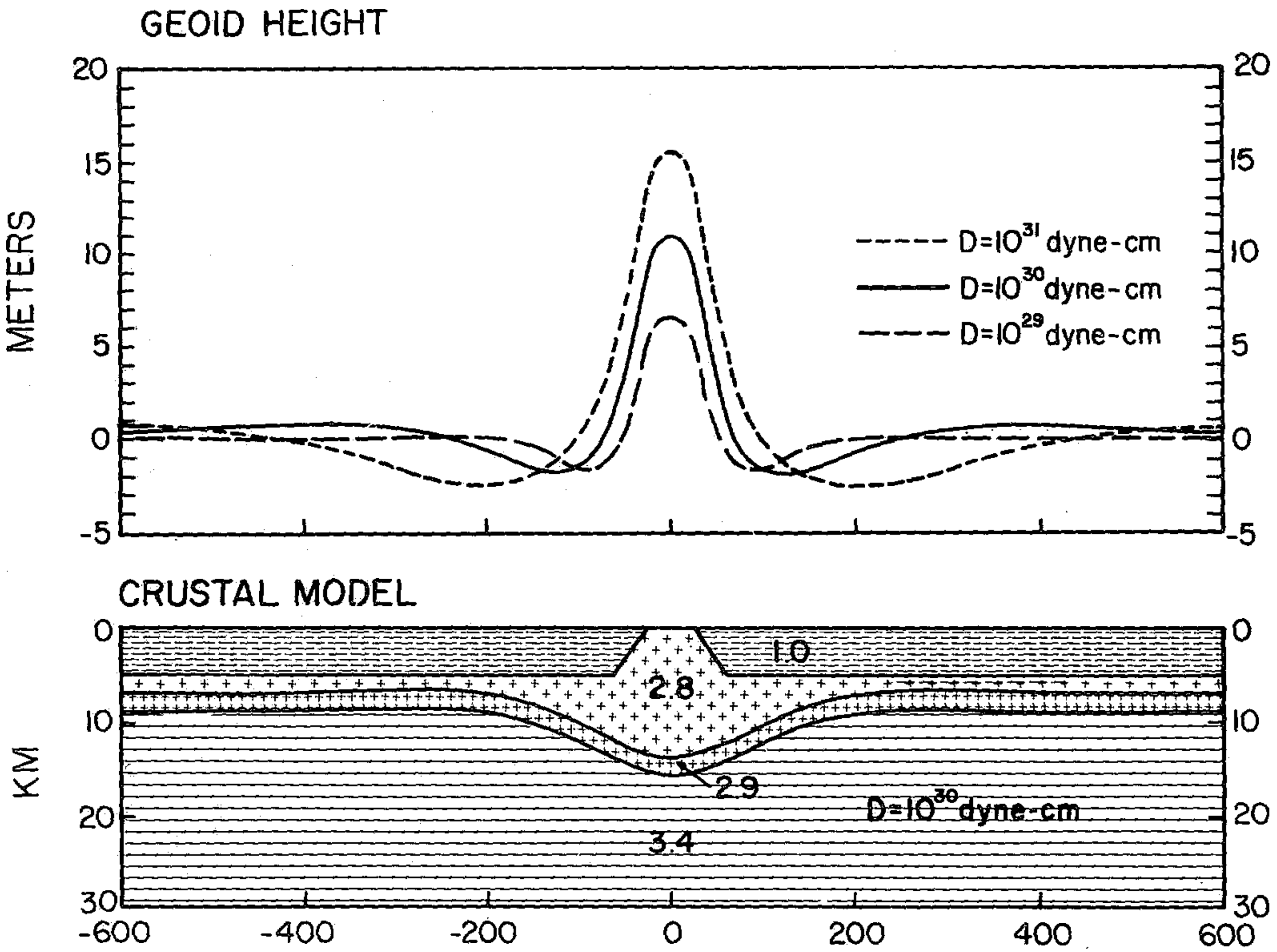
GEOID HEIGHT
METERS
20
15
10
5
0
-5
D=10^{31} dyne-cm
D=10^{30} dyne-cm
D=10^{29} dyne-cm
CRUSTAL MODEL
KM
0
10
20
30
1.0
2.8
2.9
3.4
D=10^{30} dyne-cm
-600
-400
-200
0
200
400
600

Figure 4

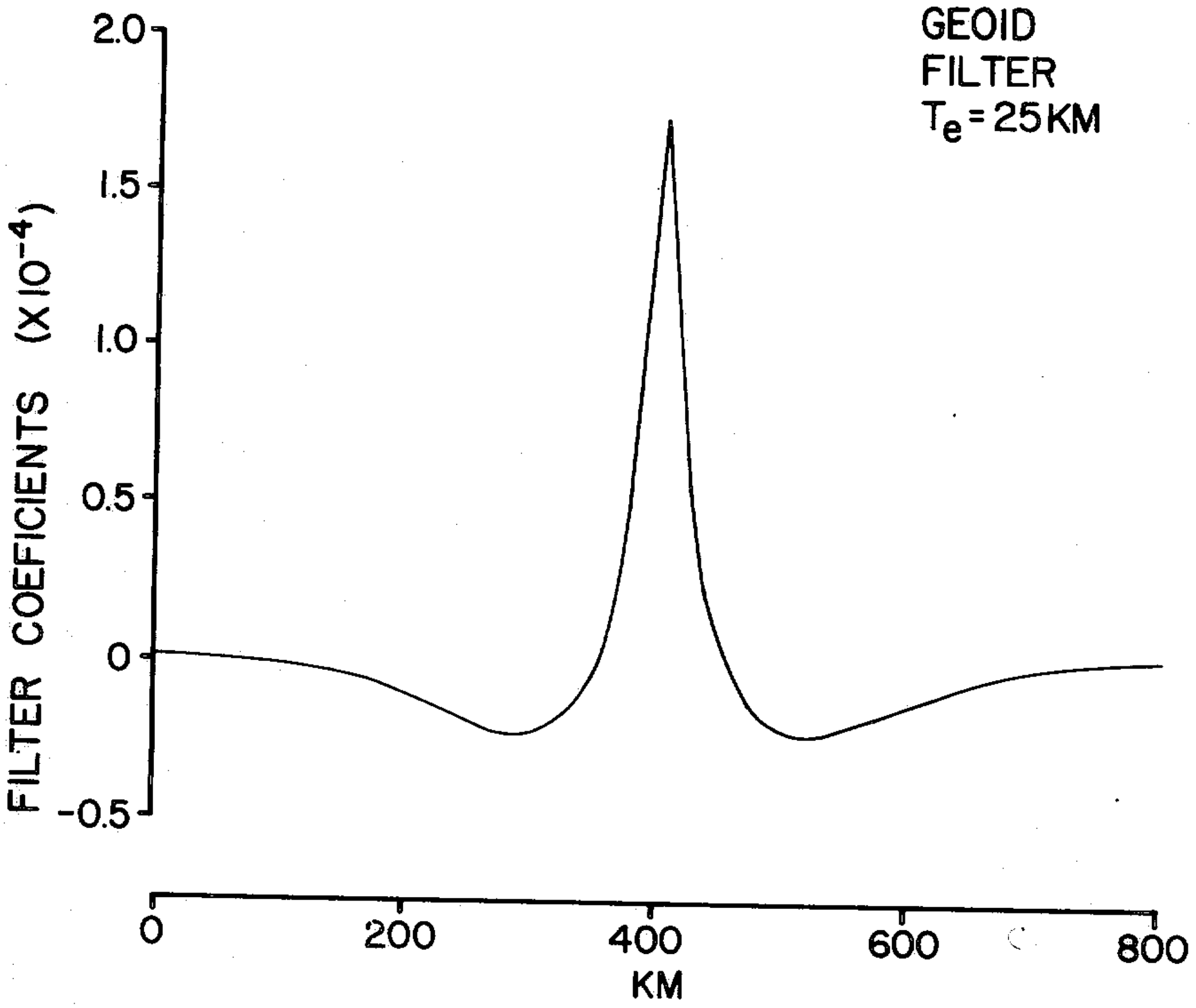
GEOID
FILTER
T_e=25KM
FILTER COEFICIENTS (X10^{-4})
2.0
1.5
1.0
0.5
0
-0.5
0
200
400
600
800
KM

Figure 5

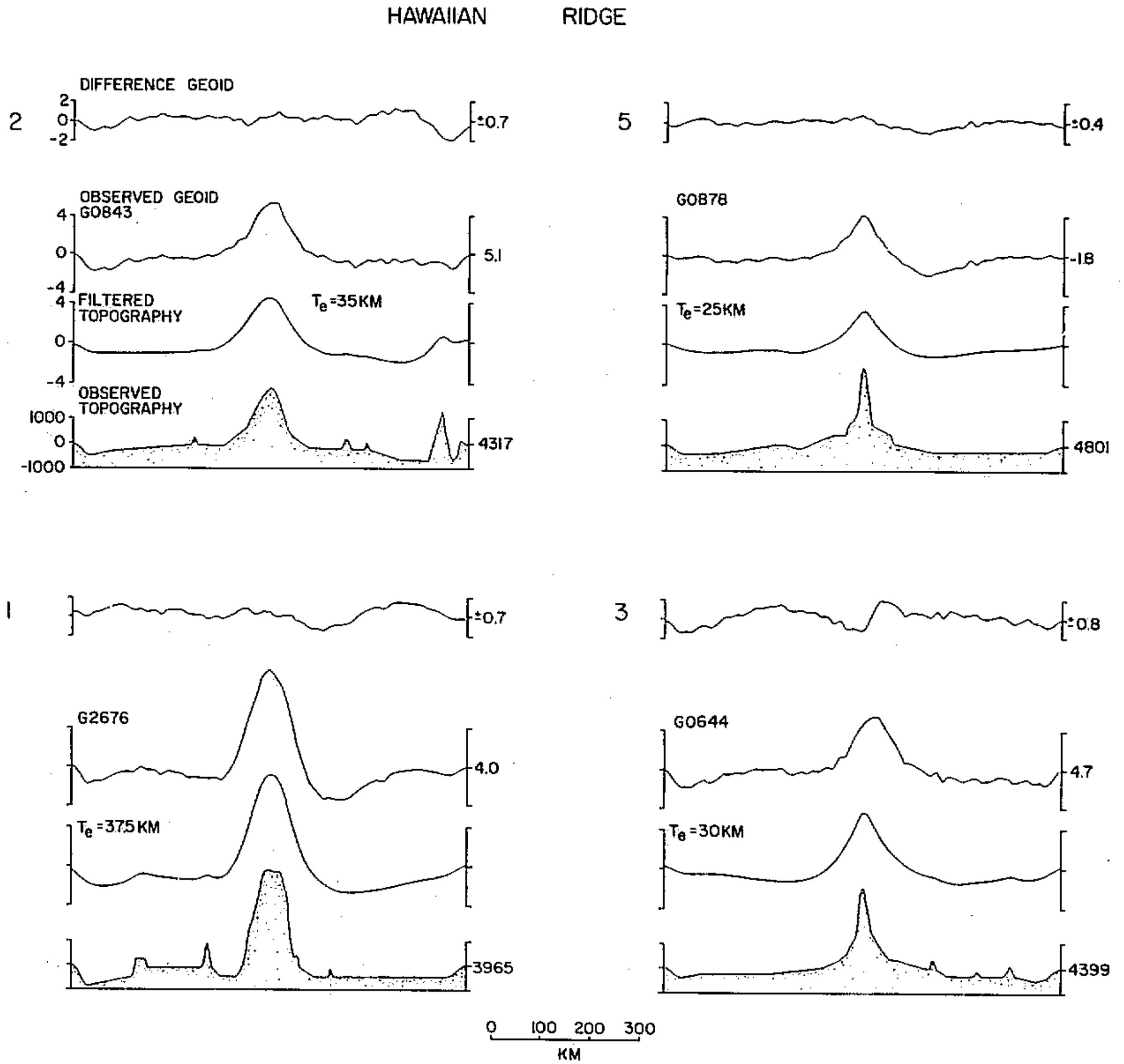
HAWAIIAN RIDGE
DIFFERENCE GEOID
2
2
0
-2
±0.7
OBSERVED GEOID
G0843
4
0
-4
5.1
FILTERED
TOPOGRAPHY
T_e=35KM
4
0
-4
OBSERVED
TOPOGRAPHY
1000
0
-1000
4317
5
±0.4
G0878
-1.8
T_e=25KM
4801
1
±0.7
G2676
4.0
T_e=37.5KM
3965
3
±0.8
G0644
4.7
T_e=30KM
4399
0
100
200
300
KM

Figure 6

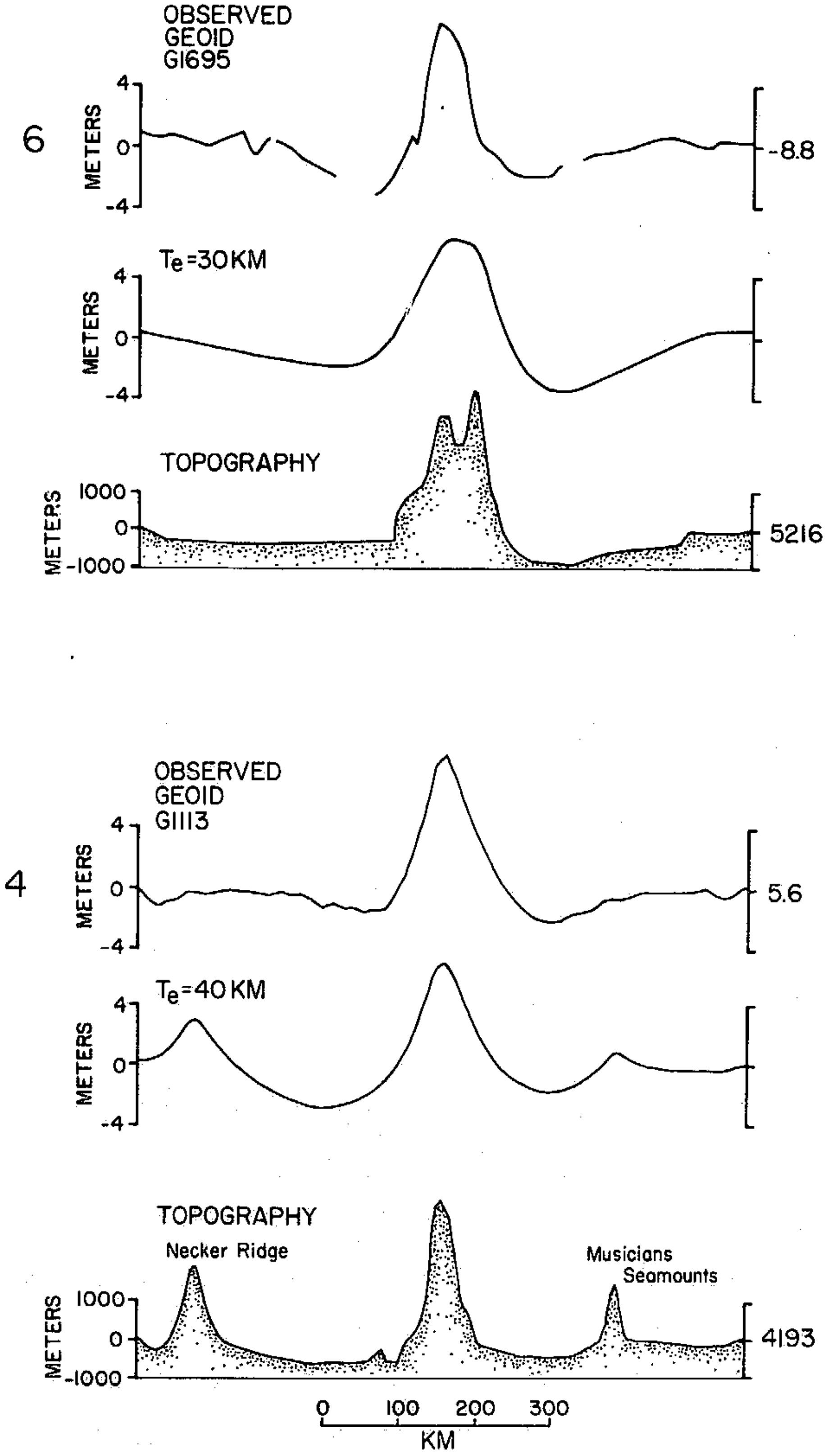
6
OBSERVED GEOID G1695
METERS
4
0
-4
-8.8
Te=30KM
METERS
4
0
-4
TOPOGRAPHY
METERS
1000
0
-1000
5216
4
OBSERVED GEOID G1113
METERS
4
0
-4
5.6
Te=40KM
METERS
4
0
-4
TOPOGRAPHY
Necker Ridge
Musicians Seamounts
METERS
1000
0
-1000
4193
0
100
200
300
KM

Figure 7

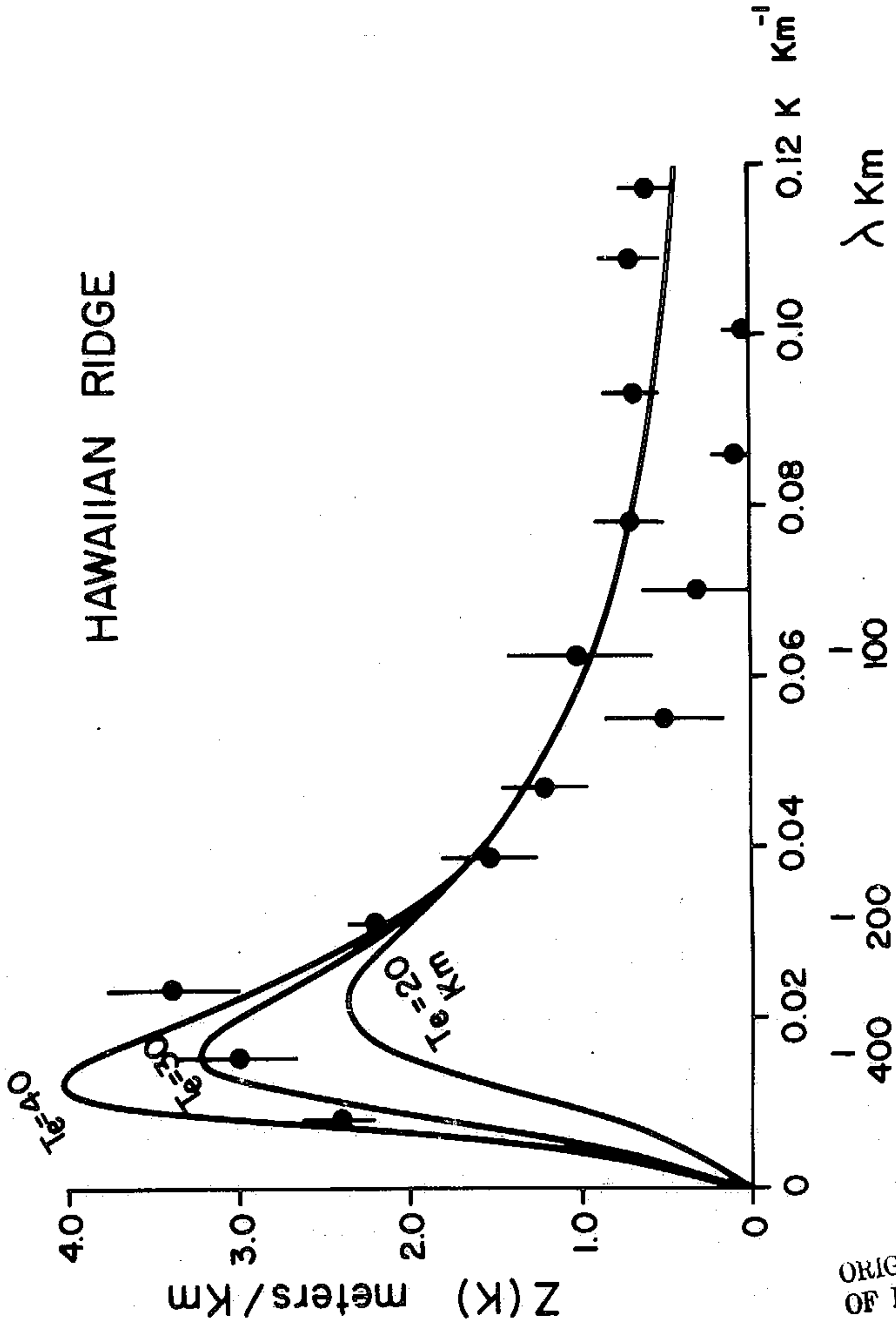
HAWAIIAN RIDGE
Z (K) meters / Km
4.0
3.0
2.0
1.0
0
0
0.02
0.04
0.06
0.08
0.10
0.12 K Km^{-1}
400
200
100
λ Km
Te=40
Te=30
Te=20 Km

Figure 8

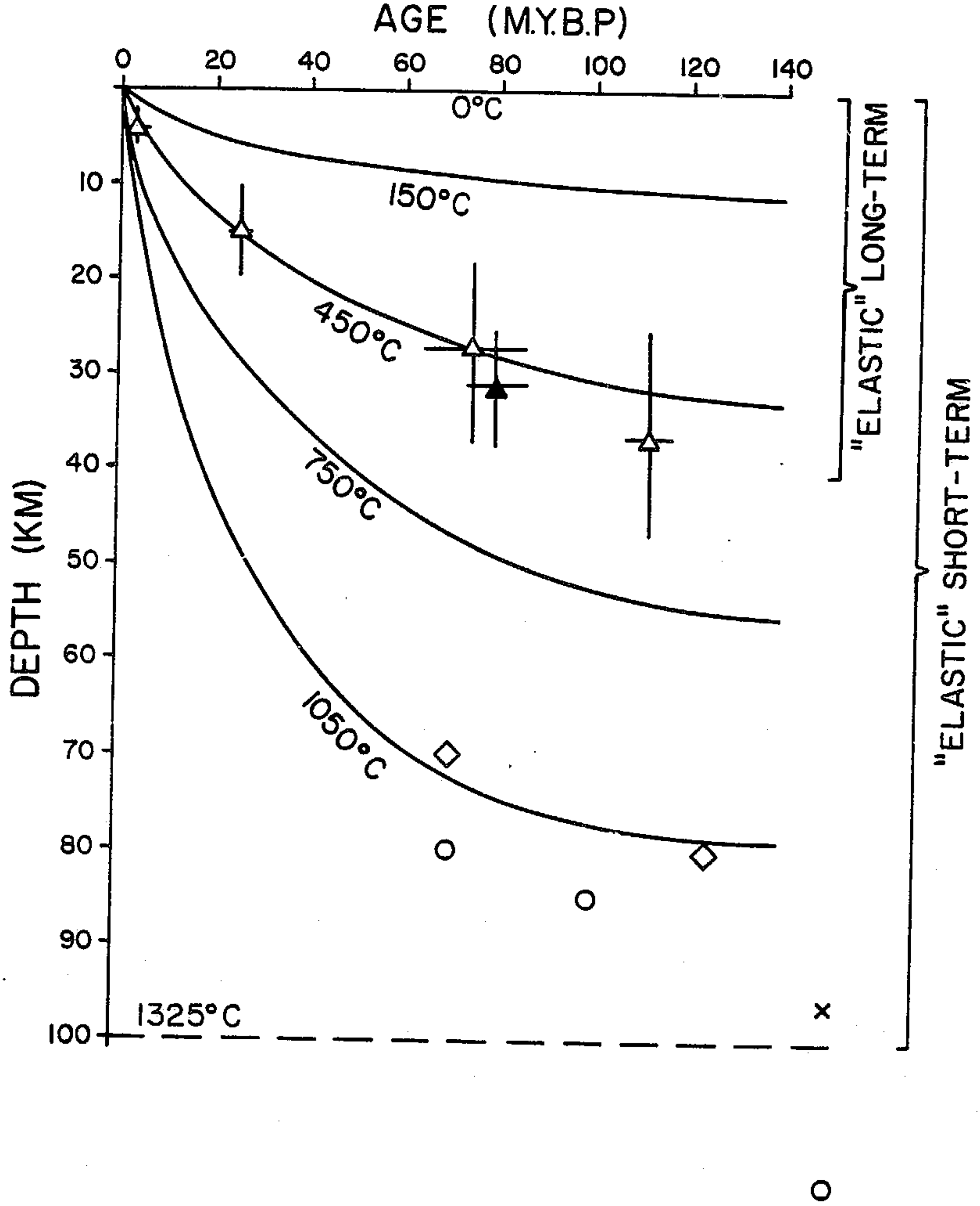
AGE (M.Y.B.P)
0
20
40
60
80
100
120
140
0°C
150°C
450°C
750°C
1050°C
1325°C
DEPTH (KM)
10
20
30
40
50
60
70
80
90
100
"ELASTIC" LONG-TERM
"ELASTIC" SHORT-TERM

Figure 9

TABLE 1

SUMMARY OF GEOS-3 ALTIMETER DATA USED IN FIGURE 3

PROFILE	ORBIT NUMBER	LAMONT NUMBER	YEAR	JULIAN DAY	PROJECTED PROFILE PARAMETERS			
					LAT.	LONG.	APPROX. TIME (SECS.)	AZIMUTH
1	2361	G2676	1975	266	21.098	-157.418	76680.6	200.0
2	1821	G0843	1975	228	23.000	-161.700	62015.9	190.5
3	2674	G0644	1975	289	23.022	-162.881	960.3	190.5
4	2859	G1113	1975	302	23.932	-166.586	7553.0	198.5
5	599	G0878	1975	142	26.277	-174.492	29474.3	196.5
6	1993	G1695	1975	240	35.300	171.550	75398.8	84.5

TABLE 2

SUMMARY OF PARAMETERS ASSUMED IN MODEL COMPUTATIONS

Thickness of Layer 2 = 1.5 km

Mean thickness of oceanic crust = 5 km

Density of mantle = 3.4 g cm^{-3}

Density of Layer 3 = 2.9 g cm^{-3}

Density of topography = 2.8 g cm^{-3}

Mean water depth = 4.3 km

Young's Modulus = 10^{12} dyn cm^{-2}

TABLE 3

SPECTRAL ESTIMATES FOR GEOS-3 ALTIMETER PROFILES

1, 2, 3 and 5 for $0.078 < K < 0.0626$

WAVENUMBER K km^{-1}	COHERENCE γ^2	PHASE ϕ	SAMPLE ADMITTANCE METERS/KM	NOISE PARAMETER σ
0.0078	0.929	-3.1	2.4	0.097
0.0156	0.910	-6.3	3.0	0.111
0.0235	0.915	-2.1	3.4	0.107
0.0313	0.972	8.4	2.2	0.060
0.0391	0.747	3.3	1.5	0.206
0.0469	0.780	7.1	1.2	0.187
0.0548	0.198	33.9	0.5	0.711
0.0626	0.392	6.2	1.0	0.440

FUTURE DIRECTIONS IN SATELLITE ALTIMETRY

The Relative Usefulness of Surface Ship Data, Altimeter Data and Data from the Observation of Satellite Orbits

Geoidal undulations can be obtained by other methods than the altimeter. It is well known that if the gravity anomalies were known at all points in the earth's surface, the Stokes theorem can be utilized to obtain the geoidal heights at all points. Or, if the geopotential were known to harmonics of high enough order and degree from studies of satellite orbits again the geoid height is determined at all points from the earth's surface. In order, therefore, to establish the utility of altimeter data we first have to show that these data give better information in some cases about the earth's gravity field than can be obtained by other methods.

As far as the determination of the field from the study of satellite orbits is concerned, it is recognized that for spherical harmonics of order and degree less than 10 this is the best method. Beyond (10,10) or perhaps (16,16) only a few of the spherical harmonic coefficients are determined from orbit studies with unchallenged accuracy and in the past, combination solutions which utilize surface gravity data have been used for establishing the field corresponding to shorter wavelengths.

The general approach in the past for estimating geoid heights at short wavelengths and thereby establishing the usefulness of the altimeter data has been to use some model (such as is based on Kaula's rule) for the earth's gravitational field. In the following we have used a slightly different approach to establishing the usefulness of geoid data. Without making any assumptions regarding the amplitudes of gravity anomalies or geoid undulations at different wavelengths, we ask the question - which method - surface ship gravity measurement or the geoid determined by the altimeter - is more sensitive in terms of the minimum anomaly resolvable by either method, at any given wavelength. If Δg_n is amplitude of the gravity anomaly corresponding to spherical harmonic of order n then $(\Delta g_n) = \frac{g}{r_e} \times (n-1)\, N_n$ where g is the value of gravity of the earth, and r_e is the radius of the earth and N_n is the geoidal undulation corresponding to Δg_n. If we further assume that surface ship gravity data are able to resolve anomalies of 10 mgal in amplitude and that the altimeter can resolve undulations of 1.25 m, then it is easily seen that the wavelength of 640 km corresponding to n = 62 the surface ship gravity and the altimeter method are equally sensitive. For wavelengths higher than that the altimeter method is more sensitive and for wavelengths lower than that the surface gravity method is more sensitive. This is shown graphically in Figures 1 and 2.

However, for three reasons the altimeter geoid measurements may be more useful than the surface gravity measurements even at wavelengths shorter than 640 km (say in the range 200-640 km):

(i) poor coverage of surface gravity in large parts of the world's oceans. Figure 3 shows how large portions of the Pacific, S. Atlantic, Indian and even the central Atlantic are inadequately covered.

(ii) shorter wavelengths (less than 200 km) generally dominate the surface gravity measurements. Not only do they constitute "noise" as far as anomalies of intermediate wavelength are concerned, they demand a closer sampling interval than would otherwise be necessary because of aliasing problems.

(iii) the altimeter may be able to resolve undulations that are even smaller than 1.25 m.

Mid Ocean Ridges

Mid ocean ridges comprise a fundamental geological unit of the earth's surface. An understanding of the structure, composition and the stresses associated with the ridge system are basic to our understanding of how the ridge system comes about and what is the driving mechanism for the plates.

Potentially, a most powerful geophysical method in the study of the lithosphere and the asthenosphere underlying this ridge is the gravity method. But this method has been hindered by a lack of gravity coverage over a major part of the world's oceans and by the small amplitude of the intermediate wavelength gravity anomalies over the ridge especially in the presence of short wavelength gravity "noise" due to near surface features.

In the following we will show that there is a systematic gravity "signal" associated with mid ocean ridges, but that this signal is small and it has been difficult to separate it from noise. Because of the more complete coverage of the world's oceans by the altimeter than by surface ships and because the geoid undulations constitute a more powerful method of examining the wavelengths in question than gravity anomalies, it will be very productive to systematically study the altimeter geoid undulations over the mid ocean ridge system.

Figure 4 taken from a recent study by Cochran and Talwani (1977) summarizes the existing data from surface ships over the mid ocean ridges. It also indicates the problems in dealing with surface ship data where an examination of wavelength several hundreds of km is required.

Figure 4a shows plots of gravity anomaly (averaged over 1° x 1° squares of latitude and longitude) against the age of underlying basement (determined from independent studies of magnetic anomalies). There is a general decrease in gravity anomalies with distance away from the ridge crest but there is a large amount of scatter. The bars represent the standard derivations about mean values at selected isochrons. To remove some of the scatter, Figure 4b was constructed in which the curves were adjusted to superimpose where they level off at 40 m.y. The mean anomalies at various isochrons and the standard deviation are again shown as vertical bars. In addition an empirical gravity-age curve shown by the thick line in Figures 4a and b was selected (it passes roughly through the mean anomalies). This empirical curve is also shown separately in Figure 5, and has been subtracted from the curves in Figure 4c to obtain the residual anomaly versus age plots.

This procedure demonstrates the existence of a systematic relationship between gravity anomalies and distance from ridge crest, but it also demonstrates that the residual gravity anomalies which can be considered "noise" from the point of view of the study of gravity anomalies over ridges are as large in magnitude as the ridge anomalies. Furthermore, if we assume that 10 mgal anomalies are the smallest that can be detected over large regions from surface ship data (limit imposed by coverage and by instrument inaccuracies), then the signals that we are concerned with here are barely a factor of two greater than the minimum resolvable anomaly.

On the other hand, if we deal with the geoid at these wavelengths of interest, the amplitudes of the undulations relative to the minimum undulations resolvable by the altimeter can be larger. The empirical ridge anomaly has an amplitude of 20 mgal and can be considered to have a wavelength of 80 m.y. which corresponds to 800 km at a spreading rate of 1 cm/yr and a wavelength of 4000 km at a spreading rate of 5 cm/yr. The corresponding geoid undulations will be about 1.5 m and 7.5 m. These will, together with the large areal coverage give much more definite information about the ridge anomaly than the surface ship measurements. In particular, two questions which we cannot definitely answer from the gravity data - "is there a dependence of gravity anomalies on rate of spreading, and are flanking negative anomalies present as is demanded if the ridge is isostatically compensated," - should be answered from a study of the altimeter geoid data over the mid ocean ridge system.

Thus we believe that because of the extensive coverage of GEOS-3 altimeter data and because we expect the geoid undulation "signal" corresponding to the ridge anomaly to be large, the altimeter geoid represents the most useful method to systematically define the intermediate wavelength gravity signature of the mid ocean ridges. This will allow us to intercompare the gravity effects of different ridges; determine sensitivity to spreading rates and other parameters, and test evolutionary models for the ridges. Questions such as "are ridges isostatically compensated," "what are the stresses that the ridge anomalies imply" will be best answered from a study of the altimeter data.

Continental Margins

The rises and slopes of Atlantic-type continental margins are generally characterized by negative free-air gravity anomalies. These negative anomalies are particularly well developed off the east coast of the U.S. The corresponding geoidal undulations (see last chapter) indicate geoid highs over the shelf but lows over the rise and slope.

The geoidal signal is large enough that it can help understand the crustal structure of the continental margin in the following ways:

(i) Different crustal models yield different geoidal profiles (see last chapter). Hence the geoid height profile can serve as a constraint to crustal models.

(ii) From scattered gravity data it appears that a step in gravity occurs in many Atlantic-type continental margins between the area definitely known to be underlain by oceanic crust and the area landward of it. The origin of the latter area which is also often characterized by a magnetic quiet zone is a subject of considerable controversy - different authors have variously considered it oceanic crust, transitional crust or foundered continental crust. Examples of such areas occur south of Australia, south of India, south of South Africa, west of S. Norway, east of Newfoundland and west of Iceland. With the altimeter coverage that is available now and will be in the near future, it is possible to embark on a systematic examination of the portions of the Atlantic-type passive margins to outline areas of geoidal lows lying just landward of proven oceanic crust. These data will help define the "ocean-continent" boundary and provide constraints for the structure and origin of the area mentioned above.

(iii) It may be possible to interpret the details of the geoidal undulations in continental margin areas in terms of details of sedimentary patterns and history. This is an exciting possibility but we can only be sure that it is feasible when the details of geoidal undulations are available over extensive areas.

Geoidal studies in continental margin areas have implications regarding resource evaluation. If geoidal studies can help in distinguishing between foundered continental and true oceanic areas, the results could have profound significance in evaluating the hydrocarbon potential of the deep parts of the continental margins. If geoidal studies can help in unscrambling the details of sedimentary patterns and history, they could be of further use in resource-oriented studies.

Seamounts and Sedimentary Loads - Deformation of the Lithosphere

Geoidal data can be used in studies of the deformation of the lithosphere caused by surface loads such as sediments and seamounts. Preliminary model studies reveal that the geoid over seamounts is sensitive to the manner in which the seamount load is supported by the lithosphere. In the last chapter we briefly described the geoid data over Hawaii and indicated how such data might be useful for crustal studies.

Sediment loads such as those associated with Amazon and Niger deltas as well as sedimentary ridges such as the Blake Outer Ridge, may be expected to yield geoidal undulations of a few meters. (If we adopt a value of 500 km for wavelength and 50 mgal for amplitude of the gravity high over the body of thick sediments on the shelf and slope that are distributed by the Amazon, we expect a geoidal undulation of about 5m.) It may be possible to study the deformation of the lithosphere as well as determine the details of sedimentary loads from the altimeter geoids.

Deep Sea Trenches, Island Arcs, and Back Arc Basins

Small gravity anomalies that extend over large areas are associated with many features connected with island arcs and deep sea trenches.

The existing combination solutions show positive gravity anomalies associated with the general area of island arcs but it is not quite clear how much of the regional anomaly can be attributed to the "Outer High" seaward of trenches (Watts and Talwani, 1974) to the back arc basin and to the dipping lithospheric slab. Preliminary examination of the altimeter geoid shows gravity anomalies that are directly associated with the Outer High and with back arc basins. As in other areas, geoidal data are frequently more helpful than gravity data because of the dominance of smaller wavelength anomalies in the gravity data and the large spacing between ship tracks.

As an example of how the geoid data are better able to constrain deep crustal models than gravity data, note how the computed geoid height is more sensitive than the computed gravity anomaly to different choices in the depth of compensation in the Shikoku Basin of the Philippine Sea (see last chapter). The use of geoidal anomalies to similarly constrain deep crustal structure in other back arc basins could similarly be made.

Geoidal Anomalies and Mantle Convection

Recent numerical studies of convection in the Earth predict surface deformations of the plates and associated gravity anomalies. In one such study Parsons and Richter (1975) predict mantle convection at two scales, the shorter of these scales being of the order of 500-2000 km. In general because the gravity variations predicted for various schemes of mantel convection are expected to have wavelengths larger than 500 km, the altimeter is an excellent tool to look for geoid undulations attributed to mantle convection.

Summary

In presenting the background about the gravity field over important geological features in oceanic areas, we have demonstrated that we expect geoidal undulations in the wavelength range 500-4000 km that are large enough to be detected by the GEOS-3 altimeter. The specific tasks that can be tackled with this data are:

(i) Identifying a geoid anomaly associated with the mid ocean ridge system, investigating any dependence on spreading rates, searching for flanking negatives which would indicate isostatic compensation and constraining various models of the structure and evolution of the ridge by the geoidal data.

(ii) Investigating the geoidal undulation associated with continental margins, constraining models of the evolution and structure of the continental margins by the geoidal data, seeking the position and nature of the ocean-continent boundary from geoidal data.

(iii) Investigating the geoidal anomalies over discrete crustal loads such as seamounts and river deltas and solving for the value of flexural rigidity associated with the flexure of the lithosphere.

(iv) Identifying the various parts of the geoidal highs that are associated with deep sea trenches, island arcs and back arc basins. Identifying and interpreting geoid anomalies associated with back arc basins and outer highs.

(v) Identifying regular patterns of geoidal undulations in the Pacific Ocean that may be associated with mantle convection rolls.

References

Cochran, J.R. and Talwani, M., Free-air gravity anomalies in the world's oceans and their relationship to residual elevation. Geophys. J. R. Astr. Soc., v. 50, p. 495-552, 1977.

Kahle, H.-G. and Talwani, M., Gravimetric Indian Ocean Geoid. Zeitschrift fur Geophysik, Bank 39, Seite 167-187, 1973.

Kahle, H.-G., Chapman, M., and Talwani, M., Detailed 1° x 1° gravimetric Indian Ocean geoid and comparison with GEOS-3 radar altimeter geoid profiles. Geophys. J. R. Astr. Soc., in press.

Marsh, B.D. and Marsh, J.G., On global gravity anomalies and two-scale mantle convection. J. Geophys. Res., v. 81, p. 5267-5280, 1976.

Richter, F.M. and Parsons, B., On the interaction of two scales of convection in the mantle, J. Geophys. Res., v. 80, p. 2529-2541, 1974.

Talwani, M., Poppe, H.R., and Rabinowitz, P.D., Gravimetrically determined geoid in the western North Atlantic. Sea Surface Topography from Space, v. 2, NOAA Tech. Rept. ERL-288-AOML 7-2, p.1-34, 1972.

Watts, A.B. and Leeds, A.R., Gravimetric geoid in the Northwest Pacific Ocean. Geophys. J. R. Astr. Soc., in press.

Watts, A.B. and Talwani, M., Gravity anomalies seaward of deep-sea trenches and their tectonic implications. Geophys. J. R. Astr. Soc., v. 36, p. 57-90, 1974.

8-11

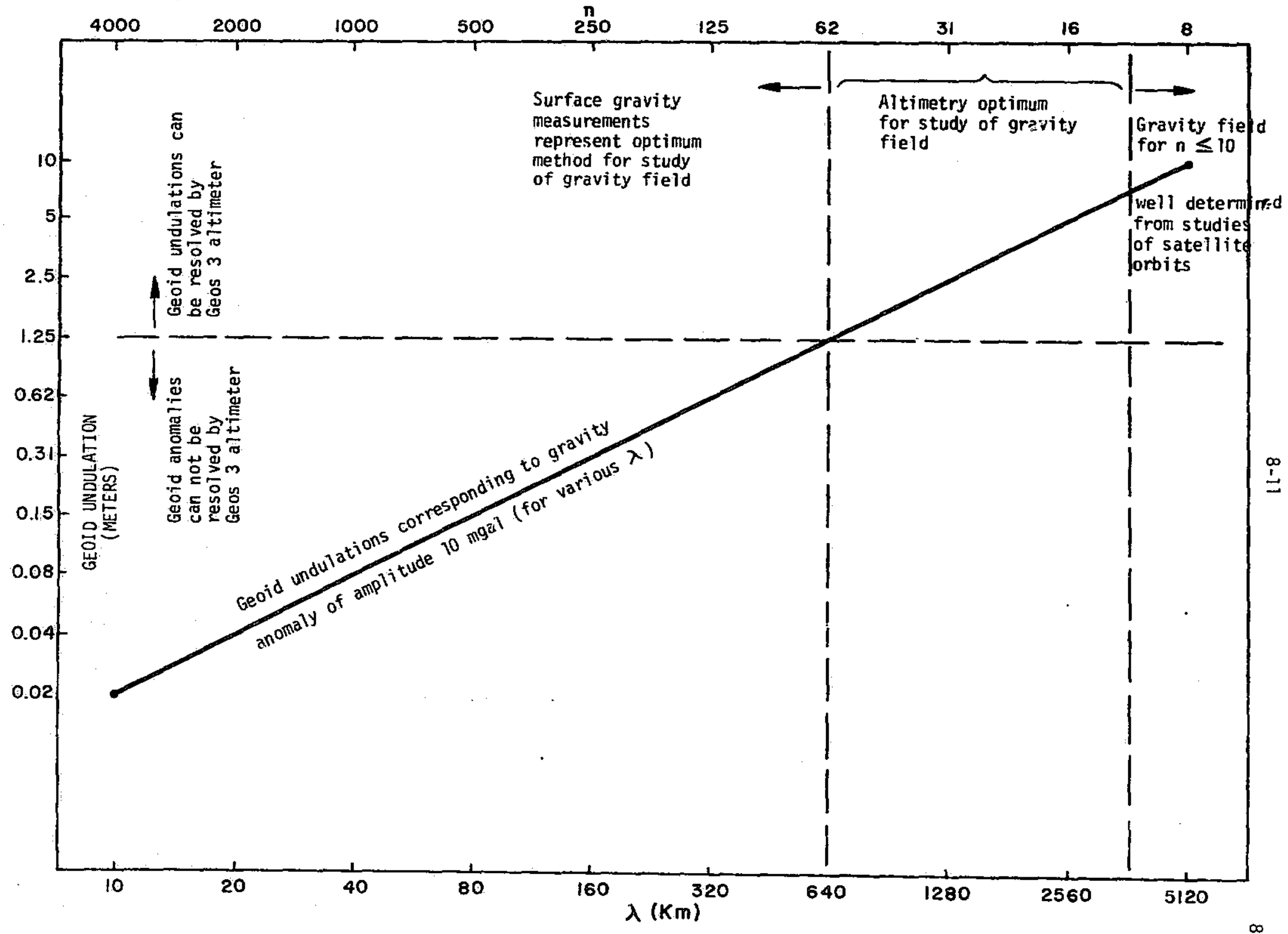
n
4000
2000
1000
500
250
125
62
31
16
8
Surface gravity measurements represent optimum method for study of gravity field
Altimetry optimum for study of gravity field
Gravity field for n ≤ 10
well determined from studies of satellite orbits
10
5
2.5
1.25
0.62
0.31
0.15
0.08
0.04
0.02
GEOID UNDULATION (METERS)
Geoid undulations can be resolved by Geos 3 altimeter
Geoid anomalies can not be resolved by Geos 3 altimeter
Geoid undulations corresponding to gravity anomaly of amplitude 10 mgal (for various λ)
10
20
40
80
160
320
640
1280
2560
5120
λ (Km)

Figure 1

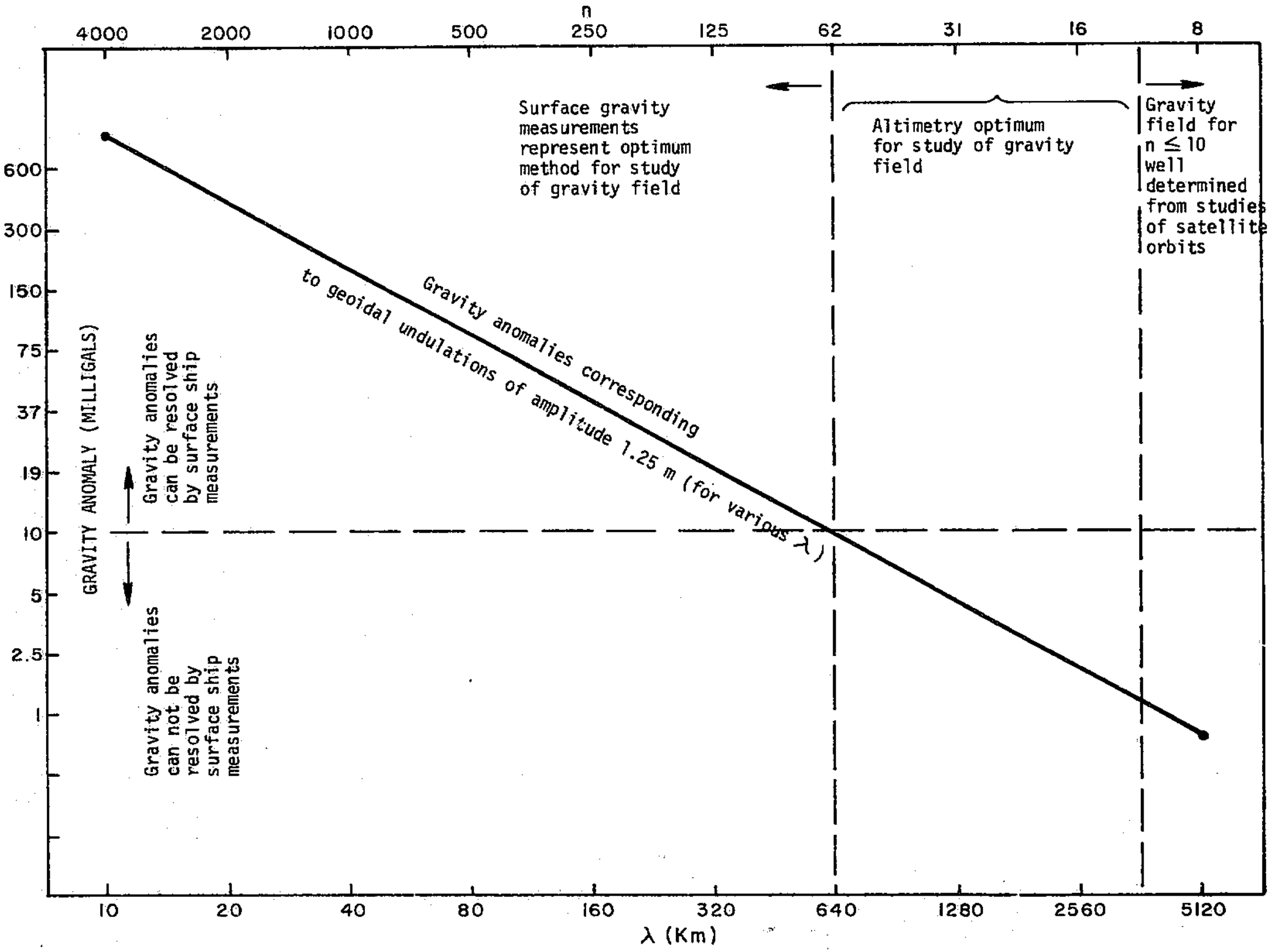
n
4000
2000
1000
500
250
125
62
31
16
8
Surface gravity measurements represent optimum method for study of gravity field
Altimetry optimum for study of gravity field
Gravity field for $n \leq 10$ well determined from studies of satellite orbits
GRAVITY ANOMALY (MILLIGALS)
600
300
150
75
37
19
10
5
2.5
1
Gravity anomalies corresponding to geoidal undulations of amplitude 1.25 m (for various λ)
Gravity anomalies can be resolved by surface ship measurements
Gravity anomalies can not be resolved by surface ship measurements
10
20
40
80
160
320
640
1280
2560
5120
λ (Km)

Figure 2

ORIGINAL PAGE IS OF POOR QUALITY

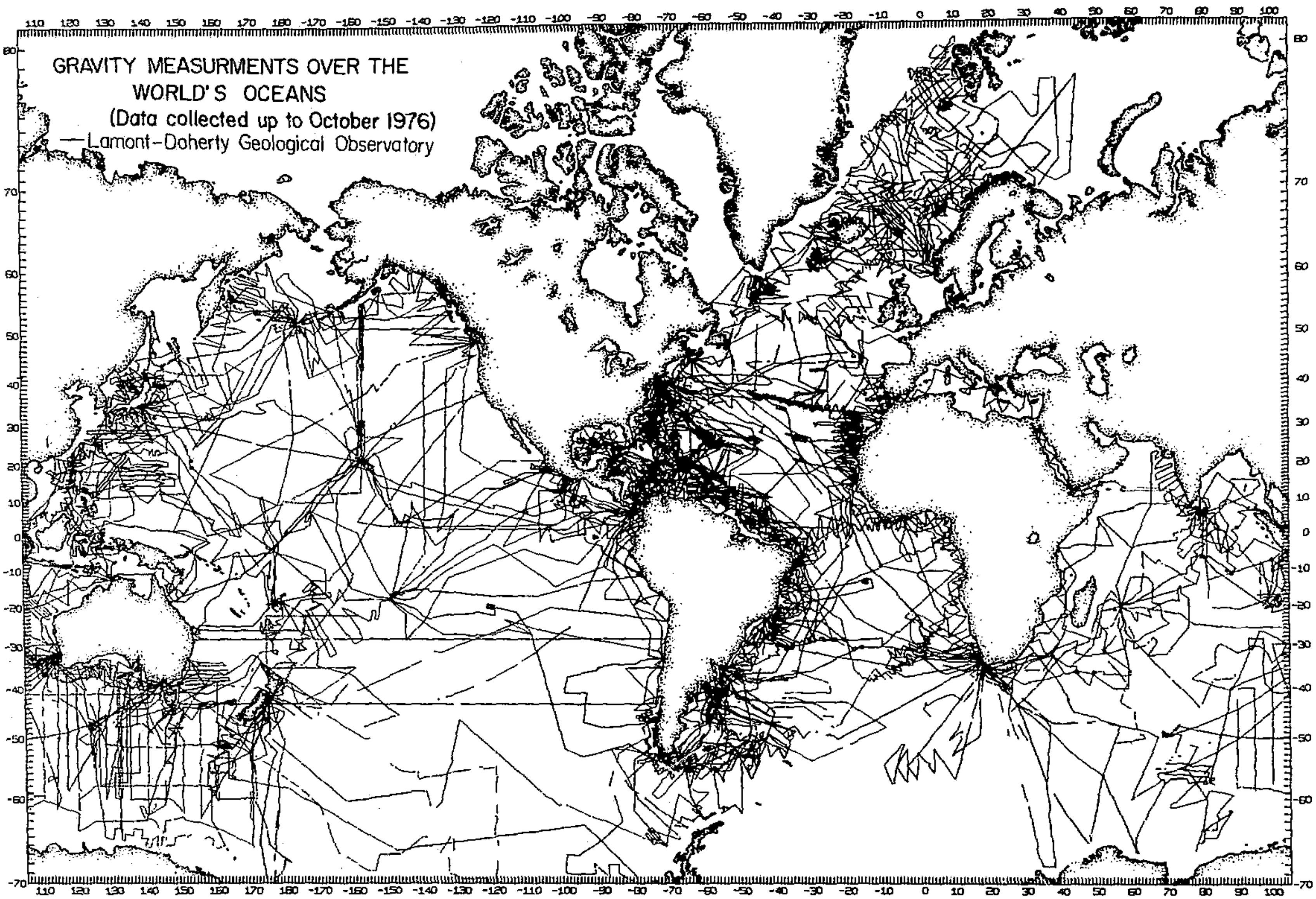

Figure 3

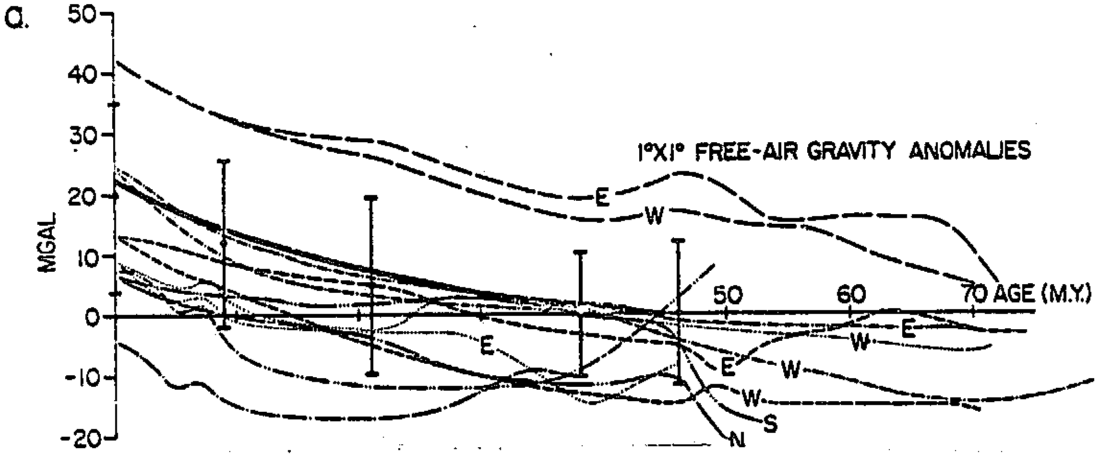

Figure 4a. 1° x 1° free air gravity anomalies over various ridges of the world's oceans. (Bars represent standard deviation about mean at selected isochrons; thick line represents empirical "ridge anomaly.")

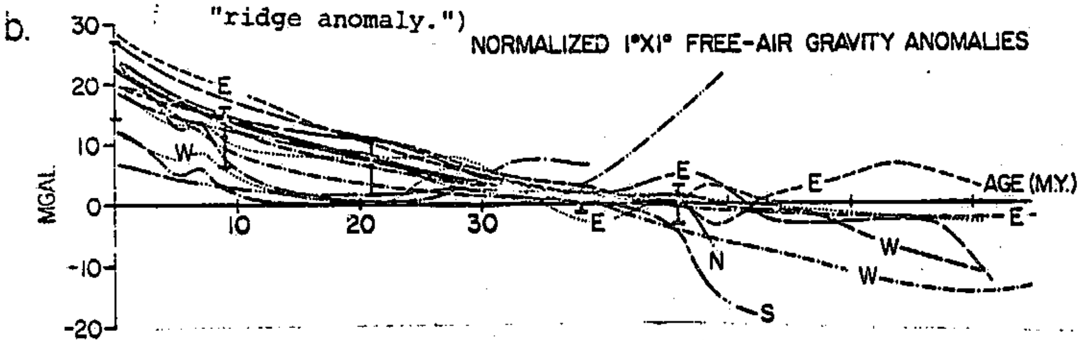

Figure 4b. The curves in Figure 4 have been adjusted to make them near zero at 40 m.y. where the curves are observed to flatten out.

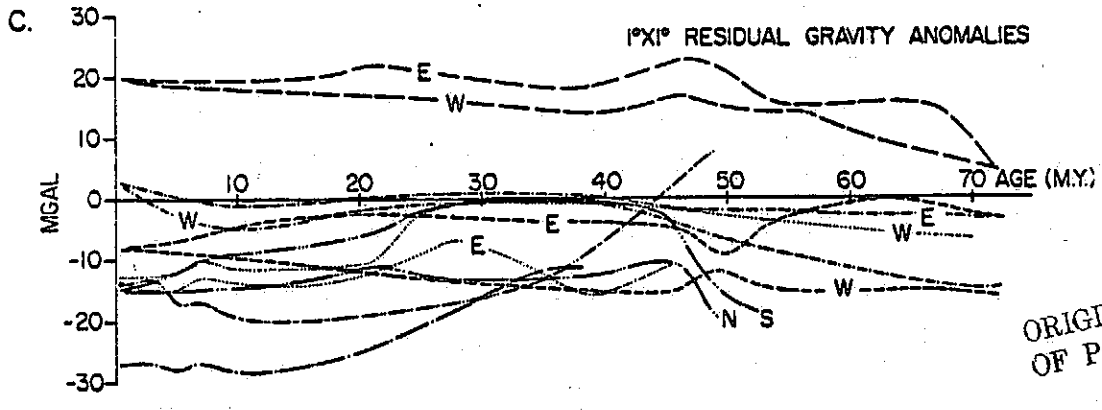

Figure 4c. The curve in Figure 4a after the "ridge anomaly" has been subtracted from them (after Cochran and Talwani, 1977).

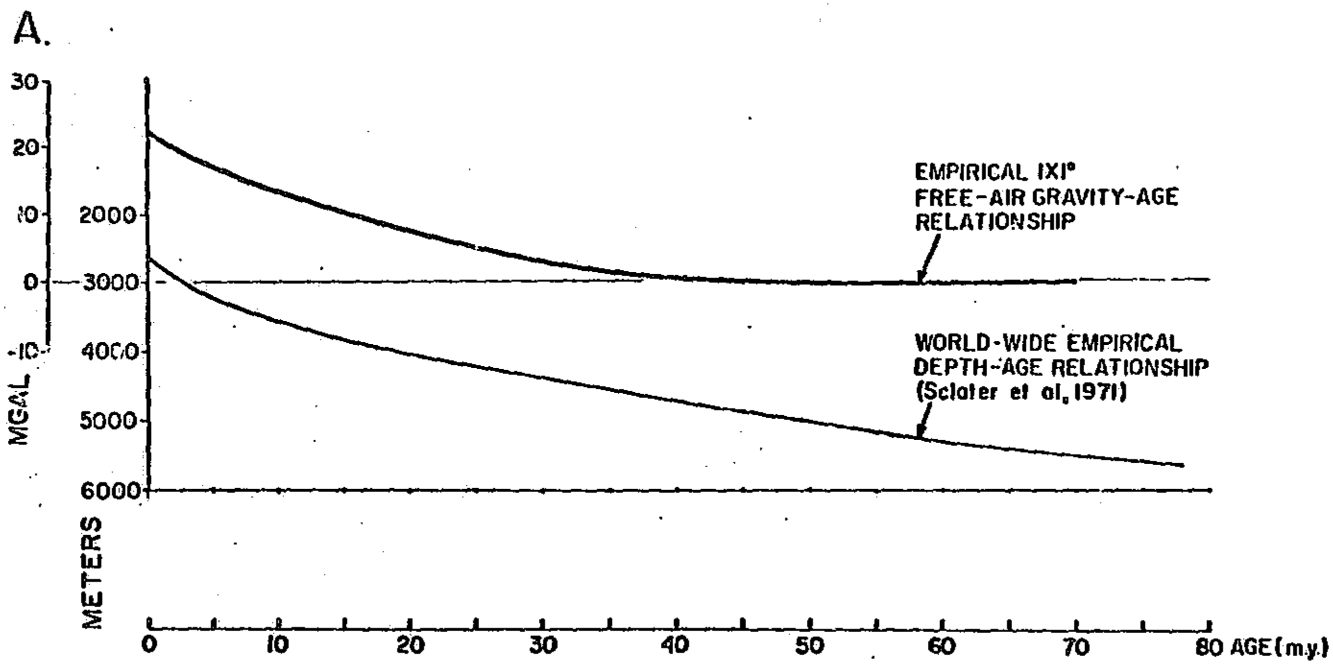

Figure 5. Empirical ridge gravity anomaly curves plotted as a function of age (after Cochran and Talwani, 1977).

SUMMARY AND CONCLUSIONS

1. Gravimetric geoids have been constructed from 1° by 1° average gravity values in the northwest Pacific Ocean, Indian Ocean, and north Atlantic.

2. The comparison of the gravimetric geoids with geoids obtained from GEOS-3 altimeter shows that

   (i) Wave lengths shorter than those used in the gravimetric geoids are actually measured by the altimeter;

   (ii) While there are causes for discrepancies, the general agreement between the geoids obtained by the two methods shows that there is great promise for the altimeter method.

3. Substantial geoidal anomalies exist over mid-ocean ridges, and in the vicinity of deep sea trenches and island arcs.

4. Geoidal anomalies also exist on continental margins, over seamounts, and even over short wavelength features such as fracture zones on transverse crossings.

5. Mathematical techniques have been developed to compute the geoid undulations caused by bodies of known geometry.

6. Future studies with altimeter geoids should lie in the direction of making geophysical interpretations of the geoidal signal over recognizable geological features. Such studies are being started.